Electronic excitations in complex systems: beyond density functional theory for real materials

Silvana Botti

Electronic excitations in complex systems: beyond density functional theory for real materials

Mémoire d'Habilitation à Diriger des Recherches

Université Claude Bernard – Lyon 1

Silvana Botti

March 3, 2010

Rapporteurs:

Claudia Amborsch-Draxl
Friedhelm Bechstedt
Claudine Noguera

Jury:

Lucia Reining
Alfonso San Miguel
Susanne Siebentritt
Ludger Wirtz

Date de la soutenance:

April 22, 2010

Contents

Résumé des Travaux

Aujourd'hui il est possible d'étudier à partir des premier principes la réponse sous excitation de matériaux utilisés dans des applications modernes très variés. En effet, grâce à de récents développements théoriques, ainsi qu'à l'optimisation des algorithmes de calcul, les simulations *ab initio* ne sont plus seulement limitées à des systèmes idéaux simplifiés, mais elles ont finalement l'ambition de capturer toute la complexité de l'échantillon testé dans l'expérience.

Dans ce contexte, ce mémoire porte sur l'étude, à l'aide de différentes approches *ab initio*, des excitations électroniques dans une gamme de matériaux complexes et nanostructurés. Pour accéder aux excitations électroniques, la connaissance de la densité de l'état fondamental du système n'est plus suffisante, ce qui signifie que l'on doit trouver le moyen approprié d'aller au-delà de la théorie de la fonctionnelle de la densité (DFT) standard. Deux voies ont été intensivement explorées: l'une est basée sur la densité dépendante du temps et l'autre sur les fonctions de Green.

La théorie de la fonctionnelle de la densité dépendante du temps (TDDFT) a été proposée en 1984 par Runge et Gross, qui ont dérivé un théorème du type Hohenberg-Kohn pour l'équation de Schrödinger en fonction du temps. Le champ d'application de cette généralisation de la théorie de la fonctionnelle de la densité inclut le calcul des spectres de photo-absorption ou, plus généralement, l'étude de l'interaction de la matière avec des champs électromagnétiques ou des particules qui la perturbent.

À présent, l'application la plus populaire de cette théorie est l'extraction des propriétés de l'état électronique excité, et en particulier des fréquences d'excitation électroniques. En appliquant la TDDFT, après avoir déterminé l'état fondamental d'une molécule ou un agrégat, nous pouvons explorer et comprendre son spectre d'absorption, ayant en même temps des informations extrêmement détaillées sur le comportement du système excité.

La complexité du problème à plusieurs corps en TDDFT est cachée dans le potentiel d'échange et de corrélation dépendant du temps qui apparaît dans les équations de Kohn-Sham et pour lequel il est primordial de trouver une bonne approximation. Beaucoup d'approximations ont été proposées et testées pour les systèmes finis, où même la très simple approximation TDLDA a souvent donné de très bons résultats. En général, les approximations existantes pour la fonctionnelle d'échange et corrélation fonctionnent assez bien pour certaines propriétés, mais elles se montrent insuffisantes pour d'autres. Dans le cas des matériaux solides, la TDDLA ne parvient pas à reproduire les spectres d'absorption optique, qui sont par contre bien décrits par la résolution de l'équation de Bethe-Salpeter en combinaison avec l'approximation GW pour les états de quasi-électron. D'autre part, la TDLDA peut déjà conduire à des résultats excellents pour la fonction de perte d'énergie d'un solide.

La solution de l'équation de Bethe-Salpeter est beaucoup plus onéreuse du point de vue numérique. Ainsi, on poursuit encore la recherche d'approximations fiables en TDDFT, et au fil du temps, on espère atteindre la même maturité qu'on trouve maintenant dans la DFT pour l'état fondamental.

En particulier, de nouvelles perspectives (et ses limites) ont étés révélées pendant ces dernières années grâce à la combinaison de deux théories distinctes : la TDDFT et l'approche des fonctions de Green (dont l'approximation GW et l'équation de Bethe-Salpeter font partie). Ces deux approches peuvent partager dans la pratique le point de départ commun de la théorie de la fonctionnelle de la densité pour le calcul de l'état fondamental électronique. Leur combinaison permet d'allier la simplicité de l'une (TDDFT) avec la précision de l'autre (GW et Bethe-Salpeter), afin d'en déduire des noyaux d'échange et de corrélation pour les solides. À partir de ces noyaux nous avons aussi travaillé sur le développement de noyaux modèles pour des applications efficaces à des systèmes de grande taille.

Le présent mémoire contient une vue d'ensemble relativement condensée de la TDDFT et des approches basées sur la théorie des fonctions de Green, avec des applications aux domaines des nanotechnologies, aux matériaux photovoltaïques et au stockage de données. Ces applications ont constitué notre principal sujet de recherche au cours des dernières années. Ce mémoire est organisée comme suit.

Avant d'entrer dans le domaine des approches pour les états excités, nous donnons dans le chapitre 1 un bref aperçu des idées de base de la DFT pour l'état fondamental, ce qui nous permet d'expliquer pourquoi il faut aller au-delà de la DFT standard, d'introduire quelques concepts-clés et de fixer la notation de base qui sera utilisée dans ce mémoire.

Les chapitres suivants font un point sur la théorie formelle, avec une brève présentation des approches théoriques utilisées pour étudier les excitations électroniques: le chapitre 2 est dédié aux approches GW et à l'équation de Bethe-Salpeter, tandis que la TDDFT et la théorie de la réponse linéaire sont décrites dans le chapitre 3. Les noyaux dérivés à partir de l'équation de Bethe-Salpeter et notre travail sur les noyaux modèles sont discutés dans le chapitre 4.

Le chapitre 5 contient des applications de la TDDFT dans le domaine de la réponse linéaire aux nanostructures. L'objectif principal est d'obtenir des spectres fiables (en général des spectres d'absorption) à partir de calculs de premiers principes. En comparant ces spectres avec des courbes expérimentales, on peut normalement déduire des informations importantes qui ne sont pas directement accessibles dans les expériences. D'autre part, la connaissance détaillée des propriétés d'excitation électronique contribue à une meilleure compréhension de la physique de ces systèmes dans leur généralité.

Le chapitre 6 présente des applications à des matériaux solides d'intérêt technologique. En particulier, nous nous sommes intéressé aux propriétés optiques des matériaux à changement de phase, utilisés dans le DVD re-inscriptibles, ainsi que aux états électroniques des absorbeurs et des oxydes transparents conducteurs pour les cellules solaires à couches minces.

Le chapitre 7 est dédié aux cruciales interactions de van der Waals et au calcul – via la TDDFT – des paramètres qui les décrivent. Nous discutons à la fois des interactions entre deux agrégats, et entre un agrégat et une surface semi-conductrice.

Le dernier chapitre 8 fait le point sur les résultats de notre réflexion.

Chapter 1

Introduction

1.1 Preliminary remarks

Most of today's quantum mechanical theoretical research in condensed matter physics and chemistry is not aimed at finding new fundamental interactions or basic laws, but it deals with solving the Schrödinger equation of a well-known Hamiltonian, and extracting useful information from the solution. This Hamiltonian, however, describes a many-body problem, and for a number of electrons above 10 it is impossible to even dream of a numerically exact solution. Moreover the exact solution would yield a wealth of information that could hardly be understood without further analysis and simplification, and contain many details that, for a given situation or question, one is probably not interested in [1]. Therefore it is often more appropriate to reformulate the problem, and work with effective Hamiltonians or selected expectation values that are suitable for the solution of a reduced problem. This procedure will ideally simplify both the calculation and the analysis of the desired quantities.

Density-Functional Theory (DFT) [2, 3] is a prominent example for such an approach. It has been designed for the calculation of ground state properties and it is based on the knowledge of the density $n(\mathbf{r})$ instead of the full many-body wavefunction $\Psi(\mathbf{r}_1, \sigma_1, \mathbf{r}_2, \sigma_2, \ldots, \mathbf{r}_N, \sigma_N)$ of the N-particle system. With the help of the Rayleigh-Ritz principle, it is possible to prove the following three statements, that constitute the celebrated Hohenberg-Kohn theorem [2] and that are the at the basis of DFT:

1. The ground state electronic density of an interacting system of electrons fully and uniquely determines the external potential, $v(\mathbf{r})$, that these electrons experience and thus the Hamiltonian, the many-body wave-function, and all observables of the system.

2. There exists a functional[1] $F[n]$ such that the total energy $E[n]$ can be written in the form
$$E[n] = F[n] + \int \mathrm{d}^3 r \, n(\mathbf{r}) v(\mathbf{r}) \,. \tag{1.1}$$
The functional F is universal, in the sense that its functional dependence on the density is the same for all systems with the same particle-particle interaction.

3. The ground state energy of this system can be obtained by minimizing the total energy functional $E[n]$ in terms of the density.

[1] By "$[n]$" we denote a functional dependence on n.

The Hohenberg-Kohn theorem is an existence theorem: it proves that the ground-state of the system can be obtained from the density alone, but, unfortunately, it does not teach us how to do it in practice. To overcome this impasse, Kohn and Sham [3] proposed the use of an auxiliary non-interacting system, the Kohn-Sham (KS) system, with the same density as the interacting system. In the KS scheme, the electrons obey a simple, one-particle, Schrödinger equation with an effective external potential v_{KS}:

$$\left[-\frac{\nabla^2}{2} + v_{\mathrm{KS}}[n](\mathbf{r})\right] \varphi_i(\mathbf{r}) = \varepsilon_i \varphi_i(\mathbf{r})\,. \tag{1.2}$$

The KS orbitals $\varphi_i(\mathbf{r})$ and KS eigenvalues ε_i do in general not have a direct physical meaning, but the former can be used to construct the true density of the interacting system according to

$$n(\mathbf{r}) = \sum_i |\varphi_i(\mathbf{r})|^2\,. \tag{1.3}$$

As v_{KS} is a functional of the electronic density, the solution of this equation has to be performed self-consistently. The effective potential v_{KS} is usually decomposed in the form

$$v_{\mathrm{KS}}(\mathbf{r}) = v_{\mathrm{ext}}(\mathbf{r}) + v_{\mathrm{Hartree}}(\mathbf{r}) + v_{\mathrm{xc}}(\mathbf{r})\,. \tag{1.4}$$

The first term is the external potential (normally the Coulomb interaction between the electrons and the nuclei), whereas the second includes the classical (Hartree) part of the electron-electron interaction. The complication of the problem is hidden in the – unknown – exchange and correlation (xc) potential $v_{\mathrm{xc}}[n](\mathbf{r})$, which is the functional derivative with respect to the density of the exchange-correlation energy contribution $E_{\mathrm{xc}}[n]$ to the total energy functional $E[n]$.

Very efficient approximations have been proposed for $E_{\mathrm{xc}}[n]$, such as the Local Density Approximation (LDA) [3] or Generalized Gradient Approximations (GGA) [4], and many ground state properties of extended systems, like lattice parameters or phonon frequencies [5], are today calculated from first principles with a precision of a few percent. There exist, however, ground state properties for which standard approximations do less well, even in simple systems: cohesive energies in particular can easily be off by 10% in LDA (because of errors in calculating the isolated atoms that enter this total energy difference), and failures are reported for static response properties, like the dielectric constant ϵ_∞, which is often substantially overestimated [6]. Other problems arise, e.g., in the description of strongly correlated systems [7], or of the van der Waals dispersion attraction [8]. These problems in calculating ground state properties can be traced back to limits of validity of the employed approximations.

Another problem of static ground state DFT-Kohn-Sham is the fact that excitations, such as those measured in the optical response to a time-dependent electric field, are in principle not accessible. This is not a question of the available approximations, but of the fact that the theory is not meant to describe these phenomena. In fact, even if one could calculate the exact Kohn-Sham eigenvalues, their differences would not necessarily be close to measured excitation energies. Neither, by definition, they stand for electron addition or removal energies [9]. Hence, the fact that the Kohn-Sham gap is in general reported to be too small with respect to measured gaps does not tell us *a priori* anything about the quality of a chosen approximation for the exchange-correlation potential.

If one wants to work with an efficient Hamiltonian that in principle yields eigenvalues meant to be electron addition or removal energies, or excitation energies, the knowledge of the static ground state density is not sufficient any more. Such energies can be found in essentially two ways.

First, by studying particle propagation and fluctuations in the system. This gives correlation functions that can then be related to response functions yielding, e.g., linear response for optical absorption. These correlation functions are one-or two body Green's functions [10] (or even higher order ones, for problems beyond the scope of this work). The one-body Green's function (that can essentially be understood as a time-dependent particle and hole density matrix) has phase fluctuations [or, in frequency (ω-) space, poles] given by electron addition and removal energies, measured, e.g., in photoemission or inverse photoemission experiments. The particle-hole part of the two-particle Green's function, in turn, has poles at the energies of neutral excitations. A contraction of the four-point reducible part $L(\mathbf{r}, \mathbf{r}_1, \mathbf{r}', \mathbf{r}'_1, \omega)$ of the two-particle Green's function leads to the two-point response function $\chi(\mathbf{r}, \mathbf{r}', \omega)$ that determines measurable spectra, like absorption or electron energy loss spectra (EELS). Many-body perturbation Theory (MBPT) yields a framework where suitable approximations for those Green's functions can be found. In particular the GW approximation, introduced in 1965 by Lars Hedin [11], has been extremely successful in describing electron addition and removal energies for metals, semiconductors and insulators, in the bulk as well as at surfaces and for confined structures, and is therefore one of the methods of choice for the description of direct and inverse photoemission experiments. Restricted self-consistent procedures [12, 13, 14] have been recently proposed and used with success for transition metal oxides, where standard perturbative GW fails. Concerning neutral excitations, the Bethe-Salpeter Equation (BSE) is a good starting point for approximations for χ [10, 15, 16, 17]. The price to be paid for a physically intuitive and in general quite reliable description is however relatively high in terms of computational cost, because now quantities like $L(\mathbf{r}, \mathbf{r}_1, \mathbf{r}', \mathbf{r}'_1, \omega)$ appear, instead of the density $n(\mathbf{r})$.

Second, by actually exposing (in the computer) the system to a time-dependent external potential and calculating the evolution of the density in time. The response function χ, for example, can then directly be determined from the linear response relation $n^{(1)}(\mathbf{r}, \omega) = \int d^3r' \chi(\mathbf{r}, \mathbf{r}', \omega) v^{(1)}_{\text{ext}}(\mathbf{r}', \omega)$ between the variation of the external potential and the induced density. This route has become accessible thanks to the extension of DFT to its time-dependent formulation (TDDFT) [18, 19, 20, 21, 22]. Put on a rigorous basis by the Runge-Gross theorem [19], one can intuitively understand that in TDDFT the quantum-mechanical "trajectory" of the system under the influence of a time-dependent external potential is found by searching for the extrema of an action (instead of the minimization of a total energy, as done for the ground state), by analogy to the case of classical mechanics. One obtains hence the time-dependent Kohn-Sham equations as generalization of the static case, and from these, response functions describing neutral excitations of a system [23]. At this point the difficulty resides in finding suitable approximations for the time-dependent exchange-correlation potential $v_{\text{xc}}[n](\mathbf{r}, t)$. Note that now the functional dependence is on the density in the whole space and at all past times.

Many approximations have been suggested and tested for finite systems. Even the very simple adiabatic local density approximation (ALDA, also called Time-Dependent LDA, TDLDA) where $v^{ALDA}_{\text{xc}}[n](\mathbf{r}, t) = v^{LDA}_{\text{xc}}(n(\mathbf{r}, t))$ has proved to be very successful in many cases [18, 24], although the lack of a long range ($1/r$) decay of the potential can lead to serious problems for questions like Rydberg states [25]. The latter shortcoming of the LDA potential is not so crucial in solids where the electron density is quite homogeneous (compared to an atom in empty space); instead, the wrong long-range behavior of the linear response kernel $f_{\text{xc}}(\mathbf{r}, \mathbf{r}', t, t') = \delta v_{\text{xc}}[n](\mathbf{r}, t)/\delta n(\mathbf{r}', t')$ can cause large errors [17]. In fact in the ALDA this kernel is proportional to $\delta(\mathbf{r} - \mathbf{r}')$, whereas in non-metallic systems it should decay as $1/|\mathbf{r} - \mathbf{r}'|$ [26]. This shortcoming already shows up, e.g., in the calculation of polarizabilities for molecular chains [27]. In the case of absorption spectra of solids, where

the imaginary part of the dielectric function ϵ for vanishing wavevector $\mathbf{q}$ (corresponding to a macroscopic average) is calculated, the lack of a $1/q^2$ divergence (stemming from the Fourier transform of $1/|\mathbf{r}-\mathbf{r}'|$) can lead to drastic failures. For example, the ALDA is not able to reproduce bound excitons [17]. On the other hand, for a finite momentum transfer or when the loss function $-\Im\mathrm{m}\,(\epsilon^{-1})$ is the quantity of interest (e.g., in Electron Energy Loss or Inelastic X-ray Scattering spectra) this term is not dominant, and the ALDA can lead to very good results (see, e.g., [28, 29, 30, 31]). For this reason, and because of recent successful developments of improved linear response kernels derived from MBPT [32, 33, 34, 35, 36, 37, 38], TDDFT is today considered to be an alternative to MBPT for the calculation of electronic spectra, even for solids.

Today, the use of approaches such as GW, BSE and TDDFT is continuously growing, in all areas where interactions are important but the direct solution of the Schrodinger equation is unfeasible. The present manuscript contains a fairly condensed overview of MBPT and TDDFT, and some examples of their applications to complex systems in the fields of nanotechnology, data storage and photovoltaics. These constitute the main research topics of the Author for the past years.

The manuscript is organized as follows.

Chapters 2 and 3 deal with fundamentals of theoretical approaches, such as GW and TDDFT, based on DFT and going beyond its limitations. In particular, we discuss the available functionals and approximations and the accuracy of results that they give in typical calculations. In chapter 4 we introduce a class of model kernels, derived from the BSE, that are successful for the description of optical absorption in some classes of solids, with a strongly reduced computational impact.

Chapters 5 and 6 deal with applications of GW and TDDFT within linear response. The main objective is to obtain reliable spectra (usually absorption) from *ab initio* calculations. By comparing theoretical spectra with experimental curves, one is usually able to deduce important information that is not directly available from experiment. Moreover, a better understanding of the excitation properties of the systems opens the way for the design of new materials with improved performances.

Chapter 7 is concerned with the important issue of van der Waals interactions, and how to extract, from TDDFT calculations, relevant parameters to describe them. We will discuss both the interaction between two finite systems, and between a finite system and a semiconducting surface.

Hartree atomic units will be used throughout this manuscript, unless explicitly stated.

Part I

Theoretical background

Chapter 2

The GW approximation and the Bethe-Salpeter equation*

To go beyond simple density functional theory (DFT) for the calculation of electronic excitations, such as single-electron addition and removal energies measured in photoemission, the GW approximation by Hedin [11], in the context of many-body perturbation theory (MBPT), has emerged over the years as an invaluable tool. The key variables are in this case the one-particle Green's functions G and the screened Coulomb interaction W. The one-particle Green's function can be viewed as a dynamical one-particle density matrix: it contains more information than a simple density, but of course much less than the many-body wavefunction. Beside to all relevant physical quantities already accessible through the density, one-particle Green's functions give access to the the single-particle excitation spectrum (i.e., the band structure) and spectral functions. The particle-hole part of the two-particle Green's function, in turn, has poles at the energies of neutral excitations. A contraction of the four-point reducible part of this quantity leads to the two-point response functions that determine measurable spectra, such as absorption or electron energy loss spectra (EELS). MBPT and in particular the Bethe-Salpeter equation (BSE) are the framework where suitable approximations for the two-particle Green's functions can be easily found.

After introducing the GW approximation, we will discuss the recently developed schemes to perform self-consistent quasiparticle calculations, in particular the one based on Hedin's COHSEX approximation [14] and the quasiparticle self-consistent GW by Faleev and coauthors [12]. Finally, we will introduce the Bethe-Salpeter equation and the approximations usually employed to solve it.

A more detailed discussion of the basic physical ideas reviewed in this chapter can be found in MBPT textbooks (see, e.g., Refs. [10, 39]), in the fundamental reviews of Hedin and Lundqvist [40] and Strinati [41].

2.1 Hedin's equations and the GW approximation

The time-ordered one-particle Green's function is defined as

$$G(1,2) = -\mathrm{i}\langle\Psi_0|T\left[\hat{\psi}(1)\hat{\psi}^\dagger(2)\right]|\Psi_0\rangle, \tag{2.1}$$

*Part of this chapter is based on the article:

- *Time-dependent density-functional theory for extended systems*, S. Botti, A. Schindlmayr, R. Del Sole, and L. Reining, Rep. Prog. Phys. **70**, 357-407 (2007).

where $|\Psi_0\rangle$ is the many-body N-particle ground state, $\hat{\psi}(1)$ [$\hat{\psi}^\dagger(1)$] is the annihilation (creation) operator of an electron in the Heisenberg picture, T is the time-ordering operator and 1 stands for the set of the real space and time coordinates plus the spin degree of freedom, $1 = \{\mathbf{r}_1, t_1, \sigma_1\}$. The Green's function G has poles that correspond to electron addition and removal energies.

The time evolution of G corresponds to the propagation of an electron (or a hole) and obeys:

$$\left[\mathrm{i}\frac{\partial}{\partial t_1} + \frac{\nabla^2}{2} - V_{\mathrm{ext}}\right] G(1,2) = \delta(1,2) - \mathrm{i}\int d3\, v(1,3) G_2(1,3,2,3^+) \tag{2.2}$$

where v is the bare Coulomb potential and V_{ext} is an external potential. The equation of motion (2.2) describes how a moving charged particle polarizes the system creating electron-hole pairs along its way. For this reason also a two-particle quantity, the two-particle Green's function G_2 (which describes the creation and annihilation of pairs of particles) is involved in Eq. (2.2). In order to derive the equation of motion for G_2, G_3, etc., higher order Green's functions must be considered. The hierarchy of equations involving Green's functions of increasing order can be evaluated using diagrammatic expansions based on the Wick theorem. Alternatively, one can use Schwinger's functional derivatives to obtain a set of equations governing G to be further approximated. Here we follow the second line to give a brief summary of the GW formalism developed in its present form by Lars Hedin [11].

Even though G is still unknown, Eq. (2.2) tells us that its evolution involves a polarization of the system (i.e., G_2). The physical idea at the heart of Schwinger's formalism is that the very polarization can be created as a response to a time-dependent perturbing external potential U. In the spirit of the linear-response theory, the time-dependent part of the potential will be made to vanish at the end of the derivation, so that $U \to V_{ext}(\mathbf{r})$ at $\pm\infty$. As a consequence, the one-particle term of the Hamiltonian in Eq. 2.2, namely $h_0 = -\frac{\nabla^2}{2} + V_{\mathrm{ext}}$, becomes now $h_0 = -\frac{\nabla^2}{2} + U$.

It is possible to show that the variation of G with respect to U gives:

$$\frac{\delta G(1,2)}{\delta U(3)} = G(1,2)G(3,3^+) - G_2(1,3,2,3^+)\,. \tag{2.3}$$

By inserting (2.3) in (2.2) one obtains:

$$\left[\mathrm{i}\frac{\partial}{\partial t_1} - h_0(1) + i\int d3\, v(1,3) G(3,3^+)\right] G(1,2) = \delta(1,2) + \mathrm{i}\int d3\, v(1^+,3)\frac{\delta G(1,2)}{\delta U(3)}\,. \tag{2.4}$$

As $-\mathrm{i}G(3,3^+) = \rho(3)$, the term $-\mathrm{i}\int d3\, v(1,3)G(3,3^+)$ is just the Hartree potential $V_{\mathrm{H}}(1)$, which means that the effects of the perturbation U on the system can be split into a classical contribution (i.e., the Hartree term) and a contribution that encompasses quantum effects. The latter term can be cast in the equivalent way, by defining the self-energy Σ as:

$$\mathrm{i}\int d3 v(1^+,3)\frac{\delta G(1,2)}{\delta U(3)} = \int d3\, \Sigma(1,3)G(3,2)\,. \tag{2.5}$$

The self-energy therefore turns out to be the effective non-local and dynamical potential that describes all the effects of exchange and correlation in the system. Physically, it represent the effective potential that the extra particle feels for the polarization that its propagation induces for exchange effects, due to the fact that it is a fermion. It is now possible to rewrite (2.2) as:

$$\left[\mathrm{i}\frac{\partial}{\partial t_1} - h_0(1) - V_{\mathrm{H}}(1)\right] G(1,2) = \delta(1,2) + \int d3\, \Sigma(1,3)G(3,2)\,. \tag{2.6}$$

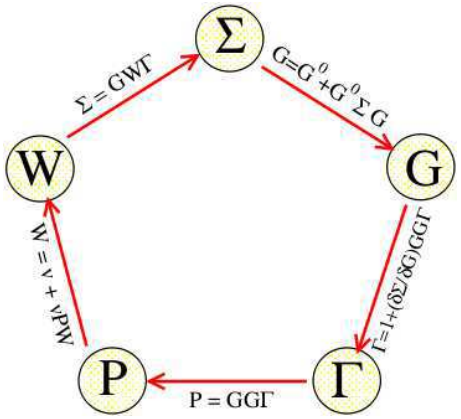

Figure 2.1: Hedin's pentagon connecting the Green's function G, the self-energy Σ, the vertex Γ, the polarizability P and the screened interaction W.

The Hartree Green's function is defined as the resolvent of the Hartree Hamiltonian (but calculated with the exact electronic density ρ), where one has $\Sigma = 0$:

$$\left[\mathrm{i}\frac{\partial}{\partial t_1} - h_0(1) - V_{\mathrm{H}}(1)\right] G_{\mathrm{H}}(1,2) = \delta(1,2)\,. \tag{2.7}$$

Combining Eq. (2.6) with Eq. (2.7) one finds the Dyson equation for G:

$$G(1,2) = G_{\mathrm{H}}(1,2) + \int d34\, G_{\mathrm{H}}(1,3)\Sigma(3,4)G(4,2)\,. \tag{2.8}$$

The self-energy describes a renormalization effect: the difference between the propagation of an independent (Hartree) particle and the propagation of an interacting fermionic particle.

From (2.5) one can then extract with a little of algebra:

$$\Sigma(1,2) = \mathrm{i}\int d34\, v(1^+,3)\frac{\delta G(1,4)}{\delta U(3)}G^{-1}(4,2) = -\mathrm{i}\int d34\, v(1^+,3)G(1,4)\frac{\delta G^{-1}(4,2)}{\delta U(3)}\,, \tag{2.9}$$

since

$$\frac{\delta G(1,2)}{\delta U(3)} = -\int d45 G(1,4)\frac{\delta G^{-1}(4,5)}{\delta U(3)}G(5,2)\,. \tag{2.10}$$

Equivalently, one can write:

$$\Sigma(1,2) = \mathrm{i}\int d34\, G(1,4)\Gamma(4,2;5)\frac{\delta V(5)}{\delta U(3)}v(3,1^+)\,. \tag{2.11}$$

where $V(1) = U(1)+V_{\mathrm{H}}(1)$ is the total classical potential, and having defined the irreducible vertex function

$$\Gamma(1,2;3) = -\frac{\delta G^{-1}(1,2)}{\delta V(3)} = \delta(1,3)\delta(2,3) + \frac{\delta\Sigma(1,2)}{\delta V(3)}\,. \tag{2.12}$$

The derivative $\delta\Sigma/\delta V$ is then usually replaced by the chain rule $(\delta\Sigma/\delta G)(\delta G/\delta V)$. Using the relation (2.10), Eq. (2.12) is transformed into an integral equation:

$$\Gamma(1,2;3) = \delta(1,2)\delta(1,3) + \int d4567\,\frac{\delta\Sigma(1,2)}{\delta G(4,5)}G(4,6)G(7,5)\Gamma(6,7;3). \tag{2.13}$$

Following a strictly analogous procedure, one obtains the remaining equations:

$$\Sigma(1,2) = i \int d34\, G(1,3)\Gamma(3,2;4)W(4,1)\,, \tag{2.14}$$

$$W(1,2) = v(1,2) + \int d34\, v(1,3)P(3,4)W(4,2)\,, \tag{2.15}$$

$$P(1,2) = -i \int d34\, G(1,3)G(4,1)\Gamma(3,4;2)\,, \tag{2.16}$$

in terms of the time-ordered polarization operator $P(1,2)$, and the dynamical screened interaction $W(1,2) = \delta V(1)/\delta U(3) v(3,2) = \epsilon^{-1}(1,3)v(3,2)$. Eqs. (2.8), (2.13), (2.14), (2.15), (2.16) are the close set of 5 equations known as Hedin's equations. They depend on one another and should be solved iteratively, following the scheme of Fig. 2.1.

Disregarding the second term on the right-hand side of Eq. (2.13) the famous GW approximation is recovered:

$$\Gamma(1,2;3) = \delta(1,2)\delta(1,3) \qquad \Longrightarrow \qquad \Sigma(1,2) = iG(1,2)W(2,1) \tag{2.17}$$

To include vertex corrections, Eq. (2.13), or an equivalent form, with its four-point kernel dominated by $\delta\Sigma(1,2)/\delta G(3,4)$, has to be solved in order to get the irreducible polarizability $P = -iGG\Gamma$ [1] and an improved self-energy from Eq. (2.14). In view of that, Eq. (2.13) is the main obstacle on the way to a calculation of polarizabilities or self-energies beyond the RPA.

We stress that in contrast to the Hartree-Fock approximation, in the GW approach the existence of polarization effects that screen the propagation of an extra particle is explicitly taken into account: while in Hartree-Fock there is no polarization and no relaxation of the system and the self-energy is static, GW is a dynamically screened approximation. Even if vertex corrections are neglected and the self-energy is evaluated in the GW approximation, still the Dyson equation is a self-consistent equation in G and should be solved iteratively. In this sense the starting point is arbitrary. In fact, it is possible to start with the Green's function of any non-interacting system and iterate self-consistently (keeping the vertex $\Gamma = 1$). This idea is represented in the scheme of Fig. 2.2. In particular, Hedin obtained the GW approximation by iterating Hedin's equations starting from $\Sigma = 0$, i.e., from the Hartree Green's function. Modern calculations, starting from the works of Strinati, Mattausch and Hanke [42] and then Hybertsen and Louie [43, 44] and Godby, Schlüter and Sham [9, 45], instead use a "best G, best W" approach [46]. In this spirit, one dismisses the idea of a strict iterative solution of Hedin's equations. Instead, the GW self-energy is constructed using the best mean-field results that are available, in general the Kohn-Sham eigenvalues and eigenfunctions. The standard use of this approach, that we will refer to as one-shot GW, starts from a DFT Kohn-Sham calculation (normally in LDA), and evaluates the quasiparticle corrections to the band-structure perturbatively, i.e., ignoring the self-consistent process.

It is clear that this procedure is justified when the departure wave-functions are already close to the quasiparticle ones. This is indeed the case in many systems, and therefore

[1] The irreducible polarizability P defined here is a time-ordered quantity. From the time-ordered P one can then obtain a physical (causal) response function with the usual conversion rules. It should be noted that in the following we do not make a distinction between time-ordered and causal quantities. However, one has to be careful because this apparent "subtlety" could cause severe errors in practice when not properly accounted for. One possible way is represented by the Keldysh formalism. In this scheme all the quantities are consistently defined on the Keldysh contour and pseudo-time-ordered. At the end, projecting from the pseudo-time to the physical time, causal physical response functions are restored.

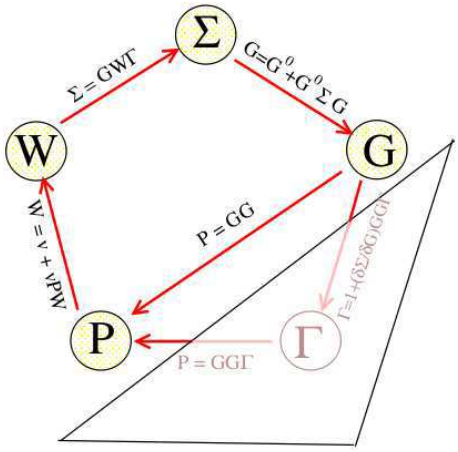

Figure 2.2: Schematic representation of the restricted self-consistent scheme.

one-shot GW has been extremely successful in describing electron addition and removal energies for metals, semiconductors and insulators [47], and is one of the methods of choice for the description of direct and inverse photoemission experiments. However, one-shot GW has proved to be insufficient for many transition metal compounds [13, 48, 14, 49, 50]. The problem in many cases is that the LDA wave-functions are not localized enough, leading often to a metallic systems. This can be traced back to a wrong hybridization of the d states of the transition metal with other states (like, e.g., the p states of O, S or Se [49, 50, 51]) close to the Fermi level that leads to a closing of the energy gap. One-shot GW may improve upon this situation by opening the gap, but usually by a largely insufficient amount. Several methods appeared in the last couple of years to solve this problem. They follow two main lines: i) Replacing the simple LDA as starting point and then performing a single-shot GW calculation. Several different starting points can be found in the literature, like GGA [52], exact exchange [53], LDA/GGA+U [54, 55] or hybrid functionals [56]. ii) Performing (restricted) self-consistent GW [12, 13, 14]. This technique has the advantage of being independent of the starting point at the price of large computational complexity. Fortunately, there is an alternative procedure that yields wavefunctions that are extremely close to those obtained in a full sc-GW calculation, namely sc-COHSEX as explained in Ref. [14]. The dynamical effects that are absent in COHSEX calculations can then be accounted for by performing a final perturbative GW step. This method, that we will refer to as sc-GW, has been applied to many oxide compounds, yielding excellent results for the band gaps and the quasiparticle band structure [48, 14, 49, 50].

2.2 The Bethe-Salpeter equation

Band structures and photoemission experiments need a description in terms of a one-particle effective Hamiltonian for one-particle excitations: the quasiparticles. In case of absorption experiments, instead, one has to deal with neutral excitations due to the simultaneous creation of a quasielectron and a quasihole which interact in the system. A one-particle description is no longer adequate. In this section we will therefore introduce the effective two-particle Hamiltonian capable of dealing with these neutral excitations.

The BSE uses the intuitive quasi-particle picture, which makes the task to identify efficient approximations easier. However, within MBPT one deals with four-point equations. In fact, a key quantity is the four-point reducible polarizability L, that can be expressed in

terms of the two-particle Green's function G_2 describing the propagation of two particles (for absorption, the relevant part describes the propagation of an electron and a hole):

$$L(1,2,3,4) = L_0(1,2,3,4) - G_2(1,2,3,4)\,. \tag{2.18}$$

L_0 is the disconnected part consisting of two one-particle Green's functions G:

$$L_0(1,2,3,4) = \mathrm{i}G(1,3)G(4,2)\,. \tag{2.19}$$

The function L satisfies a Dyson-like screening equation, known as the Bethe-Salpeter equation:

$$L(1,2,3,4) = L_0(1,2,3,4) + \int d5678\, L_0(1,2,5,6)\left[v(5,7)\delta(5,6)\delta(7,8) + \Xi(5,6,7,8)\right] L(7,8,3,4)\,. \tag{2.20}$$

In order to solve Eq. (2.20) one has to approximate the many-body interaction kernel Ξ. The standard approximation consists in using the GW self-energy of Eq. (2.17). In this way the solution of the Bethe-Salpeter equation corresponds to the inclusion of vertex corrections in P through a second iteration of Hedin's cycle of equations. When its kernel is approximated to first order in the screened Coulomb interaction W it reads:

$$L = L_0 + L_0\left({}^4v - {}^4W\right) L\,. \tag{2.21a}$$

In Eq. (2.20) we have defined the four-point extension of the Coulomb potential ${}^4v(1,2,3,4) = \delta(1,2)\delta(3,4)v(1,3)$, whereas ${}^4W = \delta(1,3)\delta(2,4)W(1,2)$ is the four-point extension of the screened Coulomb potential. The first term is the unscreened electron-hole exchange and is repulsive, while the second is the screened electron-hole Coulomb interaction and is attractive. Note that the δ-functions connect different indices in the two cases; this is due to the fact that the former stems from variations of the Hartree potential, whereas the latter is due to variations of an exchange-like self-energy contribution. Because of the way the indices are connected in this second case, the BSE can not be written in a two-point form. This issue represents the real bottleneck in practical calculations. Instead, the measurable χ is obtained via a two-point contraction of L, namely

$$P^{\mathrm{red}}(1,2) = -L(1,1,2,2)\,. \tag{2.22}$$

From the reduced polarizability P^{red} that is understood to be time (or contour) -ordered, the causal response function χ can be inferred; the relation between the time-ordered and causal response is in fact $\chi(\omega > 0) = P^{\mathrm{red}}(\omega > 0)$. Another useful quantity is the independent quasi-particle polarizability, $P_0(1,2) = -L_0(1,1,2,2)$. Note that this is *not* equal to $\chi_{\mathrm{KS}} = -\mathrm{i}G_{\mathrm{KS}}G_{\mathrm{KS}}$. The expression looks similar, but the Kohn-Sham states and eigenvalues in χ_{KS} are now replaced by their MBPT counterparts, which are, on this level of approximation, usually determined in the quasi-particle GW approximation [11] (to be precise, most realistic calculations use GW eigenvalues and Kohn-Sham wavefunctions to build G).

For simple semiconductors dynamical effects in the electron-hole screening in W and in the Green's function G tend to cancel, therefore they are usually neglected in both terms. This means that, instead of $W(1,2)$ one uses a statically screened instantaneous interaction and for G the Green's function obtained by a perturbative GWcalculation (i.e., G is built with Kohn-Sham orbitals and quasiparticle eigenvalues with GW corrections included). In practice, the Bethe-Salpeter equation (2.20) can be solved by diagonalizing a two-particle excitonic Hamiltonian which moreover provides information about the excitonic eigenstates and eigenvalues. The solution of the Bethe-Salpeter equations has yield very successful results in the calculation of optical properties of solids with continuum and bound excitons, in bulk and nanostructured systems (see Ref. [17] and references therein).

Chapter 3

Time-dependent density functional theory*

As the quantum-mechanical treatment of stationary and time-dependent systems differs in many aspects, it is not straightforward to generalize the mathematical framework of static density-functional theory. For example, the total energy, which plays a central role in the original Hohenberg-Kohn theorem [2], is not a conserved quantity in the presence of time-dependent external fields, and there is hence no variational principle for it on the basis of the density that can be exploited. In this section we start by discussing the theoretical foundations of TDDFT with a special emphasis on the linear density-response function and its connection to the electronic excitation spectrum.

3.1 The Runge-Gross theorem

The evolution of a (non-relativistic) spin-unpolarized interacting many-electron system is governed by the time-dependent Schrödinger equation

$$\mathrm{i}\frac{\partial}{\partial t}\Psi(\{\mathbf{r}\},t) = \hat{H}(\{\mathbf{r}\},t)\Psi(\{\mathbf{r}\},t)\,, \quad \Psi(\{\mathbf{r}\},t_0)\,\text{given}\,, \tag{3.1}$$

where $\hat{H}$ is the Hamiltonian operator of the system and $\{\mathbf{r}\} = \{\mathbf{r}_1,\ldots,\mathbf{r}_N\}$ are the spatial coordinates of the N electrons. The Hamiltonian can be written in the form

$$\hat{H}(\{\mathbf{r}\},t) = \sum_{i=1}^{N}\left[-\frac{1}{2}\nabla_i^2 + v_{\mathrm{ext}}(\mathbf{r}_i,t)\right] + \frac{1}{2}\sum_{i\neq j}^{N} v(\mathbf{r}_i-\mathbf{r}_j)\,, \tag{3.2}$$

where $v_{\mathrm{ext}}(\mathbf{r},t)$ is the time-dependent external potential and $v(\mathbf{r}_i-\mathbf{r}_j) = 1/|\mathbf{r}_i-\mathbf{r}_j|$ the Coulomb interaction. Being interested in spectroscopy, we consider scenarios where the system is initially at rest in a static potential $v_{\mathrm{ext}}(\mathbf{r},t) = v^0_{\mathrm{ext}}(\mathbf{r})$, before a time-dependent perturbation is switched on at $t = t_0$ in order to probe the response of the electron system. Under these circumstances the initial state at t_0 is given by the stationary ground-state wave function, which is determined up to an irrelevant phase factor for non-degenerate systems. By virtue of the Hohenberg-Kohn theorem it is also a functional of the static

*This chapter is based on the articles:

- *Time-dependent density-functional theory for extended systems*, S. Botti, A. Schindlmayr, R. Del Sole, and L. Reining, Rep. Prog. Phys. **70**, 357-407 (2007).

ground-state density $n(\mathbf{r},t_0) = n_{\rm GS}(\mathbf{r})$. We only admit physical potentials that are finite everywhere and vary smoothly in time, so that they can be expanded into a Taylor series about the initial time t_0

$$v_{\rm ext}(\mathbf{r},t) = \sum_{k=0}^{\infty} \frac{c_k(\mathbf{r})}{k!}(t-t_0)^k \quad \text{with} \quad c_k(\mathbf{r}) = \frac{\partial^k}{\partial t^k} v_{\rm ext}(\mathbf{r},t)\bigg|_{t=t_0} . \tag{3.3}$$

The theoretical basis of TDDFT is the Runge-Gross theorem [19], which asserts the one-to-one correspondence between the external potential and the density, thus playing the same role as the Hohenberg-Kohn theorem in static density-functional theory. Of course, for a given external potential it is always possible, in principle, to solve the time-dependent Schrödinger equation (3.1); the density is then given by

$$n(\mathbf{r},t) = N \int d^3r_2 \int d^3r_3 \ldots \int d^3r_N \, |\Psi(\mathbf{r},\mathbf{r}_2,\ldots,\mathbf{r}_N,t)|^2 . \tag{3.4}$$

What remains to be proved, in order to demonstrate the one-to-one correspondence, is that if two potentials $v_{\rm ext}(\mathbf{r},t)$ and $v'_{\rm ext}(\mathbf{r},t)$ differ by more than a purely time-dependent function, then the associated densities $n(\mathbf{r},t)$ and $n'(\mathbf{r},t)$ must be distinct. The addition of a purely time-dependent function is exempt because it only changes the phase of the wave function but not the density. One assumes that both systems evolve from the same initial ground-state wave function $\Psi(\{\mathbf{r}\},t_0)$. The expansion coefficients of the two potentials around t_0 are denoted by $c_k(\mathbf{r})$ and $c'_k(\mathbf{r})$, and one defines $u_k(\mathbf{r}) = c_k(\mathbf{r}) - c'_k(\mathbf{r})$. If the potentials differ by more than a purely time-dependent function, then at least one coefficient $u_k(\mathbf{r})$ is not a mere constant but a spatially varying function. For the proof of the Runge-Gross theorem given in [19] one makes use of the current density

$$\begin{aligned}\mathbf{j}(\mathbf{r},t) = -\frac{\mathrm{i}}{2}N \int d^3r_2 \int d^3r_3 \ldots \int d^3r_N \, \{&\Psi^*(\mathbf{r},\mathbf{r}_2,\ldots,\mathbf{r}_N,t)\nabla\Psi(\mathbf{r},\mathbf{r}_2,\ldots,\mathbf{r}_N,t) \\ &-\nabla\Psi^*(\mathbf{r},\mathbf{r}_2,\ldots,\mathbf{r}_N,t)\Psi(\mathbf{r},\mathbf{r}_2,\ldots,\mathbf{r}_N,t)\} ,\end{aligned} \tag{3.5}$$

which can also be written in a second quantization formalism as

$$\mathbf{j}(\mathbf{r},t) = -\frac{\mathrm{i}}{2}\langle\Psi(t)|\hat{\psi}^\dagger(\mathbf{r})\left[\nabla\hat{\psi}(\mathbf{r})\right] - \left[\nabla\hat{\psi}^\dagger(\mathbf{r})\right]\hat{\psi}(\mathbf{r})|\Psi(t)\rangle , \tag{3.6}$$

The time evolution of the current density can be discussed by means of the equation of motion

$$\mathrm{i}\frac{d}{dt}\mathbf{j}(\mathbf{r},t) = \langle\Psi(t)\,\Big|\,\Big[\hat{\mathbf{j}}(\mathbf{r}),\hat{H}(t)\Big]\,\Big|\,\Psi(t)\rangle . \tag{3.7}$$

Moreover, $\mathbf{j}(\mathbf{r},t)$ is related to the density through the continuity equation

$$\frac{\partial}{\partial t}n(\mathbf{r},t) = -\nabla\cdot\mathbf{j}(\mathbf{r},t) . \tag{3.8}$$

This identity expresses the conservation of the total particle number in a differential form: the change in the number of electrons within a certain volume equals the flux through its surface. In the first step one shows that the current densities $\mathbf{j}(\mathbf{r},t)$ and $\mathbf{j}'(\mathbf{r},t)$ induced by the two potentials differ. To this effect one examines the time derivative

$$\begin{aligned}\mathrm{i}\frac{d}{dt}\left\{\mathbf{j}(\mathbf{r},t) - \mathbf{j}'(\mathbf{r},t)\right\}_{t=t_0} &= \langle\Psi_0\,\Big|\,\Big[\hat{\mathbf{j}}(\mathbf{r}),\hat{H}(t_0) - \hat{H}'(t_0)\Big]\,\Big|\,\Psi_0\rangle \\ &= \langle\Psi_0\,\Big|\,\Big[\hat{\mathbf{j}}(\mathbf{r}),\hat{v}_{\rm ext}(\mathbf{r},t_0) - \hat{v}'_{\rm ext}(\mathbf{r},t_0)\Big]\,\Big|\,\Psi_0\rangle \\ &= \mathrm{i}n(\mathbf{r},t_0)\nabla\left\{v_{\rm ext}(\mathbf{r},t_0) - v'_{\rm ext}(\mathbf{r},t_0)\right\} = n(\mathbf{r},t_0)\nabla u_0(\mathbf{r}) ,\end{aligned} \tag{3.9}$$

which follows from the definition (3.6) together with the known evolution of the current density (3.7). If $u_0(\mathbf{r})$ is not a constant, then the right-hand side is non-zero, and consequently the derivatives of the current densities at t_0 must be distinct. The potential might also differ by a coefficient u_k with $k \neq 0$; in this case one can take an appropriate higher time derivative

$$\frac{d^{k+1}}{dt^{k+1}} \left\{ \mathbf{j}(\mathbf{r},t) - \mathbf{j}'(\mathbf{r},t) \right\}_{t=t_0} = n(\mathbf{r},t_0) \nabla u_k(\mathbf{r}) \,, \tag{3.10}$$

with the non-constant $u_k(\mathbf{r})$ establishing hence that at least one term in the Taylor expansions of $\mathbf{j}(\mathbf{r},t)$ and $\mathbf{j}'(\mathbf{r},t)$ differs. This implies that the current densities themselves deviate for $t > t_0$. In the second step one proves that the corresponding densities also differ. For this purpose one takes the (k+1)st time derivative of the continuity equation (3.8) and again examine the difference

$$\frac{\partial^{k+2}}{\partial t^{k+2}} \left\{ n(\mathbf{r},t) - n'(\mathbf{r},t) \right\}_{t=t_0} = -\nabla \cdot \frac{\partial^{k+1}}{\partial t^{k+1}} \left\{ \mathbf{j}(\mathbf{r},t) - \mathbf{j}'(\mathbf{r},t) \right\}_{t=t_0} = \\ - \nabla \cdot \{ n(\mathbf{r},t_0) \nabla u_k(\mathbf{r}) \} \tag{3.11}$$

between the two systems. If the quantity on the right-hand side is non-zero, then the (k+2)nd terms in the Taylor expansions of $n(\mathbf{r},t)$ and $n'(\mathbf{r},t)$ around t_0 differ, and the densities themselves must hence deviate for $t > t_0$. The original proof [19] refers only to finite systems, where both the potential and the density decay to zero at large distances, but for extended systems it is easy to see that the right-hand side of (3.11) vanishes only if $u_k(\mathbf{r})$ is of the form

$$u_k(\mathbf{r}) = u_k(\mathbf{0}) - \int_{\mathbf{0}}^{\mathbf{r}} \frac{n(\mathbf{0},t_0)}{n(\mathbf{r}',t_0)} \mathbf{E}_k \cdot d\mathbf{r}' \,, \tag{3.12}$$

with an arbitrary but constant vector $\mathbf{E}_k$. As the density is always positive, $u_k(\mathbf{r})$ then grows beyond all bounds as $|\mathbf{r}| \to \infty$, which implies that at least one of the potentials $v_{\text{ext}}(\mathbf{r},t)$ or $v'_{\text{ext}}(\mathbf{r},t)$ becomes infinite. However, this case was explicitly excluded. For all finite physical potentials the right-hand side of (3.11) is indeed non-zero. This concludes the proof of the Runge-Gross theorem. Note that potentials of the type (3.12) are also incompatible with the Hohenberg-Kohn theorem in static density-functional theory: as the energy of the electrons can always be lowered by a translation in the direction of the field vector, there is no ground-state solution [57].

The Runge-Gross theorem is, in fact, a very strong statement: From the knowledge of the density alone it is possible to deduce the external potential and hence the many-body wave function, which in turn determines every observable of the system. Therefore, all observables can ultimately be regarded as functionals of the density. We note that, in contrast to more general cases [58, 59], there is no additional initial-state dependence in this scenario if one starts from the ground state, because the stationary wave function at t_0 itself is determined by the static ground-state density $n_0(\mathbf{r}) = n(\mathbf{r},t_0)$ of the unperturbed system.

3.2 The time-dependent Kohn-Sham equations

The Runge-Gross theorem states that all observables are functionals of the density, but it contains no prescription on how this central quantity can actually be calculated. To overcome the analogous problem in static density-functional theory, Kohn and Sham [3] suggested to use an auxiliary system of non-interacting electrons moving in an effective local potential, which is designed in such a way that the densities of the non-interacting system

and the real interacting electrons coincide. This scheme has the big advantage to include the exact non-interacting kinetic energy, which represents almost all the true kinetic energy of the N-electron system. The main task is then to find a good approximation for this *a priori* unknown effective potential. This idea was generalized to the time-dependent case, where the Kohn-Sham electrons obey [19]

$$\mathrm{i}\frac{\partial}{\partial t}\varphi_j(\mathbf{r},t) = \left[-\frac{1}{2}\nabla^2 + v_{\mathrm{KS}}[n](\mathbf{r},t)\right]\varphi_j(\mathbf{r},t) \tag{3.13}$$

and the density is given by

$$n(\mathbf{r},t) = \sum_{j=1}^{N} |\varphi_j(\mathbf{r},t)|^2 \ . \tag{3.14}$$

The Kohn-Sham scheme assumes that one can always find a local potential $v_{\mathrm{KS}}[n](\mathbf{r},t)$ with the property that the orbitals obtained from Eq. (3.13) reproduce the given density of an interacting electron system, but the validity of this assumption, known as "non-interacting v-representability", is not obvious and requires a careful examination. If such a potential exists, however, then by virtue of the Runge-Gross theorem it is unique up to a purely time-dependent function. Giving a constructive proof, van Leeuwen [60] showed that an effective local potential with the desired property exists if one can find a stationary wave function that yields the initial density $n(\mathbf{r},t_0)$ and is the ground state of a non-interacting electron system. The problem is thus reduced to the question of non-interacting v-representability in static density-functional theory. Despite much progress, the latter is still unresolved. Examples of well-behaved densities that do not correspond to the ground state of a non-interacting system are known [61, 62]; the implications of this discovery remain however unclear. In actual calculations, where the initial Kohn-Sham wave function is obtained from the constrained minimization of a smooth approximate energy functional, a solution can always be found [63].

If non-interacting v-representability is assumed, then $v_{\mathrm{KS}}[n](\mathbf{r},t)$ is determined completely by the requirement that Eq. (3.14) equals the density of the real interacting electron system. As in the case of ground state DFT, one has then to find an explicit expression for the effective potential that can be exploited to construct useful approximations. For this purpose it is convenient to employ the same separation

$$v_{\mathrm{KS}}[n](\mathbf{r},t) = v_{\mathrm{ext}}(\mathbf{r},t) + v_{\mathrm{H}}[n](\mathbf{r},t) + v_{\mathrm{xc}}[n](\mathbf{r},t) \tag{3.15}$$

as in static density-functional theory. The first term is the external potential, the second is the Hartree potential

$$v_{\mathrm{H}}[n](\mathbf{r},t) = \int d^3r' \frac{n(\mathbf{r}',t)}{|\mathbf{r}-\mathbf{r}'|} \tag{3.16}$$

and the third incorporates all remaining exchange and correlation effects. In the static case one can exploit the variational principle and determine the orbitals of the Kohn-Sham electrons in such a way that the total energy is minimized; all potential terms are then obtained as functional derivatives of the corresponding energy contributions with respect to the density. The energy in turn is a well defined physical quantity and amenable to approximations. In systems driven by time-dependent external fields the total energy is not a conserved quantity and there cannot be minimization principle. There exists, however, a quantity analogous to the energy, the quantum-mechanical action functional

$$A[\Phi] = \int_{t_0}^{t_1} dt \langle\Phi(t)| \left[\mathrm{i}\frac{\partial}{\partial t} - \hat{H}(t)\right] |\Phi(t)\rangle \ , \tag{3.17}$$

which has the property that its derivative with respect to a N-body function $\langle\Phi(t)|$ vanishes at the true many-body wave function, i.e., the solution of the Schrödinger equation

$$\left.\frac{\delta A[\Phi]}{\delta\langle\Phi(t)|}\right|_{|\Phi(t)\rangle=|\Psi(t)\rangle} = \left[\mathrm{i}\frac{\partial}{\partial t} - \hat{H}(t)\right]|\Psi(t)\rangle = 0\ . \tag{3.18}$$

Therefore, it is possible to solve the time-dependent problem by searching for the stationary point of the action. In contrast to the energy in the static case, the stationary point is not necessarily a minimum, however. Furthermore, the value of the action itself does not provide any relevant additional information, since for the true many-body wavefunction $A[\Psi] = 0$.

By virtue of the Runge-Gross theorem we may consider the action as a functional of the density. The obvious definition of $A[n]$ is to evaluate Eq. (3.17) at the wave function $\Phi[n](\{\mathbf{r}\},t)$ that evolves from the given initial state and yields the density $n(\mathbf{r},t)$. In analogy to the total energy in static density-functional theory, one would expect that the true density makes this functional stationary and can thus be identified. A suitable decomposition of the action would then define the exchange-correlation potential in terms of the functional derivative

$$v_{\mathrm{xc}}(\mathbf{r},t) = \frac{\delta A_{\mathrm{xc}}[n]}{\delta n(\mathbf{r},t)}\ . \tag{3.19}$$

Unfortunately, this procedure is doomed to failure. A first problem arises because the density determines the potential only up to a purely time-dependent function. Therefore, the wave function $\Phi[n](\{\mathbf{r}\},t)$ and the value of the action derived from it are not unique. Even if the phase of the wave function is fixed by imposing additional constraints, there is another more fundamental problem, which becomes evident if one examines the second functional derivative

$$\frac{\delta v_{\mathrm{xc}}(\mathbf{r},t)}{\delta n(\mathbf{r}',t')} = \frac{\delta^2 A_{\mathrm{xc}}[n]}{\delta n(\mathbf{r},t)\,\delta n(\mathbf{r}',t')}\ . \tag{3.20}$$

Whereas the expression on the right-hand side of (3.20) is symmetric in $(\mathbf{r},t)$ and $(\mathbf{r}',t')$, the exchange-correlation potential can only be influenced by the density at earlier times. Therefore, causality dictates that the left-hand side must vanish for $t < t'$ but not for $t > t'$. The symmetry and causality requirements contradict each other and cannot be satisfied simultaneously. This observation became known as the causality dilemma [64, 65] and prompted sophisticated resolutions, the best known of which is the van Leeuwen's construction[63] of a "Keldysh action" in pseudotime [66]. More recently Mukamel [67] showed how to construct causal response functions from symmetrical functional derivatives corresponding to "Liouville space pathways". The essence of these approaches is that causality is not violated, but one must resort to more abstract mathematical techniques in order to connect functional derivatives of the action to causal response functions. In 2008 Vignale solved the causality paradox from a more elementary point of view, by showing that the variational principle for the time evolution of the wave function, when properly implemented as a variational principle for the density, yields an expression for the potential as the sum of two terms: (i) the functional derivative of the Runge-Gross action and (2) a boundary term, which cannot be expressed as a functional derivative, but is still simple enough to be included in all the formal proofs. This approach explains why theorems that were originally proved under the incorrect assumption (3.20), turned out to be true after all.

We summarize here the procedure of van Leeuwen as we will need it in the following. In this approach to non-equilibrium dynamics the physical time t is parametrized by an underlying parameter τ called pseudotime in such a way that $t(\tau)$ runs from t_0 to t_1 and

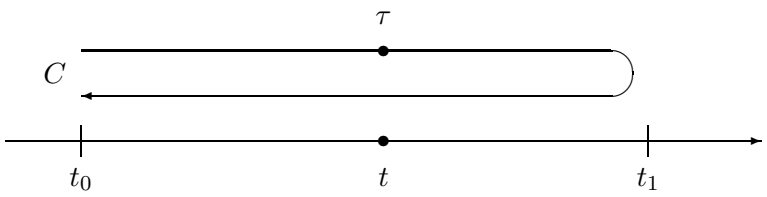

Figure 3.1: The Keldysh contour C, starting at t_0 and turning back at t_1. Pseudotime values τ on the forward and backward branches are distinct.

back to t_0 if τ runs along the contour C illustrated in Fig. 3.1. As pseudotime values on the forward and backward branches are distinct, the ordering along the contour differs from that on the physical time axis. The solution of the dilemma hence consists in satisfying the causality and symmetry requirements in different variable spaces. To this effect the action is first defined as a functional of the external potential in a form that does not explicitly contain $\partial/\partial t$

$$\tilde{A}[U] = \mathrm{i} \ln \langle \Psi(t_0) | T_C \exp\left(-\mathrm{i} \int_C d\tau t'(\tau) \hat{H}(\tau) \right) | \Psi(t_0) \rangle \; . \tag{3.21}$$

For the derivation of Eq. (3.21) the reader can see Ref. [63]. The potential $U(\mathbf{r}, \tau)$ is contained in the Hamiltonian, and T_C sorts the subsequent operators in order of ascending pseudotime arguments from right to left. For physical potentials of the form $U(\mathbf{r}, \tau) = v_{\mathrm{ext}}(\mathbf{r}, t(\tau))$ the value of the action is zero, because the contributions along the two time-contour directions cancel each other, but its derivative can be non-zero. In fact, the action (3.21) is defined in such a way that its functional derivative yields the density

$$\frac{\delta \tilde{A}[U]}{\delta U(\mathbf{r}, \tau)} = n(\mathbf{r}, \tau) \; . \tag{3.22}$$

An unambiguous functional of the density can then be constructed by means of a Legendre transform

$$A[n] = -\tilde{A}[U] + \int_C d\tau t'(\tau) \int d^3 r U(\mathbf{r}, \tau) n(\mathbf{r}, \tau) \; . \tag{3.23}$$

Finally, for practical purposes the action is decomposed according to

$$A[n] = A_{\mathrm{KS}}[n] - \frac{1}{2} \int_C d\tau t'(\tau) \int d^3 r \int d^3 r' \frac{n(\mathbf{r}, \tau) n(\mathbf{r}', \tau)}{|\mathbf{r} - \mathbf{r}'|} - A_{\mathrm{xc}}[n] \; . \tag{3.24}$$

The first term is the action of the non-interacting Kohn-Sham system, whose Legendre transform $\tilde{A}_{\mathrm{KS}}[U_{\mathrm{KS}}]$ is defined in analogy to Eq. (3.21) in terms of the initial Kohn-Sham wave function and the effective local potential. The second term is related to the Hartree potential, and the third gives rise to the exchange-correlation potential

$$v_{\mathrm{xc}}(\mathbf{r}, t) = \left. \frac{\delta A_{\mathrm{xc}}[n]}{\delta n(\mathbf{r}, \tau)} \right|_{n = n(\mathbf{r}, t)} \; . \tag{3.25}$$

Defining the action in the pseudotime domain instead of the real time axis guarantees the proper symmetry of the second functional derivative in $(\mathbf{r}, \tau)$ and $(\mathbf{r}', \tau')$. On the other hand, the exchange-correlation potential (3.25), which is obtained by inserting the physical time argument *after* performing the functional derivative with respect to $n(\mathbf{r}, \tau)$, respects causality on the time axis. From a theoretical point of view, all quantities that enter the Kohn-Sham scheme are thus well defined, and working approximations can be derived by

finding a suitable expression for the action functional, for example through an expansion in powers of the Coulomb interaction. This approach is known as the time-dependent optimized effective-potential method [68]. Unfortunately, the leading term, which is linear in the Coulomb interaction and retains only exchange and no correlation [69], has already a high computational cost. In fact, at present the design of specific approximations for the exchange-correlation potential in TDDFT is still at an early stage. Today, most calculations take however a pragmatic point of view and simply use one of the established functionals of static density-functional theory. The most popular choice is the adiabatic local-density approximation (ALDA) [18], which is obtained by evaluating the standard LDA potential with the time-dependent density $n(\mathbf{r},t)$:

$$v_{\rm xc}^{\rm ALDA}[n](\mathbf{r},t) = v_{\rm xc}^{\rm HEG}[n](\mathbf{r},t)\big|_{n=n(\mathbf{r},t)} \,. \tag{3.26}$$

The adiabatic approach is a drastic simplification, however, and *a priori* only justified for systems with a weak time-dependence that are always locally close to equilibrium. This adds to the problems that are related to the spatial locality of the LDA.

3.3 Linear-response theory

If the time-dependent external perturbation in $v_{\rm ext}(\mathbf{r},t) = v_{\rm ext}^{(0)}(\mathbf{r}) + v_{\rm ext}^{(1)}(\mathbf{r},t)$ is weak, then linear-response theory can be exploited to describe the dynamics of a system more efficiently than a full solution of the Kohn-Sham equations (3.13). In this case the density is expanded in orders of $v_{\rm ext}^{(1)}(\mathbf{r},t)$ according to $n(\mathbf{r},t) = n^{(0)}(\mathbf{r}) + n^{(1)}(\mathbf{r},t) + \ldots$, where the first-order correction is given by

$$n^{(1)}(\mathbf{r},t) = \int_{-\infty}^{\infty} dt' \int d^3r'\, \chi(\mathbf{r},\mathbf{r}',t-t') v_{\rm ext}^{(1)}(\mathbf{r}',t') \,, \tag{3.27}$$

in terms of the linear density-response function

$$\chi(\mathbf{r},\mathbf{r}',t-t') = \left.\frac{\delta n(\mathbf{r},t)}{\delta v_{\rm ext}(\mathbf{r}',t')}\right|_{v_{\rm ext}(\mathbf{r}',t')=v_{\rm ext}^{(0)}(\mathbf{r}')} \,. \tag{3.28}$$

Causality requires $\chi(\mathbf{r},\mathbf{r}',t-t') = 0$ for $t < t'$, of course, because the density cannot be influenced by later variations of the potential. To calculate the linear density-response function in practice one exploits the fact that the density of the real system is identical to that of the non-interacting Kohn-Sham electrons. As the latter move in the effective potential $v_{\rm KS}(\mathbf{r}'',t'')$, one starts by applying the chain rule for functional derivatives

$$\chi(\mathbf{r},\mathbf{r}',t-t') = \int_{-\infty}^{\infty} dt'' \int d^3r'' \, \frac{\delta n(\mathbf{r},t)}{\delta v_{\rm KS}(\mathbf{r}'',t'')} \frac{\delta v_{\rm KS}(\mathbf{r}'',t'')}{\delta v_{\rm ext}(\mathbf{r}',t')} \,. \tag{3.29}$$

The first term on the right-hand side corresponds to the linear density-response function $\chi_{\rm KS}(\mathbf{r},\mathbf{r}'',t-t'')$ of the non-interacting Kohn-Sham system, since the effective potential plays the role of the "external potential"of the Kohn-Sham system. It can be calculated explicitly from time-dependent perturbation theory and is given by

$$\chi_{\rm KS}(\mathbf{r},\mathbf{r}'',\omega) = \lim_{\eta\to+0} \sum_{j=1}^{\infty}\sum_{k=1}^{\infty} (f_j - f_k) \frac{{\varphi_j}^*(\mathbf{r})\varphi_k(\mathbf{r})\varphi_j(\mathbf{r}'){\varphi_k}^*(\mathbf{r}'')}{\omega - \varepsilon_k + \varepsilon_j + {\rm i}\eta} \tag{3.30}$$

in frequency space. The energies ε_j appearing in the denominator are the eigenvalues of the unperturbed stationary Kohn-Sham wave functions $\varphi_j(\mathbf{r})$. In order to evaluate the second term in Eq. (3.29) one uses the separation (3.15), which yields

$$\frac{\delta v_{\mathrm{KS}}(\mathbf{r}'',t'')}{\delta v_{\mathrm{ext}}(\mathbf{r}',t')} = \delta(\mathbf{r}''-\mathbf{r}')\delta(t''-t') + \frac{\delta v_{\mathrm{H}}(\mathbf{r}'',t'')}{\delta v_{\mathrm{ext}}(\mathbf{r}',t')} + \frac{\delta v_{\mathrm{xc}}(\mathbf{r}'',t'')}{\delta v_{\mathrm{ext}}(\mathbf{r}',t')} \; . \tag{3.31}$$

As both the Hartree potential and the exchange-correlation potential are functionals of the density, one can apply the chain rule once more and rewrite these two contributions as

$$\frac{\delta v_{\mathrm{H}}(\mathbf{r}'',t'')}{\delta v_{\mathrm{ext}}(\mathbf{r}',t')} = \int_{-\infty}^{\infty} dt''' \int d^3r''' \, \frac{\delta v_{\mathrm{H}}(\mathbf{r}'',t'')}{\delta n(\mathbf{r}''',t''')} \frac{\delta n(\mathbf{r}''',t''')}{\delta v_{\mathrm{ext}}(\mathbf{r}',t')} \tag{3.32}$$

and analogously for $\delta v_{\mathrm{xc}}(\mathbf{r}'',t'')/\delta v_{\mathrm{ext}}(\mathbf{r}',t')$. The last term on the right-hand side of Eq. (3.32) is easily recognized as the linear density-response function $\chi(\mathbf{r}''',\mathbf{r}',t'''-t')$. The functional derivative of the Hartree potential with respect to the density follows from the definition (3.16) and simply equals the Coulomb potential

$$\frac{\delta v_{\mathrm{H}}(\mathbf{r}'',t'')}{\delta n(\mathbf{r}''',t''')} = \frac{1}{|\mathbf{r}''-\mathbf{r}'''|}\delta(t''-t''') \; . \tag{3.33}$$

The last term of Eq. (3.31) contains the so-called exchange-correlation kernel

$$f_{\mathrm{xc}}(\mathbf{r}'',\mathbf{r}''',t''-t''') = \left.\frac{\delta v_{\mathrm{xc}}(\mathbf{r}'',t'')}{\delta n(\mathbf{r}''',t''')}\right|_{n(\mathbf{r}''',t''')=n^{(0)}(\mathbf{r}''')} \; . \tag{3.34}$$

After collecting all terms and performing a Fourier transform to frequency space, whereby convolutions on the time axis turn into simple multiplications, one obtains the final integral equation [23]

$$\begin{aligned}\chi(\mathbf{r},\mathbf{r}',\omega) &= \chi_{\mathrm{KS}}(\mathbf{r},\mathbf{r}',\omega) \\ &\quad + \int d^3r'' \int d^3r''' \, \chi_{\mathrm{KS}}(\mathbf{r},\mathbf{r}'',\omega) \left(\frac{1}{|\mathbf{r}''-\mathbf{r}'''|} + f_{\mathrm{xc}}(\mathbf{r}'',\mathbf{r}''',\omega) \right) \chi(\mathbf{r}''',\mathbf{r}',\omega) \; .\end{aligned} \tag{3.35}$$

The TDDFT equations in the linear-response regime can be cast in numerous different forms. For solids, in most implementations the integral equation (3.35) is solved routinely by projecting all quantities onto a suitable set of basis functions. Very often, one uses a plane wave representation within the pseudopotential approximation (see, e.g., the codes [70, 71, 72]), but localized basis sets can equally be used to allow for all-electron calculations (see, e.g., the code [73]). The Dyson equation (3.35) thus turns into a matrix equation $\chi(\omega) = \chi_{\mathrm{KS}}(\omega) + \chi_{\mathrm{KS}}(\omega)[v + f_{\mathrm{xc}}(\omega)]\chi(\omega)$ for example in reciprocal lattice vectors in case of periodic systems where $\chi = \chi_{\mathbf{G},\mathbf{G}'}(\mathbf{q})$.

Alternatively, absorption spectra can be calculated by propagating the full TD Kohn-Sham equations in real-time [74]. This description decreases storage requirements, it allows the entire frequency-dependent dielectric function to be calculated at once, and the scaling with the number of atoms is quite favorable. However, the prefactor is fairly large as such calculations typically require ≈ 10000 time-steps with a time-step of $\approx 10^{-3}$ fs [75].

Another efficient approach, based on linear-response within Ghosh and Dhara's time-dependent density functional formalism [76], was proposed [77]. It uses an iterative scheme in real-space, in which the density and the potential are updated in each cycle, thereby avoiding the explicit evaluation of the Kohn-Sham response kernels.

Finally, a method to calculate the dynamical polarizability using only occupied states has been proposed recently [78]. The dynamical polarizability is represented by a matrix continued fraction whose coefficients can be obtained from a Lanczos method. This methods scales favorably with system size, and it becomes useful for large scale systems. [78, 79].

3.4 Excitation energies

In static DFT the interpretation of the one-particle Kohn-Sham eigenvalues ε_j as quasi-particle energies is not formally justified and it leads to the well known problem of the underestimation of transition energies in the independent-particle transition picture. In the framework of TDDFT the relevant information about the excited states is contained in the linear density-response function: in fact it can be shown that the true excitation energies are the poles of $\chi(\mathbf{r},\mathbf{r}',\omega)$. In contrast to other attempts to calculate electronic excitations within a density-functional framework [80, 81, 82], TDDFT has the great advantage that it is not restricted to a subset of excited states but, in principle, yields the complete excitation spectrum.

In order to see this, one can calculate the density change due to the external potential at the first order. The stationary eigenstates of the original unperturbed Hamiltonian are labeled by $\Psi_j(\{\mathbf{r}\},t) = \Psi_j(\{\mathbf{r}\})\exp(-\mathrm{i}E_j t)$, where E_j denotes the corresponding energy eigenvalues. After the onset of the time-dependent perturbation it is possible to expand the wave function $\Psi(\{\mathbf{r}\},t)$ that evolves from the ground state $\Psi^{(0)}(\{\mathbf{r}\},t) = \Psi_0(\{\mathbf{r}\})\exp\left(-\mathrm{i}E_0 t\right)$ in orders of $v_{\mathrm{ext}}^{(1)}(\mathbf{r},t)$. The first-order correction is

$$\Psi^{(1)}(\{\mathbf{r}\},t) = -\mathrm{i}\sum_{j=0}^{\infty}\Psi_j(\{\mathbf{r}\},t)\int_{-\infty}^{t}dt'\int d^3r_1'\ldots\int d^3r_N'\Psi_j^*(\{\mathbf{r}'\},t') \left(\sum_{i=1}^{N}v_{\mathrm{ext}}^{(1)}(\mathbf{r}'_i,t')\right)\Psi_0(\{\mathbf{r}'\},t')\ . \quad (3.36)$$

The corresponding change in the density is

$$n^{(1)}(\mathbf{r},t) = N\int d^3r_2\ldots\int d^3r_N\left\{\left[\Psi^{(1)}(\mathbf{r},\mathbf{r}_2,\ldots,\mathbf{r}_N,t)\right]^*\Psi^{(0)}(\mathbf{r},\mathbf{r}_2,\ldots,\mathbf{r}_N,t)+ \left[\Psi^{(0)}(\mathbf{r},\mathbf{r}_2,\ldots,\mathbf{r}_N,t)\right]^*\Psi^{(1)}(\mathbf{r},\mathbf{r}_2,\ldots,\mathbf{r}_N,t)\right\}\ . \quad (3.37)$$

In order to simplify the notation we introduce the overlap functions

$$n_j(\mathbf{r}) = N\int d^3r_2\ldots\int d^3r_N\Psi_0^*(\mathbf{r},\mathbf{r}_2,\ldots,\mathbf{r}_N)\Psi_j(\mathbf{r},\mathbf{r}_2,\ldots,\mathbf{r}_N)\ , \quad (3.38)$$

and after inserting Eqs. (3.36) and (3.38) into Eq. (3.37) we obtain

$$n^{(1)}(\mathbf{r},t) = \int_{-\infty}^{\infty}dt'\int d^3r'\left[-\mathrm{i}\sum_{j=0}^{\infty}\Big(n_j(\mathbf{r})n_j^*(\mathbf{r}')e^{-\mathrm{i}(E_j-E_0)(t-t')} - n_j^*(\mathbf{r})n_j(\mathbf{r}')e^{\mathrm{i}(E_j-E_0)(t-t')}\Big)\Theta(t-t')\right]v_{\mathrm{ext}}^{(1)}(\mathbf{r}',t')\ . \quad (3.39)$$

Comparing this expression with Eq. (3.27), one finds that the term in square brackets equals the linear density-response function $\chi(\mathbf{r},\mathbf{r}',t-t')$. The Heaveside step function $\Theta(t-t')$ has been introduced to replace the integral over time $\int_{-\infty}^{t}dt'$ with $\int_{-\infty}^{\infty}dt'$. After a Fourier transform to frequency space, and using $\Theta(t) = \mathrm{i}/2\pi\lim_{\eta\to 0+}\int_{-\infty}^{\infty}d\omega\frac{1}{\omega+\mathrm{i}\eta}e^{-\mathrm{i}t\omega}$ one arrives at the Lehmann representation of the density response function:

$$\chi(\mathbf{r},\mathbf{r}',\omega) = \lim_{\eta\to 0+}\sum_{j=1}^{\infty}\left(\frac{n_j(\mathbf{r})n_j^*(\mathbf{r}')}{\omega-E_j+E_0+\mathrm{i}\eta} - \frac{n_j^*(\mathbf{r})n_j(\mathbf{r}')}{\omega+E_j-E_0+\mathrm{i}\eta}\right)\ , \quad (3.40)$$

where η is a positive infinitesimal. From Eq. (3.40) it is evident that the poles of $\chi(\mathbf{r}, \mathbf{r}', \omega)$ correspond to the exact excitation energies $E_j - E_0$. Furthermore, all quantities on the right-hand side depend only on the Hamiltonian of the unperturbed stationary system. By virtue of the Hohenberg-Kohn theorem the linear density-response function is hence a functional of the static ground-state density $n_0(\mathbf{r})$.

The form of Eq. (3.40) is valid for finite systems with discrete eigenvalues. As the energies E_j of the eigenstates of the many-electron system are real, it appears that the poles of $\chi(\mathbf{r}, \mathbf{r}', \omega)$ are at real energies. For extended systems, on the other hand, the spectrum is continuous, and the sum in Eq. (3.40) turns into an integral that gives rise to a branch cut along the real energy axis. The infinitely close-lying resonances thus merge into broad structures that can be identified with elementary quasiparticles, such as plasmons or excitons. As these structures have a certain width, they are described by poles in the complex plane with a real part, which corresponds to the energy of the excitation, and a finite imaginary part, whose inverse is proportional to the excitation lifetime.

Chapter 4

Kernels from many-body perturbation theory*

4.1 Time-dependent density functional theory in practice

Linear response theory can be applied now to study the response of an extended system to a small time-dependent perturbation $v_{\rm ext}(\mathbf{r},t)$. The linear variation of the density induced by the perturbation is given by (3.27). As a consequence of the polarization of the system due to the applied perturbation, the total potential becomes a sum of the external potential and the induced potential: $v_{\rm tot} = v_{\rm ext} + v_{\rm ind}$. The basic quantity that gives information about the screening of the system in linear response is the microscopic dielectric function ϵ, that relates the total potential $v_{\rm tot}$ to the applied potential $v_{\rm ext}$:

$$v_{\rm tot}(\mathbf{r},t) = \int_{-\infty}^{\infty} dt' \int d^3r'\, \epsilon^{-1}(\mathbf{r},\mathbf{r}',t-t')v_{\rm ext}(\mathbf{r}',t')\,. \tag{4.1}$$

The microscopic dielectric function ϵ and the reducible polarizability χ are hence related by

$$\epsilon^{-1}(\mathbf{r},\mathbf{r}',t-t') = \delta(\mathbf{r}-\mathbf{r}')\delta(t-t') + \int d^3r'' v(\mathbf{r}-\mathbf{r}'')\chi(\mathbf{r}'',\mathbf{r}',t-t'). \tag{4.2}$$

For periodic systems, the most natural way to deal with spatial periodicity is to apply a Fourier transform and rewrite Eq. (4.2) in reciprocal space

$$\epsilon^{-1}_{\mathbf{G}\mathbf{G}'}(\mathbf{q},\omega) = \delta_{\mathbf{G}\mathbf{G}'} + v_{\mathbf{G}}(\mathbf{q})\chi_{\mathbf{G}\mathbf{G}'}(\mathbf{q},\omega)\,, \tag{4.3}$$

where $\mathbf{G}$ is a vector of the reciprocal lattice, while $\mathbf{q}$ is a vector in the first Brillouin zone. In Eq. (4.3) a Fourier transform has also been applied to move from time to frequency space.

From the microscopic dielectric function one has to obtain measurable quantities. In the case of absorption spectra, this means to calculate the imaginary part of the macroscopic

*This chapter is based on the articles:

- *Long range contribution to the exchange-correlation kernel of time-dependent density functional theory*, S. Botti, F. Sottile, N. Vast, V. Olevano, L. Reining, H-Ch. Weissker, A. Rubio, G. Onida, R. Del Sole, and R.W. Godby, Phys. Rev. B **69**, 155112 (2004).
- *Energy dependence of the exchange-correlation kernel of time-dependent density functional theory*, S. Botti, A. Fourreau, F. Nguyen, Y-O. Renault, F. Sottile, and L. Reining, Phys. Rev. B **72**, 125203 (2005).
- *Time-dependent density-functional theory for extended systems*, S. Botti, A. Schindlmayr, R. Del Sole, and L. Reining, Rep. Prog. Phys. **70**, 357-407 (2007).

dielectric function [83, 84, 85]

$$\epsilon_{\rm M}(\omega) = \lim_{\mathbf{q}\to 0} \frac{1}{\left[\epsilon^{-1}_{\mathbf{G}\mathbf{G}'}(\mathbf{q},\omega)\right]_{\mathbf{G},\mathbf{G}'=0}} \,. \tag{4.4}$$

We have dealt so far with the response to a potential whose electric field is longitudinal with respect to the wavevector. Light, instead, is a transverse perturbation, i.e., its electric field is perpendicular to the wavevector. Hence, it would seem inappropriate to use the present treatment. However, since the light wavevector is very small, one can think to rotate it such as to become parallel to the electric field and apply the present formalism [86]. The validity of this approach has been rigorously demonstrated for cubic crystals in Ref. [16]. Furthermore, we observe that, in general, for anisotropic systems (4.3) and (4.4) depend on the direction of the vector $\mathbf{q}$ (i.e., on the polarization of the incoming radiation), thus both microscopic and macroscopic responses are described by a dielectric tensor, instead of simple scalar functions.

The same quantity $\epsilon_{\rm M}$ is also related to electron energy loss spectra (EELS) for vanishing momentum transfer, through the loss function $-\Im\mathfrak{m}\{1/\epsilon_{\rm M}\}$. For non-vanishing momentum transfer $\mathbf{Q} = \mathbf{q}+\mathbf{G}$, the loss function is $-\Im\mathfrak{m}\left\{\epsilon^{-1}_{\mathbf{G}\mathbf{G}}(\mathbf{q},\omega)\right\}$. In this case the longitudinal formulation of the dielectric response is obviously appropriate. From (4.3) it follows that the loss function can be related to the linear density response function χ:

$$\mathrm{EEL}(\mathbf{q}+\mathbf{G},\omega) = -v_{\mathbf{G}}(\mathbf{q})\,\Im\mathfrak{m}\,\left\{\chi_{\mathbf{G}\mathbf{G}}(\mathbf{q},\omega)\right\}\,, \tag{4.5}$$

where the $\mathbf{G}\mathbf{G}'$-matrix χ can be obtained by solving the Dyson-like screening equation (3.35). In (3.35) the full response function is expressed in terms of the independent-particle $\chi_{\rm KS}$ via a kernel composed by two terms, the bare Coulomb potential and the exchange-correlation contribution $f_{\rm xc}$. A similar expression can be written also in the case of the optical absorption, provided one builds a modified response function $\bar{\chi}$:

$$\Im\mathfrak{m}\,\{\epsilon_{\rm M}\} = -\lim_{\mathbf{q}\to 0} v_{\mathbf{G}}(\mathbf{q})\Im\mathfrak{m}\,\{\bar{\chi}_{\mathbf{G}\mathbf{G}'}\}\,, \tag{4.6}$$

which satisfies the Dyson-like screening equation

$$\bar{\chi} = \chi_{\rm KS} + \chi_{\rm KS}(\bar{v} + f_{\rm xc})\bar{\chi}\,, \tag{4.7}$$

where the modified Coulomb interaction is defined as

$$\bar{v}_{\mathbf{G}} = \begin{cases} v_{\mathbf{G}} & \text{for} \quad \mathbf{G}\neq 0 \\ 0 & \text{for} \quad \mathbf{G}=0 \end{cases}\,. \tag{4.8}$$

Following [17], the description of both absorption and EELS for $\mathbf{q}\to 0$ can be unified by introducing the generalized spectrum $A(\omega)$ and a generalized function $X_{\mathbf{G}\mathbf{G}'}(\mathbf{q},\omega)$. The function X stands for the modified response function $\bar{\chi}$ in the case of absorption and for the reducible response function χ in the case of EEL:

$$\left.\begin{matrix}\text{Abs}\\ \text{EEL}\end{matrix}\right\} = A(\omega) = -\Im\mathfrak{m}\left\{\lim_{\mathbf{q}\to 0} v_{\mathbf{G}=0}(\mathbf{q})X_{\mathbf{G}=\mathbf{G}'=0}(\mathbf{q},\omega)\right\}\,. \tag{4.9}$$

In any formulation, the basic ingredients to obtain either the absorption or the EELS are the Kohn-Sham eigenfunctions and eigenenergies that enter the expression for the independent-particle Kohn-Sham response function $\chi_{\rm KS}$ (3.30). These are usually obtained through a ground-state DFT calculation using an approximate exchange-correlation potential. In the total kernel of (3.35) and (4.7) $\bar{v}$ accounts for classical depolarization effects [also

known as crystal local field effects (LFE) in a solid]. It reflects the microscopic induced Hartree potential created by polarizable inhomogeneities in the system. The apparently subtle difference between absorption and EELS, i.e., the inclusion or the exclusion of the long-range term $v_{\mathbf{0}}$, is crucial for extended systems - for example, $v_{\mathbf{0}}$ is responsible for the plasmons - , whereas its contribution in finite systems becomes vanishingly small [87].

We have therefore two key approximations: (i) the ground-state exchange-correlation potential, and (ii) the exchange-correlation kernel. Of course, these two quantities are in principle linked, due to the fact that the exchange-correlation kernel is the functional derivative of the time dependent exchange-correlation potential. The relative importance of the two approximations depends, as we will see in the following, on the physical system under study. For example, when dealing with finite systems it is often essential to have good Kohn-Sham eigenstates – and therefore a good ground-state exchange-correlation potential – while the role of the exchange-correlation kernel is less relevant [88, 25]. The opposite is usually true for extended systems, where a good approximation to the exchange-correlation kernel turns out to be essential, especially when it comes to describe optical absorption spectra [17].

Searching for approximations several approaches are possible. For the ground-state exchange-correlation potential, 40 years of development have led to a swarm of functionals (for more information, see one of the numerous review articles on the subject, e.g., Ref. [89]). For the exchange-correlation kernel, one can either look for a good approximation for the time-dependent exchange-correlation potential and then use the definition of $f_{\rm xc}$ (3.34) or find directly an expression for the exchange-correlation kernel. Either choice has clear advantages and disadvantages. On the one hand, the exchange-correlation kernel is a simpler object, in the sense that it is a functional of the ground-state density, and is therefore amenable to more controllable approximations. On the other hand, if we are in possession of a good time-dependent exchange-correlation functional, we can tackle both linear and non-linear response properties. Instead, only linear response is accessible through the knowledge of the exchange-correlation kernel. Most often, the standard approximations used for $v_{\rm xc}(\mathbf{r},t)$ are adiabatic, and lead to very simple $f_{\rm xc}$'s.

4.1.1 Basic approximations and problems

The lowest level approximation to perform real calculations consists in setting to zero the terms in (3.35) and (4.7) coming from the microscopic components of the induced Hartree potential ($\bar{v}=0$) and the variations of the exchange-correlation potential ($f_{\rm xc}=0$). By comparing (4.4) with (4.6), with vanishing $\bar{v}$ and $f_{\rm xc}$, it is possible to see that this is equivalent to neglecting all the off-diagonal components of the matrix $\epsilon^{-1}_{\mathbf{G}\mathbf{G}'}$. We will refer to this as the independent particle approximation (IPA). The excitation energies in the IPA are simply given by the differences between the eigenenergies of the unoccupied and occupied Kohn-Sham states, which are used to build $\chi_{\rm KS}$. Independently of the quality of the states entering in $\chi_{\rm KS}$, this usually leads to absorption peaks that are systematically red-shifted in relation to the experimental spectra [17]. This is a consequence of the well known gap problem of DFT: the gap between filled and empty states is substantially underestimated [44].

By neglecting only the exchange-correlation kernel we obtain the so-called random-phase approximation (RPA) [84, 85]:

$$f_{\rm xc}^{\rm RPA}=0\,. \tag{4.10}$$

In this case, the only part of the total kernel in (3.35) and (4.7) which is taken into account is the classical Coulomb term. This term describes the well known Lindhard theory of

screening with the addition of LFE [90]. Although very simple, the RPA yields results of reasonable accuracy for a wide-range of systems, and it is still widely employed in actual calculations. We will see some examples in the following of this section.

In the next step in the ladder of complexity come the already mentioned adiabatic approximations. At the level of the time-dependent exchange-correlation potential the adiabatic approximation implies

$$v_{\rm xc}^{\rm adiabatic}[n](\mathbf{r},t) = \tilde{v}_{\rm xc}\left[n(t)\right](\mathbf{r},t) \ , \tag{4.11}$$

where $\tilde{v}_{\rm xc}[n]$ is some given ground-state exchange-correlation functional. Note that, regardless of the choice of $\tilde{v}_{\rm xc}[n]$, the resulting kernel is instantaneous: $f_{\rm xc}(\mathbf{r},\mathbf{r}',t,t') = \delta(t-t')f_{\rm xc}(\mathbf{r},\mathbf{r}')$, i.e., its Fourier transform is frequency independent (it can be of course non-local in space). If the LDA static potential is inserted in (4.11), one obtains the most common functional of TDDFT: the ALDA potential. Using definition (3.34), one can then derive the local and static ALDA (also called TDLDA) exchange-correlation kernel [20, 21]

$$f_{\rm xc}^{\rm TDLDA}(\mathbf{r},\mathbf{r}',t,t') = \delta\left(\mathbf{r}-\mathbf{r}'\right)\delta\left(t-t'\right)\left.\frac{d^2 e_{\rm xc}^{HEG}(n)}{dn^2}\right|_{n=n_{\rm GS}(\mathbf{r})} , \tag{4.12}$$

where $e^{\rm HEG}$ is the energy per unit volume of the homogeneous electron gas, and $n_{\rm GS}$ is the ground-state electron density.

It is clear that the TDLDA retains all the problems already present in the LDA. The most important of these are perhaps, for neutral finite systems, the incorrect asymptotic behavior of the LDA potential (instead of decaying as $-1/r$, the LDA exchange-correlation potential goes to zero exponentially) and, for infinite systems, its local dependence on the density. These drawbacks can not be corrected by using in (4.11) most of the GGAs [91], nor most of the more modern meta-GGAs functionals [92, 93].

Nevertheless, for the calculation of optical response spectra in a large variety of finite systems, the TDLDA has proved to be able to reproduce low energy peaks with an accuracy of around 0.1–0.4 eV [94]. For solids, the situation is a bit more complicated. EELS or X-ray scattering (IXS) spectra are often of good quality, especially when the transferred momentum $\mathbf{q}$ is finite [95, 29, 28]. Instead, the description of $\Im\mathrm{m}\left\{\epsilon_{\rm M}(\omega)\right\}$ for vanishing momentum transfer, which is the case in optical response, is perhaps the best known failure of TDLDA. Note that in an extended system the TDLDA kernel for vanishing $\mathbf{q}$ yields always a relatively small correction to the RPA results, because it is constant for $q \to 0$ and multiplied with $\chi_{\rm KS}$ that goes to 0 as q^2. It can hence only have an effect via the LFE [30]. We will discuss this issue more in detail in the following of this section.

It is clear from the above that the behavior of the different approximations depends strongly on the spectroscopy and on the dimensionality of the physical system. Therefore, it is interesting to present some examples of results for finite systems (molecules, clusters) to be compared to analogous results for infinite systems. In view of that, the following two subsections handle separately optical absorption in finite (Sec. 4.1.2) and periodic systems (Sec. 4.1.3). We then turn to EELS and IXS in Sec. 4.1.4. Finally, we try to understand the failures of the TDLDA (Sec. 4.1.5), and discuss possible routes to overcome them.

4.1.2 Optical absorption of finite systems

The first calculations of excitation energies within TDDFT were performed before the formal demonstration of the Runge-Gross theorem. In 1977 Ando determined intersubband transitions in semiconductor heterostructures [96]. Shortly after, Zangwill and Soven [18]

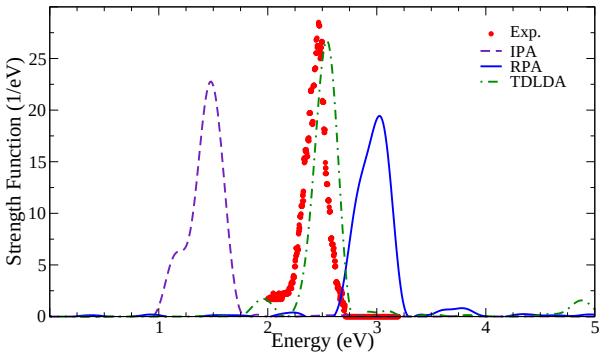

Figure 4.1: Photoabsorption spectrum for a Na_8 cluster from Ref. [17]. Dots: experimental data; dashed line: IPA Kohn-Sham transitions; solid line: RPA; dashed-dotted line: TDLDA.

applied TDLDA to the calculation of the photo absorption cross section of rare gas atoms, obtaining a very good agreement with experimental data.

However, it was only in recent years that TDDFT became one of the most popular tools for the calculation of excitation properties. By now, the TDLDA kernel (4.12) has been successfully applied to atoms, organic and biological molecules, metallic and semiconducting clusters, fullerenes, etc. [97, 98, 99, 94, 100]. Besides some more problematic cases (see Sec. 4.1.5) the calculated excitation energies and absorption spectra are, in general, in excellent agreement with available experimental data [101]. As a general feature, present in both metallic and semiconducting clusters, the RPA peaks are blue-shifted with respect to the IPA peaks. Adding the TDLDA kernel brings a further correction, this time as a shift towards lower energies. The resulting transition energies then accurately reproduce the experiment. It is important to observe that, already in the RPA, absorption at low energies is correctly suppressed with respect to IP calculations. In fact this suppression of the oscillator strength is essentially due to the induced classical depolarization potential. From (4.4) it can be observed that the LFE come from the off-diagonal terms of the matrix $\epsilon_{\mathbf{G}\mathbf{G}'}$. In other words, they express the fact that the electronic response of an inhomogeneous structure is position-dependent (and not only distance-dependent). It is intuitive that such an effect has to be the stronger the larger the inhomogeneity of the system. Since a finite object represents a strong inhomogeneity in the otherwise empty space, it is not surprising that the LFE are particularly important for this kind of systems.

It should not be forgotten that in some cases TDLDA is not adequate to describe excitations of finite systems: a typical example is the failure in reproducing Rydberg series [25]. Moreover, when the molecules become more extended, this quality in general degrades. An example is the calculation of optical properties of long conjugated polymers [27, 102]. The problem is related to a non-local dependence of the exchange-correlation potential: In a system with an applied electric field, the exact exchange-correlation potential develops a linear part that counteracts the applied field [27, 103]. This term is completely absent in both the LDA and the GGA. It is present in more non-local functionals, like the exact exchange functional (see Sec.4.2.1).

In the following we will investigate more closely this problem.

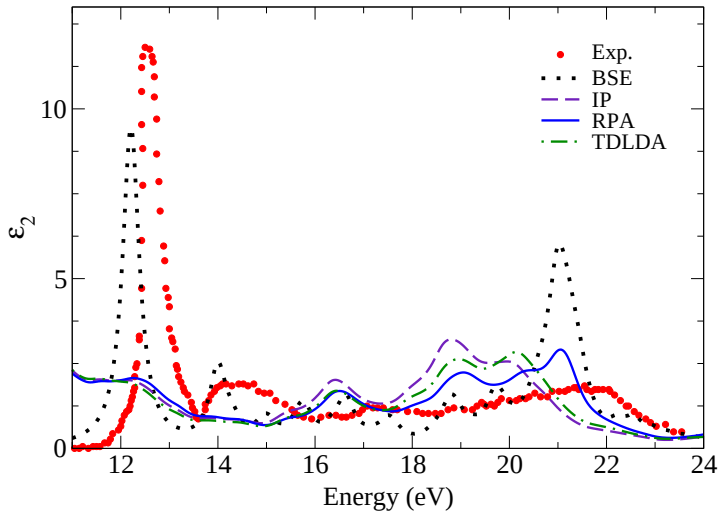

Figure 4.2: Imaginary part of the macroscopic dielectric function for LiF [104]. Dots: experiment [105]; dotted-line: BSE calculation; dashed line: IPA calculation; solid line: RPA calculation; dot-dashed line: TDLDA calculation.

4.1.3 Optical absorption of extended systems

The simplest approach to the optical properties of semiconductors or wide-gap insulators within TDDFT is the TDLDA. In view of the excellent quality of the results obtained for the photoabsorption of clusters, one could perhaps expect that the same would occur for extended systems. This is unfortunately not the case. As we can see in Fig. 4.2 for the optical absorption of a LiF crystal, the TDLDA (dash-dotted line) induces only some minor modifications with respect to the RPA (solid line), and both are very far from the experimental curve (dots). The largest disagreement concerns the absence of the strong excitonic peak at about 12.5 eV. Good agreement can be found using the many-body Bethe-Salpeter approach (dotted line) at the price of a significantly larger computational effort [106, 107, 108, 109]: in that framework, electron addition and removal energies as well as the electron-hole interaction are explicitly calculated within many-body Green's function theory (see Sec. 2.2).

This situation is quite general and is found in a wide range of semiconductors (Si – see also the inset of Fig. 4.3 – Ge, GaAs, etc.) and wide-band gap semiconductors or insulators (diamond, MgO, SiO_2, etc.). It is typical for absorption, as opposed to loss spectroscopies, even when both techniques are employed to study the same system. A detailed analysis of the problem will be the subject of Sec. 4.4.

4.1.4 Longitudinal response of extended systems

In Fig. 4.3 we can observe both the absorption and EELS at vanishing q (within RPA) for bulk silicon [87]. To interpret this picture it is useful to use the generalized spectrum $A(\omega)$ of Eq. (4.9). The modified RPA polarization function X 4.9 can be further generalized as

$$X(\omega) = (1 - \chi_{\rm KS}\gamma v_{\mathbf{0}} - \chi_{\rm KS}\bar{v})^{-1}\chi_{\rm KS}\ . \tag{4.13}$$

If $\gamma = 1$, $A(\omega) = \mathrm{EELS}$, and if $\gamma = 0$, $A(\omega) = \mathrm{Abs}$. Moreover, it is possible to follow the evolution of the spectrum when γ varies continuously from 1 to 0. In Fig. 4.3 we show how the EELS turns continuously into the absorption when $v_{\mathbf{0}}$ is switched off. This exemplifies the

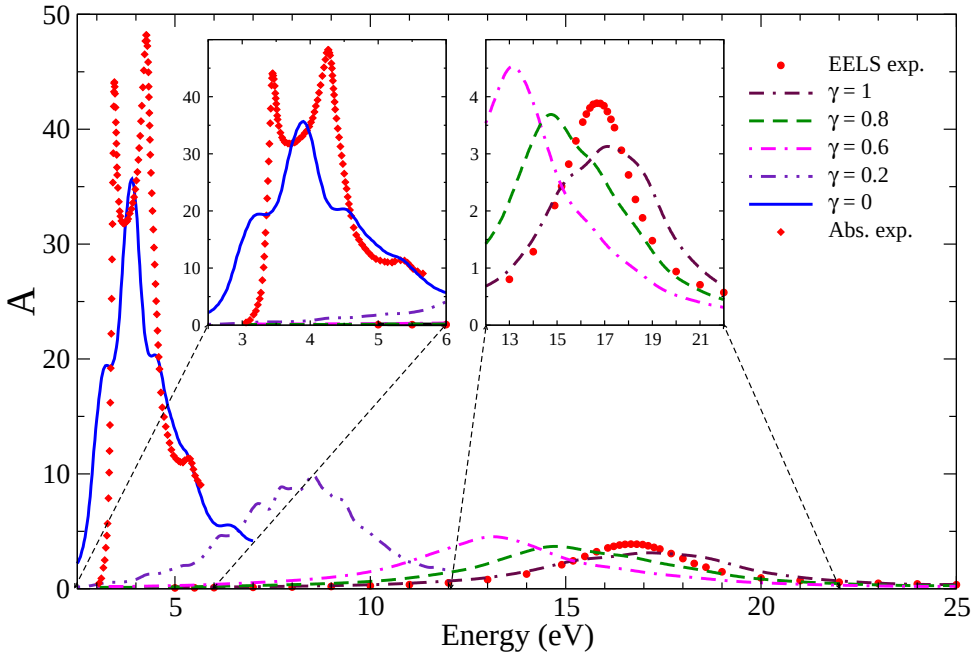

Figure 4.3: Continuous connection between EELS and absorption spectrum of bulk silicon, via v_0 [87]. Experiments from references [110] (absorption) and [111] (EELS).

action of the long-range component v_0, that is responsible for the huge difference between an EELS and an absorption spectrum.

Let us go back to the EELS of bulk silicon: a comparison between the experimental and the RPA spectrum is shown in the second inset of Fig. 4.3. Olevano and Reining [112, 17] showed that the TDLDA gives better agreement with experiment than RPA, even though the difference is small (see Fig. 16 of Ref. [17]). Some improvement can be found when the BSE approach is used (see again Fig. 16 of Ref. [17]). But since the full BSE calculation of a valence plasmon is still a computationally involved task, the use of TDLDA (or even RPA) is often well justified.

When the electron density does not present particular inhomogeneities, it can be enough to include only v_0 in the kernel (3.35) to obtain an accurate calculation of the loss spectra of extended systems. In the case of layered or low dimensional structures [113], or in presence of localized states [114, 115], also the contribution of $\bar{v}$ becomes essential and only a RPA, or often better TDLDA, calculation can yield a good agreement with the experimental data. The similarity between RPA and TDLDA is a quite general feature for the loss function at small transferred momentum $\mathbf{q}$. It holds, e.g., for the loss function of graphite [113], and for the integrated loss function of TiO_2 [114]. A good agreement with experimental spectra was obtained within RPA also for the EELS of diamond [30] and ZrO_2 [115], always at low momentum transfer. As a general rule, when $\mathbf{q}$ gets larger, the contributions of LFE and of the exchange-correlation kernel within TDLDA become more important. Also in this case RPA and TDLDA allow a good agreement with experiment, as it is shown by recent calculations of IXSS at the RPA and TDLDA level for Al [28], rutile TiO_2 [95] and various $3d$ transition metals [29]. In some cases, TDLDA can give a sizable improvement with respect to RPA [31].

In conclusion, we can state that the TDLDA is often very reliable for EELS and IXSS (both for small and large momentum transfer), and for photoabsorption in finite systems.

The LFE often give a sizable contribution to this success. One of the main remaining problems is the optical absorption in extended systems.

4.1.5 What is missing in the standard approximations?

We can summarize now the situation as it was explored so far:

- For excitation properties of *finite systems*, in general, RPA and TDLDA work quite well. There are of course many exceptions, most of which are related to the incorrect tail of the LDA (or GGA) exchange-correlation potential at large r. Some problems related to this deficiency are the already mentioned impossibility to reproduce Rydberg series, the overestimation of polarizabilities in long chain molecules, the large underestimation of ionization energies or the wrong description of any situation where the electrons are pushed to regions far away from the nuclei (e.g., by a strong laser). These issues can be solved by the use of functionals with the correct asymptotic behavior, like the EXX or the adiabatic LB94. [116].

- For *extended systems*, EELS and IXSS at small and large momentum transfer are often well reproduced within TDLDA. Instead, TDLDA fails in the calculation of optical ($q = 0$) spectra of non-metallic solids [26]. To explain this failure, the wrong asymptotic behavior of the exchange-correlation potential is less relevant, while the wrong asymptotic limit of the exchange-correlation kernel is crucial. For infinite systems, the $q = 0$ component of $\chi_{\rm KS}$ vanishes as q^2. It is then clear from the response Eq. (4.7) that if $f_{\rm xc}$ has to correct the non-interacting response for $q \to 0$ it will have to contain a term that behaves asymptotically as $1/q^2$ when $q \to 0$. This term will be particularly important in absorption calculations, where the Coulomb part of the kernel does not contain $v_{\mathbf{0}} \sim 1/q^2$. This crucial term cannot be found in the local or gradient-corrected approximations.

Finally, we recall that the TDLDA exchange-correlation potential is local in time. Few attempts to derive functionals which are nonlocal in time, i.e., that include memory effects, have been done so far. By analogy with hydrodynamics, Dobson *et al.* assumed that in the electron liquid memory resides not with each fixed point $\mathbf{r}$, but rather within each separate "fluid element" [117]. Thus the element which arrives at location $\mathbf{r}$ at time t "remembers" what happened to it at earlier times when it was at locations different from its present location $\mathbf{r}$. Using this concept, Dobson *et al.* proposed a functional that satisfies Galilean invariance and Ehrenfest's theorem. Unfortunately, no applications of this functional exist to date. This approach was further extended by Tokatly within time-dependent current DFT [118]. Furthermore, the frequency dependence of the exchange-correlation kernel has been proved to be essential to describe charge transfer between open-shell species [119] and double excitations[120, 121, 122, 123, 124]. An example of a frequency dependent model exchange-correlation kernel is presented in Sec. 4.5.1.

Several attempts have been done to correct shortcomings of RPA and TDLDA. In the next section we will start by considering the case of metallic systems and discuss explicit density functional beyond the ALDA.

4.2 Orbital-dependent functionals

In contrast to explicit density functionals, orbital-dependent functionals are constructed from the Kohn-Sham wave functions (of course they still depend implicitly on the electron

density through the self-consistency condition). Although the computational cost is typically much higher than the straightforward evaluation of a parametrization in terms of the density, this approach has the advantage that it offers a systematic route to successively more accurate approximations. Orbital-dependent functionals can be obtained in various ways. One can get a potential and kernel from a functional derivative of a suitable approximation of the action, for example by expanding the latter in powers of the Coulomb interaction. Alternatively, one can exploit links between many-body perturbation theory (MBPT) and the density-functional formulation. In the next subsection we briefly show how known results can be obtained from a linearized version of this link.

4.2.1 Kernels from the linearized Sham-Schlüter equation

The density-functional and the MBPT framework are linked by the requirement that the former has to yield the correct density given by the one-particle Green's function G of the latter, via $n(\mathbf{r},t) = -iG(\mathbf{r},\mathbf{r}',t,t^+)$, for the static as well as for the time-dependent case. (Note that in the latter case it is recommended to use Keldysh Green's functions in order to obtain the physical densities via the simple relation above [125]). From the Dyson equation one obtains hence

$$0 = \int d2\, d3\, G_{\rm KS}(1,2)\left(\Sigma(2,3) - v_{\rm xc}(2)\delta(2,3)\right) G(3,1^+)\,, \tag{4.14}$$

where Σ is the self-energy [11, 41]. This is the so-called Sham-Schlüter equation [126, 125]. If G is replaced by $G_{\rm KS}$ everywhere (including in the construction of Σ, as symbolized by $\Sigma^{\rm KS}$) the solution of this linearized equation yields for the potential

$$v_{\rm xc}(1) = -i\int d2d3\int d4\; \chi^{-1}_{\rm KS}(1,2)G_{\rm KS}(2,3)\Sigma^{\rm KS}(3,4)G_{\rm KS}(4,2^+)\,. \tag{4.15}$$

The kernel $f_{\rm xc}$, the functional derivative with respect to the density of $v_{\rm xc}$, has a contribution $f^{(2)}_{\rm xc}$ that stems from the derivative of Σ^{KS} and other terms $f^{(1)}_{\rm xc}$ coming from the derivative of the Green's functions and the inverse response function [127]. Both are explicitly orbital-dependent.

As an example, one can use the simplest case where Σ^{KS} is approximated by the (Kohn-Sham) Fock operator $\Sigma^{\rm KS}_{\rm x}(1,2) = iG_{KS}(1,2)v(2,1)$. In that case, Eq. (4.15) yields the so-called exact-exchange (EXX) OEP potential [128, 129]

$$v_{\rm EXX}(1) = -i\int d2d3\int d4\; \chi^{-1}_{\rm KS}(1,2)G_{\rm KS}(2,3)\Sigma^{\rm KS}_{\rm x}(3,4)G_{\rm KS}(4,2^+)\,, \tag{4.16}$$

where all KS quantities are calculated self-consistently using the EXX potential. The contributions to the kernel become

$$f^{(2),{\rm EXX}}(1,2) = \int d3d4d5d6\; \chi^{-1}_{KS}(1,3)G_{\rm KS}(3,4)G_{\rm KS}(5,3) \times v(4,5)G_{\rm KS}(4,6)G_{\rm KS}(6,5)\chi^{-1}_{\rm KS}(6,2)\,, \tag{4.17}$$

(which is nothing else but the electron-hole attraction term of time-dependent-EXX, TD-EXX [69, 129, 127]). The rest of the terms – which have the difficult task to open the

bandgap with respect to the KS one in TD-EXX – reads

$$f^{(1),\mathrm{EXX}}(1,2) = \int d3d4d5d6\ \chi_{\mathrm{KS}}^{-1}(1,3)G_{\mathrm{KS}}(3,6)G_{\mathrm{KS}}(6,4) \times \left[\Sigma_x^{\mathrm{KS}}(4,5) - \delta(4,5)v_{\mathrm{KS}}(4)\right] G_{\mathrm{KS}}(5,3)\chi_{\mathrm{KS}}^{-1}(6,2) + \int d3d4d5d6\ \chi_{\mathrm{KS}}^{-1}(1,3)G_{\mathrm{KS}}(6,3)G_{\mathrm{KS}}(3,4) \times \left[\Sigma_x^{\mathrm{KS}}(4,5) - \delta(4,5)v_{\mathrm{KS}}(4)\right] G_{\mathrm{KS}}(5,6)\chi_{KS}^{-1}(6,2)\,. \quad (4.18)$$

4.2.2 The time-dependent optimized-potential method from an action formalism

The TD-OEP potential can also be obtained from the action formalism. In this case, the time-dependent optimized-potential method [68] treats the Coulomb interaction as a perturbation that is switched on adiabatically in the interval $(-\infty, t_0)$, while a compensating local potential ensures that the density remains constant and equal to the static ground-state density $n_{\mathrm{GS}}(\mathbf{r})$ throughout the entire switching-on process. In this way it provides an adiabatic connection between the stationary ground state of the non-interacting Kohn-Sham system at $t \to -\infty$ and the wave function Ψ_0 of the true interacting electrons at $t = t_0$ that enters in the definition of the action (3.21). In order to incorporate the switching-on process in the theoretical description of the evolution of the system, the beginning and end of the pseudotime contour C must be extended to $-\infty$. The combination of the adiabatic connection with the time-contour method makes it possible to apply standard perturbation techniques and expand $A_{\mathrm{xc}}[n]$ in terms of the Kohn-Sham orbitals and the Coulomb interaction [125].

For an orbital-dependent action, two equivalent expressions for $\delta A_{\mathrm{xc}}[n]/\delta v_{\mathrm{KS}}(\mathbf{r},\tau)$ can be derived by applying the chain rule with different intermediate quantities:

$$\int_C d\tau' \int d^3r' \frac{\delta A_{\mathrm{xc}}[n]}{\delta n(\mathbf{r}',\tau')}\frac{\delta n(\mathbf{r}',\tau')}{\delta v_{\mathrm{KS}}(\mathbf{r},\tau)} = \int_C d\tau' \int d^3r' \sum_{j=1}^{\infty}\left(\frac{\delta A_{\mathrm{xc}}[n]}{\delta\varphi_j(\mathbf{r}',\tau')}\frac{\delta\varphi_j(\mathbf{r}',\tau')}{\delta v_{\mathrm{KS}}(\mathbf{r},\tau)} + \frac{\delta A_{\mathrm{xc}}[\varphi_j]}{\delta\varphi_j^*(\mathbf{r}',\tau')}\frac{\delta\varphi_j^*(\mathbf{r}',\tau')}{\delta v_{\mathrm{KS}}(\mathbf{r},\tau)}\right)\,. \quad (4.19)$$

The first functional derivative on the left-hand side gives rise to the exchange-correlation potential (3.25), which can be determined from this identity because all other terms are known: The linear Kohn-Sham density-response function $\delta n(\mathbf{r}',\tau')/\delta v_{\mathrm{KS}}(\mathbf{r},\tau)$ is obtained with the help of time-dependent perturbation theory by applying the same techniques as in Ch. 3 in the pseudotime domain, while the derivatives of $A_{\mathrm{xc}}[n]$ on the right-hand side of Eq. (4.19) can be calculated analytically for a given orbital-dependent functional. The variations of the orbitals

$$\frac{\delta\varphi_j(\mathbf{r}',\tau')}{\delta v_{\mathrm{KS}}(\mathbf{r},\tau)} = -\mathrm{i}\varphi_j(\mathbf{r},\tau)\sum_{k=1}^{\infty}\varphi_k^*(\mathbf{r},\tau)\varphi_k(\mathbf{r}',\tau')\Theta(\tau'-\tau) \quad (4.20)$$

and the corresponding formulas for the conjugate orbitals $\delta\varphi_j^*(\mathbf{r}',\tau')/\delta v_{\mathrm{KS}}(\mathbf{r},\tau)$ again follow from time-dependent perturbation theory. Finally, an expression for the exchange-correlation kernel is obtained by manipulating in an analogous way the second functional

derivative

$$\frac{\delta^2 A_{\rm xc}[n]}{\delta v_{\rm KS}(\mathbf{r},\tau)\,\delta v_{\rm KS}(\mathbf{r}_2,\tau_2)} = \int_C d\tau' \mathrm{d}\tau_1 \int \mathrm{d}^3r'\,\mathrm{d}^3r_1\, \frac{\delta^2 A_{\rm xc}[n]}{\delta n(\mathbf{r}',\tau')\delta n(\mathbf{r}_1,\tau_1)} \frac{\delta n(\mathbf{r}',\tau')}{\delta v_{\rm KS}(\mathbf{r},\tau)} \frac{\delta n(\mathbf{r}_1,\tau_1)}{\delta v_{\rm KS}(\mathbf{r}_2,\tau_2)} + \int_C \mathrm{d}\tau' \int \mathrm{d}^3r'\, \frac{\delta A_{\rm xc}[n]}{\delta n(\mathbf{r}',\tau')} \frac{\delta^2 n(\mathbf{r}',\tau')}{\delta v_{\rm KS}(\mathbf{r},\tau)\delta v_{\rm KS}(\mathbf{r}_2,\tau_2)}; \quad (4.21)$$

here the term on the right side containing the double derivative of $A_{\rm xc}[n]$ is nothing else but $\chi_{\rm KS} f_{\rm xc} \chi_{\rm KS}$, which allows one to solve for $f_{\rm xc}$ after evaluation of all other terms.

4.2.3 Exact exchange

The leading term in the expansion of $A_{\rm xc}[n]$ in powers of the Coulomb interaction is the exchange part, which is of first order and given by

$$A_{\rm x}[n] = -\frac{1}{2}\int_C d\tau \sum_{j=1}^{\infty} f_j \sum_{k=1}^{\infty} f_k \int d^3r \int d^3r' \, \frac{\varphi_j^*(\mathbf{r},\tau)\varphi_k(\mathbf{r},\tau)\varphi_j(\mathbf{r}',\tau)\varphi_k^*(\mathbf{r}',\tau)}{|\mathbf{r}-\mathbf{r}'|}\,, \quad (4.22)$$

while the correlation part $A_{\rm c}[n]$ includes all higher-order contributions. Inserting this expression into (4.19) and evaluating all quantities with the static density $n_{\rm GS}(\mathbf{r})$ on the physical time axis yields the "exact exchange potential" (4.16) [130, 131]. For the static ground state potential this yields a relatively simple expression

$$\int d^3r'\, v_{\rm EXX}(\mathbf{r}')\chi_{\rm KS}(\mathbf{r}',\mathbf{r};\omega=0) = \int d^3r' \int d^3r''\, \Sigma_{\rm x}(\mathbf{r}',\mathbf{r}'') \sum_{j=1}^{\infty}\sum_{k=1}^{\infty} (f_j - f_k) \frac{\varphi_j^*(\mathbf{r}')\varphi_k(\mathbf{r}'')\varphi_j(\mathbf{r})\varphi_k^*(\mathbf{r})}{\varepsilon_j - \varepsilon_k}\,, \quad (4.23)$$

with the non-local exchange self-energy

$$\Sigma_{\rm x}(\mathbf{r}',\mathbf{r}'') = -\sum_{j=1}^{\infty} f_j \frac{\varphi_j(\mathbf{r})\varphi_j^*(\mathbf{r}')}{|\mathbf{r}-\mathbf{r}'|}\,. \quad (4.24)$$

As pointed out above the latter takes the same form as the Hartree-Fock exchange operator but is here constructed from the Kohn-Sham orbitals. Solving Eq. (4.23) for the exact exchange potential requires an inversion of the static linear density-response function $\chi_{\rm KS}(\mathbf{r}',\mathbf{r};0)$, which is in practice achieved by a matrix inversion after projection on a suitable basis set, such as plane waves for extended systems [132, 133]. The matrix elements with reciprocal lattice vectors $\mathbf{G} = \mathbf{0}$ or $\mathbf{G}' = \mathbf{0}$ and $\mathbf{q} = \mathbf{0}$ must be omitted in this case [134]. The restriction to this submatrix is necessary to guarantee a one-to-one correspondence between variations of the density and the effective potential and hence to obtain an invertible operator; it excludes constant potential shifts that leave the density unchanged as well as density variations that violate particle-number conservation.

Compared to the evaluation of explicit density functionals, the construction of $v_{\rm EXX}(\mathbf{r})$ is considerably more expensive, because it requires not only the occupied conduction states but also a summation over the unoccupied part of the spectrum. In addition, the linear density-response function must be inverted in each cycle of the self-consistency loop. Practical calculations were therefore initially restricted to atoms and small molecules, but the method is now also routinely applied to bulk semiconductors, insulators and metals [134, 135, 136, 137, 138, 139, 140].

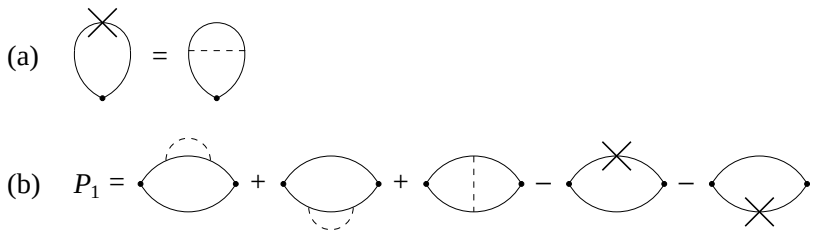

Figure 4.4: Diagrammatic form of (a) the equation for the exact exchange potential and (b) the first-order irreducible polarizability. A solid line represents the Green function of the non-interacting Kohn-Sham electrons, a broken line represents the Coulomb interaction, and the local exchange potential is indicated by a cross.

From a theoretical point of view, the exact exchange potential has definite advantages. In particular, it is free of self-interaction and exhibits the correct asymptotic behavior for finite systems [131], where it decays like $-1/r$, while the LDA and GGA fall off exponentially. The exact exchange potential further features a discontinuity with respect to a change in the number of electrons [139]. Such a discontinuity is also contained in the exact functional; it is the difference between the Kohn-Sham eigenvalue gap and the true quasiparticle band gap in semiconductors [141, 126].

The "exact exchange" kernel is similarly obtained, following the outline of Eq. (4.21), from the relation

$$\int d^3r'' \int d^3r''' \, \chi_{\mathrm{KS}}(\mathbf{r},\mathbf{r}'';\omega) f_{\mathrm{x}}(\mathbf{r}'',\mathbf{r}''';\omega) \chi_{\mathrm{KS}}(\mathbf{r}''',\mathbf{r}';\omega) = P_1(\mathbf{r},\mathbf{r}';\omega) \; . \tag{4.25}$$

The right-hand side equals the first-order contribution to the irreducible polarizability in an expansion in powers of the Coulomb interaction. It consists of five distinct terms, which can be derived in matrix notation [128] but are more easily summarized in terms of Feynman diagrams [142]. The diagrammatic form of $P_1(\mathbf{r},\mathbf{r}';\omega)$ is shown in Fig. 4.4 together with the representation of Eq. (4.23). The first two terms are the self-energy insertions with the non-local exchange operator for independent electrons and (contributions due to Σ_{x} in Eq. (4.18)), while the third arises from the attractive electron-hole interaction (4.17). The last two terms contain the exact local exchange potential (contributions due to v_{xc} in (4.18)) and must be subtracted in order to avoid double counting.

In contrast to the ALDA, the exact exchange kernel is both non-local and frequency-dependent. Furthermore, in the case of semiconductors its Fourier transform diverges in the limit of small wave vectors, as required for the exact functional [128].

As a first practical test of its performance for electronic excitations in extended systems we display the plasmon dispersion for the homogeneous electron gas at $r_{\mathrm{s}} = 4$ calculated with the exact exchange kernel in Fig. 4.5. The ALDA and the results obtained with the parametrization by Richardson and Ashcroft [143] are shown for comparison. The exact exchange kernel is evidently in very good agreement with the RA reference values in the entire region outside the electron-hole pair continuum and constitutes a definite improvement over the ALDA. Based on our earlier analysis, we attribute this to a close match with the wave-vector-dependence of the complete functional and conclude that the exact exchange kernel is a suitable starting point for the quantitative investigation of collective excitations in free-electron metals [144].

Early results from the time-dependent exact exchange method for semiconductors indicated a good performance: Kim and Görling [129] calculated the optical absorption spectrum of silicon and found good agreement with experimental data. However, it was later

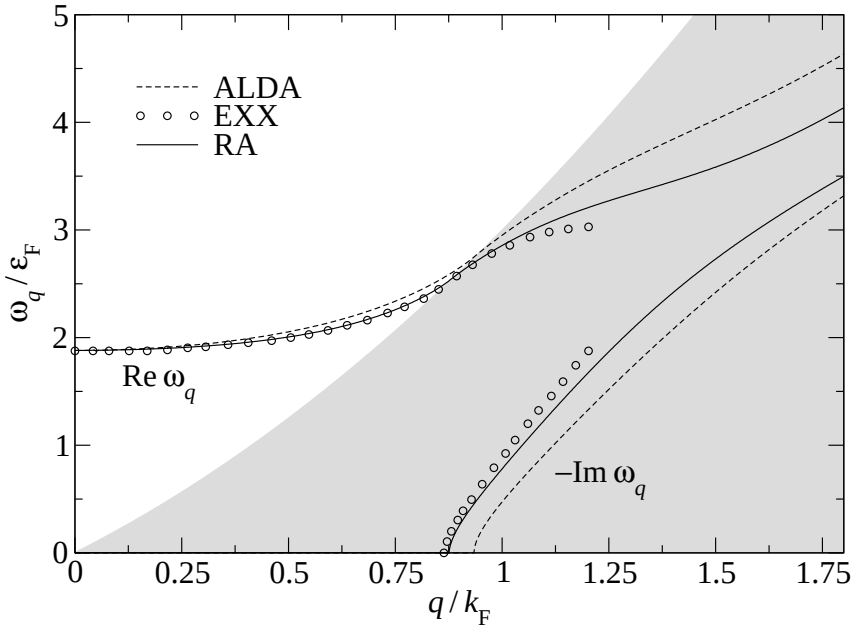

Figure 4.5: Plasmon dispersion for the homogeneous electron gas at $r_\mathrm{s} = 4$ with the exact exchange kernel (EXX) compared to the ALDA and the reference values obtained with the parametrization by Richardson and Ashcroft (RA) [143].

observed that those calculations contained a cutoff of the divergent Coulomb potential at small wave vectors, which actually had a large effect on the results and was in fact responsible for the good quantitative performance [127]. As the singularity reflects the long range of the Coulomb interaction in real space, this cutoff means that the kernel was effectively evaluated with a short-range, screened interaction. If the singularity is properly taken into account, TD-EXX should indeed be similar to time-dependent Hartree-Fock [127]. The results change then drastically, which can be understood by considering the effect on the polarizability $P_1(\mathbf{r}, \mathbf{r}'; \omega)$: The Kohn-Sham eigenvalues obtained from the exact exchange potential are closer to the experimental band structures than LDA ones [134], but the self-energy insertion in the first two terms in 4.4 increases the eigenvalue gap close to the Hartree-Fock result, leading to a far too high absorption threshold. In addition, the unscreened electron-hole interaction in the third term gives rise to a strongly overbound exciton with an incorrect line shape [127]. If the bare Coulomb potential is replaced by a screened interaction, then the self-energy insertion is comparable to the GW approximation, which yields generally good quasiparticle band gaps (see e.g., Ref. [145]), and the exciton line shape is reproduced correctly by the *screened* electron-hole interaction W.

It has also been shown recently [146] that consistent inclusion of screening beyond EXX in the OEP potential reduces the Kohn-Sham eigenvalue gap and brings its value close to the LDA one; the discontinuity yields then the correct quasiparticle gap. A proper treatment of correlation (i.e., here: screening) is hence crucial for semiconductors, and computational schemes based only on exact exchange are not sufficient in this case. In addition, the linearization of the equations is problematic for the gap-opening contribution $f(1)$, because the latter has to simulate a discontinuity [35]. This problem can be overcome by using the full, non-linearized term.

4.3 The exchange-correlation kernel from the Sham-Schlüter equation

In the previous section the Sham-Schlüter equation has been introduced. This equation makes a link between many-body perturbation theory (MBPT) and the density-functional framework. Since recent results indicate that exploiting this link can be very fruitful, the present section is dedicated to the comparison and combination of the two approaches.

Within MBPT one deals with four-point equations. In fact, a key quantity is the four-point reducible polarizability L, that can be expressed in terms of the two-particle Green's function G_2 describing the propagation of two particles (for absorption, the relevant part describes the propagation of an electron and a hole):

$$L(1,2,3,4) = L_0(1,2,3,4) - G_2(1,2,3,4)\,. \tag{4.26}$$

As we have seen in Sec. 2.2, the BSE can not be written in a two-point form. As the two sets of equations (3.35), (4.7) and (2.20) have a similar mathematical structure, it is natural to try to extract information about the TDDFT exchange-correlation kernel through their comparison. Different authors reached very similar expressions for the exchange-correlation kernel starting from the BSE but using different approaches [32, 33, 34, 35, 147, 142, 36, 38]. Tested for real materials, these kernels proved to be successful in reproducing the quality of the BSE spectra via a TDDFT formalism. In present implementations their computational cost still remains comparable to the cost of solving the BSE but memory requirements are significantly reduced, and the expressions can be rewritten leading to algorithms with better scaling. Moreover, they are a very convenient starting point for further approximations. In the following we summarize some of these derivations. We will also briefly outline how the combination BSE-TDDFT can be used to improve upon current approximations of MBPT, by introducing the TDDFT concept into MBPT. Some applications are also shown.

Let us first come back to the non-linearized Sham-Schlüter equation. This is equivalent to the condition $n(\mathbf{r},t) = -iG(\mathbf{r},\mathbf{r}',t,t^+)$. In order to obtain an exact expression for $f_{\rm xc}$, Bruneval *et al.* [147] started from this equality and took its functional derivative with respect to the density. $\delta G/\delta n = -G(\delta G^{-1}/\delta n)G$ leads to

$$\mathrm{i}G(13)G(41^+)\frac{\delta G^{-1}(34)}{\delta n(2)} = \delta(12)\,. \tag{4.27}$$

Since the same exact density, and hence the same Hartree potential, should also be obtained from the Kohn-Sham potential $v_{\rm KS} = V + v_{\rm xc}$ one can write

$$G^{-1}(12) = G_0^{-1}(12) - \delta(12)(v_{\rm KS}(1) - v_{\rm xc}(1)) - \Sigma(12)\,. \tag{4.28}$$

As $\delta G_0^{-1}/\delta n = 0$, Eq. (4.27) becomes

$$P_0(13)\chi_{\rm KS}^{-1}(32) - \mathrm{i}G(13)G(41^+)\frac{\delta\Sigma(34)}{\delta n(2)} - P_0(13)f_{\rm xc}(32) = \delta(12)\,. \tag{4.29}$$

As in the linearized case, the exact $f_{\rm xc}$ turns out to consist of two terms $f_{\rm xc} = f_{\rm xc}^{(1)} + f_{\rm xc}^{(2)}$ [36, 147]. Those read now

$$f_{\rm xc}^{(1)}(12) = \chi_{\rm KS}^{-1}(12) - P_0^{-1}(12) \tag{4.30}$$

and

$$f_{\rm xc}^{(2)}(12) = -\mathrm{i}P_0^{-1}(1,1')G(1'3)G(41'^+)\frac{\delta\Sigma(34)}{\delta n(2)}\,. \tag{4.31}$$

$f_{\rm xc}^{(1)}$ exactly changes the Kohn-Sham response function into the independent QP one, in particular, it solves hence the band gap problem. $f_{\rm xc}^{(2)}$ accounts for the electron-hole interaction. Altogether, TDDFT yields then for the irreducible polarizability

$$\chi = \chi_{\rm KS} + \chi_{\rm KS}(v + \chi_{\rm KS}^{-1} - P_0^{-1} + f_{\rm xc}^{(2)})\chi = P_0 + P_0(v + f_{\rm xc}^{(2)})\chi\,. \tag{4.32}$$

After having established the link between TDDFT and QP frameworks, it is now interesting to get an explicit expression for $f_{\rm xc}^{\rm eff}$. To get an explicit approximation for $f_{\rm xc}$, one has to choose a starting approximation for the self-energy and the Green's functions. A simple choice could be to take Σ, G and P_0 as derived from a *local* and *adiabatic* exchange-correlation potential, e.g., the LDA one. This leads of course to the TDLDA and the $GW\Gamma$ approach of Ref. [46]. A better choice is to start from the GW approximation for Σ, taking W as a screened (e.g., static RPA) Coulomb interaction. For the functional derivative, it is then reasonable to do two further approximations: (i) as is usually done in the BSE, we neglect the derivative of W as usually done in the BSE; (ii) to approximate $\delta G/\delta n = -G(\delta G^{-1}/\delta n)G$ by $GP_0^{-1}G$. The latter approximation truncates the chain of derivatives $\delta\Sigma/\delta n$ that would appear if one continued to calculate all terms of $\delta G^{-1}/\delta n$ (Note that this is equivalent to supposing that G is created by a local potential). Eq. (4.31) yields then

$$f_{\rm xc}^{(2)}(34) = \int d5d6d7 P_0^{-1}(36)G(65)G(5'6)W(55')G(57)G(75')P_0^{-1}(74)\,. \tag{4.33}$$

Eq. (4.33) is the successful electron-hole exchange-correlation kernel of Refs. [32, 33, 34, 35, 147, 142, 36, 147, 38].

4.4 Comparing and combining different approaches

It is instructive to have a look also at the alternative derivations of this kernel. In fact, instead of starting from the *density* it may be more straightforward to start from the observation that MBPT and TDDFT should yield the same *two-point response function*. Since χ can in principle be obtained via $P^{\rm red}$ from Eq. (2.22), one could invert the screening equation and determine $f_{\rm xc}$ from $f_{\rm xc} = \chi_{\rm KS}^{-1} - \chi^{-1} - v$ [148, 149]. The latter relation is of course not of practical interest, but can give insight about general features of the kernel, like its overall frequency behavior, an idea that has been exploited in [150]. Reining *et al.* [32, 33] instead used the equality of the response functions in order to obtain an approximate expression for the exchange-correlation kernel of TDDFT by mapping directly the matrix elements of the BSE (2.20) onto the matrix elements of the TDDFT linear response equation (3.35). The derivation starts by rewriting the TDDFT Dyson equation (3.35) in a four-point formalism

$${}^4\bar{\chi} = {}^4\chi_{\rm KS} + {}^4\chi_{\rm KS}({}^4\bar{v} + {}^4f_{\rm xc}){}^4\bar{\chi}\,, \tag{4.34}$$

where the four-point Coulomb interaction ${}^4\bar{v}(1,2,3,4) = \delta(1,2)\delta(3,4)\bar{v}(1,3)$ and the four-point kernel ${}^4f_{\rm xc}(1,2,3,4) = \delta(1,2)\delta(3,4)f_{\rm xc}(1,3)$ are defined [33]. On the other hand, the BSE (2.21a) has the same structure as Eq. (4.34), but with ${}^4\chi_{\rm KS}$ replaced by its four-point MBPT counterpart ${}^4L_0$, and the TDDFT kernel replaced by

$${}^4K = \delta(1,2)\delta(3,4)\bar{v}(1,3) - \delta(1,3)\delta(2,4)W(1,2)\,. \tag{4.35}$$

In [32, 33], an approximation for both $f_{\rm xc}^{(1)}$ and $f_{\rm xc}^{(2)}$ were derived; since in practice it is convenient to use the exact expression (4.30) for the former contribution, only the derivation

of $f_{\rm xc}^{(2)}$ will be discussed in the following. We thus replace $\chi_{\rm KS}$ by P_0 and focus on the second part of the exchange-correlation kernel. The first term of the total kernel in both TDDFT and BSE, i.e., the bare Coulomb interaction $\bar{v}$, is identical. One might hence try to identify the remaining part of the kernel $f_{\rm xc}^{(2)}$ with the screened Coulomb interaction of the BSE kernel (4.35):

$$\delta(1,2)\delta(3,4)f_{\rm xc}^{(2)}(1,3) \leftrightarrow -\delta(1,3)\delta(2,4)W(1,2)\,. \tag{4.36}$$

However, as the δ - functions do not contract the same indices expression (4.36) cannot be an equality.

Different approaches have been proposed to overcome this difficulty and nevertheless use the similarity of the equations.

1. The assumption that kernels could be similar for a limited number of transitions: For this approach, it is useful to write Eq. (4.36) on a basis of pairs of Kohn-Sham LDA states (transition space) [151]

$$F^{\rm TDDFT}_{(vc\mathbf{k})(v'c'\mathbf{k}')} \leftrightarrow F^{\rm BSE}_{(vc\mathbf{k})(v'c'\mathbf{k}')}, \tag{4.37}$$

with the matrix elements

$$F^{\rm TDDFT}_{(vc\mathbf{k})(v'c'\mathbf{k}')} = 2\int d^3r\, d^3r' \Phi(v\mathbf{k}c\mathbf{k},\mathbf{r}) f_{\rm xc}^{(2)}(\mathbf{r},\mathbf{r}',\omega)\Phi^*(v'\mathbf{k}'c'\mathbf{k}',\mathbf{r}') \tag{4.38a}$$

$$F^{\rm BSE}_{(vc\mathbf{k})(v'c'\mathbf{k}')} = -\int d^3r\, d^3r' \Phi(v\mathbf{k}v'\mathbf{k}',\mathbf{r}) W(\mathbf{r},\mathbf{r}',0)\Phi^*(c\mathbf{k}c'\mathbf{k}',\mathbf{r}')\,, \tag{4.38b}$$

where $\Phi(i\mathbf{k}j\mathbf{k}',\mathbf{r})$ is the product of a pair of Kohn-Sham wavefunctions; The indices $\{i,\mathbf{k}\}$ stand for the band-index and momentum of the Kohn-Sham state. Only the resonant contribution is shown (transitions from occupied to empty states) and the momentum transfer is supposed to be vanishing since the approach has been derived for optical spectra; both conditions can however easily be generalized. As usual in calculations based on the Bethe-Salpeter equation, W is moreover supposed to be static. Note that in practice, the equality in (4.37) is then imposed for transitions belonging to a a certain frequency range. The TDDFT spectra will match the BSE spectra only in this region. The quantity $F^{\rm TDDFT}_{(vc\mathbf{k})(v'c'\mathbf{k}')}$ is now a static quantity over that energy range, as a consequence of the static approximation for W. (However, since because of (i) a different kernel will be obtained for a different group of transitions, there is an overall effective frequency dependence). Reining *et al.* [32] have formally inverted Eq. (4.37). A Fourier transform to reciprocal space leads then to

$$f_{\rm xc}^{(2)}(\mathbf{q}\to 0,\mathbf{G},\mathbf{G}') = \sum_{vc\mathbf{k}\,v'c'\mathbf{k}'} \Phi^{-1}_{\mathbf{G}}(v\mathbf{k}c\mathbf{k};\mathbf{q}\to 0) F^{\rm BSE}_{(vc\mathbf{k})(v'c'\mathbf{k}')} \left(\Phi^*\right)^{-1}_{\mathbf{G}'}(v'\mathbf{k}'c'\mathbf{k}';\mathbf{q}\to 0). \tag{4.39}$$

The TDDFT exchange-correlation kernel derived in this way has correct asymptotic behavior (see the discussion in Sec. 4.5); it stems from the asymptotic behavior of the Φ, *not* from the Coulomb interaction W as one might have suspected. The inversion of the matrices Φ is purely formal; the kernel (4.39) itself was in fact not evaluated in Ref. [32], but used to derive a TDDFT-like screening equation. A more direct way to arrive at the same screening equation along similar lines has been proposed by Sottile et al. [33]. One starts by writing the TDDFT-like response equation (4.7) in a symmetrized form (the same can be done with Eq. (3.35)):

$$\bar{\chi} = P_0\left(P_0 - P_0\bar{v}P_0 - P_0 f_{\rm xc}^{(2)}P_0\right)^{-1}P_0\,. \tag{4.40}$$

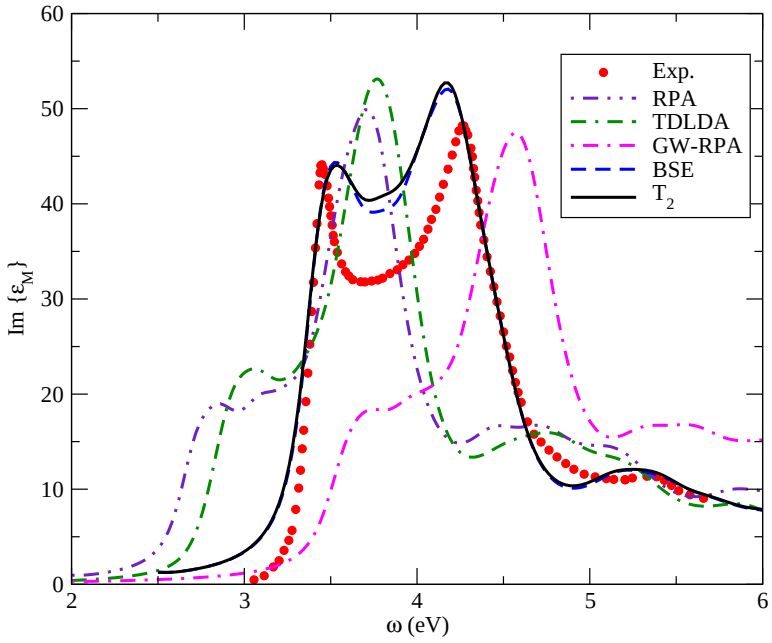

Figure 4.6: Imaginary part of the macroscopic dielectric function for Si from Ref. [33]. Dots: experiment [110]; dash-dot-dot line: RPA calculation; dash-dash-dot line: TDLDA calculation; dash-dot line: GW-RPA calculation; dash line: BSE calculation; solid line: T_2 kernel.

It appears that in order to calculate $\bar{\chi}$ one only needs $P_0 f_{\rm xc}^{(2)} P_0$, and not $f_{\rm xc}^{(2)}$ explicitly. This integral contains sums over transitions involving $F^{\rm TDDFT}_{(vc\mathbf{k})(v'c'\mathbf{k}')}$. Enforcing hence the equality in 4.37 yields

$$P_0 f_{\rm xc}^{(2)} P_0 = T_2 \,, \tag{4.41}$$

where T_2 is calculated as :

$$T_2(\mathbf{G},\mathbf{G}',\omega) = \frac{2}{N_k^2} \sum_{vc\mathbf{k}v'c'\mathbf{k}'} \frac{\Phi^*(v\mathbf{k}c\mathbf{k};\mathbf{G})}{\varepsilon^{\rm QP}_{c\mathbf{k}} - \varepsilon^{\rm QP}_{v\mathrm{k}} - \omega} F^{\rm BSE}_{(vc\mathbf{k})(v'c'\mathbf{k}')} \frac{\Phi(v'\mathbf{k}'c'\mathbf{k}';\mathbf{G}')}{\varepsilon^{\rm QP}_{c'\mathbf{k}'} - \varepsilon^{\rm QP}_{v'\mathbf{k}'} - \omega} \,; \tag{4.42}$$

(here we give again only the expression for the resonant contribution, which is the dominant term in absorption spectra). This is a result that can be used in practice. The first calculation has been done for bulk silicon; the result shown in 4.6 obtained by Sottile *et al.* shows almost perfect agreement with a result obtained by solving the BSE. From a computational point of view, one still has to calculate W; in today's implementation moreover the two-particle matrix elements $W_{(vc\mathbf{k})(v'c'\mathbf{k}')}$ are calculated, which is often the most expensive part of a BSE calculation. In principle the sum over transitions could be performed in a different order and the latter calculation avoided. Moreover by studying Eq. (4.42), one can derive model kernels, which can decrease drastically the computational cost. The performance of the kernel as well as efficient approximations will be illustrated in Sec. 4.5.

2. A perturbative approach leading to the same exchange-correlation kernel was proposed by Adragna *et al.*[34]: Their starting point is again the requirement that the TDDFT and the BSE two-point response functions should be equal. The polarizabilities are then developed perturbatively to the same order. Truncation to first order

leads again to Eq. (4.41) with Eq. (4.42). Marini *et al.* used this kernel for the calculation of optical absorption of insulators, including a bound exciton, and loss spectra at non-vanishing momentum transfer [35]. Both cases were in good agreement with experiments. It was also shown that the inclusion of the second-order term in the perturbative expansion did not affect significantly the calculated spectra. For more details see chapters 10 and 20 of Ref. [152]

3. The perturbative approach was also explored in terms of Feynman diagrams [142, 153, 36, 118]: Stubner, Tokatly and Pankratov [36] derived an integral equation which leads to Eq. (4.42) when non-locality beyond the first order is neglected. Also the separation of $f_{\rm xc}^{(1)}$ and $f_{\rm xc}^{(2)}$ naturally comes out from that derivation.

   Finally we mention the work of von Barth *et al.* [38]: here the kernel is derived from a functional approach. Again, this yields $f_{\rm xc}^{(1)}$ in its linearized version as well as the above approximation for $f_{\rm xc}^{(2)}$, when GW diagrams are chosen. The advantage of deriving a kernel as double derivative of a functional is that the symmetry of the expression guarantees that important conservation laws are fulfilled.

This kernel is hence the result of the work of several groups.

In order to complete the section about links between MBPT and TDDFT, it is useful to remind that improved TDDFT response functions and kernels can in turn be inserted into many-body calculations in order to go beyond existing approximations, in particular the RPA-based GWapproximation. The kernel of linear-response TDDFT stems from the variations of the Hartree and exchange-correlation potentials with respect to the density. Within MBPT, the variations are taken with respect to the one-particle Green's function. However, when one is only interested in the self-energy and the Green's function (and not in the full four-point response function) also in the case of MBPT these variations can be created by a local external potential, for which the Runge-Gross theorem holds [19]. As a consequence, also in the MBPT scheme it is possible to rely on the fact that the density variations determine the physics of excitations. Starting from this observation, Bruneval *et al.* suggested an alternative way to find approximations for the self-energy Σ [147]. This operator, that accounts for all the many-body effects on the one-particle Green's function beyond the Hartree term and is a key quantity of MBPT, is defined as [11, 41]

$$\Sigma(1,2) = \mathrm{i}\int d3\; d4\; d5\; G(1,4)\Gamma(4,2;5)\frac{\delta V(5)}{\delta U(3)}v(3,1^+)\,, \tag{4.43}$$

where G is the one-particle Green's function, U is a local external potential, $V(1) = U(1) + v_{\rm H}(1)$ is the total classical potential – including also the Hartree contribution $v_{\rm H}$, and $\delta V(5)/\delta U(3) = \epsilon^{-1}(5,3)$. The irreducible vertex function Γ is defined as

$$\Gamma(1,2,3) = -\frac{\delta G^{-1}(1,2)}{\delta V(3)} = \delta(1,3)\delta(2,3) + \frac{\delta\Sigma(1,2)}{\delta V(3)}\,. \tag{4.44}$$

Bruneval *et al.* proposed to replace the chain rule usually employed to obtain $\delta\Sigma/\delta V$, namely $(\delta\Sigma/\delta G)(\delta G/\delta V)$ [40, 41], with the alternative chain rule $(\delta\Sigma/\delta\rho)(\delta\rho/\delta V)$. This step is justified by the one-to-one relation between the time-dependent density and external potential, or consequently between the density and the classical potential V. Eq. (4.44) then becomes

$$\Gamma(1,2;3) = \delta(1,3)\delta(2,3) + \int d4\;\frac{\delta\Sigma(1,2)}{\delta\rho(4)}P(4,3), \tag{4.45}$$

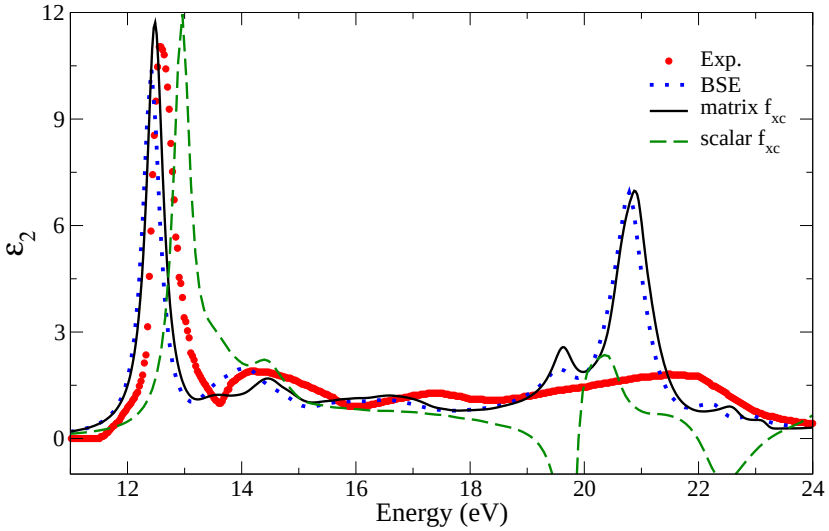

Figure 4.7: Optical absorption spectra of LiF from Ref. [35] calculated within the BSE (dots), and TDDFT (solid line) compared with experiments (circles) [105]. The results obtained using a scalar $f_{\rm xc}$ (dashed line) are shown to stress the importance of the $\mathbf{G}, \mathbf{G}' \neq 0$ terms in $f_{\rm xc}$.

where $P = \delta\rho/\delta V$ is the *irreducible* polarizability

$$P(1,2) = -i \int d3\; d4\; G(1,3)G(4,1)\Gamma(3,4,2)\,. \tag{4.46}$$

On the other hand, if one multiplies Eq. (4.45) with two Green's functions G and integrates, the result is

$$P(1,2) = P_0(1,2) + \int d3\; d4\; P_0(1,3) f_{\rm xc}^{(2)}(3,4) P(4,2) \tag{4.47}$$

with 4.31. This constitutes hence an alternative derivation of the exact kernel. Moreover, once P is known Eq. (4.45) allows one to calculate the three-point vertex, and hence an improved self-energy, without solving a four-point integral equation. It has been shown [147] that, besides the better description of the test-charge–test-charge screened W, a major contribution to the correction beyond GW stems from the induced exchange-correlation potential that acts on an additional particle or hole on top of the induced Hartree potential; only the latter is contained in GW (moreover, it is approximated in the RPA).

4.4.1 Applications

When coming to actual calculations it should be noted that in general (i) as mentioned above, only $f_{\rm xc}^{(2)}$ is explicitly used, whereas the GW correction is included by using P_0; (ii) most calculations are restricted to the resonant contribution; (iii) the diagonal contribution $F^{\rm BSE}_{(vc\mathbf{k})(vc\mathbf{k})}$ is extracted from $f_{\rm xc}^{(2)}$ and included in P_0. Strictly speaking, this contribution should be zero in a solid, but for a finite k-point sampling it is non-vanishing. These three points are important for the quality of the final results. An example of the application of the BSE-derived kernel (4.42) to real systems can be found in Fig. (4.7) [35], where the optical absorption spectrum of LiF is shown. One can observe that, as anticipated, the agreement between the BSE calculation and the TDDFT calculation using the BSE-derived kernel is excellent. The importance of the matrix character of $f_{\rm xc}$ (i.e., the importance of

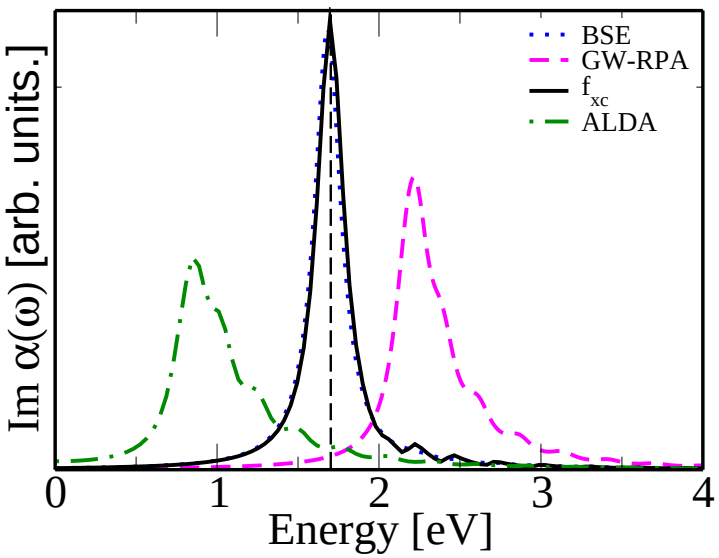

Figure 4.8: Optical absorption spectra of polyacethylene compared with experiment (vertical dashed-line) from Refs. [156, 157]. The BSE calculation (dots) and the TDDFT calculation using the many-body $f_{\rm xc}$ (solid line) are in excellent agreement with the experiment. GW-RPA (dashed-line) and TDLDA calculations (dot-dashed line) are also shown.

$\mathbf{G}, \mathbf{G}' \neq 0$ terms) in wide-gap insulators is demonstrated by looking at the curve obtained with a scalar ($\mathbf{G} = \mathbf{G}' = 0$) $f_{\rm xc}$. Although the kernel is strongly frequency dependent, only the main peak is reproduced correctly, while some unphysical regions of negative absorption appear at higher energies. In contrast, when dealing with systems with continuum exciton effects (Si, diamond, etc.) the use of the head of $f_{\rm xc}$ is often sufficient to recover the BSE spectrum. This is related to the different degree of inhomogeneity of the induced density in simple semiconductors and wide-gap insulators. The BSE-derived kernel (4.42) has also been successfully applied to the study of low-dimensional systems. An example are conjugated polymers. We have already pointed out in Sec. 4.1.2 that simple adiabatic local and gradient corrected functionals fail in describing the dielectric response of long molecular chains [27]. Current density functional approaches can partially solve this problem [154, 155]. The non-local frequency dependent BSE-derived kernel restores the good agreement between the calculated and the measured polarizabilities. This can be observed in Fig 4.8, where the calculated optical absorption spectrum of polyacethylene is compared with experimental data [156, 157].

In brief, the BSE derived $f_{\rm xc}$ kernel is able to reproduce the optical and energy-loss spectra of a large class of materials including semiconductors and large band-gap insulators [33, 35], as well as systems of low dimensionality [156]. Although calculations are today still relatively cumbersome, improved algorithms and/or efficient approximations are expected to make this approach clearly competitive with respect to a BSE calculation, when one is interested in an efficient determination of spectra.

4.5 Simple models

In Sec. 4.4 we introduced a class of parameter-free kernels that are particularly successful for the description of optical absorption in solids – the kernels derived from the BSE. Even though they have a potentially reduced computational effort with respect to the BSE,

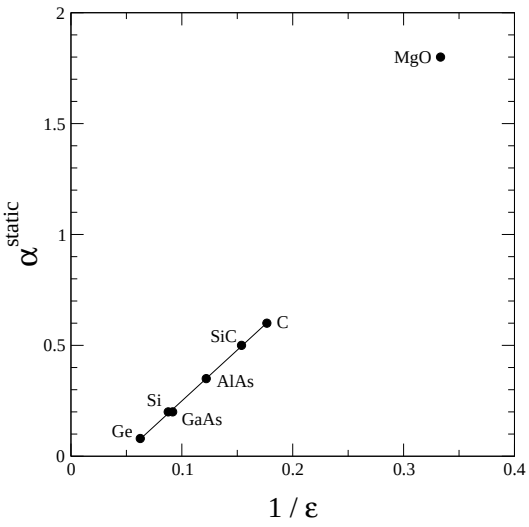

Figure 4.9: Material dependence of $\alpha^{\rm static}$ with respect to the inverse of the dielectric constant [37].

calculations using these kernels are however still significantly more involved than those within the RPA or the TDLDA. Therefore, the question of finding simple and efficient, but also reliable, models for $f_{\rm xc}$ is still open. In this quest, there are several important lessons to be learned from the BSE-derived kernels. In the following we discuss some model kernels, inspired by the BSE, that combine simplicity with a reasonably good description of response properties.

4.5.1 Long-range exchange-correlation kernels

One of the most striking characteristic of the TDLDA kernel is that it is static and local in space. Therefore, one can expect that the inclusion of either dynamical (memory) effects, long-range nonlocal terms [24, 142] or both improves, in principle, the results yielded by the simple TDLDA. In this section, we introduce some model kernels, obtained by approximating the BSE-derived kernel of Eqs. (4.31) and (4.41), that accounts for such further terms.

The exchange-correlation kernel of Eqs. (4.31) and (4.41) contains a long-range contribution (LRC) of the form $1/q^2$. This LRC is instead completely absent within the TDLDA, as the TDLDA kernel goes to a constant in the limit $q \to 0$. The simplest model that exhibits the correct LRC has the form

$$f_{\rm xc}^{\rm static}(\mathbf{q}) = -\frac{\alpha^{\rm static}}{q^2}, \tag{4.48}$$

where $\alpha^{\rm static}$ is a material dependent parameter. The use of this particular form can be motivated starting from the BSE, following the lines of Sec. 4.4 [32]. In fact, the function $\Phi_{\mathbf{G}=0}\left(v\,\mathbf{k}\,c\,\mathbf{k};\mathbf{q}\right)$ in (4.39) goes to zero as $\Phi \sim$q for $q \to 0$. Since in this limit $F^{\rm BSE}_{(vc\mathbf{k})(v'c'\mathbf{k}')}$ behaves like a constant, this implies that $f_{\rm xc}(\mathbf{q}, \mathbf{G}=0, \mathbf{G}'=0)$ goes as $1/q^2$ in the optical limit. Moreover, as it can be seen in Fig. 4.9 the LRC to the exchange-correlation kernel is inversely proportional to the macroscopic dielectric constant ϵ_∞ [37].

Note that there is also a positive long-range contribution to the exchange-correlation kernel stemming from the QP shift of eigenvalues (as predicted in Ref. [158]), that competes with the negative one resulting from the BSE, i.e., the electron-hole interaction. This

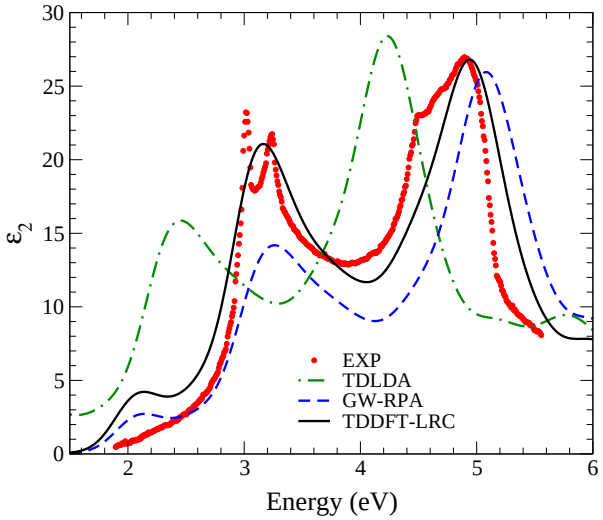

Figure 4.10: Imaginary part of the macroscopic dielectric function of GaAs [37]. Dots: experiment [159]; dot-dashed curve: TDLDA; dashed curve: GW-RPA; solid line: TDDFT-LRC.

contribution is contained in Eq. (4.30). In Refs. [32, 37] it was shown that the LRC alone is sufficient to reproduce the contribution of the electron-hole interaction $f_{\rm xc}^{(2)}$ to the optical spectra of simple semiconductors. The same is not true concerning the the self-energy contribution $f_{\rm xc}^{(1)}$, where a LRC approximation does not work. For this reason in the following discussion we will focus on models for the term $f_{\rm xc}^{(2)}$.

Fig. 4.10 shows the optical absorption spectra of GaAs [37]. As previously discussed in Sec. 4.1.3, the TDLDA result is close to the RPA curve, and both show the well known discrepancies with experiment: the peak positions are redshifted, and the intensity of the first main structure is strongly underestimated. The dashed curve (GW-RPA) is obtained by replacing the Kohn-Sham eigenvalues with GW quasiparticle energies in the RPA calculation of ϵ. This corresponds to applying the Dyson equation (3.35) for the first part of the exchange-correlation kernel $f_{\rm xc}^{(1)}$. The resulting spectrum is blueshifted and, moreover, the lineshape has not been corrected. Finally, the curve representing a TDDFT calculation starting from GW quasiparticle energies to calculate the independent-particle response and using the LRC kernel (4.48) gives an excellent fit to the experiment. This curve was obtained using $\alpha^{\rm static} = 0.2$.

The simple static LRC model, together with the linear dependence of α on $1/\epsilon_\infty$, allows one to predict the absorption spectrum from the knowledge of the experimental dielectric constant of the material in question. However, the model $f_{\rm xc}^{\rm static}$ of Eq. (4.48) has clear limits that become more and more evident as the band gap increases.

For example, already in diamond [37, 150] the first shoulder and the main peak in the spectrum cannot be both described with good precision using a single parameter $\alpha^{\rm static}$. The problem gets even more serious when bound exciton peaks appear in the spectrum, as e.g., for LiF [104] (see Fig. 4.11) or solid argon [160]. In fact, the only possible action of the LRC exchange-correlation kernel is to redistribute oscillator strength. In contrast to the full BSE kernel, this remains true also in cases where poles should appear in the bandgap, like, e.g., in LiF where bound excitons occur in the experimental spectrum (see Fig. 4.11). Furthermore, approximations as outlined above are based on a limited range of transitions. When the spectral range gets larger, e.g., when response beyond the absorption region is

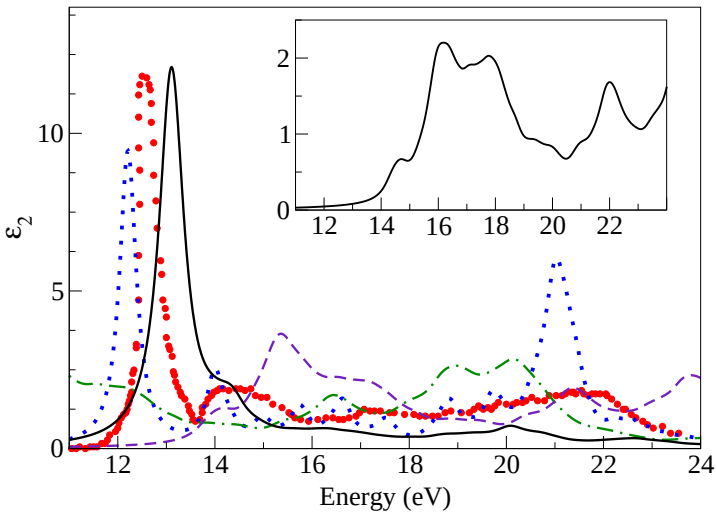

Figure 4.11: Imaginary part of the macroscopic dielectric function for LiF [104]. Dots: experiment [105]; dotted curve: BSE; dot-dashed curve: TDLDA; dashed curve: TDDFT using the static LRC model kernel; solid line: TDDFT using the dynamical LRC model kernel. In the inset: GW-RPA.

considered, as a consequence of the change of the limited range of transitions also $f_{\rm xc}$ has to change. In the case of the model kernel (4.48) this introduces an effective ω-dependence of the parameter $\alpha^{\rm static}$. In order to describe the plasmon of silicon one could for example still use Eq. (4.48), but with an $\alpha^{\rm static}$ that is an order of magnitude larger than the one that yields a good optical spectrum [37]. This will be further discussed below, after a brief summary of other approaches leading to a LRC.

The simple static LRC model (4.48) does not in fact represent the first attempt to account for long-range effects in semiconductors. Already in 1994 Godby and Sham [161] pointed out that long-range density variations give rise to an effective exchange-correlation field. It was then proved [26] that the origin of this exchange-correlation field lies in the macroscopic polarization. Alternatively, one could avoid the use of the macroscopic polarization by introducing a scissor-operator quasiparticle correction to the Kohn-Sham gap. The LRC stemming from this discussion has hence the task of increasing the gap (like $f_{\rm xc}^{(1)}$), and has, consequently, a positive sign.

Aulbur, Jönsson and Wilkins [162] studied the problem of determining static dielectric constants. They related an effective exchange-correlation field to the difference between the true and the Kohn-Sham static susceptibilities, and, by using calculated Kohn-Sham and measured (i.e., "true") values, fixed the prefactor of a LRC to the kernel for a series of materials. It resulted a contribution $\Delta f_{xc} = \gamma/q^2$, where γ is of the order of 0.25 for several small-, and medium-gap semiconductors. According to this work, the LRC correction should account for both $f_{\rm xc}^{(1)}$ and $f_{\rm xc}^{(2)}$, which is the reason why γ turns out to be small and positive. However, this model can not be extended to the description of spectra, as the quasiparticle corrections simulated by $f_{\rm xc}^{(1)}$ are too complex to be written as a simple LRC model.

Another approach to the description of the dynamical susceptibility was proposed by Boeij *et al.*[154] who obtained a polarization-dependent functional derived from current density functional theory [163]. This functional involves two parameters: one (material-dependent) accounting for a positive shift of transition energies (in fact, a scissor operator),

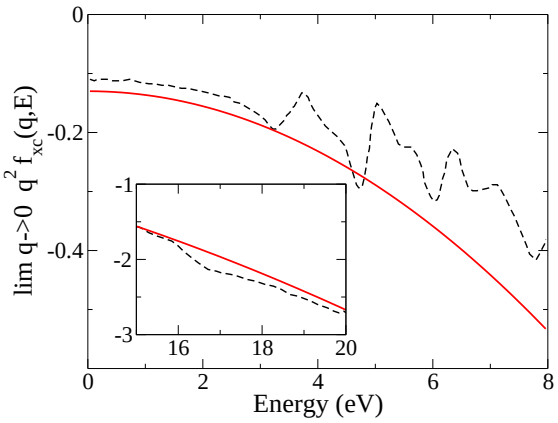

Figure 4.12: Real part of the LRC component of the exchange-correlation kernel needed to reproduce the BSE optical spectrum of silicon. The inset shows the same function in an energy region close to the plasma frequency. Dashed lines: calculation from [150]; solid line: dynamical LRC model.

and a second (constant) one, chosen to be 0.4, that multiplies a tensor $\boldsymbol{Y}$ containing the polarization effects. The tensor $\boldsymbol{Y}$ is in principle frequency-dependent, but its static value is used. This approach yields identical results to the static LRC model described here, if one identifies $0.4Y = -\alpha^{\mathrm{static}}$, and if the scissors are replaced by the quasiparticle corrections.

In consideration of the limits of the static LRC model, it is natural trying to guess how to further improve the kernel. One can either work along the lines of [32] and add a more complicated spatial behavior, or one can keep the simple $1/q^2$ form of the LRC, but introduce a frequency dependent α [150]. Clearly, this latter choice allows for each structure of the spectrum to have its own effective correction. Botti *et al.* [104] proposed a frequency dependent LRC kernel of the form

$$f_{\mathrm{xc}}^{\mathrm{dyn}}(\mathbf{q},\omega) = -\frac{1}{q^2}\left(\alpha + \beta\,\omega^2\right). \tag{4.49}$$

This choice was guided by recent calculations [150] for bulk silicon and diamond, that yielded the frequency dependence of the LRC term of the exchange-correlation kernel from the inversion of the BSE. Fig. 4.12 shows, for f_{xc} of silicon, that the dynamical model $f_{\mathrm{xc}}^{\mathrm{dyn}}$ is indeed a good approximation in a large energy range, even including the plasmon region (see inset of Fig. 4.12).

Starting from (4.42) it is possible to prove that the two parameters α and β of Eq. (4.49) can be related to physical quantities, namely the dielectric constant and the plasma frequency. For simple semiconductors, this model yields the same result as the static LRC model [104]. In the case of wide-gap insulators, like diamond or cadmium selenide, or for the EELS of silicon, the dynamical model heals the shortcomings of the static LRC kernel [104]. The improvement is significant even in the presence of bound excitons. We consider again as an example LiF (see Fig. 4.11). Setting α^{static} to the value 2.0 gives a reasonable compromise (dashed line), enhancing slightly the low energy structures without provoking the collapse of the spectrum. The worst disagreement concerns the absence of the large excitonic peak at about 12.5 eV. On the other hand, the dynamical model (solid line) is able to describe the strong bound exciton peak. A better agreement can only be found using the BSE approach (dotted line) or the full kernel derived by the BSE (see Fig. 4.7), both of which involve a much larger computational effort [106, 164, 108, 109]

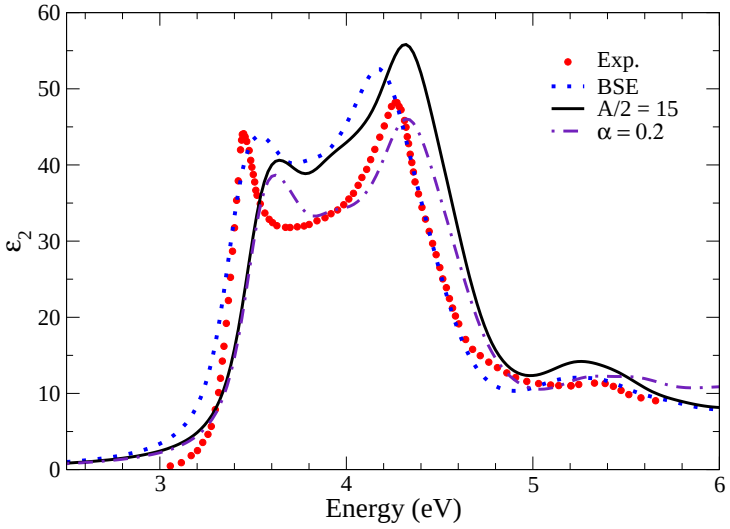

Figure 4.13: Imaginary part of the macroscopic dielectric function for bulk silicon from Ref. [160]. Dotted curve: BSE; Dot-dashed curve: TDDFT with static LRC ($\alpha^{\rm static} = 0.2$; Continuous curve: TDDFT contact kernel ($A/2 = 15$); Dots: experiment [110].

than the application of the simple dynamical LRC model. Note that the objective of these model kernels is not to provide an *ab initio* approximation to the exact TDDFT kernel, but to offer a numerically efficient framework for the calculation of response properties of complex solids and nanostructures. A key feature is that the model kernels depend on a reduced number of parameters, and that these can be related in a straightforward manner to known physical quantities. The drawback of these models is, of course, the reduced range of validity of the underlying approximation, which implies that one should carefully check the applicability of a model to a specific system.

4.5.2 Contact exciton

The contact exciton model was successfully used in the 70's for the description of continuum exciton effects in a wide range of systems [165, 166, 167, 168]. Model calculations could also show that the contact exciton is able to produce one bound state [169, 168]. This simple model gives rise to the equation

$$\epsilon_{\rm M}(\omega) - 1 = \frac{\epsilon_{\rm M}^{\rm RPA}(\omega) - 1}{1 + g(\epsilon_{\rm M}^{\rm RPA}(\omega) - 1)} \,. \tag{4.50}$$

Inspection reveals that this is the LRC kernel approximation derived in the previous section [150, 160], provided that $f_{\rm xc} = -g4\pi/q^2$. Moreover, in [165] the parameter g is dependent on ω^2, similarly to the parameter β of the dynamical LRC model of Sec. 4.5.1.

A different exchange-correlation kernel can be derived in the same spirit by replacing the screened electron-hole interaction in the BSE by a local contact potential [160]. When W in Eq. (4.36) is approximated by $\delta(12)A$, the equality is possible in Eq. (4.37) and one obtains

$$f_{\rm xc}^{\rm contact}(\mathbf{r}_1, \mathbf{r}_3) = -\frac{1}{2}\delta(\mathbf{r}_1 - \mathbf{r}_3)A \,, \tag{4.51}$$

where A is an adjustable parameter. This is obviously a ultra-short range kernel.

In Fig. 4.13 we compare optical absorption calculations performed within the different approximations with the experimental optical spectrum of silicon. The curve obtained for the ultra-short ranged $f_{xc}^{\mathrm{contact}}$ using $A/2 = 15$ (continuous curve) turns out to be in very good agreement with the result of a full BSE calculation (dotted curve) and the long-range kernel $f_{\mathrm{xc}}^{\mathrm{static}} = -\alpha/q^2$ with $\alpha = 0.2$ (dot-dashed curve). All calculations are also in good agreement with experiment (circles).

In order to understand how a short-range and a long-range f_{xc} can yield similar spectra for simple semiconductors, one has to realize that we are talking about effective exchange-correlation kernels, and not the real one. These kernels are chosen to reproduce a certain number of properties. It is clear that more than one kernel (even with very different analytical forms and physical interpretation) can lead to the same optical spectrum. The contact exciton is a very good illustration of this.

To a certain extent, a short-ranged but strong electron-hole Coulomb interaction can simulate the effect of the true, screened long-ranged one: continuum exciton effects can be well reproduced, and even one bound exciton can be created. However, in the latter case the continuum is not well described, and no higher-order peaks of the series are obtained.

The choice of which model to use should finally depend both on computational convenience and on the possibility to determine the parameters of the model without fitting to experiment. The stronger are the requirements on the precision of the results, the closer the chosen model should resemble to the exact f_{xc} and, for example, have a long range component when the system is a semiconductor or insulator. We remark that all these methods discussed above are the result of quite recent investigations, so it is very reasonable to expect further developments in the near future.

Part II

Applications

Chapter 5

Nanostructures

Electronic excitations in nanostructured materials are nowadays at the heart of many fundamental and technological research projects. Much of the progress made in modern technology is based on a deeper understanding of the properties of materials. Indeed, the characterization of electronic, structural, and bonding properties of nanosctructures is a real necessity in order to understand the origin of the unique properties that make them so appealing for applications. From both experimental and theoretical side, optical, electron and time-resolved spectroscopies open many possibilities, allowing the study of static and dynamic electron-electron correlations.

The electronic properties are particularly sensitive to the reduced dimensionality of the nanostructures: the energy levels evolve as the size of the system decreases, as a consequence of quantum confinement. Also effects due to electron-electron and electron-hole interactions can be enhanced due to the spacial confinement and anisotropy of the system. The optical spectra provide important insight into the electronic structure. In particular, the optical response of a nanostructure depends on its size and also on the atomic arrangement. This is an important feature, since the determination of the geometry is, in general, a hard task, either for experimental techniques or for sophisticated total energy calculations, and the comparison of calculated and measured spectra can allow to distinguish among different possible structures. Of course, this is true only if calculations are accurate enough to guarantee to be predictive.

In the following sections we show several illustrative examples of how TDDFT or many-body calculations within linear response can be used to unravel the physics of interesting nanostructured systems.

5.1 Excitonic effects in the optical spectra of CdSe nanowires*

5.1.1 Introduction

Nanowires exhibit a wide range of unique properties [170], including tunable band gaps, ballistic transport [171], optical anisotropy [172] and strong excitonic effects [173]. It is therefore not surprising that for the past twenty years nanowires have emerged as one of the most active fields of research in material science [170]. This growing interest is mainly

*This section is based on the article:

- *Excitonic effects in the optical properties of CdSe nanowires*, J. G. Vilhena, S. Botti and M. A. L. Marques, accepted for publication in Appl. Phys. Lett. (2010).

due to their short term promising applications [171, 174, 173] and is empowered by a strong demand from industries for smaller and more effective devices. To a large extent, the novel properties emerge from the lateral confinement of the electrons in the wire, leading to the blue shift of the electronic band gap with decreasing diameter.

In this section we focus on the optical properties of CdSe nanowires from a first-principle perspective, based and going beyond standard DFT. Beside analyzing how optical properties evolve with the diameter of the wire, we test some approximations that are commonly used for bulk materials and discuss their applicability to electronic excitations in 1D systems. Several studies of the optical properties of CdSe wires have appeared in the past years [175, 176, 177]. Classical [172] and semi-empirical [177] methods have been quite successful in describing large-diameter wires, but they fail for small and medium diameters. Furthermore, none of the articles using first-principle methods present in the literature [175, 176] was capable of capturing the physics of electronic excitations in these confined systems. This was due to the neglect of at least one of the following physical effects that are fundamental for an accurate description of nano-scale objects:

(a) Crystal local-field effects. When the polarization of the light is perpendicular to the long axis there is an accumulation of charges at the wire surface, which in turn is responsible for the attenuation of the electric field inside the nanowire. This leads to a strong suppression of the absorption for light polarized perpendicular to the nanowire axis, increasing dramatically the optical anisotropy of the system [178, 179]. This huge effect has already been measured [172] in polarized photo-luminescence experiments, but unfortunately some recent theoretical works [176, 180] still neglect it.

(b) Electron-electron interaction and excitonic effects. These effects are very pronounced in semi-conducting nanowires due to the attenuation of the screening. The strong electron-hole binding is responsible for a red shift of the fundamental absorption frequency. Due to this effect, nanowires can be seen as exciton traps, a property that endows them of great technological interest [173].

5.1.2 Ab initio calculations

To study the importance of local-field corrections, we calculated the absorption spectra of unpassivated CdSe nanowires of 5 different diameters (0.73, 1.17, 1.59, 1.77, and 2.01 nm) starting from DFT Kohn-Sham states and applying the random-phase approximation (RPA) to obtain the dielectric tensor (for details on this and all the other approximations employed in the following, refer to Ref. [181]). The neglect of local-field effects is equivalent to applying Fermi's golden rule, i.e., to treat only independent particle transitions, and completely ignores the inhomogeneity in the dielectric response due to the reduced dimensionality of the nano-object.

All CdSe nanowires were assumed to be infinitely long with periodic length 7.01 Å and with their axis parallel to the wurtzite (001) axis. Ground state calculations were performed using the DFT code ABINIT [182], and the core electrons of Cd ([Kr]4d10) and Se ([Ar]3d10) were described by Hamann norm conserving pseudo-potentials [183]. We chose the Perdew-Burke-Ernzerhof [4] approximation to the exchange-correlation functional. Converged calculations required a cutoff energy of 20 Ha and a $1 \times 1 \times 8$ Monkhorst-Pack [184] sampling of the Brillouin zone. Atomic positions were relaxed starting from the bulk wurtzite structure. The converged spacing between the wires in our supercell approach was at least 7 Å.

The optical spectra of the wire with a diameter of 0.73 nm, calculated at the RPA level including or neglecting local fields is shown in Fig. 5.1. Without local fields, there is a small anisotropy between the absorption perpendicular and parallel to the nanowire axis,

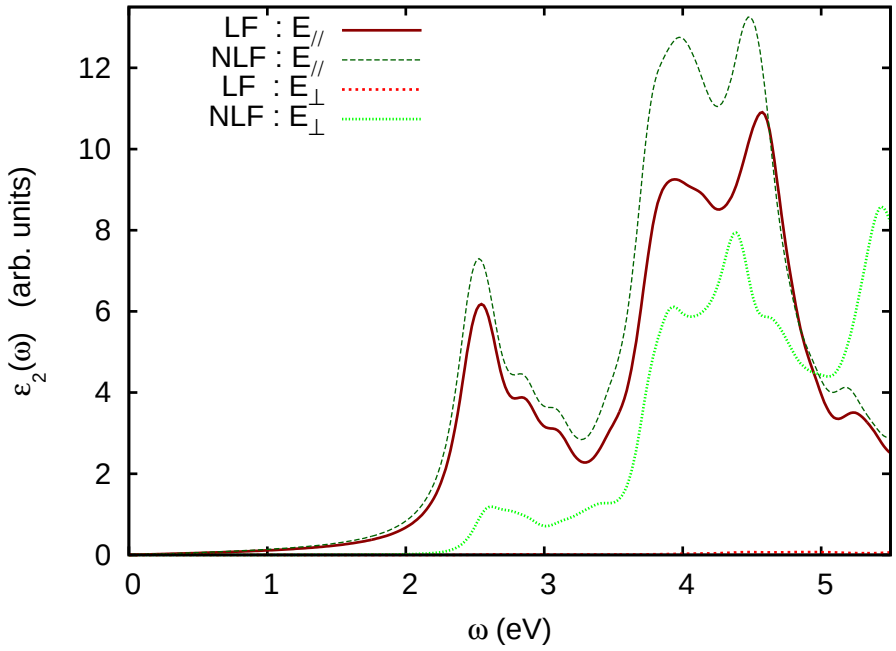

Figure 5.1: Imaginary part of the dielectric function for the smallest nanowire ($d = 0.73$ nm), calculated in the RPA with (LF) and without (NLF) crystal local fields, for light polarized parallel ($E_{\|}$) and perpendicular ($E_{\perp}$) to the wire axis. Note that the absorption is zero for NLF : $E_{\perp}$.

comparable to the anisotropy in bulk CdSe. However, and as expected, turning on local-field effects suppresses completely the low energy absorption peaks in the perpendicular direction, rendering the wire almost transparent below 6.5 eV. This optical anisotropy, in agreement with experimental results [172], clearly decreases with the diameter, but it is known to be still relevant for nanowires with a diameter of 100 nm.

To observe how the optical properties vary with increasing diameter, we plot the RPA spectrum (including local fields) for five small wires in Fig. 5.2. It is expected that the RPA gives a poor quantitative result due to the inappropriate treatment of electron-electron and electron-hole interactions, but it is however possible to extract qualitative trends thanks to the partial cancellation of these two terms (see below). We see that increasing the diameter, and thereby decreasing the confinement effect, leads to a red-shift of the spectrum, with the absorption threshold moving towards the RPA bulk value. There is also a redistribution of the oscillator strengths, with the first peak loosing intensity.

To go beyond the RPA and to include the relevant missing contributions, we performed calculations solving the Bethe-Salpeter equation (BSE) [17] and using TDDFT [181] — both in the adiabatic local density approximation (ALDA) and with the model long range (LRC) kernels [104, 37] derived from the BSE. The BSE approach is the state-of-the-art method for calculations of optical absorption and gives results in excellent agreement with experiments [17, 181]. For the LRC and BSE calculations, one requires as a starting point the quasi-particle band structure, usually obtained within the GW approximation [11]. Note that the GW approximation predicts accurate band gap energies for CdSe, in contrast to the systematic underestimation of the gap obtained in DFT. Unfortunately, GW calculations are computationally demanding, even for the small wires studied here. We therefore used the following approach to obtain the quasi-particle corrections: we solved the GW

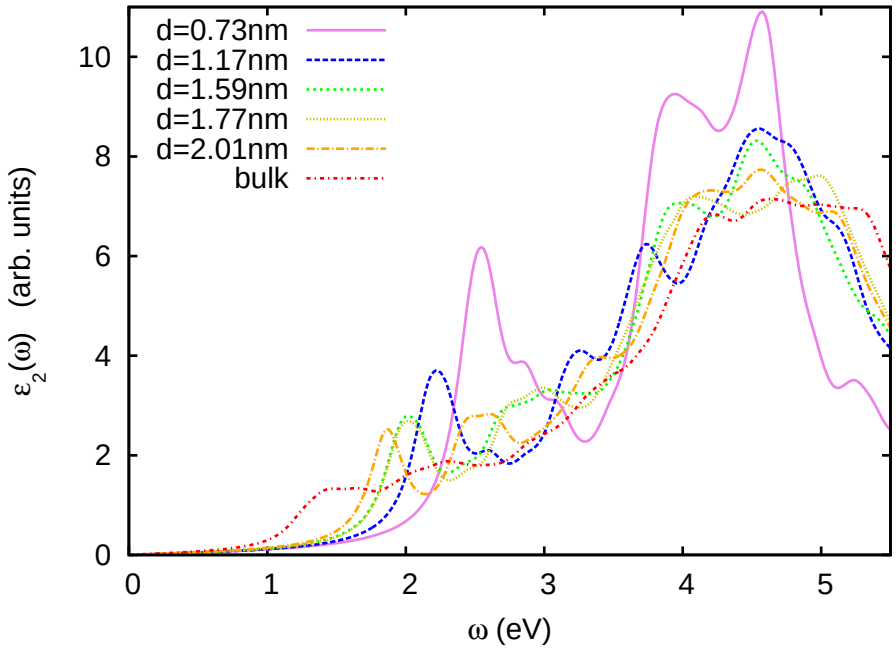

Figure 5.2: Dependence of the RPA absorption spectrum on the diameter of the nanowire. For comparison we also show the RPA result for the wurtzite CdSe bulk material.

equations for our smallest nanowire ($d = 0.73$ nm), and then used a simple simple analytical model [185] that accounts for surface and size effects to interpolate between this result and the GW gap of the bulk [186].

The GW calculations were performed with ABINIT, applying the standard plasmon-pole approximation. An energy cutoff for the dielectric matrix of 9 Ha and the technique of Ref. [187] to reduce the number of unoccupied states in the sums over states were employed. Despite the use of a cylindrical cutoff for the Coulomb interaction [188], a distance of 10 Å between the wires was required to converge the GW corrections to the Kohn-Sham band structure. These corrections turned out to be quite insensitive to the k-point and band index, in agreement with other results for Si and Ge nanowires [180, 189], and in contrast with findings for graphene nanoribbons [190]. The GW gap for the smallest wire was $E_{\rm gap}^{\rm GW} = 4.84$ eV, and the final form of the model relating the quasi-particle gap with the diameter of the wire (d in nm) turned out to be $E_{\rm GWgap}^{\rm model}(d) = 1.91 + 2.14/d$ (eV). Note that a simple effective mass approximation, accounting for confinement, would give a $1/d^2$ scaling. However, the $1/d$ law [185, 191] is in better agreement with theoretical and experimental data, even for small nanowires.

The BSE results (see Fig. 5.3), obtained using the code YAMBO [72], prove the existence of strong excitonic effects, with the excitonic peaks in the visible energy range. The excitonic binding energy compensates almost entirely for the large blue-shift coming from the quasi-particle corrections, and leads to a transfer of the oscillator strength from the higher energy absorption peaks to the first peak. On the other hand, the LRC kernels derived from the BSE, that yield results comparable to the solution of the BSE for bulk CdSe [104], fail dramatically for nanowires — in fact, as shown in Fig. 5.3 , even the optical gap resulting from DFT+RPA calculation is in better agreement with the BSE result. The attempt to increase the excitonic effect by modulating the empirical parameters of the LRC kernel did not lead to improvements. The reason is that the simple LRC approximations are only

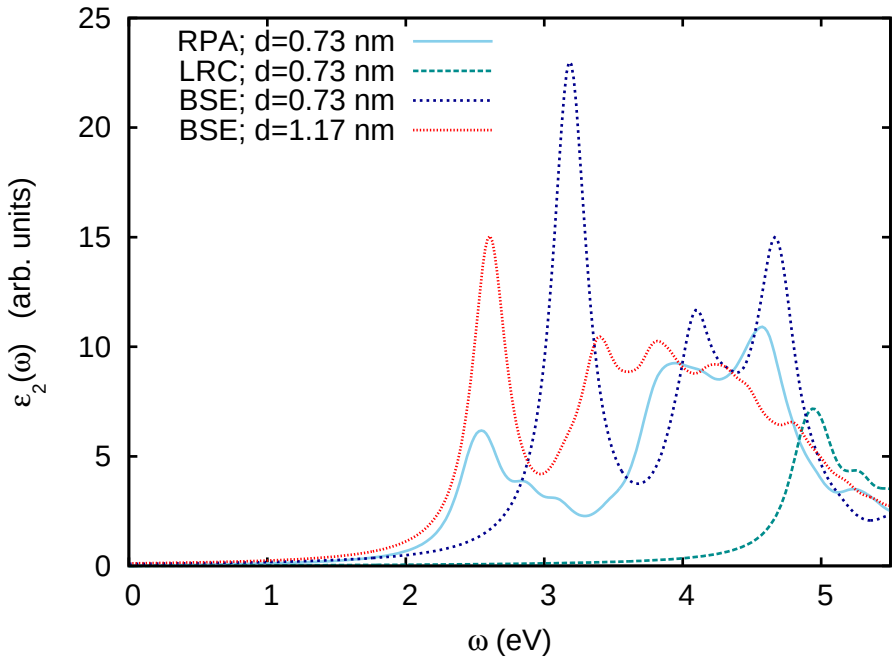

Figure 5.3: Imaginary part of the dielectric constant in the different approximations: RPA, LRC kernel, and BSE for the $d = 0.73$ nm nanowire. The ALDA results (not shown) are almost identical to the RPA. Also shown is the BSE results for the $d = 1.17$ nm nanowire.

valid for delocalized excitons, but fail to reproduce the considerable binding energy of the very localized excitons existing in nanowires.

The exciton binding energies from BSE calculations, for the nanowire with diameters of 0.73 and 1.17 nm are respectively 1.6 and 1.13 eV. These values are much larger than the binding energy in bulk CdSe [173], 15 meV, and almost twice as large as the ones found in carbon nanotubes [192]. The decrease of the binding energy with the nanowire diameter, also followed by a transfer of the intensity of the absorption-edge peak to the higher energy ones (see Fig. 5.3), reflects the weakening of the excitonic effects with the increasing of the exciton spatial extent. In fact, the exciton radius of bulk CdSe is 5.6 nm [173]: A nano-object where one of its dimensions is smaller than this value will have strongly bound excitons, due to a large overlap between electron and hole. Furthermore one expects that the larger the confinement the larger is the excitonic binding energy. Finally, in our BSE results we also found spin singlet dark excitons throughout the spectra, with the first one appearing at 3.2 eV for the smallest wire. This dark exciton may play a role in non-radiative decay processes and thus affect the luminescence properties.

Based on our BSE results for the two smallest wires and on the experimental optical gap of the bulk [193], we constructed a simple model to interpolate the optical gaps of CdSe nanowires. The form is the same as the previous model for the GW gaps, and the formula connecting optical gaps and the diameter of the wire turns out to be $E^{\rm model}_{\rm BSEgap}(d \text{ in nm}) = 1.74 + 1.05/d\,(\text{eV})$. We can see, from Fig. 5.4 , that this model describes extremely well the experimental results [193] not only for large nanowires but also in the intermediate regime. Finally, from Fig. 5.4 we conclude that although the RPA results are red-shifted with respect to the latter they still conserve approximately the correct slope.

In conclusion, the first-principle calculations reported here reveal how indispensable is the inclusion of local-field and excitonic effect to describe quantitatively the optical re-

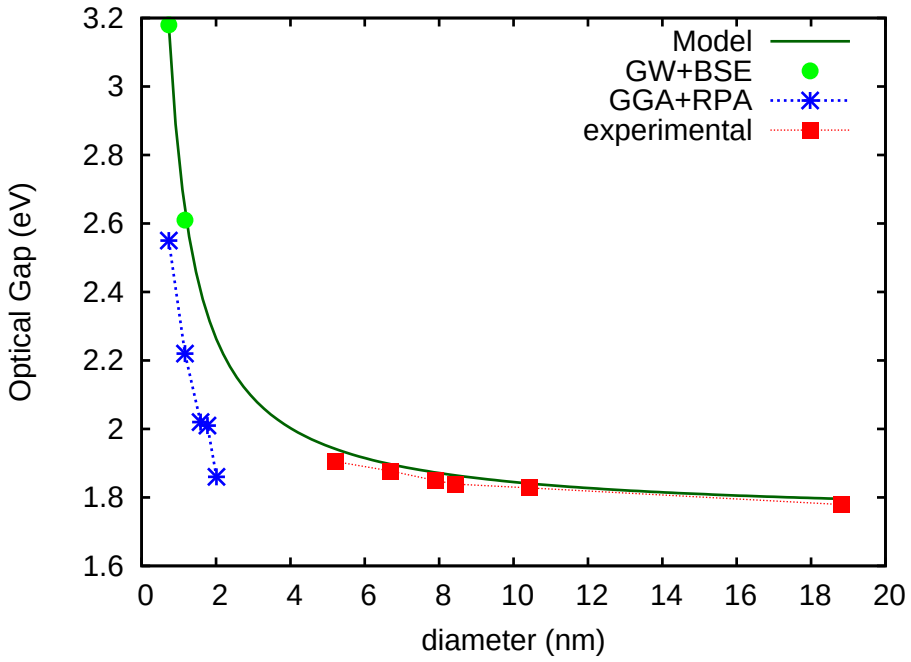

Figure 5.4: Optical gaps calculated with the RPA and the BSE compared to experiment [193]. The lines connecting the RPA and the experimental points are a guide to the eye. The green line is the model interpolation between the smallest nanowires and the bulk.

sponse of CdSe nanowires. In fact, calculations based on the Fermi's golden rule will never be able to catch the physics arising from the low dimensionality of the system, which is at the heart of the novel properties of nanowires. We have then provided a simple model for the dependency of the optical gap with diameter, which is in excellent agreement with available experimental results. Furthermore we have observed the failure of long-range model kernels of time-dependent density functional theory for these nano-scale systems, in spite of their success in the calculation of the optical properties of bulk CdSe.

5.2 Identification of fullerene-like CdSe nanostrutures*

5.2.1 Introduction

Cadmium selenide (CdSe) is a binary compound made of cadmium and selenium, that crystallizes in the hexagonal closed-packed wurtzite structure. Its optical band gap measures 1.85 eV at low temperature [194]. Current research on CdSe has focused mostly on nanoparticles, i.e., small portions cut out from bulk CdSe, with diameters between 1 and 100 nm. The interest in these nanosized systems can be understood by their special properties, significantly different from the properties of the parent bulk compound, that open the

*This section is based on the article:

- *Identification of CdSe fullerene-like nanoparticles from optical spectroscopy calculations*, S. Botti and M. A. L. Marques, Phys. Rev. B **75**, 035311 (2007).
- *Fullerene-like CdSe nanoparticles*, S. Botti, to be published in Handbook of Nanophysics (Klaus D. Sattler, Editor, Taylor&Francis Publisher, CRC Press, May 1, 2010).

possibility of novel technological applications. Furthermore, the very small size of these nanoparticles makes them particularly suited for miniaturization purposes. In fact, while the miniaturization of conventional silicon-based electronics is approaching fundamental performance limits, researchers are actively working to find new nanosized materials that are able to overcome these limits.

All nanoparticles exhibit a fundamental property known as "quantum confinement" [195], due to the modification of the energy states of electrons confined in a very small volume. Quantum confinement is dependent on the confinement volume, i.e., on the size of the nanoparticle. This means that the electronic properties of CdSe nanoparticles can be tailored by controlling their size. As a consequence, CdSe nanoparticles have size-tunable absorption and luminescence spectra. This characteristic makes them particularly attractive to be employed in optical devices, such as in light-emitting diodes that have to cover a large part of the visible spectrum [196, 197]. Along the same lines, CdSe nanoparticles have already proved to be excellent components for a variety of applications, such as in optically pumped lasers [198], photovoltaic cells [199, 200], telecommunications [201], and in biomedicine as chemical markers [202, 203].

The common requirement that makes possible all these different applications of CdSe nanoparticles is the high proficiency achieved in the control of a remarkably narrow size distribution (even lower than 5% [204]) during the synthesis process. In fact, it is the size distribution that determines the sharpness of the optical peaks. A further advantage of CdSe nanocrystals is the degree of efficiency attained in their synthesis, the high quality of the resulting samples, and the fact that the optical gap is in the visible range. In most common experimental setups, CdSe nanoparticles are formed by kinetically controlled precipitation, and are terminated with capping organic ligands, like, e.g., the trioctyl phosphine oxide (TOPO) molecule, which provide stabilization of the otherwise reactive dangling orbitals at the surface [204]. High quality colloidal CdSe nanoparticles have been routinely synthesized for more than a decade: their sizes range from 1 nm to hundreds of nm and their core displays the same symmetry as wurtzite.

The electronic states of any nano-object are also sensitive to the overall cluster shape, and more specifically to the deformations due to surface reconstruction, to the presence of defects, and to the symmetry properties of the arrangement of atoms in the core [205]. These geometrical details are of course more critical when the cluster is very small, i.e., when the surface/volume ratio is the largest. In particular, defects and dangling bonds are essentially localized at the surface. Moreover, for practical uses, further requirements, such as a high chemical stability of the nanostructure and an enhanced photoluminescence intensity, are of utmost importance. Unfortunately, these characteristics are inhibited by the presence of defects. As a consequence, often the quantum yields for very small CdSe nanoparticles in solution turn out to be below 1% [202, 206]. The reason is that these colloidal nanoparticles contain a large number of defects, especially at the surface, where radiationless recombination of the charge carriers can occur. Therefore, controlling the quality of the growth of small clusters, and in particular controlling the formation of dangling bonds at their surface, is essential for any kind of application.

In this context, the recent synthesis and probable identification of the very small, and highly stable, $(CdSe)_{33}$ and $(CdSe)_{34}$ nanoparticles grown in a solution of toluene [207, 208] came as a breakthrough. The experimental absorption spectra of these nanoparticles at low temperature exhibit sharp peaks, similar to the ones that characterize TOPO-capped clusters of the same size [204]. However, the surfactant molecules employed in the synthesis process are, in this case, removed by laser vaporization. Furthermore, an X-ray analysis indicates that the coordination number of Se is between 3 (the coordination of a fullerene)

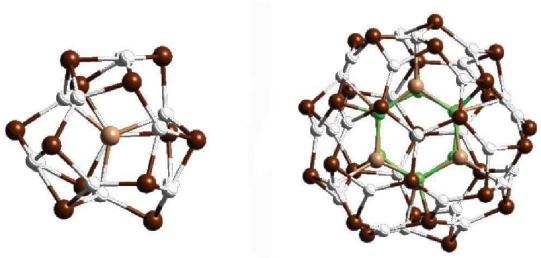

Figure 5.5: Structures of the $(CdSe)_n$ core-cage nanoparticles calculated to be most stable by Kasuya et al. [207], viewed down a threefold symmetry axis. a) $(CdSe)_{13}$ has four-membered and 10 six-membered rings on the cage of 12 Se (dark brown) and 13 Cd (white) ions with a Se (light brown) ion inside. b) $(CdSe)_{34}$ has a truncated-octahedral morphology formed by a $(CdSe)_{28}$ cage (Se, dark brown; Cd, white) with 6 four-membered and 8×3 six-membered rings. A $(CdSe)_6$ cluster (Se, light brown; Cd, green) encapsulated inside this cage provides additional network and stability. Reprinted by permission from Macmillan Publishers Ltd: Nature Materials [207], copyright 2004.

and 4 (the coordination of the bulk crystal). In view of this, and in absence of direct structural data, the non-passivated compound nanoparticles were predicted to have a core-cage structure, composed by a puckered fullerene-like $(CdSe)_{28}$ cage accommodating a $(CdSe)_n$ (n=5,6) wurtzite unit inside (see Fig. 5.5). Further ab initio calculations of structural and optical properties validated this interpretation [207, 209].

These very small fullerene-like systems, in the size range of 1–2 nm, are particularly interesting, as they have an increased probability to take the form of magic-sized nanocrystals, leading to ultra-stable single sized ensembles, which are in principle characterized by very sharp absorption peaks. The concept of magic-size has been well known for several years in the field of metal clusters, but it is less common for semiconductor nanoparticles.

Furthermore, the recent discovery of CdSe and other fullerene-like semiconducting cluster has renewed the interest for the so-called “cluster-assembled materials”. In fact, cluster-assembled materials form one of the most promising frontiers in the design of nano-devices. They are composed by three dimensional arrays of ultrastable size-selected nanoparticles, organized in a similar way as atoms are organized to form a crystal. Cluster-assembled materials ideally combine the properties of the single nano-object with novel collective behaviors arising from the periodic arrangement of the solid. Of course, the interaction between clusters cannot be too strong, in order not to destroy the discrete nature of the optical transitions. This means that the surface of the cluster has to be well saturated, with no dangling bonds. Unfortunately, up to now most attempts to design cluster-assembled matter have lead to metastable materials, which can be stabilized only by a dielectric matrix that prevents the individual clusters from reacting with their neighbors. Only few cluster materials are known at present, the most famous are made of carbon fullerenes (C_{60} and C_{70}). However, the recently synthesized CdSe fullerenes are very small clusters (1.5 nm of diameter), extremely stable, and which can be produced in macroscopic quantities: all these characteristics point to the possibility of using them to produce new cluster-assembled materials.

5.2.2 Synthesis and spectroscopic characterization

Numerous approaches [210, 211, 212, 213, 214, 205, 215, 216, 217, 218, 219, 220, 221, 222, 221, 223, 224, 225, 226] have been developed to synthesize highly crystalline and monodisperse II-VI semiconductor nanocrystals, following the path opened by Murray et al. [204]. However, these approaches are mostly suitable to produce regular-sized nanocrystals (>2 nm), but cannot be commonly employed to synthesize magic-size small clusters (1–2 nm). In particular, in the magic size regime, a large percentage of the atoms are at the surface, which makes the control of dangling bonds much more important.

Very small CdSe nanocrystals have been synthesized by the over-layering method [227], the etching preparation starting from larger nanocrystals [228], and the reverse-micelle approach [207]. Peculiar optical properties were obtained by magic-size nanoparticles grown by hot injection [197]: these ultra-small clusters exhibit broadband emission (420–710 nm) throughout most of the visible light spectrum, while not suffering from self-absorption. This property makes them ideal materials to produce white-light LED's. In general, it is assumed that these clusters are saturated with ligands, even if there is no direct information about the reconstruction at the surface.

However, ligand-free fullerene-like core-cage particles were for the first time produced by Kasuya et al. [207, 208] only in 2004. Since then, other groups tested new reproducible and controllable methods to grow in solution magic-sized small CdSe clusters. The exact control of the size of the nanocrystal and the sharpness of the optical peaks are both essential for any practical application. Of course, also the stability in time of the clusters is an important parameter to consider.

Kudera et al. [229] reported a method for controlling the sequential growth of CdSe clusters in solution that yields only magic-size nanocrystals of progressively larger sizes. The resulting nano-objects are characterized by sharp optical absorption spectra with peaks at well defined energies, in agreement with the ones reported by Kasuya et al. [207]. Also the cluster sizes, estimated by X-ray diffraction analysis, are compatible with the findings of Kasuya et al. [207]. Further transmission electron microscopy analysis revealed that all clusters are roughly spherical and that they are not aggregated. The mechanism of growth is determined by the competition between the attachment and detachment of single atoms at the surface. Once a cluster has grown to a magic size, its structure is so stable that no atom can detach from it. Therefore, it can only grow further, but it cannot shrink. This growth mechanism is compatible with the creation of cage-like structures, even if there is no direct proof of the fact that fullerene-like clusters are actually produced in this experiment. Unfortunately, these clusters have rather weak luminescence properties. Kudera et al. [229] also proved that the optical properties of their clusters could be improved by passivating their surfaces with a ZnS shell.

Dai et al. [230] reported an injection approach for the synthesis of nanocrystals with long existence period, using cheap cadmium oleate as the source of cadmium. The resulting CdSe clusters are saturated by ligands. They exhibit strong and fixed absorption features and a narrow red-shifted emission. Higher injections/growth temperatures favor a white light emission, but also transform the magic-size nanocrystals into regular-size ones. This same approach was also used by the same authors to synthesize CdTe clusters.

On the other hand, Ouyang et al. [231] used a non-injection one-pot synthetic approach to achieve colloidal CdSe ensembles consisting of single-sized nanocrystals exhibiting bright bandgap photoluminescence emission. Their systematic study suggests that the growth of large CdSe clusters is favored by long ligands at high growth temperature, while the growth of small CdSe magic-size clusters is favored by short ligands at low growth temperature.

Finally, Kuçar et al. [232] reported an efficient top-down synthesis in an amine-rich solution of small stable CdSe nanocrystals. They are produced by decomposition of initial nanocrystals within several days. The most stable clusters were characterized by spectroscopic methods and the comparison of absorption and photoluminescence spectra with previous studies suggests a predominant cage-like structure. The analysis of the absorption peaks revealed a preferred synthesis of $(CdSe)_{33,34}$ clusters. The emission decay rate of these clusters is comparable with that of organic dyes.

Despite the important contributions coming from all these recent studies, the preparation and understanding of highly luminescent, thermodynamically stable, small size CdSe clusters is still at the beginning. We are optimistic, however, that the next few years will bring new optimized techniques for the production of these clusters, that will open the way for development of the exciting and innovative applications that have already been foreseen.

5.2.3 Ab initio calculations

From the theoretical side, it is desirable to obtain from reliable calculations all possible complementary information on the atomic arrangement and surface deformation of CdSe clusters, in order to understand and complement experimental evidences. In fact, experimental measurements alone are usually not able to provide conclusive results concerning the surface reconstruction and the role of passivating ligands. Moreover, theoretical calculations can give a deeper insight on how surface reconstructions produce modifications of the electronic states, and consequently of the optical properties at the basis of all technological applications.

For ligand-terminated small and regular-size CdSe clusters, transmission electron microscopy data [204, 233], molecular dynamics simulations or first-principles techniques without self-consistency [234, 235], and self-consistent *ab initio* structural relaxations [236, 209] agree on predicting an atomic arrangement of the inner Cd and Se atoms analogous to the one in the wurtzite CdSe crystal. The extent to which the cluster surface retains the crystal geometry is more controversial as the surface cannot be easily resolved experimentally. Generally, if the surface is properly passivated, the reconstruction is assumed to be small and limited to the outermost layer (and eventually the layer just beneath it), which is in agreement with molecular dynamics simulations [234]. However, Puzder *et al.* [236] recently predicted for clusters with diameters up to 1.5 nm a strong surface reconstruction, remarkably similar in vacuum and in the presence of passivating ligands.

The core-cage structures proposed by Kasuya et al. [207] are significantly different from all bulk-derived arrangements previously studied. These geometries were found to be particularly stable by first-principles total energy calculations [207, 209]. Furthermore, calculations of optical spectra [209] have offered a definitive proof for the identification of the observed nanoparticles with the fullerene-like structures, through the comparison between measured [207] and simulated spectra. In fact, as the electronic states (and, as a consequence, absorption or emission peaks) are strongly modified by changes of size and shape, optical spectroscopy can thus be a powerful tool (especially if it can be combined with other spectroscopic techniques) to probe the atomic arrangement of synthesized nanoparticles.

In the following of this section we will discuss how the well-known DFT [2] has been applied to access information concerning the structural and electronic properties of CdSe fullerenes. Moreover, we will see how the comparison between theoretical and experimental results provides a deeper insight into the properties of complex nanostructured materials.

We chose to restrict our discussion to DFT, as it is the most popular and versatile

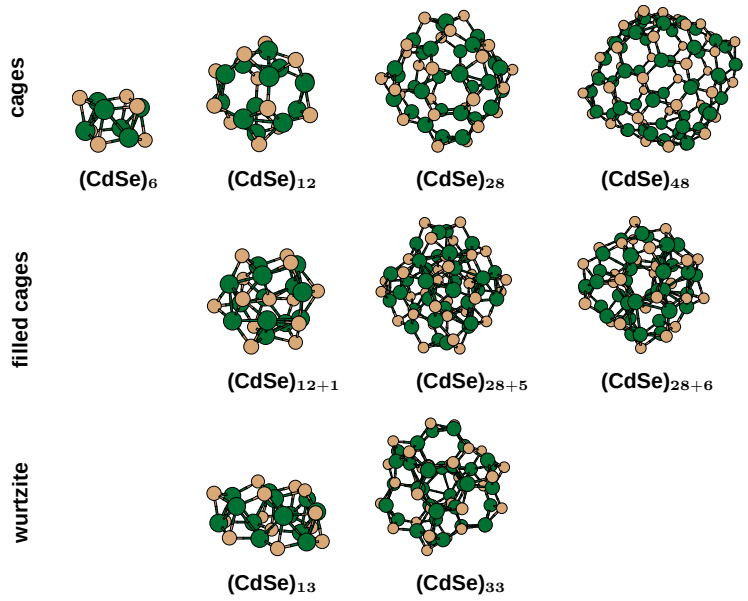

Figure 5.6: Examples of relaxed cages, relaxed filled cages and relaxed wurtzite structures of $(CdSe)_n$ with a diameter smaller than 2 nm. Cd atoms are in green and Se atoms are in beige.

method available in condensed-matter physics, computational physics, and computational chemistry.

Structures of energetically stable CdSe nanoparticles

The atomic positions of CdSe nanoparticles can be routinely obtained by geometry optimization using any quantum chemistry or solid state physics code. The starting point of any structural optimization procedure is to consider a series of candidate structures with different geometries and sizes. Here we consider $(CdSe)_n$ aggregates with sizes ranging up to about 1.5 nm. To build these atomic arrangements it is possible to start from three different kinds of ideal geometries: (i) bulk fragments cut into the infinite wurtzite crystal, (ii) octahedral fullerene-like cages made of four and six-membered rings and (iii) the core-cage structures of Ref. [207], composed of puckered CdSe fullerene-type cages which include $(CdSe)_n$ wurtzite units of adequate size to form a three-dimensional network. Following Ref. [209], we can assume that the Cd-Se distance before structural relaxation is the distance in the CdSe wurtzite crystal, calculated within DFT [237] in the same approximations used for the nanoparticles: its value (0.257 nm) compares well with the experimental value (0.263 nm).

In the following we will analyze as an illustration the structural calculations of Ref. [209], comparing them with the analogous DFT calculations for wurtzite-like clusters of Ref. [236] and for core-cage clusters of Ref. [207]. We used an implementation of DFT [237] within the local density approximation (LDA) [238] for the exchange and correlation potential and norm-conserving pseudopotentials [183, 239]. Puzder et al. [236] used a similar technique, but with another implementation of DFT. Finally, Kasuya et al. [207] performed DFT calculations [240] using ultrasoft pseudopotentials [241] and the generalized gradient approximation (GGA) [4] for the exchange-correlation potential.

Atomic arrangements after optimization using DFT are depicted in Fig. 5.6 (see [209]).

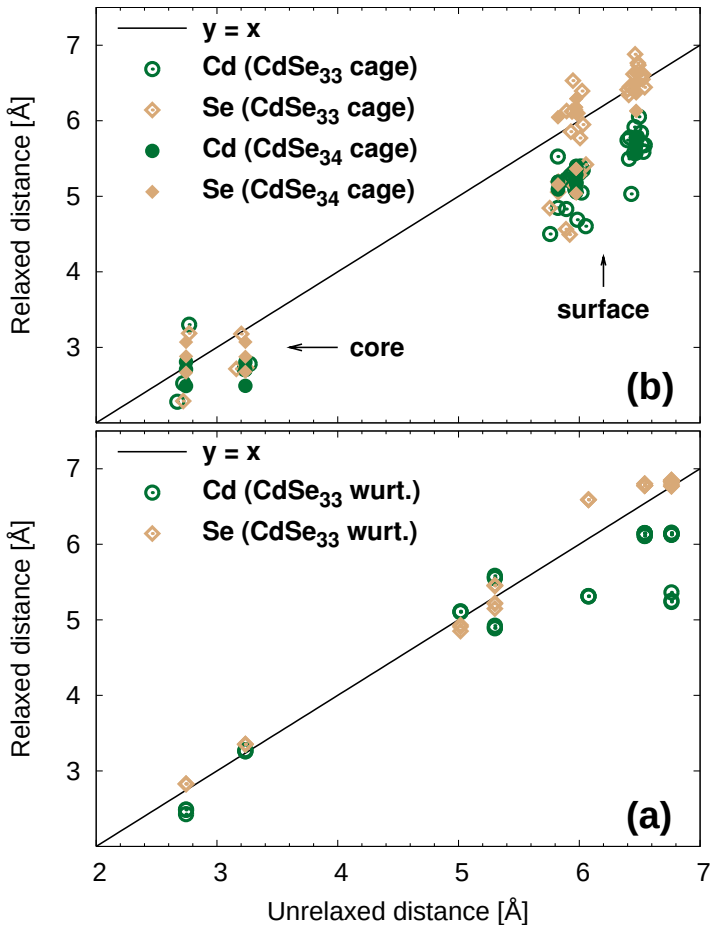

Figure 5.7: Distance of Cd atoms (circles) and Se atoms (diamonds) from the center of the cluster after geometry optimization, as a function of their distance before optimization. An atom that lies on the straight line $y = x$ did not change its position. In panel (a) results of the analysis for $(CdSe)_{33,34}$ core-cage clusters, in panel (b) for the $(CdSe)_{33}$ wurtzite cluster.

All clusters suffer contraction upon geometry minimization. For example, $(CdSe)_{33,34}$ clusters experience a size reduction of about 1–1.5%. The theoretical results are in agreement with the X-ray analysis of [207]. However, as the relaxation affects mainly the outermost atoms, the overall effect is more pronounced in smaller structures, where the average Cd-Se distance decreases up to 4%. This contraction does not conserve the overall shape, as Cd atoms are pulled inside the cluster and Se atoms are puckered out. As a consequence, Cd-Cd average distances can be reduced by 30%, while Se-Se distances remain essentially unvaried. This is clearly visible in Fig. 5.7, where the relaxed distance of Cd (circles) and Se (diamonds) atoms from the center of the cluster is plotted for $(CdSe)_{33,34}$ clusters as a function of their distance before relaxation. If the atoms remained in their initial position, all data points would fall on the straight line $y = x$. The fact that most Cd atoms lie below the line, while most Se atoms are above it, shows that in our simulation Cd atoms prefer to move inward and Se atoms outward. That puckering happens independently of the cluster size [207, 236, 209].

All wurtzite fragments get significantly distorted upon relaxation and break their original symmetry. However, the strong modification of bond lengths and angles concerns es-

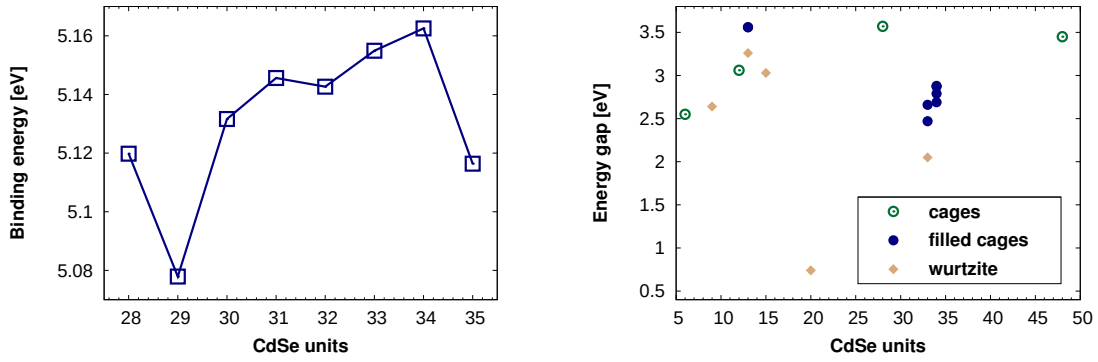

Figure 5.8: Left panel: Calculated binding energies per CdSe unit as a function of the number of CdSe units (data from [207]). The binding energies are calculated per CdSe molecule of $(CdSe)_n$ composed of a cage-like $(CdSe)_{28}$ with $(CdSe)_m$ inside ($n = 28 + m$, $m = 0, 1, \ldots, 7$). Right panel: HOMO-LUMO gaps as a function of the number of CdSe units. The empty (filled) circles refer to cage (core-cage) clusters, while the diamonds refer to wurtzite-based structures.

sentially the surface layer [236, 209]. In particular, we can see in Fig. 5.7(a) that the wurtzite-type $(CdSe)_{33}$ is already large enough to conserve a bulk-like crystalline core. In fact, the spread of the points from the straight line is pronounced only for the external shell of atoms. The calculated overall contraction of the cluster is consistent with experimental data [242]. Also the empty cages [$(CdSe)_{12}$, $(CdSe)_{28}$, and $(CdSe)_{48}$] get puckered, but conserve their overall shape. Their binding energies are smaller by about 0.05 eV per CdSe unit with respect to the binding energies of the corresponding filled cages [see Fig. 5.8(a)], showing the importance of preserving the three-dimensional sp^3 Cd-Se network.

Models based only on the wurtzite structure of bulk CdSe fail to predict the existence of stable "magic clusters" with well defined sizes and number of atoms. In contrast, the core-cage structures proposed by Kasuya et al. can appear only for well defined sizes and number of atoms, as fullerene cages can be built only for 12, 16, 28, 48, 76, etc. atoms and only some of these cages can be filled conveniently with wurtzite-coordinated CdSe units. To optimize the core-cage structures [209] [$(CdSe)_{12+1=13}$,$(CdSe)_{28+5=33}$, and$(CdSe)_{28+6=34}$] we created different starting arrangements assuming different orientations for the encapsulated $CdSe_{n=1,5,6}$ units. In the relaxed assemblies the distributions of bond lengths and angles result very similar despite of the distinct initial configurations. The fact that the surfaces of core-cage clusters do not show neither strong reconstruction nor deleterious dangling bonds, in contrast to surfaces of wurtzite-like cluster not cured by passivation, explains why fullerene-like CdSe clusters are particularly non-reactive and prevent them from merging together to form larger clusters. This is crucial to have promising building blocks for three-dimensional cluster solids.

The right panel of Fig. 5.8 shows the DFT Kohn-Sham gap between the highest occupied and lowest unoccupied molecular orbitals (HOMO-LUMO) for a series of clusters of different types: wurtzite, cages, and filled cages. Both empty and filled cages exhibit much larger HOMO-LUMO gaps than their wurtzite counterparts, indicating therefore that there are no dangling bonds at their surface. In the left panel we show the results from [207] for the binding energy of the filled cages. The two most stable structures are clearly $(CdSe)_{33}$ and $(CdSe)_{34}$. It is curious that the first is significantly more deformed under optimization than $(CdSe)_{34}$, but it turns out to have a very similar binding energy. The filled cage structure

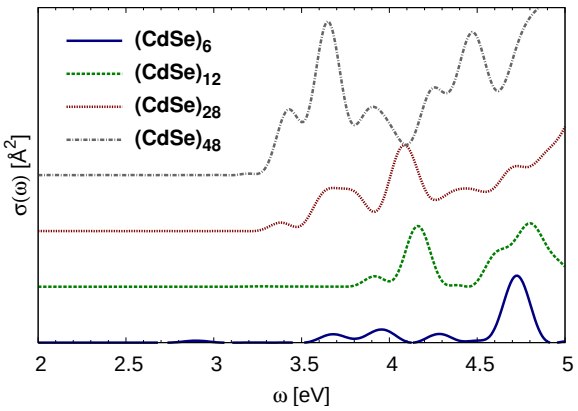

Figure 5.9: Calculated photoabsorption cross section $\sigma(\omega)$ of the empty cages $(CdSe)_6$, $(CdSe)_{12}$, $(CdSe)_{28}$ and $(CdSe)_{48}$. The spectra were shifted vertically for visualization purposes.

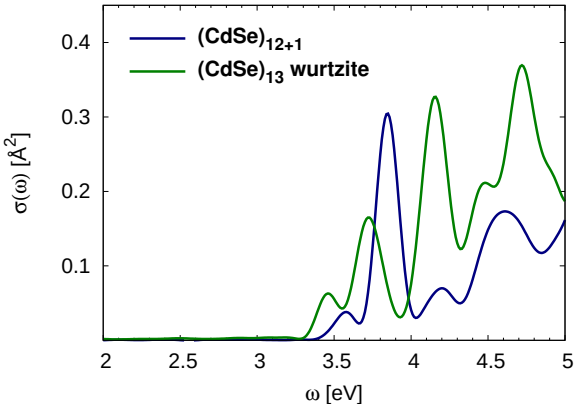

Figure 5.10: Calculated photoabsorption cross section $\sigma(\omega)$ of the isomers of $(CdSe)_{13}$.

made of 13 units gives as well a relative minimum in the total energy per pair [209]. In the case of $(CdSe)_{13}$ and $(CdSe)_{33}$ it is possible to compare the total energies of the different three-dimensional isomers [209]: the core-cage nanoparticles have a slightly higher binding energy per CdSe unit [0.15 eV for $(CdSe)_{13}$ and 0.05 eV for $(CdSe)_{33}$]. However, we should not forget that the energy differences we are discussing here are all very tiny, sometimes of the same order of magnitude as the accuracy of the calculations. That fact confirms how difficult it can be to extract structural information from a single number (the total energy) and leads to the conclusion that the simple analysis of total energy differences cannot be considered conclusive to demonstrate the existence of fullerene-like CdSe clusters.

Optical absorption spectra

From the relaxed geometries it is possible to obtain the optical spectra at zero temperature using TDDFT [19, 20].

For the calculation of the photoabsorption cross section Botti and Marques [209] employed a real-time TDDFT approach [243, 244], based on the explicit propagation of the

time-dependent Kohn-Sham equations. In this approach, one first excites the system from its ground state by applying a delta electric field $E_0\delta(t)\mathbf{e}_m$. The unit vector $\mathbf{e}_m$ determines the polarization direction of the field, and E_0 its magnitude, which must be small if one is interested in linear response. The reaction of the non-interacting Kohn-Sham system to this sudden perturbation can be readily computed: each ground state Kohn-Sham orbital $\varphi_i^{\rm GS}(\mathbf{r})$ is instantaneously phase-shifted: $\varphi_i(\mathbf{r}, t = 0^+) = e^{{\rm i}E_0\mathbf{e}_m\cdot\mathbf{r}}\varphi_i^{\rm GS}(\mathbf{r})$. The Kohn-Sham equations are then propagated forward in real time, and the time-dependent density $n(\mathbf{r}, t)$ can then be computed. The induced dipole moment variation is an explicit functional of the density:

$$\delta\mathbf{D}^m(t) = \delta\langle\hat{\mathbf{R}}\rangle(t) = \int {\rm d}^3r\ [n(\mathbf{r}, t) - n(\mathbf{r}, t = 0)]\,\mathbf{r}\,. \tag{5.1}$$

The superindex m reminds that the perturbation has been applied along the m-th Cartesian direction. The components of the dynamical dipole polarizability tensor $\underline{\alpha}(\omega)$ are directly related to the Fourier transform of the induced dipole moment function:

$$\alpha_{mn}(\omega) = \frac{\delta D_n^m(\omega)}{E_0}\,. \tag{5.2}$$

The spatially averaged absorption cross section is trivially obtained from the imaginary part of the dynamical polarizability:

$$\sigma(\omega) = \frac{4\pi\omega}{c}\mathfrak{Im}\ [\alpha(\omega)]\ , \tag{5.3}$$

where α is the spatial average, or trace, of the tensor

$$\alpha(\omega) = \frac{1}{3}{\rm Tr}\,[\underline{\alpha}(\omega)]\ . \tag{5.4}$$

Here we will discuss the results for the excitation energies and the optical spectra [209] that we obtained using TDDFT within the adiabatic local density approximation (ALDA) [20]. These are the only calculations on CdSe clusters available in literature that go beyond the simple application of Fermi's golden rule, i.e. the sum of independent single particle transitions from occupied to empty states (in this case, Kohn-Sham one-particle states). It is well known that the simpler approach of taking the differences of eigenvalues between Kohn-Sham orbitals gives peaks at lower frequencies in disagreement with the experimental spectra [245]. On the other hand, TDDFT within the ALDA typically reproduces the low energy peaks of the optical spectra with an average accuracy below 0.2 eV. The accuracy in reproducing transitions of intermediate energy is known to be somewhat deteriorated, due to the wrong asymptotic behavior of the LDA exchange-correlation potential. For this reason, we focus the analysis of the spectra on the lowest energy peaks.

In Fig. 5.9 we display the photoabsorption spectra of the empty cages of different diameters, as calculated by Botti and Marques [209]. It is clear from the figure that the absorption threshold is systematically blue-shifted with respect to the bulk optical gap ($\simeq$ 1.8 eV). This blue-shift is due to the well-known quantum confinement effects, so it is not surprising that the shift increases with decreasing cluster size. Second, we can compare the absorption threshold with the Kohn-Sham HOMO-LUMO gap shown in the right panel of Fig. 5.8: the Kohn-Sham gap is systematically smaller than the TDDFT absorption threshold. This is a common observation as the Kohn-Sham transition energies are usually at lower frequencies than the experimental peaks. We note that the TDDFT optical gaps include both electron-electron and electron-hole corrections to the Kohn-Sham gap at the level of the adiabatic local density approximation.

We should keep in mind that the opening of the gap due to confinement can be counterbalanced by a closing of the gap due to surface reconstruction. This leads to a non trivial dependence of the absorption gap as a function of the cluster size. This effect is already present at the Kohn-Sham level [see the right panel of Fig. 5.8(a)] and it persists in TDDFT spectra. In fact, the calculated absorption curves are strongly dependent not only on the cluster size but also on the details of its atomic arrangement. This is evident if we compare the optical response of the different isomers of $(CdSe)_{13}$ in Fig. 5.10 and of $(CdSe)_{33}$ in Fig. 5.11 [209].

The absorption threshold is lower in wurtzite-type clusters since the HOMO-LUMO gap is reduced due to the presence of defect states in the gap as a consequence of the strong surface deformation. For a similar reason, the larger surface deformation of the core-cage $(CdSe)_{33}$ aggregate in comparison with the more stable $(CdSe)_{34}$ structure explains why the first starts absorbing at lower energies than the second. Finally, we note that the similar curves of different colors in Fig. 5.11 correspond to distinct core-cage geometries obtained in various optimization simulations. We conclude that the dependence of the relevant peak positions and shapes on the different atomic arrangements is not negligible, but the peak positions and oscillator strengths are sufficiently defined for the purpose to distinguish different geometries by comparing photoabsorption spectra.

A comparison between calculated [209] and measured spectra [207] is possible for nanoparticles made of 33 and 34 CdSe units (see Fig. 5.11). The magenta dots refer to room temperature absorption data for mass-selected nanoparticles prepared in toluene at 45°C (sample I), while the orange crosses correspond to analogous data for the solution prepared at 80°C (sample II). Both samples are characterized by strong absorption at 3 eV. For sample II the experimental data show the appearance of a broad peak extending to lower energies. This peak turns out to move to even lower energies when the temperature and the time in the synthesis process increase. In a simple quantum confinement picture, these findings suggest that larger particles, possibly reconstructed bulk fragments, are formed when the temperature increases. Moreover, the sharp peak at about 3 eV, which is always present, was hypothesized to be the signature of the highly resistant fullerene-like clusters.

The calculated spectra [209] shown in Fig. 5.11 prove the presence of fullerene-like core-cage structures. The theoretical optical response of all model core-cage $(CdSe)_{34}$ clusters is indeed characterized by a well defined absorption peak at 3 eV. Also the core-cage $(CdSe)_{33}$ cluster and the $(CdSe)_{33}$ reconstructed bulk fragment can contribute to this peak. However, they cannot be present in sample I, as that would be signaled by the appearance of a broader peak at lower energy, which is absent in the experimental spectrum. On the other hand, a peak at about 2.5 eV, connected to the peak at 3 eV by a region of increasing absorption, is present in the spectrum for sample II. Our calculations show that the $(CdSe)_{33}$ wurtzite fragment is responsible for the peak at 2.5 eV, while the broad absorption region between 2.5 eV and 3 eV can be explained by the presence of $(CdSe)_{33}$ core-cage structures. This is in disagreement with the intuition of Ref. [207] that bulk fragments of about 2.0 nm gave rise to the broad absorption below 3 eV.

In summary, by comparing our theoretical spectra [209] with measurements, we could confirm the existence of the stable core-cage fullerene-like structures hypothesized in the seminal work of Kasuya et al. [207].

The use of CdSe fullerene-like nanoparticles for technological applications in the field of cluster-assembled materials is a promising challenge for materials science. To this purpose, there is much work in progress to optimize the production procedures of magic-size small CdSe clusters. Concerning the characterization and the understanding of electronic excitations in these novel nanostructured materials, the combination of experimental and

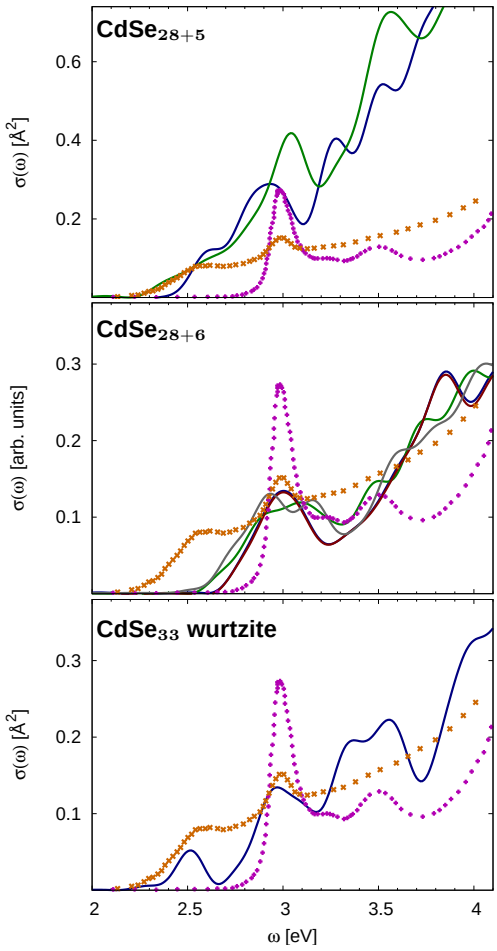

Figure 5.11: Photoabsorption cross section $\sigma(\omega)$ of the isomers of $(CdSe)_{33,34}$. The experimental data [207] in arbitrary units (magenta dots: sample I at $45°C$ and orange crosses: sample II at $80°C$) are compared with calculated spectra. The different solid curves correspond to distinct relaxed geometries obtained starting from different filled cages.

theoretical spectroscopic techniques has proved to be essential to extract reliable and conclusive information on their structural and optical properties.

5.3 Optical and magnetic properties of boron fullerenes*

5.3.1 Introduction

The hollow carbon clusters, or "fullerenes", were only theoretical predictions [246, 247, 248] for two decades, until their discovery in 1985 [249]. Recently, Gonzalez Szwacki *et al.* [250] have predicted the existence of a boron *doppelgänger* of the C_{60} fullerene: a B_{80} cage whose experimental detection seems quite likely in the near future. Indeed, the nanotubular boron structures were also suggested by first-principles calculations [251], and later con-

*This section is based on the article:

- *Optical and magnetic properties of boron fullerenes*, S. Botti, A. Castro, N. N. Lathiotakis, X. Andrade and M. A. L. Marques, Phys. Chem. Chem. Phys. **11**, 4523 (2009).

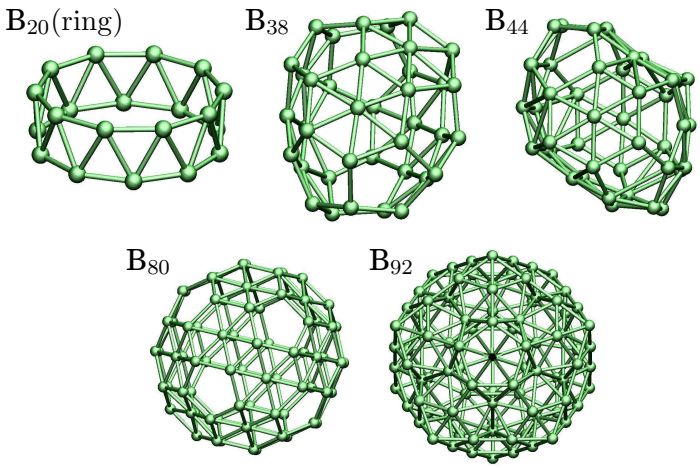

Figure 5.12: Structures of the boron cages studied in this work.

firmed experimentally [252]. In the same vein, we should also refer the new boron sheets proposed in Ref. [253], and the corresponding nanotubes proposed in Ref. [254], that use the same fundamental motif as the B_{80} cluster.

Like C_{60}, B_{80} has a remarkable stability (as measured, for example, by its cohesive energy), a relatively large energy gap between the highest occupied and lowest unoccupied molecular orbitals (HOMO and LUMO, respectively), and, like C_{60}, *almost* $I_{\rm h}$ symmetry; even though the original work of Gonzalez Szwacki *et al.* reported an icosahedral shape, they acknowledged the existence of several close local minima at distorted geometries. Later it has been defended that the geometry of the most stable structure seems to be a slight distortion of the $I_{\rm h}$ configuration. Both Gopakamur *et al.* [255, 256] and Baruah *et al.* [257] have further investigated the stability of the lowest energy isomers of B_{80}, and claim that the icosahedral structure is unstable; the ground state configuration is reported to have, in fact, $T_{\rm h}$ symmetry. However, the recent work of Sadrzadeh *et al.* [258] has also investigated the issue, and report very small energy differences (lower than 30 meV) among the three lowest lying isomers ($I_{\rm h}$, $T_{\rm h}$, and C_1), with the icosahedral shape being, in fact, a close winner.

Unlike C_{60}, B_{80} accommodates one boron atom in the center of each hexagon, accounting for the extra 20 atoms; this hexagon reinforcement is necessary to stabilize the otherwise unstable icosahedral B_{60} cage. In this manner, the *Aufbau* principle proposed by Boustani [259] is respected: stable homoatomic boron clusters are constructed with two basic bricks: hexagonal pyramids, B_7 (characteristic of convex and quasiplanar clusters), or pentagonal pyramids, B_6 (characteristics of open-spherical clusters, such as the prototypical B_{12}). Alternatively, B_{80} can also be viewed as six interwoven B_{20} double-rings [250]; the inclusion of staggered double rings in the structure of boron clusters seems to enhance their stability (see Fig. 5.12, where, among other structures, both the B_{20} double-ring cluster and the B_{80} are depicted).

The existence of cage-like boron conformations should come as no surprise, given the rich chemistry of this element: boron nanostructures have been found in very diverse forms – clusters [260, 261, 262, 263, 264, 265, 266, 267], nanowires [268] or nanotubes [269, 252, 270]. The family of boron nanostructures is unlimited, since boron has the property of catenation: it can form structures of arbitrary size by linking covalent bonds with itself – a property only shared with carbon. In fact, a wide variety of polyhedral clusters containing

boron have been known for a very long time, and have been used for a surprisingly large number of applications [271]. The rich diversity can be explained in terms of the high coordination number and the short covalent radius usually exhibited by boron, which leads to the possibility of creating strong directional bonds with many elements.

Before the work of Gonzalez Szwacki and collaborators [250] on B_{80} and other possible hollow structures [260], a significant amount of work had been reported on smaller, homoatomic boron clusters: Experimental work [261, 262, 263, 266] and calculations [261, 263, 266, 272, 273, 274, 275, 259, 276, 277, 278] led to one main conclusion regarding the structures: small clusters appear typically in either convex, quasi-planar, spherical or nanotubular shapes. This is surprising, since bulk boron, in its typical phases, is constructed from the icosahedral B_{12} unit. Below 20 atoms, the most stable shapes are planar, whereas tubular structures start to become more stable above this number [266]. Recently, some of us [100] contributed to the possible elucidation of the precise planar to tubular transition by calculating the optical absorption of the main conformers: The spectra show significant differences among them, possibly enabling the optical characterization of mass selected sample of boron clusters with unknown geometry.

Until experimentalists find a way to produce boron fullerenes, first-principle calculations remain the only route to understanding their properties. In this work we report on the linear response signatures of B_{80} and some of the other stable fullerenes proposed by Gonzalez Szwacki *et al.* : dynamical polarizabilities, static dipole polarizability and magnetic susceptibilities.

The importance of the knowledge of the static dipole polarizability is beyond doubt (e.g. it is a coarse indicator of molecular shape, it determines the long-range interaction between molecules, etc), as it is the case for its dynamical generalization (e.g. the excitation energies are determined by the peak positions of this function; the absorption cross section is trivially related to the imaginary part of the dynamical polarizability, etc).

Furthermore, it is interesting to realize if boron fullerenes share the anomalous magnetic properties present in traditional carbon fullerenes. The nature and magnitude of the electronic ring currents that circulate around the carbon rings is intriguing; Elser and Haddon [279, 280] calculated the contribution of these ring currents to the magnetic susceptibility by making use of London's theory [281]. The finding was surprising since this contribution was found to be vanishingly small; this result was later backed by the experiment [282]: the measured susceptibility had almost the same value as the estimated local contributions to the diamagnetism, which implies a small ring current contribution. However, this fact does not imply that currents do not circulate around the carbon cycles; the truth is that fullerenes exhibit both diamagnetic and paramagnetic ring currents, which cancel each other [283]. This result is surprising if we attempt to explain the ring current induced magnetism with a more naïve approach – such as Pauling's model [284].

It is then clear how the phenomenon of ring currents – usually linked to the "aromatic" character of a molecule –, and its effect on the magnetic susceptibility of clusters, can be subtle. The "spherical aromaticity" of fullerenes [285], in particular, demands for a careful theoretical study of the magnetic response. Boron clusters, including boron fullerenes, also contain rings of delocalized π orbitals, and its aromatic character has also been discussed [286, 287]. It is therefore in order to investigate, at an accurate level of theory, the magnetic properties of the newly proposed B_{80} and its family of fullerenes.

5.3.2 Methodology

The cluster geometries are those reported by Gonzalez Szwacki *et al.* [250], the ones optimized within the DFT framework with the Perdew-Burke-Ernzerhof [4] (PBE)

Table 5.1: HOMO-LUMO gaps (H-L in eV), ionization potentials calculated through total energy differences (IP in eV) magnetic susceptibilities (χ in cgs ppm/mol), static dipole polarizabilities (α in Å^3), and static dipole polarizabilities per number of boron atoms for the selected boron clusters. For these two latter quantities, we present both average values (e.g., $\bar{\chi} = \mathrm{Tr}\,\chi/3$) and anisotropies (e.g., $\Delta\chi = \sqrt{[3\mathrm{Tr}\,\chi^2 - (\mathrm{Tr}\,\chi)^2]/3}$).

	H-L	IP	$\bar{\chi}$	$\Delta\chi$	$\bar{\alpha}$	$\bar{\alpha}/N$	$\Delta\alpha$
B_{20} (r)	1.45	7.5	-250.2	330.1	44.0	2.20	18.2
B_{38}	0.95	7.4	-468.3	37.7	73.8	1.94	12.3
B_{44}	0.96	7.3	-614.4	156.3	83.1	1.89	15.0
B_{80}	1.01	6.6	219.3	3.9	147.9	1.85	0.5
B_{92}	1.07	6.5	-831.3	0.8	162.6	1.77	0.01

parametrization. The core electrons were frozen thanks to the ultrasoft Vanderbilt pseudopotentials [241]. The minimized geometries, which we used without further relaxation are depicted in Fig. 5.12. Besides the cage solutions, we include, for completeness, the prototypical B_{20} ring.

We then performed density-functional perturbation theory [288] in order to obtain the static magnetic susceptibilities, finite-differences to calculate the static polarizabilities, and TDDFT [152] in order to obtain the optical absorption spectra. In all cases we used the code `octopus` [243, 244]. The most salient features of this approach are: the relevant functions (Kohn-Sham wave functions, densities) are discretized on a real-space regular mesh; the ion-electron interaction is modeled with norm-conserving pseudopotentials [239]. The grid spacing was chosen to be 0.18 Å, and the simulation boxes were built large enough to ensure the convergence of the results – in practice, by placing the box boundaries at least 5 Å away from the closest atom. In all calculations, we approximated the exchange and correlation functional by the PBE [4] parametrization. The HOMO-LUMO gaps calculated in this way are shown in Table 5.1, and are in very good agreement with previously published results [250].

Regarding the calculation of the dynamical polarizabilities, we employed a real-time TDDFT approach, based on the explicit propagation of the time-dependent Kohn-Sham equations. In this approach, one first excites the system from its ground state by applying a delta electric field $E_0\delta(t)\mathbf{e}_m$ (the unit vector $\mathbf{e}_m$ determines the polarization direction of the field, and E_0 its magnitude, which must be small to ensure that the response is linear). The Kohn-Sham equations are then propagated forward in real time [75], and the time-dependent density $n(\mathbf{r}, t)$ readily computed. From this quantity one can then obtain the absorption cross-section as explained in Refs. [97, 243]. In this work, the total propagation time was chosen to be 30 $\hbar/\mathrm{eV} \approx 20$ fs, and the time step 0.002 $\hbar/\mathrm{eV} \approx 1.3$ as. This approach has already been used for many cluster and molecular systems: metal and semiconducting clusters [88, 245, 94, 209], aromatic hydrocarbons [97, 289], or protein chromophores [99, 290]. The accuracy to be expected from this technique is around 0.1–0.2 eV for the position of the spectral peaks in the visible and near ultraviolet wavelength interval.

Regarding the calculation of the magnetic susceptibilities, we have employed density-functional perturbation theory – the reformulation of Sternheimer's equation within the DFT framework [288]. Details of our specific implementation can be found in Ref. [291]. Note that due to the use of non-local pseudopotentials, special care has to be taken in order

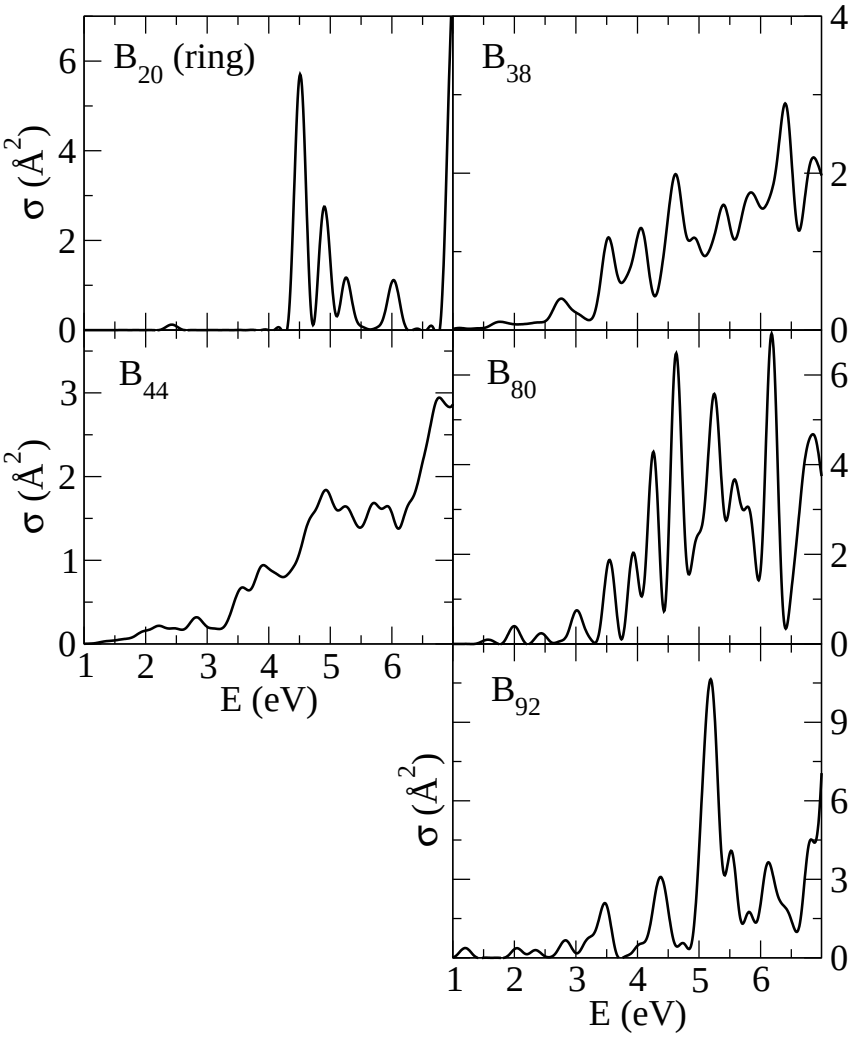

Figure 5.13: Absorption cross section (in Å^2) for B_{20} (ring isomer), B_{38}, B_{44}, B_{80} ("slightly-off" I_h), and B_{92} as predicted by TDDFT. Most of the energy range showed is below the calculated ionization potential of these clusters (see Table 5.1).

to ensure the gauge invariance of the underlying equations. To solve this problem, we used the GIPAW approach of Pickard and Mauri [[292]].

5.3.3 Ab initio calculations

We start the discussion of our results by the magnetic susceptibilities (see Table 5.1). With the exception of B_{80}, all clusters studied are diamagnetic, with the absolute value of the susceptibility increasing with the number of atoms. Furthermore, the magnetic susceptibility tensor is quite isotropic for most fullerene-like clusters, reflecting the global symmetry of these systems. The exception is obviously the ring isomer of B_{20}, and to a lesser extent B_{44}.

For B_{80} we find a completely different situation, with the fullerene being now slightly paramagnetic ($\bar{\chi} = 219.3$ cgs ppm/mol). The small absolute value for the susceptibility indicates that there is indeed a strong cancellation between the paramagnetic and diamagnetic currents. This value should be compared to C_{60} (which has a susceptibility of about -260 cgs ppm/mol [282, 283]). In the C_{60} case, the reason for the small diamagnetism is

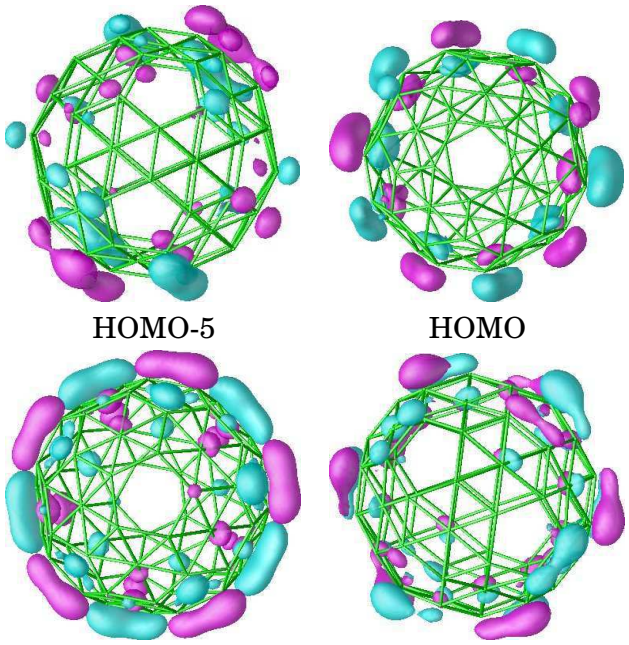

Figure 5.14: Kohn-Sham states of the B_{80} clusters. The states HOMO-1, HOMO-2, HOMO-3, and HOMO-4 are nearly degenerate with the HOMO, and the very similar to the HOMO. Also LUMO+1 is similar to LUMO, so it is not displayed here. The magenta (cyan) isosurface corresponds to the positive (negative) part of the wave functions.

the negligible value of the ring current susceptibility (the π-electron contribution to the susceptibility); the paramagnetic and diamagnetic ring currents circulating around the pentagons and hexagons, respectively, cancel each other. In the case of B_{80}, the geometry is more complex with boron atoms occupying the center of the hexagons, complicating this simple picture, and leading to a slightly larger value of the paramagnetic current relatively to the diamagnetic term.

Note, however, that like for C_{60} the total value for magnetic susceptibility of B_{80} depends strongly on the geometry and in particular on the ratio between different B–B bond lengths. Changing the bond lengths alters the equilibrium between the diamagnetic and paramagnetic contributions: as these contributions are both large and with different signs, but more or less of the same magnitude, their sum depends strongly on small variations of their individual values. To study this effect, we calculated the magnetic susceptibility for the three geometries optimized with the B3LYP functional in Ref. [250]. We found 42.8 cgs ppm/mol for the I_h geometry, 46.2 cgs ppm/mol for the C_1, and 29.7 cgs ppm/mol for the T_h. The differences can be explained by looking at the different B–B bond lengths. For all structures the length of the bonds connecting the atoms in the center of the hexagons to their neighbors is around 1.70 Å (with some dispersion especially in the T_h geometry). However, for the other two bond-lengths, d_h measuring the side of the hexagons and d_p measuring the side of the pentagons, we can see how the different exchange-correlation functionals influence the structure. For the cluster optimized with the PBE we find $d_h \sim 1.68$ Å and $d_p \sim 1.73$ Å, while the B3LYP yields a small contraction of the side of the hexagon to ~ 1.67 Å and a small expansion of the pentagons to ~ 1.74 Å. These are very small differences, but due to the subtle cancellation between the paramagnetic and diamagnetic currents they lead to a large difference in the susceptibility.

Looking at the values for the static polarizability we see that they increase essentially linearly with the number of boron atoms, with a slope of approximately $2\,\text{Å}^3$ per atom. The slope, however, decreases slightly with increasing number of atoms. This simple result reflects the fact that, as all boron atoms in these clusters have a similar chemical environment, the static polarizability is mainly additive and determined by the overall size of the cluster.

More insight can be obtained from the *dynamical* polarizability, in particular from the optical absorption cross section spectra given in Figs. 5.13. The low energy spectrum of B_{20} "double ring" isomer [100] is characterized by well defined peaks, and is dominated by one sharp peak at around 4.8 eV – which originates from electron fluctuations perpendicular to the cylinder axis. The absorption strength is suppressed below 4 eV (with the exception of a couple of small peaks) as the low energy transitions are dipole forbidden. The spectra of B_{38}, B_{44} are not so well defined – there are many peaks whose respective widths overlap, creating a broad, structureless response whose onset is below 2 eV. This fact can also be rationalized by looking at their geometries: these clusters are not so symmetric (distorted D_3 and distorted D_{3h} for B_{38}, B_{44} respectively), and have a larger distribution of bond lengths. The most stable of the clusters studied, B_{80}, also has some weak absorption peaks in the visible, although the strongest peaks are positioned at energies higher than 3 eV. Finally, the absorption cross section of the largest fullerene studied here, B_{92}, is qualitatively similar to B_{80}.

It is curious to compare the results for B_{80} to the known absorption spectrum of its carbon counterpart C_{60}. The latter is dominated by a π-plasmon at around 6.3 eV [293] and has a large optical gap of more than 3 eV. This is also the typical absorption spectrum of the planar polycyclic aromatic hydrocarbons [289]. On the other hand, B_{80} exhibits a much smaller optical gap (of around 1.5 eV) and a much less structured spectrum. This can be explained by two factors. First the HOMO-LUMO gap of C_{60} (around 1.6 eV) is larger than the one of B_{80} (around 1 eV). Looking at the Kohn-Sham states of B_{80} around the HOMO-LUMO gap reveals the second factor (see Fig 5.14). The HOMO state (and the other states immediately below) are located around the three B_{20} rings and retain a certain "π-like" character, i.e. the wave-functions change sign going from outside to inside the cage. The first occupied state of different character is the HOMO-5, that is mainly located around the pentagons, but spreading considerably to other regions of the cluster. The situation is considerably more complicated for the LUMO states: they are no longer of "π-like" symmetry, and extend over considerable regions of the cluster. It is then clear that the dipole matrix elements between the lowest occupied and unoccupied states will not vanish (as it happens, e.g., for the B_{20} ring), and absorption will start shortly after the HOMO-LUMO gap.

In conclusion, we performed first-principle calculations of electrical and magnetic linear response properties of the boron fullerenes recently proposed by Gonzalez Szwacki *et al.*[250]. In particular, we investigated the signatures of the counterpart of C_{60}, the B_{80} cage, the most stable of these clusters. Regarding the magnetic response, all clusters except B_{80} turn out to be diamagnetic. On the other hand, B_{80} turns out to be slightly paramagnetic. This arises from the presence of a strong cancellation between diamagnetic and paramagnetic effects, as it is known to happen in the carbon fullerene. The static polarizability increases monotonically with the number of boron atoms. More precisely, it is roughly proportional to the number of atoms, pointing to an additive behavior justified by the fact that boron atoms in all clusters studied here have a similar chemical environment. The absorption spectra of the boron cages display similar features, with absorption thresholds close to the HOMO-LUMO gaps and many peaks overlapping in the visible and near

ultraviolet region. On the other hand, the optical spectrum of the double-ring B_{20} is dominated by large peaks above 4 eV, while absorption is suppressed at low energies due to the presence of many dipole forbidden transitions. The physical properties of boron fullerenes, and in particular of the stable B_{80} are by now fairly well described and understood through theoretical calculations. Unfortunately, these clusters have not been produced experimentally yet. It is however our belief that, like for C_{60} and the carbon nanotubes before, the experimental ingenuity will lead in the near future to the creation and detection of these interesting nanostructures.

5.4 Alloying effects on the optical properties of $Ge_{1-x}Si_x$ nanocrystals*

5.4.1 Introduction

The semiconductors silicon and germanium can form a substitutional solid solution of the form $Ge_{1-x}Si_x$ covering the whole range of compositions x. Pure Si is the most widely used material for electronic applications since many years and its fabrication technology is highly developed. However, the indirect band gap of bulk Si presents a problem for light-emitting applications. A solution that has been proposed to circumvent this problem is nanostructurization of Si in structures comprising porous Si [294], nanowires [295], as well as Si nanocrystals. Moreover, ample use has been made of the fact that Ge can easily be combined with Si in heterostructures. In addition, Ge nanocrystals in a matrix of SiO_2, SiC, sapphire, or Si have been investigated by many groups [296, 297, 298]. In many of those cases, intermixing between Ge and Si is found in the nanostructures.

The two materials show different properties upon nanostructurization. While Si retains its character of an indirect material [299, 300, 301], the work of several groups showed that, depending on the structure, strain, etc., Ge nanostructures can become quasi-direct, i.e., they exhibit very strong transitions at or very close to the HOMO-LUMO transition [299, 300, 301, 302, 303, 304, 305]. The different behavior reflects the different character of the band gaps in the bulk materials. While both are indirect, the minimum gap in Si lies between Γ and a point near the X point, and the direct gap is much larger. In Ge, the minimum gap between Γ and L is energetically very close to the direct gap at Γ. The effects of confinement and structural relaxation result in a strong contribution of the Γ–Γ transition to the HOMO-LUMO transition, thus resulting in short radiative lifetimes of Ge clusters [301, 306].

Therefore, when mixing both materials two questions arise: what is the effect of the intermixing on the electronic properties of the nanocrystals, and how are the different characters of the two materials combined. While the answer to these questions is essentially well known for the bulk alloy, there are still few investigations concerning the mixed nanostructures. Most experimental studies use Stranski-Krastanov growth, (see, e.g., Ref. [307]), which results in relatively large structures in which it is safe to assume that the effects of confinement and alloying act independently. However, for smaller structures this cannot be taken for granted. For small nanocrystals, photoluminescence experiments [308] have been compared with theoretical results [309]. Furthermore, Ge-Si nanowires have been

*This section is based on the article:

- *Alloying effects on the optical properties of $Ge_{1-x}Si_x$ nanocrystals from time-dependent density functional theory and comparison with effective-medium theory* , S. Botti, H-Ch. Weissker, and M. A. L. Marques, Phys. Rev. B **79**, 155440 (2009).

investigated experimentally [310] and theoretically [311].

Previous theoretical studies have focused on the interplay of confinement and alloying [309, 311]. However, these *ab initio* calculations were performed within the independent-particle approximation based on the Kohn-Sham scheme of *static* DFT. Therefore, important many-body effects have been neglected, viz., the self-energy corrections describing the effect of the excitation of the electrons or holes individually, as well as the electron-hole interaction. (Nonetheless, these two effects are found to cancel each other to a large extent for many systems [312]). Furthermore, these calculations miss the very important depolarization or crystal local-field effects.

The way we choose to improve upon the independent-particle results is provided by TDDFT [19, 152, 181] in which the many-body effects neglected in static DFT are introduced by the so-called exchange-correlation kernel f_{xc}. With respect to the independent-particle results, the excitation energies are corrected, and the transitions between the independent-particle states are mixed. The degree of the mixing indicates the degree to which the independent-particle approximation fails to provide a good description of the system.

Within TDDFT, we use the adiabatic local-density approximation (ALDA, also known as TDLDA) of the exchange-correlation kernel. The choice is motivated by the fact that TDLDA yields good results for optical spectra of isolated systems [88] as well as for non-zero momentum transfers [313]. Note, however, that the ALDA is well known to fail in some cases, the most important of which are perhaps extended systems [17, 181]. Within TDDFT, the random-phase approximation (RPA) is obtained by neglecting the exchange-correlation kernel, i.e., by setting $f_{\text{xc}} = 0$. From this, the independent-particle approximation results from the neglect of the microscopic terms of the variation of the Hartree potential. In other words, the difference between the independent-particle approximation and the RPA are the depolarization effects which are due to the inhomogeneity of the system.

The simplest way to account for depolarization effects within an approximated classical picture is to apply the Maxwell-Garnett effective-medium theory to the complex dielectric function of the bulk alloy crystals. We applied the effective medium theory to our alloy clusters in order to check if the depolarization effects are dominant with respect to confinement effects and further many-body corrections. In fact, if it is the case, the spectra obtained using the effective-medium theory are in good agreement with full TDLDA results. These model calculations thus give a good overall description of the optical spectra at a much lower computational cost than TDLDA.

In the present section we first present TDLDA results for $\text{Ge}_{1-x}\text{Si}_x$ nanocrsytals with a diameter of about 1.8 nm, focusing on alloying effects.

The results are then compared with the previous independent-particle calculations of Ref. [309], highlighting the effects of the depolarization, as well as of the mixing of transitions. We will also consider depolarization effects alone, decoupled from confinement effects, by applying Maxwell-Garnett classical effective-medium theory. Finally, the emission properties of the nanocrystals are investigated by considering the geometries obtained after excitation of an electron-hole pair.

5.4.2 Ab initio calculations

We used the same modeling scheme as used in Ref. [309] considering $\text{Ge}_{1-x}\text{Si}_x$ nanocrystals of a fixed size made of 83 Ge and Si atoms. Quasi-spherical nanocrystals were built starting from one atom and adding nearest neighbors shell by shell, assuming bulk-like tetrahedral coordination. The outer bonds were saturated by hydrogen atoms. Alloying between Ge

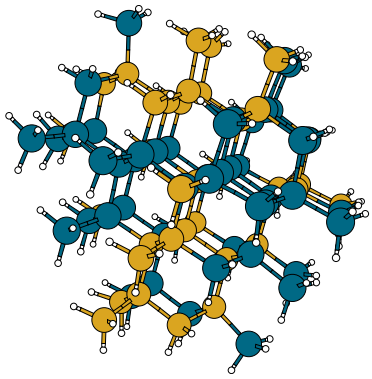

Figure 5.15: Example of the studied nanocrystal structures: $Ge_{48}Si_{35}H_{108}$. The colors are: Si (yellow), Ge (blue), and H (white).

and Si was introduced by randomly exchanging Ge atoms by Si. The surface was then passivated with H atoms to saturate the remaining dangling bonds.

In Ref. [309], the study of $Ge_{1-x}Si_x$ nanocrystals with the same number of atoms for ten different atomic configurations demonstrated that those with nearly uniformly distributed Ge and Si atoms possess the lowest total energies and nearly equal excitation energies. On the other hand, nanocrystals with deliberately clustered Si atoms and, hence, rather different excitation energies give rise to total energies substantially higher than the average. As their probability of occurrence is, consequently, small, the configurational average can be replaced by the study of only one nanocrystal with nearly uniformly distributed Si and Ge atoms for each composition x. We selected nanocrystals with a total number of 83 atoms of Ge and Si, having a diameter of about 1.5 nm. This radius corresponds to a sphere of the volume occupied by 83 atoms in the bulk. These nanocrystals are large enough to exhibit the characteristics of nanocrystals as opposed to much smaller structures which show a molecular-like behavior [299, 314, 306]. Moreover, they are small enough to present significant confinement effects on the electronic states. An example of the atomic arrangement is shown in Fig. 5.15 for $Ge_{48}Si_{35}H_{108}$.

To obtain the relaxed geometries of the $Ge_{1-x}Si_x$ nanocrystals, we used the plane-wave code VASP [315, 240] within the local-density approximation (LDA) in the parametrization of Perdew and Zunger [238] and the projector-augmented wave (PAW) method [316]. This computational set-up is the same as the one employed in Ref. [309].

Starting from the relaxed geometries we obtained the optical spectra at zero temperature using TDDFT as implemented in the computer code `octopus` [243, 244]. The LDA [238] is employed in the adiabatic approximation for the xc potential (i.e., we applied the TDLDA) and the electron-ion interaction is described through norm-conserving pseudopotentials [239]. To build our pseudopotentials for Si and Ge, we included in each case 4 electrons in the valence ($4s^2$ and $4p^2$ for Ge, $3s^2$ $3p^2$ for Si) and, in the case of Ge, we employed non-linear core corrections [317]. These pseudopotentials have already been validated by the calculation of electronic excitations in Si and Ge bulk crystals [37]. The time-dependent Kohn-Sham equations, in this code, are represented in a real-space regular grid, using a spacing of 0.275 Å at which the calculations are converged. The simulation box is constructed by joining spheres of radius 4.5 Å, centered around each atom.

To calculate the optical response we excite the system from its ground state by applying a delta electric field $E_0\delta(t)$. The real-time response to this perturbation is Fourier transformed to get the dynamical polarizability $\alpha(\omega)$ in the frequency range of interest. The

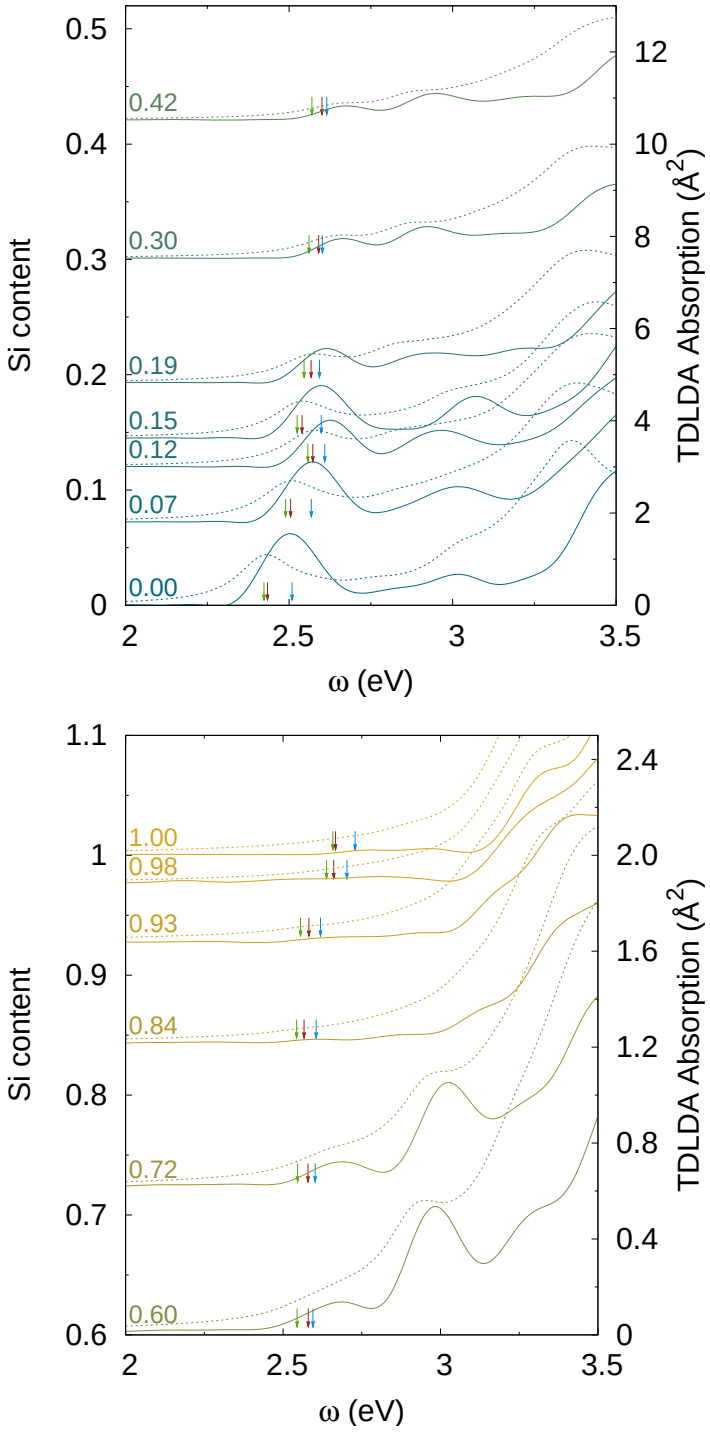

Figure 5.16: Absorption spectra as a function of the Si content of the clusters: Independent-particle spectra (dashed lines) compared with TDLDA results (solid lines). The green arrows (arrows at lowest energy) mark the HOMO-LUMO gap, while the red arrows (middle arrows) mark the ΔSCF excitation energies and the blue arrows (arrows at highest energy) mark the first transitions of the Casida's analysis. The independent-particle curves are divided by a factor of 15. Note the different scale in the two panels.

absorption cross section $\sigma(\omega)$, is then obtained from the relation:

$$\sigma(\omega) = \frac{4\pi}{c}\omega \, \mathfrak{Im}\, \alpha(\omega)\,, \tag{5.5}$$

where c is the velocity of light in vacuum. For a technical description of this method we refer to Refs. [243] and [94]. To obtain the RPA spectra in this approach we just kept the exchange-correlation potential fixed during the propagation (which amounts to making $f_{\rm xc} = 0$). The independent-particle spectra were calculated by further fixing the Hartree potential to its initial value. A time step of $0.0055\,\hbar$/eV and a total propagation time of $37.5\,\hbar$/eV were sufficient to ensure a stable propagation. We estimate our numerical precision in the spectra to be better than 0.05 eV. The mixing of independent-particle transitions in the spectra has subsequently been investigated using the Casida's formulation of linear-response TDDFT [151, 318].

In order to test the coherence of our calculations, we compared independent-particle spectra computed using matrix elements calculated with the VASP code [319, 320, 299] to spectra obtained by time propagation by means of the `octopus` code. No substantial differences were found between the results.

Due to the interest in the luminescence of this kind of systems, the lowest excitation energies are of particular importance. As a consequence, we decided to compare three different quantities. Besides the lowest excitations of the TDLDA absorption spectra, we present the Kohn-Sham HOMO-LUMO gap of the ground state and the ΔSCF excitation energies calculated as the difference $E_{\Delta\rm SCF} = E(N, \text{e–h}) - E(N)$, where $E(N)$ is the total energy of the ground-state and $E(N, \text{e–h})$ is the total energy of the excited-state configuration where one electron has been promoted from the HOMO into the LUMO. In this way, an excited configuration is modeled and the electron-hole interaction is partially taken into account. This approach enables also a subsequent ionic relaxation with the electron-hole pair present, which yields the description of the excited-state geometries. Using the excited-state geometries we were also able to evaluate emission spectra.

Results for the photoabsorption of the $\rm Ge_{1-\mathit{x}}Si_{\mathit{x}}$ nanocrystallites are presented in Fig. 5.16. In the figure we compare the independent-particle response (dashed lines) with full TDLDA calculations (solid lines) for the whole range of compositions. The dependence of the curves on the composition turns out to be quite smooth. When going from Ge-rich clusters to Si-rich clusters, we observe a shift to higher energies of the onset and a suppression of the absorption strength of the first peak (note the different scales of both panels). Moreover, the dependence of the peak position on the composition x is roughly the same in the independent-particle and the TDLDA schemes. For the clusters studied, the total intensity of the independent-particle spectra is strongly suppressed in TDLDA (the independent particle curves are divided by a factor of 15 in Fig. 5.16). Indeed, this quenching of the absorption is a well known effect that is due to the inclusion of classical depolarization effects, and not from the exchange-correlation effects accounted for by the TDLDA kernel. This can be verified by calculating the absorption spectrum within the RPA, which includes all classical effects due to the variations of the Hartree potential but neglects quasi-particle and excitonic effects. Indeed, the spectra we calculated within RPA are so close to the TDLDA spectra shown in Fig. 5.16 that we chose not to show them.

For Ge-rich nanoparticles, both the position and the composition dependence of the peaks are already well described at the level of the independent-particle approximation. This perhaps surprising fact can be explained in terms of compensation of quasiparticle corrections and binding energies of the excitons. previous independent particle calculations [299] with experimental data [321]. For small x at the absorption edge, the first peak is strong and appears essentially at the HOMO-LUMO energy gap. The absorption

edge has a completely different nature in Si-rich clusters. In fact, in this case the peaks of lowest energy have a vanishing oscillator strength in TDLDA, thereby blue-shifting the absorption edge with respect to the HOMO-LUMO gap.

In order to analyze the origin of the different peaks in the spectra as a function of the composition of the $Ge_{1-x}Si_x$ alloy, we decomposed the excitations in sums of Kohn-Sham particle-hole transitions through the solution of Casida's equation [151, 318]. We found that on the Ge side of the composition range, the lowest peak of the spectra which defines the absorption edge is produced essentially by a strong, pure transition between the Kohn-Sham HOMO and LUMO. This is certainly one more reason for the similarity between the independent-particle and the TDLDA spectra. The large peak with HOMO-LUMO character decreases in intensity with increasing percentage of Si in the $Ge_{1-x}Si_x$ alloy, until the composition of about $x = 0.2$ when it disappears. For even smaller x the absorption at the onset is determined by a strong mixture of transitions between states close to HOMO and LUMO. However, the very lowest transitions are forbidden, producing a significant blue shift of the absorption edge. In the intermediate energy range and for all compositions, excitations can be decomposed as a sum of many contributions.

In Fig. 5.16 we also show the HOMO-LUMO gap (green arrows), the lowest excitation calculated within the ΔSCF approximation (red arrows), and the first excitation within TDLDA (blue arrows, these excitations are dark on the Si side of the composition). For all cases we find that the first ΔSCF excitation is, as expected, blue-shifted with respect to the HOMO-LUMO gap, and that the first TDLDA transition is at slightly higher energies. The differences are, however, quite small, and of the order of one tenth of an eV. This is known for this class of systems [322], part of it being due to the cancellation of self-energy and excitonic effects [312]. However, the differences appear to be slightly larger in the region of intermediate composition x, i.e., of a greater degree of structural disorder. Similarly, Degoli *et al.*found in Si nanocrystals that the differences become larger in cases of stronger localization [322]. It is also clear from the plot how the first transition becomes forbidden while going from Ge-rich to Si-rich clusters — this behavior is reminiscent of the different character of the band gap in the parent bulk Ge and Si.

A much simpler approach to model the absorption cross section of a $Ge_{1-x}Si_x$ nanocrystal is to start from the complex dielectric function of the corresponding bulk alloy crystal and to apply the effective-medium theory [323, 324]. This classical approach is based on Maxwell's equations and neglects completely the microscopic details, such as atoms and bonds. Of course, this assumption is better justified when the size of the system is large. However, it always handles correctly the boundary conditions for the Maxwell's equations at the interfaces, which give the very important contributions to the dielectric response through the classical depolarization effects. Often, these classical contributions are enough to describe the physics of the dielectric response of a composite system made of objects embedded in some matrix [87, 325, 326]. Our clusters can be considered as a family of spheres of volume V_{obj} cut from a $Ge_{1-x}Si_x$ bulk alloy. The Maxwell-Garnett expression [323] in the specific case of an isolated spherical object in vacuum yields:

$$\sigma(\omega) = 9\frac{\omega}{c}V_{\text{obj}}\frac{\mathfrak{Im}\,\epsilon(\omega)}{\left[\mathfrak{Re}\,\epsilon(\omega)+2\right]^2+\left[\mathfrak{Im}\,\epsilon(\omega)\right]^2}\,, \tag{5.6}$$

where ϵ is the experimental complex dielectric function of the bulk alloy. To represent well the extension of the polarizable nanocrystals, we took an average distance of the furthermost saturating hydrogen atoms to obtain the radius of the cluster, and consequently V_{obj}. This results in a radius slightly larger than the one mentioned above which takes into account only the Ge and Si atoms. We used the value of $R_{\text{obj}} = 9.1\,\text{Å}$, but the results are fairly

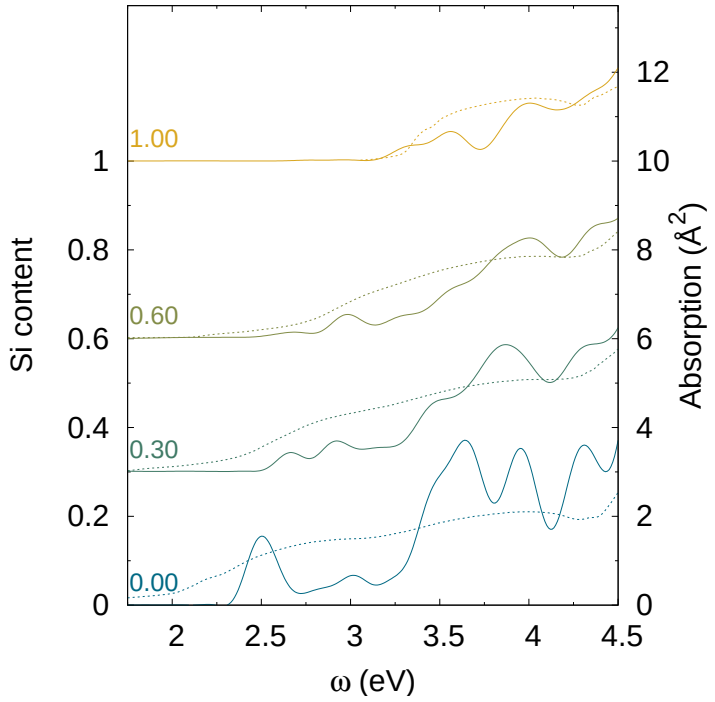

Figure 5.17: Absorption spectra as a function of the Si content of the clusters: Effective-medium theory (dashed lines) using the dielectric function of bulk $Ge_{1-x}Si_x$, compared with TDLDA results (solid lines).

insensitive to a (reasonable) choice of this value. The experimental dielectric function of the bulk alloy with precisely the needed composition x was obtained from a discrete set of measurements [327] using a recently developed interpolation scheme [328]. This scheme interpolates $\Im\mathfrak{m}\ \epsilon(\omega)$ making use of the screening sum rule and the positive definiteness of the spectra. $\Re\mathfrak{e}\ \epsilon(\omega)$ was subsequently obtained by means of the Kramers-Kronig relations after fitting appropriate tails to the imaginary parts. The latter procedure was tested on the input curves to insure the quality of the real part.

In Fig. 5.17 we show spectra calculated using the effective-medium theory for selected compositions. Comparing to the first-principles TDLDA curves, we can see that, already for this relatively small size of clusters, the classical theory gives a quite good overall description of the absorption spectrum. As expected, effective-medium theory is not capable of describing the peaks of the individual transitions, but it describes correctly the intensity and the trends of the spectrum. Once again these results confirm that the dependence on the composition of the optical spectra is smooth and that the confinement and alloying effects act independently to a large degree. In fact, within this classical scheme, only the alloying effects determine the variation of the absorption response as a function of x. In particular, the confinement-induced opening of the HOMO-LUMO gaps and the resulting blue-shift of the absorption onset are not accounted for. The confinement effects could be described by introducing a size-dependent nanocrystallite dielectric function which can then be used to calculate the spectra of the crystallites in a different environment [314]. In this sense, comparison of the TDLDA results with the present effective-medium approach gives an idea of the importance of the confinement effects on the overall spectra.

We note that these model calculations can be performed at negligible computational cost, and therefore provide a simple and fast method to obtain reasonable spectra for

medium and large nanocrystallites.

Given the strong influence of the depolarization effects, the question arises as to why the independent-particle spectra have been successfully compared previously with experiment [299]. This agreement is, in fact, not a fortuitous coincidence, but due to the experimental conditions. The experiment has been done on Ge nanocrystals inside a matrix of sapphire [321]. This reduces strongly the depolarization effects because it reduces the inhomogeneity of the system. The calculations, on the other hand, treated nanocrystals in vacuum but neglected the depolarization effects. Therefore, together with the cancellation between self-energy effects and electron-hole interaction mentioned above, the independent-particle approximation provides in fact a good description of the spectra of this particular experiment.

In order to calculate the emission properties, we consider the geometry of the relaxed nanocrystals where the ionic relaxation has been carried out after transferring an electron from the HOMO to the LUMO Kohn-Sham orbital. As the radiative lifetimes are usually much longer than the times that the electrons (holes) take to relax to the LUMO (HOMO), we can assume thermalized electron-hole pairs. As their lifetimes are then determined by the exponential factor describing their distribution [329, 330], it is the onset of the emission which reflects the emission properties, while the higher parts of the spectrum are suppressed.

Stimulated emission spectra can be easily obtained within our formalism by calculating the absorption cross-section $\tilde{\sigma}_{\mathrm{abs}}(\omega)$ at the excited-state geometry. Luminescence spectra can then be calculated from the van Roosbroeck-Shockley model [331]:

$$\sigma_{\mathrm{lum}}(\omega) \sim \omega^2 \frac{1}{e^{\hbar\omega/k_{\mathrm{b}}T} - 1} \tilde{\sigma}_{\mathrm{abs}}(\omega)\,, \tag{5.7}$$

where k_{b} is the Boltzmann constant and T is the temperature.

In Fig. 5.18 we compare the absorption cross sections for the ground-state (solid lines) and the excited-state (dashed lines) geometries for $\mathrm{Ge}_{1-x}\mathrm{Si}_x$ clusters in all the composition range. The energy difference between the onsets of absorption and emission corresponds to the structural contribution to the Stokes shift.

thatIn Fig. 5.19 we compare the independent-particle result with the TDLDA for the absorption $\tilde{\sigma}_{\mathrm{abs}}(\omega)$ at the excited-state geometry. The conclusions with respect to their similarity drawn for the ground state remain valid for the excited-state geometries. The same applies to the transition analysis using Casida's equation. The character of the emission onset on the Ge side of the composition range is already well described within the independent-particle approximation. The decomposition of the excitations as a sum of Kohn-Sham transitions provides a picture strictly analogous to the one for the absorption spectra: the lowest transitions of the Ge-rich nanocrystals correspond to almost pure Kohn-Sham transitions, while for large x and for the higher transitions, independently of x, strong mixing is found.

However, it is important to note that a very weak peak appears at about 1.95 eV. This is red-shifted by about 0.5 eV with respect to the ground-state calculation. The peak, which can be easily seen in Fig. 5.19, is clearly present in both the independent-particle result and the TDLDA result. It occurs for all compositions on the Ge side of the x range and is almost composition independent. It appears to be connected with the lowering of the symmetry as compared to the ground state where the pure Si or Ge nanocrystals without alloying have T_d symmetry and the HOMO-LUMO transition is threefold degenerate. The symmetry breaking due to the geometry relaxation under excitation has therefore a much stronger effect than the introduction of the alloying, which at the Ge-rich side splits the degeneracy only slightly and which does not change the character of the strong absorption onset at

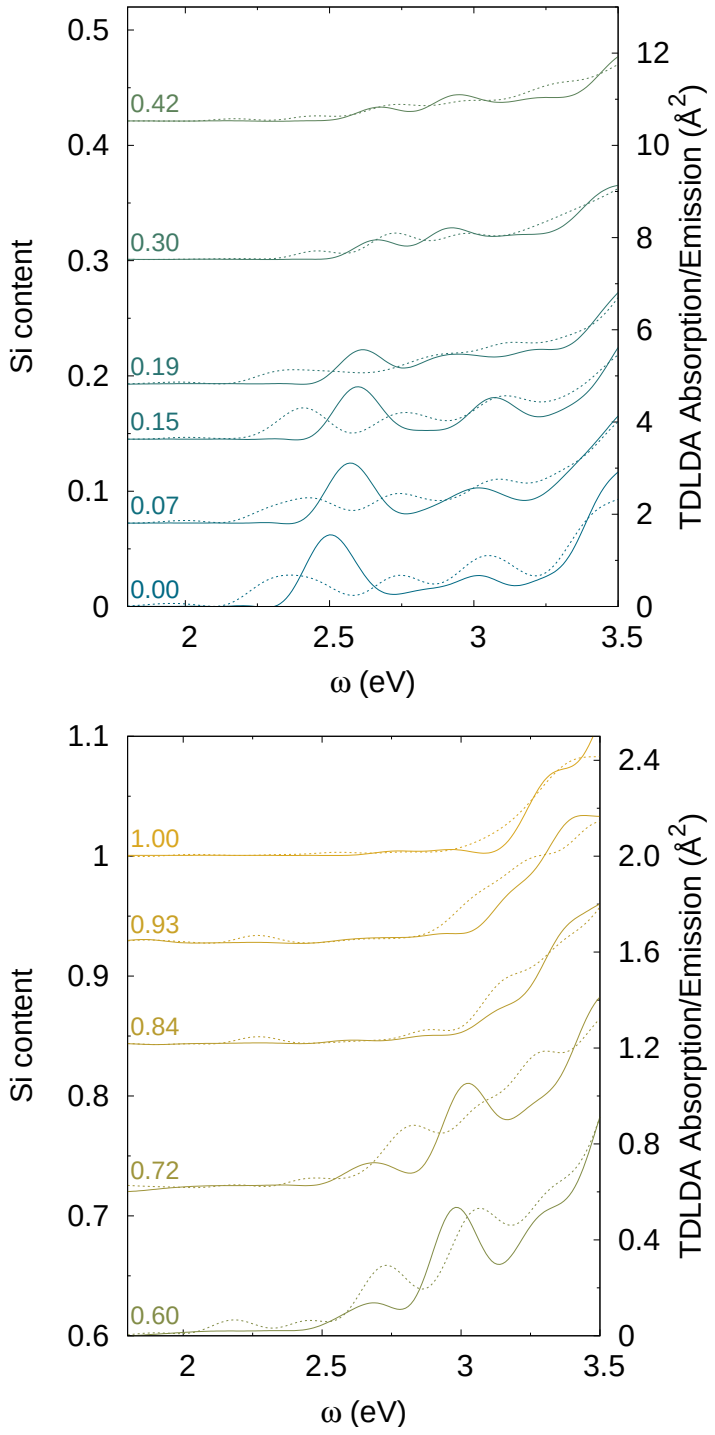

Figure 5.18: Absorption (solid lines) and emission (dashed lines) spectra as a function of the Si content of the clusters. Note the different scales.

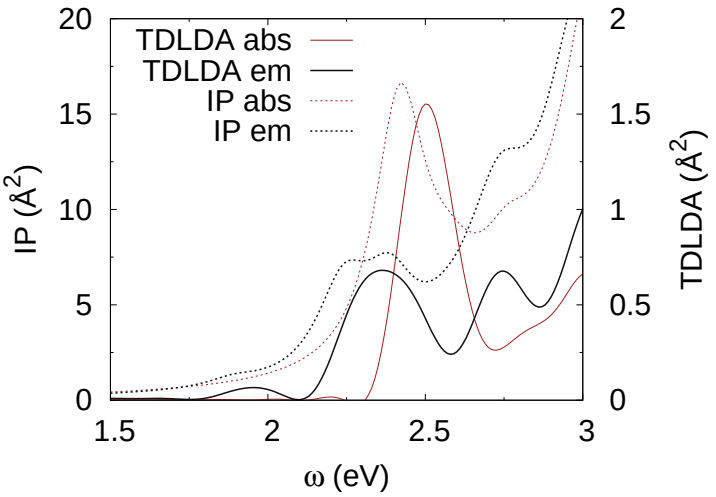

Figure 5.19: Absorption (red) and emission (black) spectra of the pure Ge nanocrystal in the independent-particle approximation (dashed) and the TDLDA (solid). Note the different scales.

the HOMO-LUMO transition. Due to the argument above [see Eq. 5.7], the appearance of this weak peak will strongly increase the radiative lifetimes of the systems. We conjecture that this might be responsible for the fact that even though several theoretical predictions coincide in that Ge nanostructures should have strong transitions at the absorption onset, few experiments have been able to detect luminescence from excitons in Ge nanocrystals.

The absorption spectra of free $Ge_{1-x}Si_x$ nanocrystals with a diameter of about 1.8 nm have been calculated within time-dependent density-functional theory in the adiabatic local-density approximation. The changes of the spectra upon changing composition x are smooth. In particular at the absorption onset, the position and the composition dependence of the spectra is found to be already well represented by independent-particle results. The analysis of the solutions of Casida's equation shows that this is due to the fact that the first transition of Ge-rich nanocrystals corresponds to an almost pure independent-particle transition. The TDLDA onsets are slightly blue-shifted with respect to their independent-particle counterpart, their composition dependence at the Ge side of the compositional range is practically the same. For higher Si contents, a mixing of many independent-particle transitions is found.

Depolarization effects are strong and their inclusion alone, even within a simplified classical model, on top of an independent-particle calculation allows to get the correct physical picture of the optical response. They can be approximately taken into account at a negligible computational cost using Maxwell-Garnett effective-medium theory. Further many-body terms do not modify significantly the spectra due to the cancellation of opposite contributions given by quasiparticle corrections and excitonic effects.

Emission spectra have been investigated using the geometry of excited nanocrystals. A Stokes shift of about 0.5 eV is found. Very weak peaks appear at the absorption onset for all systems on the Ge side which strongly reduce the radiative transition probability and lead to long radiative lifetimes.

We focused in this work on the effect of alloying in the quasi-spherical model structures with bulk coordination, saturated by hydrogen. This means that several questions are left to future work. First, better structural models should be used, possibly obtained using a combination of *ab initio* and semi-empirical or empirical methods. [332] This includes the

question if under certain conditions the quasi-uniform distribution of the alloy atoms might be replaced by other arrangements. Moreover, possible surface reconstructions or defects might locally change the situation and therefore the composition dependence of the quantities that we have studied. Finally, the description of the experiments of alloy nanocrystals embedded in a matrix of, e.g., SiO_2 or sapphire remains a task to be accomplished. While a rough description of the main features can immediately be done using effective-medium theory as described above, this neglects the details at the atomistic level. However, these details, in particular of the nanocrystal-matrix interface, are expected to play an important role as well.

Chapter 6

Advanced materials: applications to data storage and photovoltaics

First-principle calculations of electronic excitations can now be applied not only to prototype simple crystal, but also to real materials of technological interest. In this chapter we discuss three illustrative examples of how DFT based calculations that go beyond the ground state framework of DFT can be used to tackle the problem of electronic excitations in complex materials for important applications in the field of data storage and photovoltaics.

The first example are the so-called Phase-Change Materials (PCM), which exhibit a significant optical contrast – a change of optical reflectivity upon the phase transition from the amorphous to the crystalline state. This property change is fundamental for the application of PCM's in optical data storage, in particular in rewritable storage devices such as DVD-RW's or, since recently, rewritable Blue-Ray discs. One of the most interesting questions is how their optical properties are related to the underlying geometrical structure.

The second example concerns copper indium diselenide/disulfide $CuGa(Se,S)_2$ (CIS) thin-films. The semiconductors of this family are used as absorbers in the thin film solar cell technology that shows the highest efficiencies for lab cells (19.9%), as well as for large modules (13.4%). These materials are doped by native defects. The defects play an important role in the definition of the exceptional stability of this material that, together with the very high absorption coefficient at the absorption edge, make them ideal absorbers.

The third example is again related to photovoltaics. In fact, solar cells, among other technological applications, require the use of materials that are transparent in the visible range, but that have fairly high electric conductivity. These normally incompatible properties can be found together in three different classes of materials: very thin pure metals, highly doped conjugated organic polymers, and doped wide band gap oxide or nitrite semiconductors. During the past years, the latter, commonly referred to as transparent conductive oxide (TCO) materials, have attracted a considerable amount of interest, especially due to their applications in displays and in solar cells. In particular, the CIS thin film solar cells, use TCOs as contacts.

There has been a substantial experimental effort to study the properties of advanced materials, not only to understand them from a fundamental point of view, but also to optimize their properties. This is clearly not surprising due to the extremely important applications that these materials have found in the recent years. However, there is a clear lack in the literature of consistent theoretical and computational studies that can explain and describe properties related to electronic excitations. This better understanding is also essential to help and direct further experimental work.

The relative scarcity of theoretical, first principles, studies can be explained by two reasons: the first is practical, and regards the relative complexity of these systems, often including transition metals with localized d states. One can then be interested in the study of defects or amorphous phases – usually treated in the supercell approximation. These issues increase substantially the computational burden, that only became affordable with the recent advent of powerful supercomputers. The second reason is more fundamental: the most widespread technique used in computational solid state physics, i.e. density functional theory, fails dramatically in describing both the quasiparticle band structure and absorption spectra of semiconductors. These, one should remind, are the two most important electronic properties for the technological applications discussed in this chapter. In fact, DFT, in its common implementations, systematically underestimates band gaps and completely ignores excitonic effects in the spectra. More sophisticated techniques, like the standard GW method, improved the overall calculated properties, but sometimes, like for some transition metal compounds discussed in the following, these methods yield band gaps still far from a good agreement with experiment.

Very recently, several new approaches to GW, including finding better starting points for the perturbative treatment or performing partial self-consistent calculations, appeared as a solution to these problems.

6.1 Origin of the optical contrast in phase-change materials*

6.1.1 Introduction

Several chalcogenide alloys exhibit a pronounced contrast between the optical absorption in the metastable rocksalt and in the amorphous phase. This phenomenon is the basis for their application in optical data storage.

Here we present *ab initio* calculations of the optical properties of GeTe and $GeSb_2Te_4$ in the two phases. The analysis of our computations and experimental data reveal the correlation between local structural changes and optical properties as well as the origin of the optical contrast in these materials. In particular, we find that the change in optical properties cannot be attributed to a smearing of transition energies as commonly assumed for amorphous semiconductors.

Tellurides containing Ge and Sb such as $GeSb_2Te_4$ and $Ge_2Sb_2Te_5$ are characterized by a fast and reversible phase-transition from the metastable, crystalline (c-) phase to the amorphous (a-) phase. This transformation is accompanied by a profound change of electrical conductivity and optical reflectivity [333, 334, 335]. The pronounced optical contrast in phase change materials (PCM) such as GeSbTe alloys is employed in optical data storage, e.g. in rewritable DVD's. The change in electrical properties –e.g. the resistivity change– is one of the crucial features that would be used in phase change random access memories, a very promising candidate for future non-volatile memories [336, 337].

Conventional covalent semiconductors such as Si, Ge or III-V alloys behave very differently; in particular they do not exhibit such a strong optical contrast [338]. A recent remarkable observation provided some clues to the origin of this effect. EXAFS studies of

*Part of this chapter is based on the article:

- *Origin of the optical contrast in phase change materials*, W. Welnic, S. Botti, L. Reining, and M. Wuttig, Phys. Rev. Lett. **98**, 236403 (2007).
- *Local atomic order and optical properties in amorphous and laser-crystallized GeTe*, W. Welnic, M. Wuttig, S. Botti, and L. Reining, C.R. Physique **10**, 514-527 (2009).

the local order of $Ge_2Sb_2Te_5$ as well as GeTe showed a marked change of short range order upon crystallization of the a-state [339, 340]. Such a finding is not observed for conventional covalent semiconductors, suggesting that the short-range structural rearrangement could be closely related to the optical contrast.

However, the change in optical properties upon amorphization of the PCM was still far from being understood. Experiments can show trends, but it is difficult to correlate from experiment alone a macroscopic measurement, like the optical properties, with microscopic details, like the local atomic structure. First-principle calculations provide an ideal complementary tool in this study as structural models with different local order can be explored. We hence performed a joint experimental and numerical study in order to elucidate several major questions, in particular (i) can a change in local order explain the strong optical contrast in PCM's? (ii) is this contrast governed by the corresponding change of the electronic energies (the joint density of states)? (iii) can a simple and general model reproduce this phenomenon so that the results could be used in the search for improved materials?

6.1.2 Origin of the optical contrast

The experimental data presented here were obtained for magnetron sputtered thin films (150-250 nm) of GeTe and $GeSb_2Te_4$ on glass. The measurements, performed at room temperature, include Fourier Transform Infrared (FTIR) spectroscopy and ellipsometry in the combined energy range of 0.1–5.4 eV.

Density Functional Theory calculations of the electronic ground state of GeTe and $GeSb_2Te_4$ were performed with the code ABINIT [182], using norm-conserving pseudopotentials [183] and a generalized gradient approximation [4] for the exchange-correlation potential. The c-phases exhibit a rocksalt structure where Te atoms occupy one sublattice, while the second one is occupied either by Ge atoms (in GeTe) or by Ge/Sb atoms and 25% of vacancies (in $GeSb_2Te_4$) [341, 342]. The atomic positions in the c-phase were relaxed, resulting in a rocksalt-like structure with local distortions as reported recently [339, 343]. The a-states were studied in a supercell configuration containing 56 atoms ($GeSb_2Te_4$) and 64 atoms (GeTe), respectively. Based on the observation that in a-GeTe a fraction of Ge atoms occupies tetrahedrally coordinated positions [340] instead of the octahedral environment in the c-phase, we constructed simple structural models: In a supercell containing 64 atoms (32 Ge and 32 Te atoms) in octahedral coordination 2, 4 and 8 Ge atoms are displaced into tetrahedrally coordinated positions in order to obtain different models for the a-state. For $GeSb_2Te_4$ two simple models were used for the same purpose: in one model all eight Ge atoms exhibit tetrahedral coordination (am_1) in accordance with earlier EXAFS results [339]. In order to test the possibility of a mixture of short-range order as found in a-GeTe, in the second model 4 Ge atoms remain octahedrally coordinated and 4 become tetrahedrally coordinated (am_2). The models used here still exhibit long range order, which should not be present in the a-state. However, in covalent materials the optical properties are mainly defined by short ranged nearest-neighbor interactions. In order to study the correlation between the unusual changes in short-range order and the optical properties it is thus well justified to neglect the change in long-range order upon amorphization. The chosen structural models are expected to reproduce the experimentally observed density decrease of 5-10% [344, 345] upon amorphization. Our calculations yield a decrease of 4.8-9.8% for the amorphous models, consistent with these experimental values.

The optical properties were calculated within TDDFT using the code DP [70]. For small-gap semiconductors like the materials studied here, self-energy and excitonic effects can be taken into account by replacing Kohn-Sham eigenvalues with quasiparticle energies calculated within the GW approximation for the self-energy [11], and by using a model

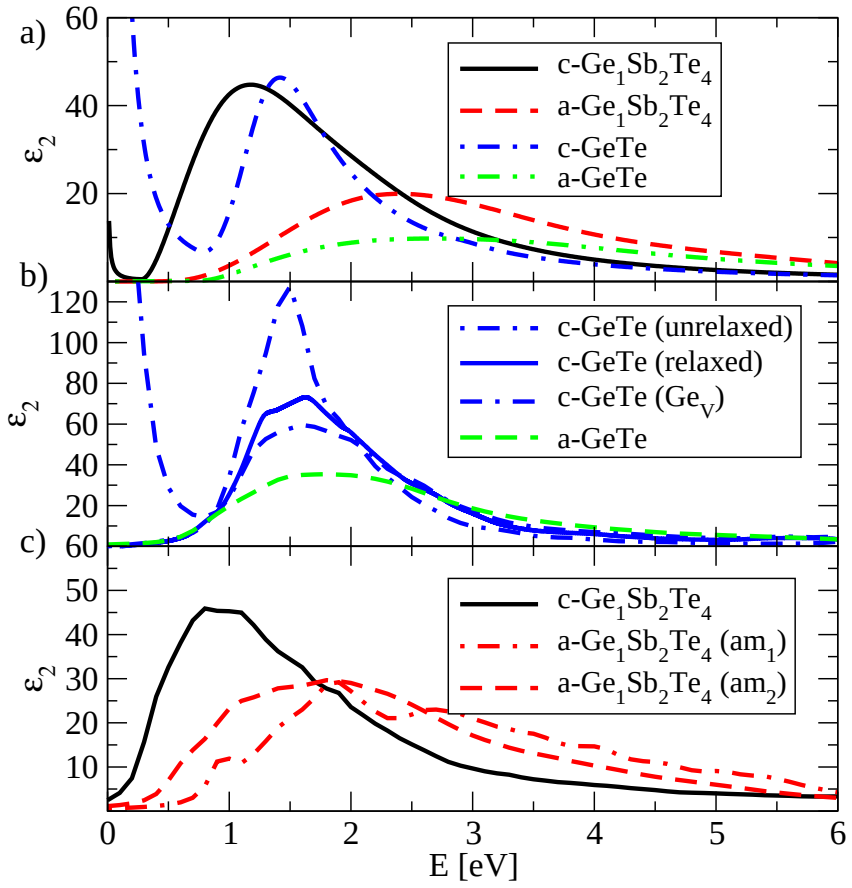

Figure 6.1: Optical absorption of GeTe and $GeSb_2Te_4$ a: experimental, b+c: calculation, here two amorphous models for $GeSb_2Te_4$ are displayed. For both alloys a decrease, a broadening and a blue-shift of the absorption, is reproduced for the a-state. Lattice distortions upon structural relaxation and Ge vacancies lead to a better agreement with the experiment in c-GeTe.

long-range exchange-correlation kernel $f_{xc} = -\alpha/q^2$ simulating the electron-hole interaction [37, 32]. Since the calculated dielectric constant ε_0 takes values between 30 and 76 for the systems considered here, screening is very large and, consequently, the excitonic contribution is negligible, i.e. $\alpha = 0$. Hence the Random Phase Approximation (RPA, i.e. $f_{xc} = 0$), using GW quasiparticle energies instead of Kohn-Sham eigenvalues represents here the best approximation to simulate many-body effects in GeTe or $GeSb_2Te_4$. The GW corrections to the quasiparticle band structure of the c-systems in their primitive unit cells give a blue shift of the absorption threshold of 0.15 eV for GeTe and of 0.1–0.2 eV for $GeSb_2Te_4$. We take the same shifts for the corresponding amorphous phases, since GW corrections can be assumed to depend weakly on the local structure (see e.g. [346]).

In Fig. 6.1 our experimental (a) and calculated spectra (b)+(c) are presented. The experimental data are in line with measurements of PCM's such as $GeSb_2Te_4$, $Ge_2Sb_2Te_5$ or $Ge_1Sb_4Te_7$ found in the literature [347, 348]. The optical contrast between the c- and the a-state is mainly caused by two features: Primarily, the absorption in the a-state decreases and broadens significantly in both alloys. Furthermore a blue-shift of the spectra is observed upon amorphization. The experimental spectrum of the c-state of GeTe exhibits a Drude peak at energies below 0.5 eV. The metallic p-type conductivity inducing this peak,

stems from unoccupied states at the valence band edge [349], which are due to Ge vacancies. Such vacancies are known to be the dominant point defects in c-GeTe (see e.g. [350]). For the comparison between theory and experiment it should be kept in mind that calculations are performed for a bulk single-crystalline solid, and measurements on thin films. In view of that, quantitative deviations between calculated and experimental spectra of the c-phases may occur.

Fig. 6.1 (b) shows calculations of the unrelaxed (i.e. the perfect rocksalt phase with six nearest neighbors) and the relaxed c-GeTe as well as of a relaxed structure containing a Ge-vacancy. The first spectrum is very different from the experiment, the second one is considerably improved while the last shows good agreement with the experiment. Most notably the Drude peak is well reproduced now. Furthermore the intensity of the main peak decreases and thus approaches the experimental value. If vacancies are considered in the a-state, a similar decrease of the absorption intensity can be observed (not shown here). The three employed models for the a-state yield similar spectra. Therefore only one model (with 4 Ge atoms occupying tetrahedral positions) is shown in Fig. 6.1. The peak of the absorption spectrum is found at the same energy in the c- and a-state, however the overall spectral weight exhibits a blue-shift in the a-state. Similarly to experiment, the spectrum broadens and decreases in intensity upon amorphization. Note that both effects, the incorporation of vacancies as well as the local order change from octahedral to tetrahedral coordination reduces the number of Ge-Te bonds.

For $GeSb_2Te_4$, as shown in Fig. 6.1 (c), both contributions to the optical contrast – the decrease and broadening of the spectrum as well as the blue-shift – are reproduced for the two amorphous models. The absorption spectrum of am_1 is more structured than the experimental spectrum. However, this might be due to the fact that this model still exhibits long range order, which is obviously not present in the experiment. The lifting of long range order should result in less well defined transition energies and thus in a smearing of the absorption spectrum. Since both models successfully describe the optical contrast due to short-range changes between the c- and the a-state, in the following analysis am_2 will be employed without loss of generality.

Further structural rearrangements, not captured by our simple structural models, certainly lead to further modifications of the spectra. However, the pronounced change of the calculated spectra provides an unambiguous answer to question (i): the shift of Ge atoms to tetrahedral positions, i.e. the change in the local order of the Ge atoms upon amorphization, is the dominant effect in the generation of the optical contrast.

In the following discussion we will focus on a deeper study of the origin of this optical contrast induced by the change in the local order. As we have verified, crystal local field effects only play a very minor role in the spectra and, as we have pointed out above, self-energy corrections are small. We can therefore base our analysis of the absorption results on Fermi's golden rule in the independent-particle approximation (see e.g. [17]) within the Kohn-Sham picture. This approach enables us to isolate the contributions to absorption of matrix elements and energy levels (ε_i). This separation is essential to answer question (ii). In this approximation the imaginary part of the macroscopic dielectric function

$$\epsilon_2(\omega) = 2\frac{4\pi^2}{\Omega N_{\mathbf{k}}\omega^2}\lim_{\mathbf{q}\to 0}\frac{1}{\mathbf{q^2}}\sum_{v,c,\mathbf{k}}|\mathbf{q}\cdot\mathbf{m}_{v,c,\mathbf{k}}|^2\delta(\varepsilon_{c\mathbf{k}}-\varepsilon_{v\mathbf{k}}-\omega) \tag{6.1}$$

where Ω is the volume of the cell and $N_{\mathbf{k}}$ the number of k-points, is governed by the joint density of states ($JDOS/\omega^2 \equiv \frac{1}{N_{\mathbf{k}}\omega^2}\sum_{v,c,\mathbf{k}}\delta(\varepsilon_{c\mathbf{k}}-\varepsilon_{v\mathbf{k}}-\omega)$) and by the velocity (**v**) matrix elements of the optical transitions $\mathbf{m}_{v,c,\mathbf{k}} \equiv \langle c|\mathbf{v}|v\rangle$. Fig. 6.2 (a) presents the JDOS/ω^2 for $GeSb_2Te_4$ and (c) presents the JDOS/ω^2 for GeTe.

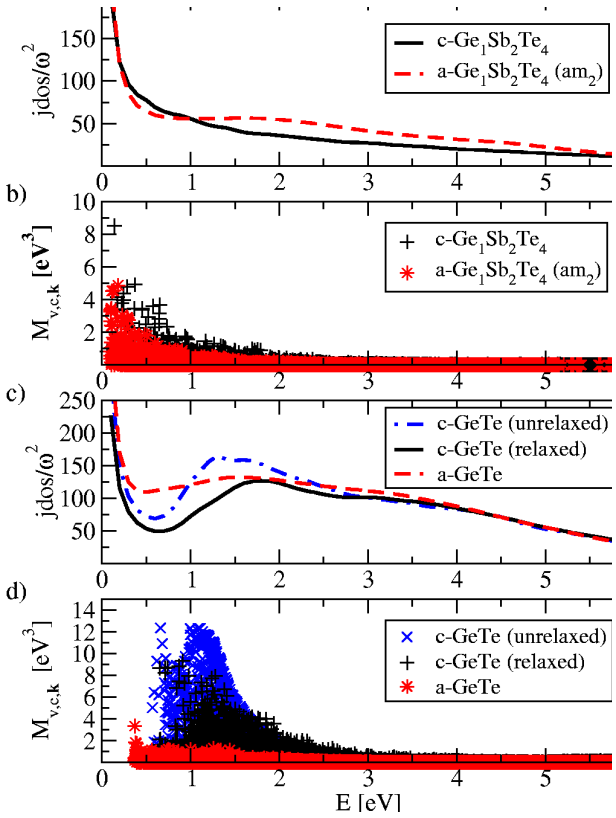

Figure 6.2: a) JDOS/ω^2 of $GeSb_2Te_4$ in the c- and the a-state in Number of transitions/eV^3 per cell and k-point. Up to 1.4 eV the JDOS in the c-phase is stronger than in the a-state, while ε_2 is stronger in the c-phase up to 1.8 eV. For GeTe (c) up to 1.7 eV more transitions are found in the a-state compared to the relaxed c-phase. For both materials the decrease in the absorption upon amorphization can only be explained taking into account the velocity matrix elements shown in (b) ($GeSb_2Te_4$) and (d) (GeTe) with $M_{v,c,\mathbf{k}} = 2\frac{4\pi^2}{\Omega}\lim_{\mathbf{q}\to 0}\frac{1}{\mathbf{q}^2}|\mathbf{m}_{v,c,\mathbf{k}}|^2$.

In $GeSb_2Te_4$ up to 1.4 eV the JDOS in the c-phase is stronger than in the a-state, while above 1.4 eV a larger number of transitions is found in the a-state. On the other side the absorption spectrum in the c-phase exhibits a higher intensity up to 1.8 eV (Fig. 6.1). Hence, assuming constant matrix elements the JDOS cannot explain the optical contrast between the two phases. In GeTe the JDOS is even less suitable to explain the optical contrast: up to 1.7 eV the JDOS is larger in the a-state, for higher energies it is very similar in both phases. With constant matrix elements one would therefore expect an absorption spectrum showing higher intensity in the a-state up to 1.7 eV and very similar spectra for both phases above this value. However, this is clearly not the case in the measured and calculated absorption spectra (see Fig. 6.1). Thus in both alloys the optical contrast can only be understood if the contribution arising from changes in the oscillator strength of the optical transitions is taken into account. This contribution is shown in Fig. 6.2 (b) ($GeSb_2Te_4$) and (d) (GeTe). For $GeSb_2Te_4$ up to about 2 eV stronger matrix elements are found in the c-phase, for c-GeTe they are significantly stronger in the entire spectral range. For GeTe we have also included the curves relative to the undistorted phase, where the oscillator strength is even stronger. As the change in oscillator strength is larger in GeTe compared to $GeSb_2Te_4$, the difference in the intensity of the absorption spectra of the c- and the a-state is more pronounced for GeTe as well. This result of the calculation is

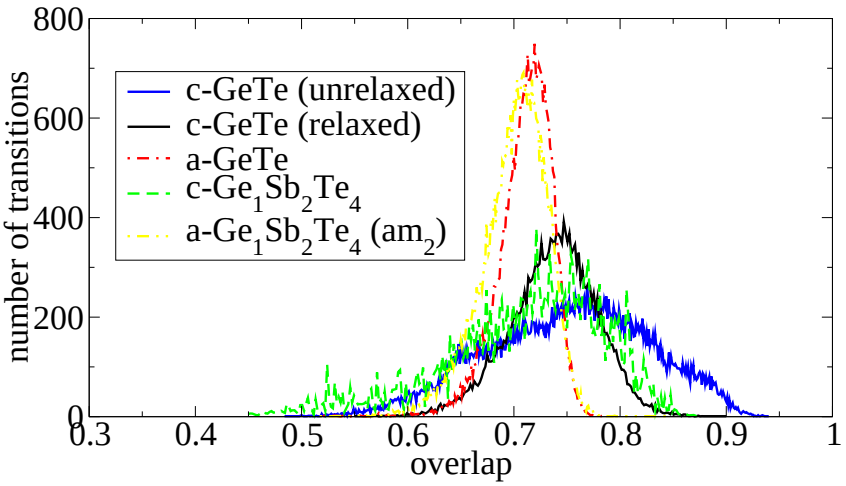

Figure 6.3: The number of matrix elements for excitation energies up to 2.5 eV vs. the overlap $\int |\phi_c(\mathbf{r})||\phi_v(\mathbf{r})|d\mathbf{r}$.

also present in the experimental spectra in Fig. 6.1. Hence Fig. 6.2 (a)-(d) show that the optical contrast between the c- and a-state of GeSbTe alloys are dominated by changes of the matrix elements, providing an unexpected answer to question (ii). In fact, this result is in striking contrast to the common explanation of the -moderate- changes in the optical absorption upon amorphization of tetrahedral semiconductors such as Si, Ge or the III-V compound GaAs. These are explained by a smearing of the JDOS resulting from the loss of long range order and the formation of defect states in the gap in the a-state [338]. Thus the unusual change in the local order in PCM's upon amorphization induces another remarkable effect, namely a significant decrease of the oscillator strength of the optical transitions.

Further studies reveal that this decrease can be mainly attributed to a change in the spatial overlap of the wave functions which contribute to the optical transitions. Fig. 6.3 shows the number of matrix elements plotted against the overlap $\int |\phi_c(\mathbf{r})||\phi_v(\mathbf{r})|d\mathbf{r}$. For both alloys the curves show similar behavior, shifting towards lower values in the a-state and thus indicating a weaker overlap. These results provide a simple model suitable to answer question (iii). The optical properties in PCM's are governed by two effects: the change from octahedral to tetrahedral coordination as well as the inclusion of vacancies reducing the number of Ge-Te bonds and thus the total oscillator strength. Moreover the change of the local geometry upon amorphization or distortion leads to a change in the overlap of the wave functions, resulting in smaller individual matrix elements. This explains the decrease of the absorption upon distortion, vacancy inclusion as well as amorphization thus providing interesting hints for optical data storage applications: As both the change from octahedral to tetrahedral coordination as well as the inclusion of vacancies reduce the number of Ge-Te bonds optical properties in PCM's can be tuned by modifying these two contributions. In particular the latter property is easily accessible. As has been shown recently [351] the vacancy concentration in PCM's can be controlled over a wide range. Furthermore [351] shows that the absorption in the c-state decreases with the degree of distortions (which again can be tuned by changing the stoichiometry).

To conclude, we demonstrate for the undistorted rocksalt phase of crystalline GeTe that the RPA calculations – despite their simplicity – contain all crucial features of the absorption spectra of GeTe. To do so we have to take into account electron-electron and electron-

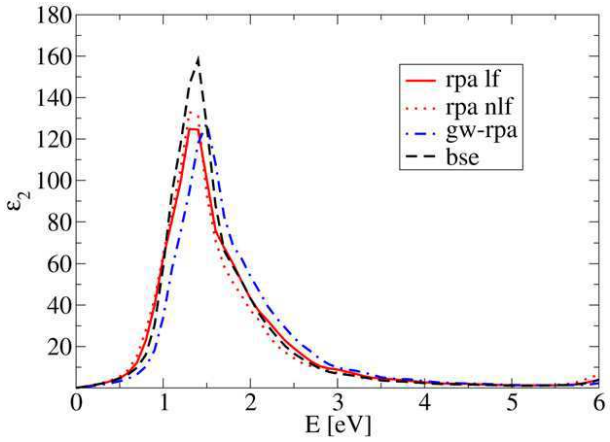

Figure 6.4: Optical spectra of the undistorted rocksalt phase based on many-body perturbation theory compared to the RPA results (red full line: with crystal local fields, red dotted without crystal local fields). The G_0W_0 calculation shifts the eigenvalues 0.15 eV to higher energies, which results in a blue-shift of the absorption peak (blue dot dashed line). Taking into account excitonic effects leads to a small red-shift with respect to the GW-RPA data and to an increase of absorption strength (black dashed line). Solving the Bethe-Salpeter equation yields a negligible exciton binding energy.

hole interactions which are not included in RPA calculations. Therefore for this system we have performed calculations based on many-body perturbation-theory to account for the underestimation of the electronic gap in DFT (electron-electron interaction) and for excitonic contributions in the absorption spectrum (electron-hole interaction). First a correction of the energies of the excited electronic states is obtained by means of a perturbative G_0W_0 calculation. To include the electron-hole interaction the Bethe-Salpeter equation is then solved (see Section 2.2). In Fig. 6.1.2 we display a comparison of the spectra obtained with the different methods.

First of all the importance of the crystal local fields, which stem from the off-diagonal elements of the matrix of the dielectric function ϵ and account for the spatial inhomogeneities, are studied. The RPA spectra obtained by the code dp including local fields (rpa lf) and not including them (rpa nlf) do not differ substantially (nevertheless crystal local fields are taken into account in the subsequent spectra presented here). The eigenvalues obtained from the G_0W_0 calculated by ABINIT are shifted to higher energies by 0.15 eV compared to the GGA eigenvalues. Thus the G_0W_0 calculation results in a minor correction of the electronic structure (gw-rpa) towards the experimental value. The electron-hole interaction in the Bethe-Salpeter absorption spectrum cancels the G_0W_0 blue shift and moves the absorption peak back to the RPA position. This is due to a redistribution of the oscillator strength of the optical transitions. Therefore, the net result of the many body effects is only a modest increase of the peak height. However, no significant features which are absent in the RPA spectrum additionally appear if we include excitonic effects in our simulations. Therefore one can conclude that many body contributions are rather small and that the RPA spectra include all crucial features in the absorption spectrum of GeTe. This is due to the strong screening present in the system. Experimentally, a value of 36 for the electronic dielectric constant is obtained for the trigonal ground state. A further reduction of many-body effects in the system is induced by lattice polarization and the free carriers present in the experimental probes. Thus we can confirm that it is sufficient to consider the RPA spectra to study the correlations between the short range order and the optical properties

as proposed in this section.

In summary we provide an explanation for the change of the optical absorption upon amorphization in PCM's and reveal the reason of differences in the optical properties of GeTe and $GeSb_2Te_4$. The changes in the number of bonds and in the local order upon amorphization result in significant changes of the oscillator strength which in turn result in the unusually pronounced optical contrast between the c-and the a-state. Thus they differ significantly from simple tetrahedral semiconductors such as Si or Ge, which retain the local order in the a-state and therefore exhibit only minor changes in their optical properties. Besides providing fundamentally new insight in the physics of the optical absorption of amorphous materials, our results reveal important trends for a systematic material optimization of phase change alloys. As promising future optical data storage techniques such as the SuperRens-discs [352], will rely on a large optical contrast between the crystalline and the amorphous phase as well, this result also provides a significant contribution for the design of alloys employed in these future data storage devices.

6.2 Chalcopyrites thin-film absorbers for photovoltaic applications*

6.2.1 Introduction

During the past years, copper indium diselenide Cu(In,Ga)(Se,S)$_2$ (CIGS) thin-film solar cells have emerged as a technology that could challenge the current hegemony of silicon solar panels [353]. This is possible thanks to the peculiar optical and structural properties of CIGS, which possess an extraordinary stability under operating conditions [354]. In fact, these compounds conserve to a very high degree their electronic properties in a large non-stoichiometric range and are remarkably insensitive to radiation damage or impurities. This appears to be a consequence of self-healing mechanisms that compensate for the creation of defects [355]. The origin of this unusual behavior is currently unknown, but it is clear that its understanding would pave the way to the tuning of new materials for more efficient photovoltaic energy conversion. In this context, theoretical calculations that can predict and analyze the interplay between structural and electronic properties can give a crucial contribution to the interpretation of numerous experiments which, in this field, is often far from straightforward.

In this section, we are interested in the electronic properties of two paradigmatic CIGS materials: $CuInSe_2$ and $CuInS_2$ (commonly referred to as CIS). Like other ternary chalcopyrites, CIS pure crystals are obtained from the zincblende structure by replacing the Zn cations alternatively with Cu and In. In this way, each anion (Se or S) is coordinated by two In and two Cu atoms, while each cation is tetrahedrally coordinated by four anions. However, the existence of two different cations results in two different bonding lengths $R_{In-(S,Se)}$ and $R_{Cu-(S,Se)}$, leading to two structural anomalies [356]: i) The tetragonal cell exhibits a distortion, defined by the parameter $\eta = c/2a \neq 1$, the ratio between the lattice constants a and c. ii) The ideal zincblende site for the anion is perturbed, yielding a deformation of the anion tetrahedron, which is measured by the anion displacement parameter

$$u = \frac{1}{4} + \left[R^2_{Cu-(S,Se)} - R^2_{In-(S,Se)}\right]/a^2 \neq \frac{1}{4}. \tag{6.2}$$

*Part of this chapter is based on the article:

- *Strong interplay between structure and electronic properties in CuIn(S,Se)$_2$: a first-principle study*, J. Vidal, S. Botti, P. Olsson, J-F. Guillemoles, and L. Reining, Phys. Rev. Lett. **104**, 056401 (2010).

Both structural anomalies are small, but not negligible. The precise experimental determination of the anion displacement u is more difficult than the measurement of the lattice constants a and c due to inhomogeneity of the samples. Indeed, the dispersion of the measured values is very small for the lattice parameters (usually $< 1\%$), while it is significant for the anion displacement ($0.22 < u < 0.235$) [356, 357].

Merino *et al.* [357] reported a relatively narrow spread in the band gap ($\approx 10\%$) as a function of the dispersion of the anion displacement u. Unfortunately, experiments alone are not conclusive, due to the lack of information on the composition and uniformity of the samples. The variation of the band gap as a function of u was also addressed theoretically using DFT [358], in some cases including empirical corrections to get closer to the experimental gap [356, 359]. An uncommonly large variation was found, in of CIS compounds apparent contradiction with the experimentally proved stability of the CIS gap with respect to any kind of damage or perturbation.

However, DFT – the standard tool in modern condensed matter theory – is plagued by two serious shortcomings when applied to these systems: (i) As it is well known, the Kohn-Sham (KS) band gaps of DFT underestimates systematically by 50%–100% the experimental ones. In particular, for CIS compounds the KS band gap is vanishing, in contrast to the experimental values of 1.54 eV and 1.05 eV for $CuInS_2$ and $CuInSe_2$ [360], respectively. On the other hand, *ad hoc* corrections, like the scissor operator, often used to adjust the DFT band gap to the experimental value, are too simplistic to analyze the dependence of the band gap on u. (ii) In spite of this problem, the local density (LDA) or the generalized gradient (GGA) approximations to the exchange and correlation energy of DFT usually yield good structural parameters of semiconductors and insulators. Unfortunately, for CIS, the theoretical range of anion displacements obtained within these approximations($0.215 < u < 0.220$) lies outside the experimental range. It is clear, thus, that to understand the paradox of the band gap dependence on the unit cell deformations in CIS one has to go beyond standard DFT.

In the past years, GW [11] has emerged as an invaluable tool to access the one-electron addition and removal energies, also called quasiparticle energies [361]. In principle, the GW equations have to be solved self-consistently, as both G, the one-particle Green's function, and W, the screened Coulomb interaction, depend on the quasiparticle wave-functions and energies. However, the standard use of this theory, that we will refer to as G_0W_0, starts from a KS calculation, and evaluates perturbatively the quasiparticle corrections to the energy levels ignoring the self-consistent process. This procedure is justified when the KS wave-functions and band structures are already close to the quasiparticle ones. In that case it gives results in good agreement with experiments [362].

In spite of the success of the G_0W_0 approach, it has recently been proved that it is insufficient to describe the physics of many materials containing localized d electrons, such as transition metal oxides [12, 48, 49]. Several strategies have been proposed to solve this problem, following two main lines: (i) Replacing the LDA with a better starting point, *e.g.* exact exchange [53], LDA+U [54], or hybrid-functional approaches [363]; (ii) Using an approximate self-consistent approach [13, 48, 14, 49].

6.2.2 Self-consistent GW calculations

In this work we chose to perform a self-consistent (sc) COHSEX (a static approximation to GW [11]) calculation, followed by a perturbative G_0W_0 step to include the dynamical effects absent in the COHSEX calculation [14]. This method has given excellent results for several transition metal compounds, very close to the quasi-particle self-consistent GW method of Refs. [12, 13], retaining however a relative computational efficiency [14]. Furthermore,

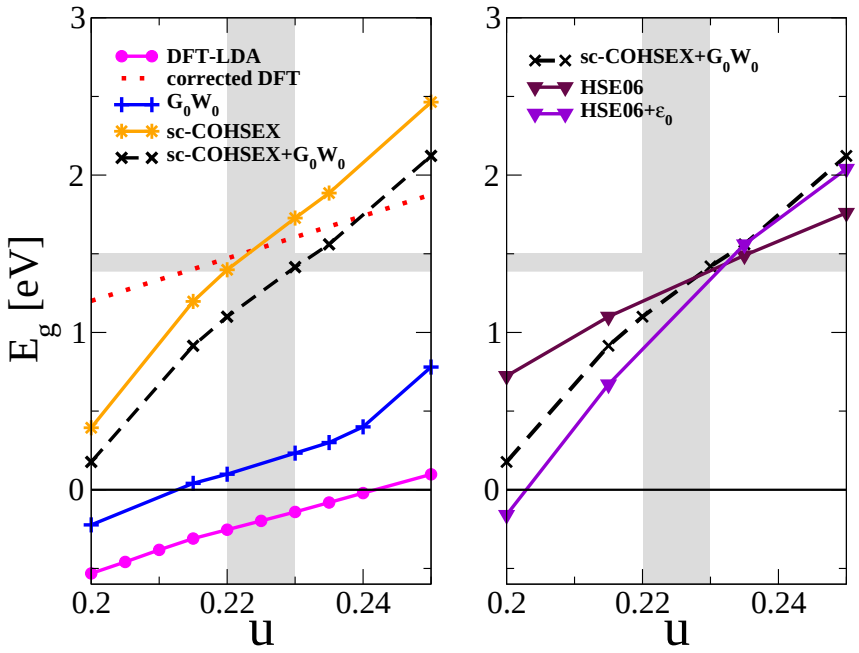

Figure 6.5: Photoemission band gap versus the anion displacement u for $CuInS_2$. The vertical shaded areas give the spread of experimental data for u, while the horizontal shaded areas give the dispersion of measured band gaps. Left panel: calculations using DFT-LDA, G_0W_0, sc-COHSEX, and sc-COHSEX+G_0W_0. The dotted line refer to the previous work of Jiang *et al.* [359]. Right panel: comparison of sc-COHSEX+G_0W_0 and hybrid functional calculations, using HSE06 and a modified HSE06 (see the text).

and unlike some of the strategies listed in (i), our choice does not rely on any non-universal parameter.

In this section we compare calculations of quasiparticle gaps for a range of anion displacements, obtained from state-of-the-art *ab initio* schemes. We performed standard DFT and GWcalculations within the plane-wave scheme implemented in ABINIT [364], using norm-conserving pseudopotentials [239] and including semi-core states in the valence. Our calculated LDA (and GGA) structural parameters and band structures agree with previous results [365, 358, 366]: the anion displacement u is systematically underestimated by 5-10%, and the bottom conduction band overlaps the top valence band, yielding negative band gaps. The negative gap is due to the overestimation of the p-d repulsion [367], which raises the valence band maximum (VBM) beyond the low lying conduction band minimum (CBM), causing a significant hybridization of the CBM with valence states close in energy. Values of u and band gaps in agreement with experiments can be obtained using the Heyd-Scuseria-Ernzerhof (HSE06) [368] hybrid functional as implemented in the Vienna ab initio simulation package (VASP) [315, 240, 369, 370]. In fact, the structural relaxation within this scheme yields u=0.226 (u=0.229) for the ideal monocrystal of $CuInS_2$ ($CuInSe_2$). In real samples, however, there is a dispersion of values of u. As a first step, it is therefore interesting to calculate and analyze the evolution of the gaps as a function of u. To this aim we use *ab initio* schemes that is designed to describe excited states, namely the GWapproximation, as well as hybrid functionals which are also known to yield reasonable band gaps for solids. We varied u in the interval $0.2 < u < 0.25$, that encompasses both experimental and theoretical ranges. After verifying that reasonable variations of the lattice parameters a and c produce negligible changes on the band structure these param-

eters were fixed to their experimental values [371]. In the following we will present only calculations for $CuInS_2$, as we found strictly analogous results for $CuInSe_2$.

The dependence on u of the band gap of $CuInS_2$ is shown in Fig. 6.5. We can see that our KS LDA curve (magenta with filled circles) has the same slope as the theoretical curve (dotted line) obtained by Jiang *et al.* [359] using the LDA corrected by a scissor operator. If we apply the perturbative G_0W_0 approach on top of DFT (blue line with crosses), bands are reordered, reversing the sign of the band gap for $u > 0.215$. In any case, G_0W_0 gaps remain quite small, and the slope of the curve do not change for most of the u-range when compared to the KS results. The slope of the G_0W_0 calculation increases when $u = 0.25$, becoming comparable to the slope of the curves obtained applying a self-consistent approach. This is the only case for which the KS gap is already positive and no band reordering occurs.

The sc-COHSEX procedure (yellow lines with stars) leads to a very different result: the gap enlarges (to values slightly larger than the experimental ones), and also the slope of the curve significantly increases. This is due to the progressive modification in the self-consistent iterations of the unsatisfactory LDA starting point.

Finally, when the sc-COHSEX eigenstates are used as a starting point for a perturbative G_0W_0 calculation (black dashed lines), the band gap gets reduced by a constant value of about 0.3 eV, without affecting the slope of the dependence on u. In particular, we find a band gap in agreement with experimental data for the anion displacement measured for the monocrystal [372]. The important finding to stress is however that according to to our sc-GW calculation small displacements of the S (Se) atoms lead to even larger variations of the gap than those predicted by previous LDA-based calculations.

In order to further investigate this intriguing feature we performed HSE06 calculations for the gaps (maroon line with filled triangles). The outcome is a curve characterized by an intermediate slope between DFT-LDA and sc-GW. The effect of the HSE06 functional is determined by the fixed amount of Hartree-Fock (HF) exchange included:

$$E_{\rm xc}^{\rm HSE06} = E_{\rm xc}^{\rm GGA} + \frac{1}{4}E_{\rm x}^{\rm HF,sr} - \frac{1}{4}E_{\rm x}^{\rm GGA,sr}\,, \tag{6.3}$$

where the exchange term $\frac{1}{4}E_{\rm HF,sr}$ can be seen as an approximated contribution to the self-energy, whose Coulomb interaction is screened by the mixing parameter $\frac{1}{4}$ and the short-range (sr) screening factor, while $\frac{1}{4}E_{\rm x}^{\rm GGA,sr}$ is a screened GGA exchange. In contrast, in a GW calculation the exchange part of the self-energy is screened by the inverse dielectric constant, as a first approximation using the static ε_∞; the latter varies for different values of u. To shed light on this point we performed a series of HSE06 calculations using $\frac{1}{\varepsilon_\infty}$, computed within sc-COHSEX for each value of u, to replace the mixing parameter in front of the screened Hartree-Fock exchange. The resulting curve (violet line with open triangles) has the same slope as the sc-COHSEX curve [1].

Hence, all theoretical results, independently of the level of sophistication, point to large band gap variations. Considering as an upper limit for Δu the range where both theoretical and experimental values are included ($\Delta u \lesssim 0.02$), we conclude that the gap variation $\Delta E_{\rm g}$ due to the anion displacement alone would be $\Delta E_{\rm g} = 32.2 \times \Delta u \approx 0.65$ eV. However, CIS thin films proved to possess stable electronic gaps [357].

[1] Of course, our argument for the use of $1/\varepsilon_\infty$ is purely qualitative. It neglects dynamical effects, lowering of the screening at finite distances, the underestimate of ε_∞ in a sc-COHSEX calculation [13], as well as the fact that HSE06 functional already contains a part of screening. This affects the absolute value of the calculated gaps although various contribution being of opposite sign, the final result is in a reasonable range. However it corrects the most important shortcoming of the hybrid functionals for the comparison of bandgaps namely, the rigid fixing of the effective screening of the non-local Fock part.

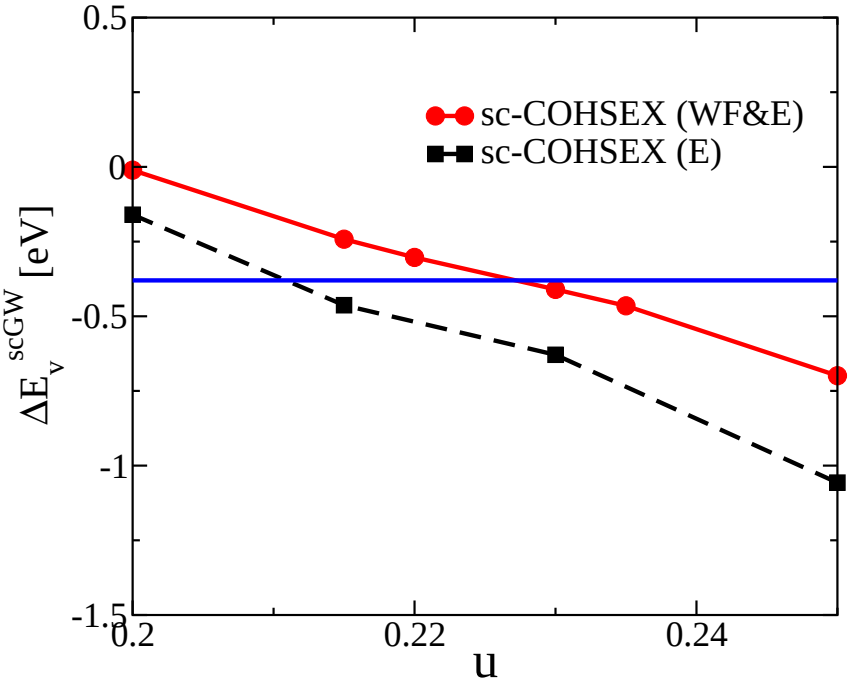

Figure 6.6: The VBM shift ΔE_v of $CuInS_2$ with respect to the LDA band edge versus the anion displacement u. We compare results for sc-COHSEX with self-consistency only in energy (dashed curve) and in both wave functions and energies (continuous curve). The blue horizontal line represents ΔE_v given by DFT+U_d [373] where U is set to 6 eV.

This apparent paradox of band gap stability can be solved by considering also the effect on the band gap due to deviations from stoichiometry, which manifest themselves in high concentrations of defects [354]. Cu vacancies V_{Cu} are shallow acceptor defects, which are known to be present in usual samples, consistently with the observation of p-type conductivity. In particular, V_{Cu} is thought to have very low formation energies [374] compared to other intrinsic defects. It is known that already at the KS level the presence of V_{Cu} opens up the band gap [374, 375], with a larger effect for increasing [V_{Cu}], once again in contradiction with the observed stability of experimental band gaps against stoichiometry deviations. We confirmed this trend by performing G_0W_0 calculations for 16-/32-/64-atom supercells [2], corresponding to concentrations of V_{Cu} in the usual experimental range of off-stoichiometry [357]. The concentration of V_{Cu} is related to the formation energy ΔE_f through a Boltzmann distribution, whose relevant temperature and chemical potentials are set by the growth conditions ($T \approx 500 - 600°C$, copper poor samples) at which defect equilibrium occurs, this equilibrium is moreover assumed to be quenched during the rapid cool down of the samples. However, previous calculations of formation energies were done at the level of DFT and suffer from the unsatisfactory description of the localized states contributing to the VBM. Lany *et al.* [376] proposed to use LDA+U to correct the formation energy as follows:

$$\Delta E_f = \Delta E_f^{LDA} - \Delta E_v^{LDA+U} . \tag{6.4}$$

[2] In particular, as the starting LDA gap of the system with vacancies is already positive, it is enough to perform G_0W_0 calculations to obtain reliable slopes for the variation of the gap versus the concentration of V_{Cu}. This is analogous to what happens in the case of the pure compound when $u > 0.215$ (see Fig. 6.5) where a positive Kohn-Sham gap allows for the correct slope as a function of u already at the G_0W_0 level, despite the underestimation of the gap value.

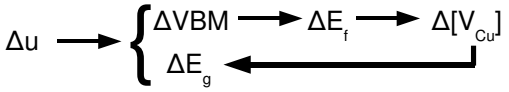

Figure 6.7: Schematic representation of the feedback-loop that stabilizes the band-gap.

We used this idea, evaluating the VBM shift $\Delta \mathrm{E}_v$ within sc-GW. In Fig. 6.6 we show the band edge corrections $\Delta \mathrm{E}_v$ with respect to the KS VBM, calculated using sc-GW and shown for different levels of self-consistency. In this case, $\Delta \mathrm{E}_v$ does not correct a shortcoming of KS theory, but improves on the LDA functional, as the exact exchange-correlation functional would give the exact VBM already within DFT. The VBM shift has a dispersion of around 1 eV in the considered range of u. This dispersion is totally absent in DFT (+U) calculations [373] (horizontal blue line). Note that the shifts are significantly different according to whether both wave functions and eigenvalues or only eigenvalues are updated in the self-consistent procedure.

6.2.3 Analysis of the feedback loop which stabilizes the gap

Following the logic of the feedback loop scheme of Fig. 6.7, we can now prove that would a distortion of the lattice occurs for any reason (e.g. extended defect, axial strain,...) it would actually have little influence on the gap value because of two canceling effects.

Let assume that the band gap is a functional of u and [$\mathrm{V_{Cu}}$] so that $\mathrm{E_g} = \mathrm{E_g(u, [V_{Cu}])}$. Any variation of the band gap $\Delta \mathrm{E_g}$ can be expressed as

$$\Delta E_g = \frac{\partial E_g}{\partial u} \Delta u + \frac{\partial E_g}{\partial [V_{\mathrm{Cu}}]} \Delta [V_{\mathrm{Cu}}], \tag{6.5}$$

where u is the anion displacement and [$\mathrm{V_{Cu}}$] is the concentration of Cu vacancies. The two variables u and [$\mathrm{V_{Cu}}$] are in fact not independent but linked through the variation of the valence band maximum (VBM) induced by variations of u. As presented in the manuscript, in the case of a shallow acceptor, its formation energy should be corrected by the correct position of the VBM as

$$\Delta E_{\mathrm{f}}(u) = \Delta E_{\mathrm{f}}^{\mathrm{DFT}} - \Delta \mathrm{E}_v^{\mathrm{sc}GW}(u)\,. \tag{6.6}$$

Indeed, shallow acceptors are supposed to behave like the VBM due to their proximity to it. This has been the common strategy used for the past 20 years in order to correct formation energies (see, e.g., Ref. [376]). Then, it is possible to relate the concentration of $\mathrm{V_{Cu}}$ to the formation energy through a Boltzmann distribution as

$$[\mathrm{V_{Cu}}] = \mathrm{N_{Cu}} \mathrm{e}^{\frac{-\Delta \mathrm{E_f}}{\mathrm{k_B T}}}\,, \tag{6.7}$$

with T being the growth temperature for which the diffusion of defects is quenched ($T \approx 500 - 600^\circ$ C). Moreover, high concentrations of $\mathrm{V_{Cu}}$ can significantly enlarge the band gap. Thus, any variation of u can change both the band gap and the formation energy of $\mathrm{V_{Cu}}$, and as a consequence vary the concentration of $\mathrm{V_{Cu}}$ which will change the band gap accordingly. Overall the effects of u and $\mathrm{V_{Cu}}$ seem to cancel each other.

We have identified Cu vacancies as the most likely defect to play a role in the stabilization of the gap. For the neutral defect $\mathrm{V_{Cu}}$, the formation energy ΔE_f depends on the chemical potentials μ:

$$\Delta E_f = E_{\mathrm{tot}}(V_{\mathrm{Cu}}) - E_{\mathrm{tot}}(\mathrm{CIS}) + \mu_{\mathrm{Cu}}^{\mathrm{solid}} + \mu_{\mathrm{Cu}}\,, \tag{6.8}$$

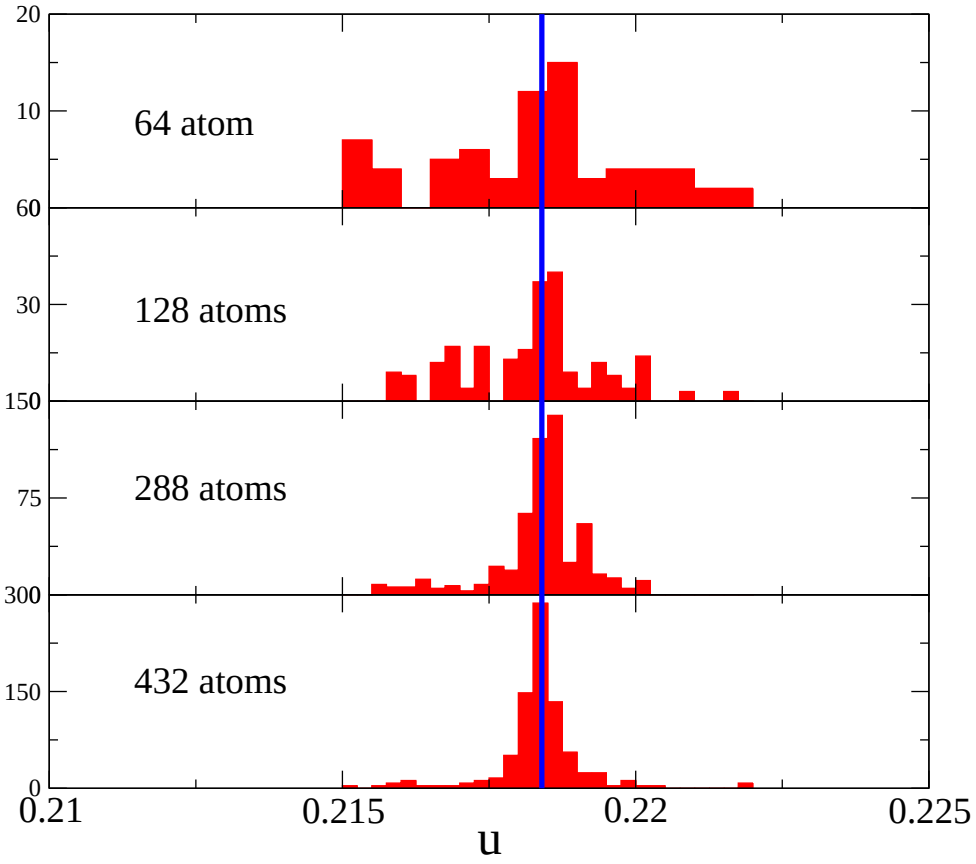

Figure 6.8: Distribution of *local* u's depending on the size of the supercell of V_{Cu}:$CuInS_2$. The blue line refers to the value of u for the perfect crystal relaxed in GGA.

where $E_{\rm tot}(\mathrm{V_{Cu}})$ and $E_{\rm tot}$(CIS) are respectively the total energy of the CIS supercell with and without $\mathrm{V_{Cu}}$, $\mu_{\rm Cu}^{\rm solid}$ is the total energy of the ground-state solid Cu and $\mu_{\rm Cu}$ is the chemical potential of Cu that depends on the growth conditions. The latter is set to -0.6 eV that corresponds to experimental observations in the case of Cu poor growth conditions. Moreover, we performed ground-state calculations in DFT-GGA for 432-atom supercells in order to calculate the difference of total energies. The resulting formation energy of neutral $\mathrm{V_{Cu}}$ is 0.1 eV, which yields a concentration $[\mathrm{V_{Cu}}] \approx 5\ 10^{20}\,\mathrm{cm}^{-3}$ at $T = 600^\circ$ C. This numerical value matches the size of the supercell used to simulate different concentration of defects. Therefore, the Boltzmann distribution is valid for the range of concentrations we are interested in.

The next step consist in asking if the creation of a Cu vacancy does modify the lattice distortion. Indeed, we assume that u can act on the concentration of Cu vacancies: but does $\mathrm{V_{Cu}}$ induce changes in the value of u? Of course, the presence of a Cu vacancy produces a void in the crystal, that result in the inward relaxation of the neighboring anions. Besides, the crystal loses all chalcopyrites symmetries, which can ensue long range structural changes. In order to assess this problem, we extracted the distribution of *local* u's from a relaxed 64-atom supercell with one $\mathrm{V_{Cu}}$. The anion displacement is defined as a *local* quantity: each anion is surrounded by 4 cations (2 Cu and 2 indium), resulting in two In-S and two Cu-S bonds. In the case of a perfect crystal, the bond lengths are equal for each anion-cation pair of the same type, resulting in one unique u. However, in a supercell with a defect these bond lengths change. One can then define for each anion, 4 different values of u. Figure 6.8 shows the distribution obtained with a GGA relaxation for different supercell sizes. The distribution presents a mean value close to the theoretical u of the perfect crystal, u=0.2184, and the standard deviation decreases with increasing supercell sizes. Furthermore, additional contributions appear at small and large values of u ($u < 0.216$ and $u > 0.219$). They originate from the region around the vacancy.

We can conclude that $[\mathrm{V_{Cu}}]$ has only a mild effect on the anion displacement except in a region localized around the Cu vacancy. We can therefore simplify Eq. (6.5) by assuming that u is not a function of $[\mathrm{V_{Cu}}]$ and that $[\mathrm{V_{Cu}}]$ is an exclusive function of u. Therefore, Eq. (6.5) can be rewritten as

$$\begin{aligned} \Delta E_g &= \left\{ \frac{\partial E_g}{\partial u} + \frac{\partial E_g}{\partial [V_{\rm Cu}]} \frac{d[V_{\rm Cu}]}{du} \right\} \Delta u \\ &= \left\{ \frac{\partial E_g}{\partial u} + \frac{\partial E_g}{\partial [V_{\rm Cu}]} \frac{[V_{\rm Cu}]}{\mathrm{k_B T}} \frac{d\Delta E_v^{\rm scGW}}{du} \right\} \Delta u \,. \end{aligned} \tag{6.9}$$

Let us go back now to the issue of the variation of the band gap as a function of the concentration of Cu vacancies. For very high doping in standard semiconductors, a shrinkage of the band gap is usually observed. In the case of CIS, where $\mathrm{V_{Cu}}$ plays the role of doping, this trend is not observed theoretically. Instead a large opening of the band gap occurs, either using DFT or more advanced methods like GW. This has been attributed to the relaxation of the *p-d* repulsion forming the top of the valence bands. We performed G_0W_0 calculations on supercells whose size ranges between 16 and 64 atoms. These supercell sizes correspond to 25% (16 atoms), 12% (32 atoms) and 6% (64 atoms) deviations of stoichiometry. Polycrystalline thin-film $\mathrm{CuIn_{1-x}Ga_xSe_2}$-based (CIGS) record solar cells recently synthesized present a compositional window in terms of atomic content ratio of the metals of $0.88 < \mathrm{Cu/(In + Ga)} < 0.95$ [353]. In [357] this value goes down to $\mathrm{Cu/In} \approx 0.77$.

The exact relation between E_g and $[\mathrm{V_{Cu}}]$ is not known. However, using a logarithmic scale, we found a linear dependence of E_g on $[\mathrm{V_{Cu}}]$. We can then perform a linear regression

as shown in Figure 6.9:

$$E_g = 0.231 \times \ln\left(\frac{[\mathrm{V_{Cu}}]}{\mathrm{N_{Cu}}}\right) + 1.67\,, \tag{6.10}$$

$$\frac{\partial E_g}{\partial [V_{\mathrm{Cu}}]} = \frac{0.231}{[V_{\mathrm{Cu}}]}\,. \tag{6.11}$$

This simple formulation of the partial derivative of E_g with respect to $[\mathrm{V_{Cu}}]$ allows to simplify further Eq. (6.9):

$$\Delta E_g = \left\{ \frac{\partial E_g}{\partial u} + \frac{0.231}{\mathrm{k_B T}} \frac{d\Delta E_v^{\mathrm{sc}GW}}{du} \right\} \Delta u\,. \tag{6.12}$$

In order to evaluate the variation of ΔE_g with and without the feedback, we needed to evaluate numerically the last two partial derivatives. The variations of respectively E_g and $\Delta E_v^{\mathrm{sc}GW}$ are almost linear with respect to u. To perform the linear regression we chose a restricted range of values of u that encompasses both the theoretical and the experimental values, i.e. [0.215-0.235]. In that way we obtained:

$$\Delta E_g = 32.2 \times \Delta u \text{ without feedback loop}\,, \tag{6.13}$$

$$\Delta E_g = -1.9 \times \Delta u \text{ with feedback loop at T=600°C}\,. \tag{6.14}$$

Considering a variation of $\Delta u = 0.02$, the band gap will change by 0.65 eV without feedback loop and by only -0.038 eV with the feedback loop (at T=600° C). It is the opposite sign of the two interplaying terms of Eq.(6.5) that stabilizes the band gap, making it understandable why large deviations from stoichiometry can have innocuous effects in CIS materials.

In conclusion, we have analyzed the dependence of the band gap and band edge shifts $\Delta \mathrm{E_v}$ of In based chalcopyrites on the internal displacement parameter u. We have found that this dependence, predicted within DFT, was strongly underestimated. Furthermore, we have demonstrated the necessity of using a self-consistent numerical scheme based on many-body perturbation theory to fully capture the structural dependence of the band gap. The HSE06 hybrid functional gives a satisfactory description of the electronic properties of CIS at a reduced cost. However in order to evaluate important trends correctly, the parameter which controls the amount of Fock exchange should be allowed to vary proportionally to the electronic screening. Finally, we explained the relative stability of the experimental band gap in realistic conditions through a coupled process between defect formation and structural relaxation. This suggestion is consistent with both the prediction of very low formation energies for $\mathrm{V_{Cu}}$ and experimental samples showing p-type conductivity with very high intrinsic defect concentration.

6.3 Delafossite transparent conductive oxides*

6.3.1 Introduction

Many high-technology devices, such as flat panel displays, touch screens, or even thin-film solar cells, require the use of thin transparent contacts. These contacts are usually built from insulating oxides that, for a certain range of doping, become conductive while

*Part of this chapter is based on the article:

- *Effects of electronic and lattice polarization on the band structure of delafossite transparent conductive oxides*, J. Vidal, F. Trani, F. Bruneval, M. A. L. Marques and S. Botti, Phys. Rev. Lett.(2010).

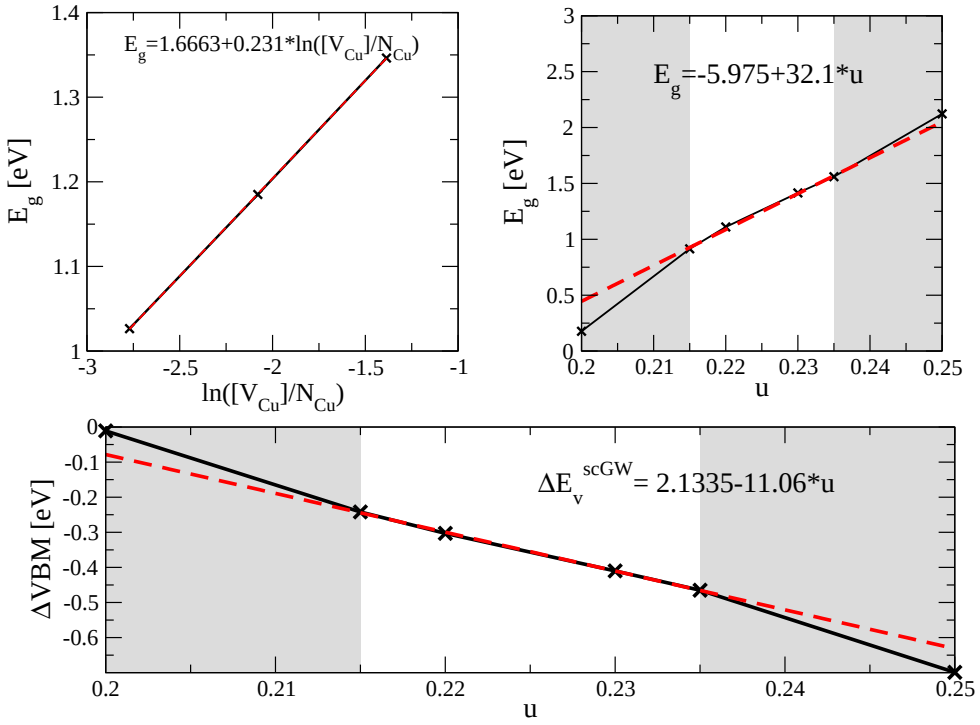

Figure 6.9: Top left panel: Value of the band gap of $CuInS_2$ calculated in G_0W_0 versus the concentration of Cu vacancies. Top right panel: Value of the band gap of $CuInS_2$ calculated in scGW versus the anion displacement. Bottom panel: $\Delta E_v^{\mathrm{sc}GW}$ of $CuInS_2$ versus the anion displacement.

retaining transparency in the visible spectrum. The most common examples of these so-called transparent conductive oxides (TCOs) are electron (n-)doped SnO_2, In_2O_3, and ZnO. Hole (p-)doping of wide gap semiconductors was for long time very hard to obtain [377, 378]. It is therefore not surprising that the discovery of p-doping in $CuAlO_2$ thin films with a carrier mobility of about $10\,\mathrm{cm}^2/(\mathrm{V\,s})$ attracted great interest [379, 380]. Other members of the delafossite family, like $CuGaO_2$ [381] and $CuInO_2$ [382], were discovered shortly after. The latter compound is particularly interesting as it exhibits bipolar (n- *and* p-type) conductivity by doping with appropriate impurities and tuning the film-deposition conditions [382]. This opens the way to the development of transparent p-n junctions, and therefore fully transparent optoelectronic devices.

$CuAlO_2$ is by far the most studied system of the family of delafossite TCOs, both theoretically and experimentally. However, there is still no agreement neither on the origin of the p-type conductivity, nor on the electronic bands of the pure crystal. Measurements of the direct *optical* band gap ($E_{\mathrm{g}}^{\mathrm{dir}}$) of $CuAlO_2$ fall in the range from 2.9 to 3.9 eV [379, 380, 383, 384, 385, 386, 387, 388, 389, 390, 391, 392, 393], with most values in the interval 3.4–3.7 eV. These experiments also yield a large dispersion of indirect gaps ($E_{\mathrm{g}}^{\mathrm{ind}}$), from 1.65 to 2.1 eV, with one experiment measuring 2.99 eV [393]. Unfortunately, there is only one photoemission experiment [383] that gives a value of 3.5 eV for the *quasiparticle* band gap. Note that the *optical* and *quasiparticle* gaps differ by the exciton binding energy. Concerning $CuInO_2$, optical experiments measured $E_{\mathrm{g}}^{\mathrm{dir}}$ between 3.9 and 4.45 eV [382, 394, 395], with only one estimation of $E_{\mathrm{g}}^{\mathrm{ind}}$ at 1.44 eV [395].

From the theoretical perspective, the situation is also quite complex, even if the full Cu $3d$ shell should exclude the strongly correlated electron regime. These materials are

usually studied within DFT, using the standard local density (LDA) or generalized gradient approximations (GGA). However, it is well known that the Kohn-Sham band structures systematically underestimate the band gaps. For similar compounds, like Cu_2O and $CuIn(S,Se)_2$, Kohn-Sham LDA calculations lead to unreasonable band structures, in particular due to the misrepresentation of the hybridization between the d electrons of the metal and p electrons of the anion [48, 50]. To overcome this situation, hybrid functionals have been recently proposed, with very promising results [396], especially for materials with small and intermediate band gaps [397, 398]. Other approaches include LDA+U, that tries to improve the description of electronic correlations through the introduction of a mean-field Hubbard-like term. This method has been quite successful in the study of the electronic structure of strongly correlated systems, but it relies on a parameter U, that is often adjusted to experiments.

Arguably the most reliable and used *ab initio* technique to obtain quasi-particle band structures is the many-body GW approach [11]. The common practice within this framework is to start from a DFT calculation, and evaluate perturbatively the GW energy corrections to the band structure. This procedure, which we will refer to as G_0W_0, is justified when the departure wave functions and band structure are already close to the quasiparticle ones. This is indeed the case in many systems, explaining why G_0W_0 has been extremely successful in describing electron addition and removal energies for metals, semiconductors and insulators [361]. However, it has been recently shown that G_0W_0 fails for many transition metal oxides [48, 49].

To solve this problem one can perform (restricted) self-consistent (sc) GW [12, 13]. This technique has the advantage of being independent of the starting point at the price of large computational complexity. Fortunately, there is an alternative procedure that yields wavefunctions that are extremely close to those obtained in a full sc-GW calculation, namely sc-COHSEX as explained in Ref. [14]. The dynamical effects that are absent in COHSEX calculations can then be accounted for by performing a final perturbative GW step. This method, that we will refer to as sc-GW, has been applied to many oxide compounds, yielding excellent results for the band gaps and the quasiparticle band structure [48, 14, 49, 50].

Note that these theoretical techniques yield quasiparticle bands, and not optical gaps. To evaluate these latter quantities one mostly resorts to the solution of the Bethe-Salpeter equation. For the delafossite structures there is one such calculation starting from a GGA+U band structure [399]. It yields for $CuAlO_2$ a very large exciton binding energy of about 0.5 eV for the first direct transition. The choice of the parameter U was found to have significant consequences on the width of the band gap, but it did not affect significantly the exciton binding energy. We can thus assume that 0.5 eV is a reasonable estimate of this latter quantity.

6.3.2 Accurate calculations of band structures

In the following, we present calculations of the band structures of $CuAlO_2$ and $CuInO_2$ using some of the most accurate theoretical tools available in the community. These include the standard LDA, hybrid functionals (namely B3LYP [400] and two flavors of Heyd-Scuseria-Ernzerhof, HSE03 and HSE06 [368, 401]), LDA+U, G_0W_0 and sc-GW. As discussed above, we expect sc-GW to be the most accurate *ab initio* approach. When the comparison was possible, we found our results in excellent agreement with previous calculations (Refs. [383, 392, 393, 402, 403, 404, 405] for LDA, Ref. [405] for B3LYP, and Ref. [406] for GGA+U).

The hybrid and LDA+U calculations were performed with VASP [315, 240] and ABINIT [182] respectively, using the PAW formalism and an energy cutoff of 44 Ha. The

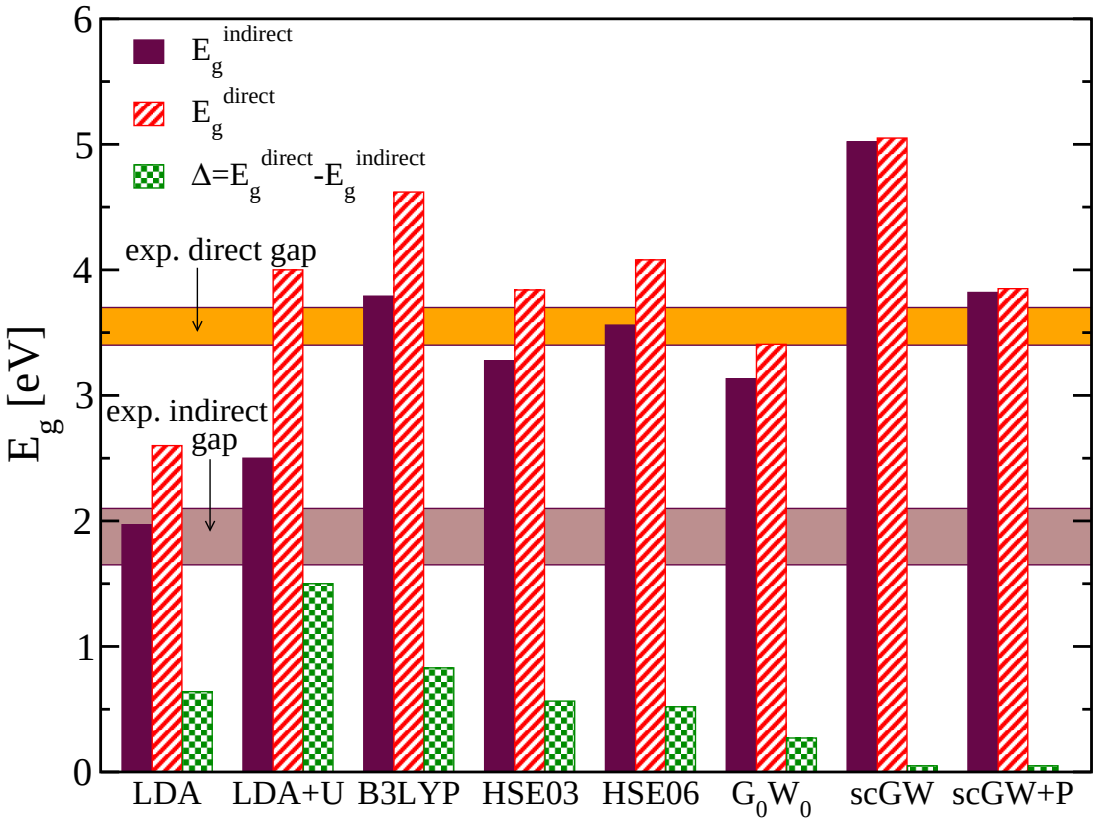

Figure 6.10: (Color online) Band gaps of $CuAlO_2$ using: LDA, LDA+U, hybrid, G_0W_0, sc-GW, and sc-GW including model polaronic corrections. The horizontal zones contain data extracted from various optical experiments (see text).

parameter U was set to 8 eV as in Ref. [399]. Our GW calculations were performed with ABINIT, starting from LDA band structures and using norm-conserving pseudopotentials with semicore states (3s and 3p for Cu and 4s and 4p for In) included in the valence. The energy cutoff was 120 Ha for the ground state calculation, and the k-point grid was a $4\times4\times4$ Monkhorst-Pack. Note that it was absolutely essential to use the method of Ref. [187], due to the extremely slow convergence with respect to the number of conduction states.

In Figs. 6.10 and 6.11 we show direct and indirect photoemission gaps and the band structures of $CuAlO_2$, obtained using different theoretical approaches. The minimum E_g^{dir} of $CuAlO_2$ is always found at L, where the dipole transition between the band edge states is allowed [404]. All calculations, except sc-GW, give a fundamental E_g^{ind} between the conduction band minimum at Γ and the valence band maximum along the Γ-F line. The experimental data for optical gaps are also presented with an error bar that reflects the dispersion of the most likely values found in literature. LDA exhibits, as expected, the smallest gaps. Basically every approach beyond it opens up the gap by different amounts and modifies the band dispersions. The direct and indirect gaps have similar behaviors in the different theories, and both increase when going from LDA<G_0W_0<HSE03<HSE06<B3LYP<sc-GW. On the other hand, the difference $E_g^{dir} - E_g^{ind}$ seems to decrease with the sophistication of the method, reaching nearly zero for the sc-GW calculation. This is a consequence of the drastic change of the conduction band dispersion, which displaces the conduction minimum from Γ to L when sc-GW is applied (see Fig. 6.11). Only LDA+U does not follow the trend, as it is the only case in which $E_g^{dir} - E_g^{ind}$ gets significantly larger than in LDA.

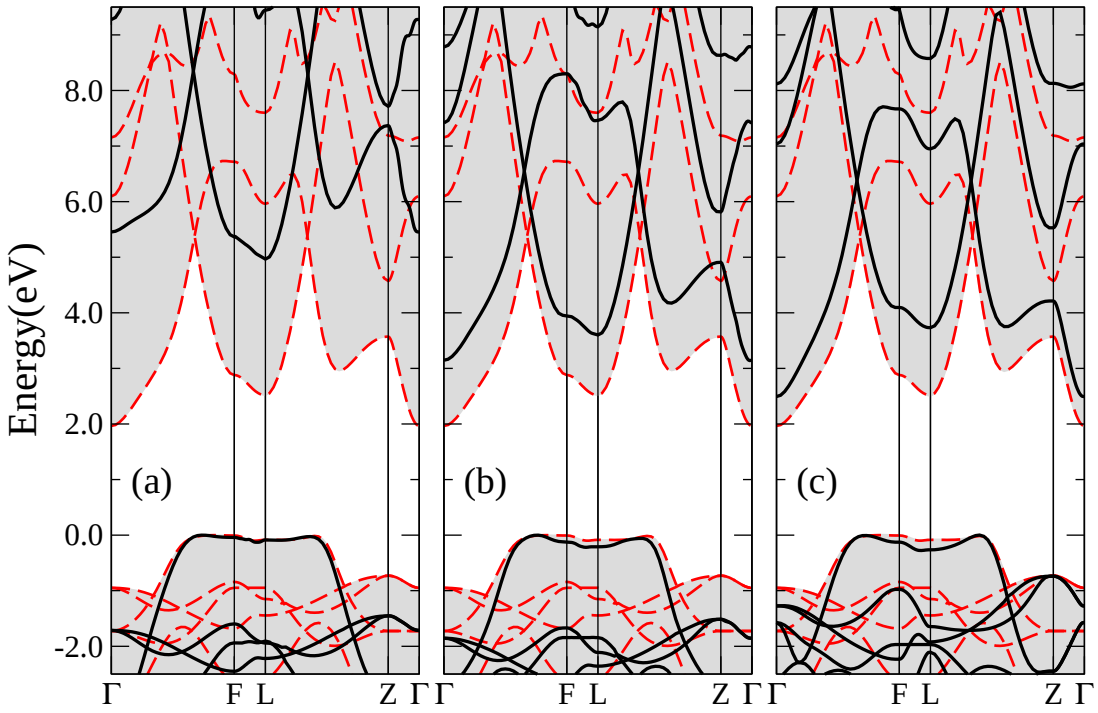

Figure 6.11: (Color online) Band structures for $CuAlO_2$: comparison of LDA (red dashed lines) with sc-GW (a), HSE03 (b), and LDA+U (c).

Looking at the direct gap, we point out that most of the methods give results that are within the experimental range, when an exciton binding energy of around 0.5 eV [399] is considered. This is true for LDA+U, G_0W_0, the hybrids HSE03 and HSE06. However, for sc-GW and even for B3LYP, the theoretical gap is larger by about 1–1.5 eV than the experimental findings. For $CuInO_2$ (see Fig. 6.12) we have to make the comparison with care, as the smallest E_g^{dir} is located at Γ, where optical transitions are forbidden [404]. A meaningful comparison with experiments must consider the gap at L. Thus, we find that both trends and quantitative results are analogous to those for $CuAlO_2$. In particular, sc-GW yields again E_g^{dir} larger by 1–1.5 eV than the experimental range.

We stress again that, to date, sc-GW is arguably the best method available to estimate band gaps of wide-gap semiconductors, and that it gives excellent results for compounds like Cu_2O and $CuIn(S,Se)_2$ [48, 50]. It is unlikely that the presence of defects can lead to such a large shrinkage of E_g^{dir}. However, there is another effect that has been neglected up to now: the change of screening due to the polarization of the lattice. The polaron constant defined as $\alpha_P = (1/\epsilon_\infty - 1/\epsilon_0)(\hbar/2ma_B^2\omega_{LO})^{1/2}$, where a_B is the Bohr radius, ω_{LO} the longitudinal optical frequency of the highest E_u phonon mode, ϵ_∞ and ϵ_0 the low frequency electronic and the static dielectric constants, respectively, measures the strength of the polaronic effect. According to the experimental data [407], unfortunately available only for $CuAlO_2$, the polaron constant for this system is large ($\alpha_p \sim 1$), indicating a non-negligible contribution of the lattice polarization to the electronic screening. It is known that in other ionic compounds with similar polaron constants this can lead to a shrinkage to the band gap by about 1 eV [408]. A full sc-GW calculation including in an *ab initio* framework the effects of the lattice polarization is to date beyond reach. However, a reliable estimate can be obtained using the model proposed by Bechstedt *et al.* [408], which gives a static representation of the polaronic effects based on difference of experimental static dielectric constants. By performing a perturbative GW step including model polaronic effects on

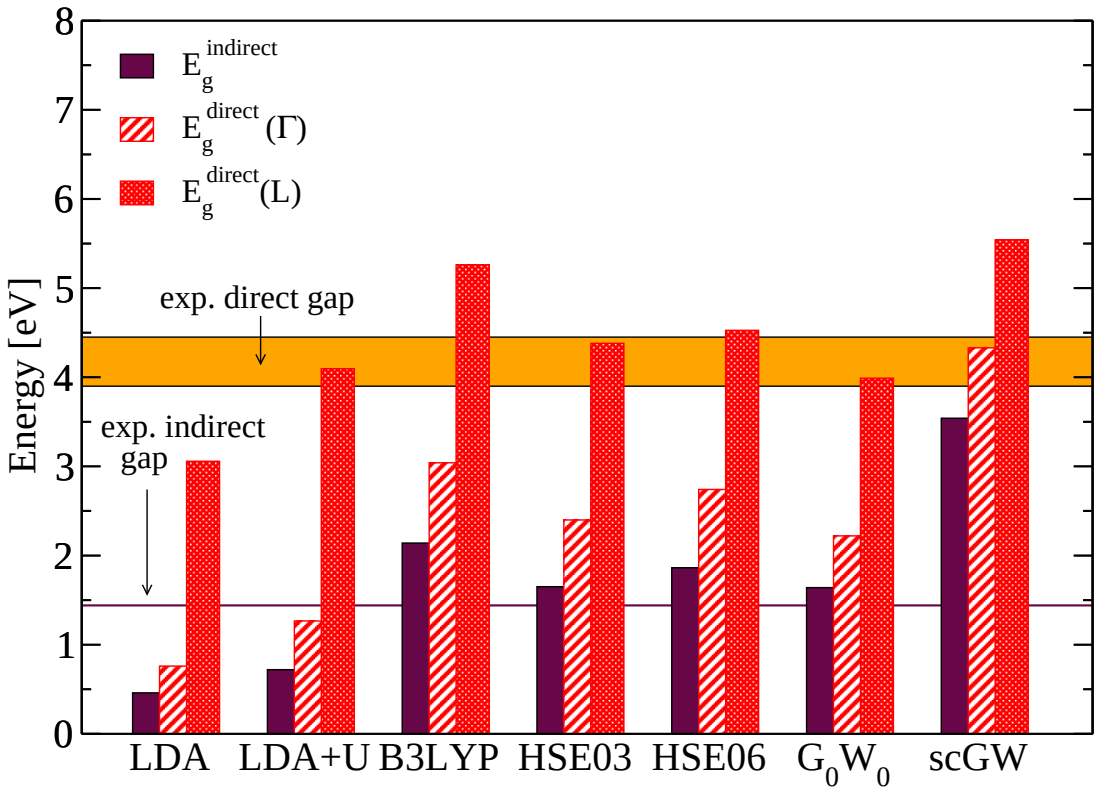

Figure 6.12: (Color online) Band gaps of $CuInO_2$ using: LDA, LDA+U, hybrid, G_0W_0, sc-GW. The horizontal zones contain data extracted from optical experiments (see text).

top of the sc-COHSEX, we found a uniform (k-independent) shrinkage of the band gap by 1.2 eV. As we can see in Fig. 6.10, this correction brings our results for E_g^{dir} well within the experimental range (once the excitonic correction of about 0.5 eV is also considered). As it is observed in Ref. [408], the polaronic model employed can only overestimate the correction. All these results point to the conclusion that the agreement of the other methods with experiment was fortuitous and due to a cancellation of errors.

Looking now at the indirect gap, we focus on Fig. 6.10 as there are more experimental data for $CuAlO_2$. All the hybrids and GW calculations yield indirect gaps much larger than the experimental range 1.65–2.1 eV, even taking into account any possible excitonic and polaronic effects. Moreover, sc-GW, the best method used in this work, yields the highest E_g^{ind} at around 5 eV, while the difference $E_g^{dir} - E_g^{ind}$ is in general much smaller than the experimental value ($\approx$2 eV), and even vanishing for the sc-GW calculation. From Fig. 6.12 we realize that these conclusions are as well valid for $CuInO_2$, where the best estimates for the indirect band gap is much larger than the experimental value of 1.44 eV [395].

These are very strong arguments in favor of Robertson *et al.* [405] that suggested that the experimental "indirect gap" absorption was due to defects, and should not be present in the defect-free compound. Also Pellicer Porres *et al.* [393] questioned the interpretation of the low energy peaks as indirect transitions, as the absorption coefficient is more than two orders of magnitude larger than in typical indirect absorption edges. The most promising defects that could be responsible are oxygen interstitials O_i, as DFT calculations within the LDA predict low formation energies and the introduction of states in the gap at 0.7 and 1.4 eV [409]. However, a full clarification of this issue will require sc-GW or hybrid calculations for these, and other more complex defects.

Finally, we analyze more in detail the band structures of $CuAlO_2$ shown in Fig. 6.11. LDA calculations (red dashed lines) are compared with sc-GW, HSE03, and LDA+U calculations. The main effect of LDA+U is to open the LDA gap by an amount that can be controlled by the parameter U. The difference $E_g^{dir} - E_g^{ind}$ is in this approximation enhanced, due to a change of the character of the lowest conduction band along the symmetry lines. Hybrid calculations using HSE03 give a comparable E_g^{dir} and a modified dispersion of both valence and conduction states close to the Fermi energy, which reduces $E_g^{dir} - E_g^{ind}$. The conduction band minimum (CBM) within HSE03 is still located at Γ, but the difference between the CBM at L and Γ gets significantly smaller. For sc-GW, besides the further increase of the band gaps, the dispersion of the bands is strongly affected by the many-body effects. In fact, the GW corrections exhibit an unusual dispersion of around 1 eV when looking at the different k-points, displacing the CBM from Γ to L. We note that often in semiconductor physics one assumes that the quasiparticle corrections can be modeled by a rigid shift (the so-called scissor operator). From our results it follows that one should refrain from using this simple approximation for these important materials. We can also conclude that hybrid calculations give a better description of band dispersions than LDA+U, even if the two approaches yield similar band gaps.

In conclusion, it is clear that the delafossite family exhibits complex and unusual band gap physics that can not be captured by standard theoretical approximations. We found that the direct band gap is well reproduced by the best many-body approaches if polaronic effects are taken into account. We can expect that this situation, of a large gap that is reduced substantially by polaronic effects, is quite general and is present in many more materials that previously expected. In fact, the apparent good agreement between calculated gaps (with hybrid functionals or G_0W_0) and experimental gaps for materials as simple and widely studied as LiF can be accidental, as preliminary calculations confirm: the underestimation of the gap by these methods (the scGW gap is indeed 2 eV larger than the experimental and G_0W_0 gap) is compensated by the neglect of large polaronic effects. Furthermore, the modifications with respect to the LDA Kohn-Sham bands are strongly $\boldsymbol{k}$-dependent, which makes questionable the common practice of using a scissor operator. The band dispersion obtained by hybrid functional calculations is in between the LDA and sc-GW dispersion, while the LDA+U calculations open up the gap but do not give a significant improvement of the band dispersion. Finally, our calculations rule out the interpretation of the low energy features in the absorption spectra as arising from a putative indirect band gap. These structures should rather come from intrinsic defects, as proposed in Refs. [393, 405]. However, a complete understanding of the electronic and excitation properties of these systems will only be achieved, in our opinion, by a high-level theoretical scheme (like sc-GW) including defects and effects from the lattice polarization in an ab initio framework. Work along these lines is in progress.

Chapter 7

Van der Waals interactions*

7.1 Introduction

The van der Waals interaction is a common presence in the worlds of physics, chemistry, and biology. It is a dispersive force that acts even between neutral bodies at large separations, and that results from the non-zero dipole-dipole attraction stemming from transient quantum dipole fluctuations. It is the interplay between the electrostatic and dispersive interactions that determines many interesting phenomena in nature, even in the macroscopic world. In fact, it is van der Waals interactions that are responsible for the remarkable ability of geckos to hold to surfaces.

But the realm of van der Waals forces, being quantum in nature, is the world of atoms and molecules — the nano world. In fact, these forces determine the structure of DNA molecules and the folding and dynamics of proteins, the orientation of molecules or nanostructures on surfaces, etc. They are also key ingredients in the building and functioning of many of the systems relevant for the emerging fields of nanotechnology and biotechnology. It is therefore not surprising that the number of theoretical studies of van der Waals interactions in these systems, has been steadily increasing over the past year. At the same time, the tools used in these studies have increased sophistication and precision.

In this Chapter, we give a step forward and present fully ab-initio calculations of the van der Waals coefficients for the interaction between nanostructures and between these nanostructures and surfaces.

The calculation of van der Waals dispersion forces can be a challenging problem [410, 411]. Three regimes have to be distinguished, according to the distance that separates the interacting molecules:

(i) *short distances*, such that there is non-negligible overlap of the electronic clouds of the two molecules. This is the most difficult situation, since it requires, in principle, a *supermolecule* calculation, i.e. the treatment of the two molecules combined together as a single entity. The valid approaches in this overlapping regime (and therefore also valid in the non-overlapping regime) are sometimes called seamless van der Waals techniques. Numerous possibilities exist, although none of them entirely satisfactory: full configura-

*This chapter is based on the articles:

- *Efficient calculation of van der Waals dispersion coefficients with time-dependent density functional theory in real time: application to polycyclic aromatic hydrocarbons*, M. A. L. Marques, A. Castro, G. Malloci, G. Mulas, and S. Botti, J. Chem. Phys. **127**, 014107 (2007).
- *Ab initio calculation and modelling of van der Waals interactions between nanostructures and surfaces*, S. Botti, A. Castro, X. Andrade, A. Rubio, and M. A. L. Marques, Phys. Rev. B **78**, 035333 (2008).

tion interaction for very small molecules [412, 413], Møller-Plesset perturbation theory [414] or Monte Carlo methods [415, 416]. Attempts to use ground state density functional theory (DFT) are specially challenging [410, 411]; In the realm of time-dependent density-functional theory (TDDFT), the recent work of Dobson [417] summarizes the current research, largely based on the adiabatic connection / fluctuation dissipation theorem. Dispersive forces can also be added to standard DFT through empirical correction terms. These, however, require the previous knowledge of the C_6 van der Waals coefficients (see below), often roughly estimated from the atomic C_6's [418]. In the present work we will not consider this regime.

(ii) *long distances*, such that we can neglect the overlap. In this case, the electrons belonging to different molecules are distinguishable, and one can isolate the Coulomb operator that corresponds to interactions between electrons of different molecules, and apply (second order) perturbation theory for this operator [419]. The first term in the perturbative expansion of the interaction energy decays as $-C_6/R^6$, where R is the intermolecular distance.

(iii) *very long distances*, such that retardation effects become important [420]. This means that the time it takes for the photons that mediate the electromagnetic interaction to travel between the two molecules is not negligible. Retardation is described by a correction factor that is equal to unit for small distances and proportional to $1/R$ for large distances.

The knowledge of the various static and dynamic multipole polarizabilities at imaginary frequencies suffices to compute the van der Waals interaction in the regimes (ii) and (iii). These response functions can be calculated within a variety of quantum chemical methods, typically through the evaluation of a wide range of excitation energies and associated transition matrix elements. Alternatively, at a lower computational cost, we can use time-dependent density-functional theory (TDDFT). The first calculation of C_6 coefficients using TDDFT was performed in 1995 by van Gisbergen et al. for a variety of small molecules [421].

7.1.1 Interaction between two finite systems

When both the wave-functions overlap and retardation effects are almost null [situation (ii)], the application of second order perturbation theory leads to an expansion of the interaction energy with respect to the inverse of the intermolecular distance $(1/R)$:

$$\Delta E(R) = -\sum_{n=6}^{\infty} \frac{C_n}{R^n} \,. \tag{7.1}$$

The coefficients C_n are usually called Hamaker constants [422]. The leading non-null term C_6 is due to the dynamic dipole-dipole polarizability. The odd terms until $n = 11$ are also null for spherical molecules (or if an average over relative orientations is taken), if we neglect retardation effects. In principle, the coefficients also depend on the relative orientation of the molecules.

The C_6^{AB} dispersion Hamaker constant for a pair of molecules A and B, averaged over all possible relative orientations, is related to the dipole molecular polarizability through the Casimir-Polder relation:

$$C_6^{AB} = \frac{3}{\pi} \int_0^{\infty} \mathrm{d}u \; \alpha^{(A)}(\mathrm{i}u) \; \alpha^{(B)}(\mathrm{i}u) \,, \tag{7.2}$$

where $\alpha^{(X)}(\mathrm{i}u)$ is the average of the dipole polarizability tensor of molecule X, $\boldsymbol{\alpha}^{(X)}$, evalu-

ated at the complex frequency $\mathrm{i}u$:

$$\alpha^{(X)}(\mathrm{i}u) = \frac{1}{3}\mathrm{Tr}[\boldsymbol{\alpha}^{(X)}(\mathrm{i}u)]\,. \tag{7.3}$$

It should be noted that: (i) If we fix the relative orientation of the molecules, the orientation dependent Hamaker constant can also be calculated from the $\boldsymbol{\alpha}$ tensors, considering the appropriate linear combination of their components; (ii) higher order Hamaker constants, useful for shorter distances, can be obtained through the use of analogous formulae involving higher order multipole polarizability tensors. The expressions accounting for these two generalizations can be found, for example, in Ref. [419]. The calculations presented below are solely concerned with Eq. (7.2); however we wish to stress that the methodology trivially yields full polarizability tensors of arbitrary order, hence providing the possibility to tackle those general cases, with almost no extra computational cost.

On the other hand, when the distance increases and retardation effects become important, the van der Waals interaction depends solely on the static polarizability [420, 423, 424], decaying as $\Delta E(R) = -K^{AB}/R^7$, where the constant is

$$K^{AB} = \frac{23c}{8\pi^2}\alpha^{(A)}(0)\;\alpha^{(B)}(0)\,, \tag{7.4}$$

where c is the velocity of light in vacuum.

7.1.2 Interaction between a finite system and a non-metallic surface

In this case, the leading term of the expansion of the van der Waals energy as a function of the distance between the cluster and a reference plane at a distance Z_0 from the atoms on the surface is given by

$$\Delta E(Z) = -\frac{C_3}{(Z - Z_0)^3}\,, \tag{7.5}$$

where C_3 is the Lifshitz coefficient that can be calculated from [425] the dynamical polarizability of the cluster and the dielectric function of the bulk material:

$$C_3 = \frac{1}{4\pi}\int_0^\infty \mathrm{d}u\;\alpha(\mathrm{i}u)\frac{\epsilon_{\mathbf{M}}(\mathrm{i}u) - 1}{\epsilon_{\mathbf{M}}(\mathrm{i}u) + 1}\,. \tag{7.6}$$

It is interesting to remark that C_3 is expressed only in terms of quantities calculated for the bulk crystal. The quantity that depends on the characteristics of the surface is the position of the reference plane Z_0. However, for semiconducting surfaces, it can be shown [425] that in absence of local field effects Z_0 is equal to $a/2$, where a is the interplanar distance. Moreover, it is known that even relatively large local field corrections give rise to rather small shifts of the reference plane [425]. The expression (7.6) for the C_3 coefficient is a general result, also valid for metallic surfaces. However, the position of the reference plane Z_0 is a more delicate issue in the case of a metal, as positioning the reference plane at a distance of $a/2$ from the surface can lead to significant errors in the interaction energy (i.e. about 30% for a noble metal surface [425]).

7.2 Methods

The main ingredients to evaluate the van der Waals coefficients are therefore the electronic polarizability α of the cluster and the dielectric constant of the bulk material ε, both evaluated at imaginary frequencies. The computational methods and the problems involved in the calculation of these two quantities are quite different, so we will discuss them separately.

7.2.1 Finite systems

One can, in principle, obtain the electronic polarizability by using any quantum-chemistry theory capable of handling time-dependent perturbations. As the nanostructures we are interested in can be fairly large, we choose TDDFT, as this approach provides an excellent compromise between accuracy and feasibility.

Several different numerical approaches can be found in the literature to calculate α at imaginary frequencies within TDDFT. For example, linear response theory can be employed to calculate the density-density response function χ, from which α directly follows:

$$\alpha_{ij}^{(X)}(\omega) = \int \mathrm{d}^3 r \int \mathrm{d}^3 r' \, r_i \, \chi^{(X)}(\boldsymbol{r}, \boldsymbol{r}', \omega) \, r_j \, . \tag{7.7}$$

This approach is quite common and has been used for the calculation of the C_6 coefficients of a wealth of molecules and clusters.

Alternatively, one can work in real time. By propagating the time-dependent Kohn-Sham equations, we obtain $\delta n(\boldsymbol{r}, t)$ and the polarizability $\alpha_{ij}(\omega)$ via Eq. x. In order to obtain values of α at imaginary frequencies one only has to substitute ω by $\mathrm{i}u$. This computational framework has been implemented in OCTOPUS.

A slightly different approach, is the polarization propagation technique, whose extension to imaginary frequencies has been used to compute C_6 coefficients [426, 427, 428, 429]. For large molecules, Banerjee and Harbola have also proposed the use of orbital free TDDFT, providing satisfactory results for large sodium clusters [430, 431].

It is also possible to use an alternative scheme based on the solution of a Sternheimer equation. Although a perturbative technique, it avoids the use of empty states and has a quite good scaling (N^2) with the number of atoms. This method has already been used for the calculation of many response properties, like atomic vibrations, electron-phonon coupling, magnetic response, etc. In the domain of optical response, this method has been mainly used for static response, although few calculations at finite (real) frequency have appeared. Beside the excellent scaling, the advantage of this technique is the relatively small prefactor with respect to the time-propagation. We therefore expect it to be an important tool for the calculation of van der Waals interactions between large systems, like nanoclusters or molecules of biological interest.

7.2.2 Extended systems

Concerning extended systems, the electronic band structure of bulk semiconductors and insulators, which is the starting point to obtain the dielectric functions, is nowadays accurately described by ab initio methods [432]. Much work has been done in the past years to determine which approximations allow a proper description of electron-electron and electron-hole interactions, which is essential to obtain optical functions (at real frequencies) in agreement with experimental data.

Within linear response for an extended system, the inverse dielectric function of a periodic system is constructed from

$$\epsilon^{-1}\left(\mathbf{q}, \mathbf{G}, \mathbf{G}', \omega\right) = \delta_{\mathbf{G},\mathbf{G}'} + v\left(\mathbf{q}, \mathbf{G}\right) \chi\left(\mathbf{q}, \mathbf{G}, \mathbf{G}', \omega\right) \, , \tag{7.8}$$

where $\mathbf{q}$ is a vector in the Brillouin zone, $\mathbf{G}$ is a reciprocal lattice vector, v is the bare Coulomb interaction, and χ obeys the matrix equation . The macroscopic dielectric function ϵ_{M} can be readily obtained form the microscopic ϵ:

$$\epsilon_M\left(\omega\right) = \lim_{\mathbf{q}\to 0} \frac{1}{\epsilon^{-1}\left(\mathbf{q}, \mathbf{G} = 0, \mathbf{G}' = 0, \omega\right)}. \tag{7.9}$$

The simplest approximation that yields the dielectric function consists in applying the Fermi's golden rule to obtain

$$\begin{aligned}\epsilon_{\mathbf{M}} &= \lim_{\mathbf{q}\to 0} \epsilon\left(\mathbf{q}, \mathbf{G}=0, \mathbf{G}'=0, \omega\right) \\ &= \lim_{\mathbf{q}\to 0} \left[1 - v\left(\mathbf{q}, \mathbf{G}=0\right) \chi_{\mathrm{s}}\left(\mathbf{q}, \mathbf{G}=0, \mathbf{G}'=0, \omega\right)\right] . \end{aligned} \tag{7.10}$$

In this approximation, the optical spectrum is calculated as a sum of independent transitions between Kohn-Sham or quasiparticle states. Unfortunately, this approximation is known to exhibit severe shortcomings compared to experiments [433]. The next step is the so-called random phase approximation (RPA), that includes the effects due to the variation of the Hartree potential upon excitation while $f_{\mathrm{x}c}$ is set to zero. Unfortunately, this approximation does not lead to any significant improvement for most solids, especially if there are no particularly pronounced polarizable inhomogeneities in the charge density. For a typical semiconductor, the RPA absorption threshold is too low, the peaks are redshifted with respect to experiment and the relative intensity of the peaks is also not correctly reproduced. Replacing the Kohn-Sham energies with the quasiparticle energies does not solve the problem: the peak positions are usually overcorrected and the oscillator strength is not modified.

It is the neglect of variations of the xc potential, which include the effect of the electron-hole Coulomb interaction, that is responsible for an overall disagreement in the absorption strength, in particular for the failure to reproduce continuum and bound excitons. The agreement with experiment can be greatly improved by including the electron-hole interaction through the solution of the Bethe-Salpeter equation (BSE) [16, 17, 181]. It is possible to obtain as well the same agreement with experiments within TDDFT, provided that a good approximation is found for the xc-kernel. In fact, this term is essential as its task is to modify the excitation energies and to redistribute the oscillator strength. The adiabatic local density approximation for the xc-kernel in the case of solids is not sufficient to yield good dielectric functions. The reason for this failure can be traced back to the short-range nature of the TDLDA f_{xc}, while the"exact" f_{xc} is expected to be long-ranged [17], decaying in momentum space as $1/q^2$.

A class of kernels that was shown to be very efficient in the description of solids are those derived from the BSE, used together with the quasiparticle band structure, instead of the Kohn-Sham states in the construction of χ_{s}. A parameter-free expression was obtained in several different ways as explained in Sec. 4.4. Although involving a potentially reduced computational effort with respect to the BSE, these calculations are still significantly more cumbersome than those within the RPA or the TDLDA. To keep the computational cost as low as possible, in many cases it is enough to use simplified versions of the nanoquanta kernel. It was shown in Sec. 4.5.1 that the BSE-derived kernel has the asymptotic form of a long-range contribution (LRC) [32, 37]

$$f_{\mathrm{xc}}^{\mathrm{static}}(\mathbf{q}) = -\frac{\alpha^{\mathrm{static}}}{q^2}, \tag{7.11}$$

where α^{static} is a material dependent parameter, that can be related to the dielectric constant. This long-range contribution alone is sufficient to simulate the strong continuum exciton effect in the absorption spectrum and in the refraction index of several simple semiconductors, like bulk silicon or GaAs, provided that quasiparticle energies are used as a starting point.

In Sec. 4.5.1 we have seen that a dynamical extension of this LRC model [104] of the form

$$f_{\mathrm{xc}}^{\mathrm{dyn}}(\mathbf{q}) = -(\alpha + \beta\omega^2)/q^2 \tag{7.12}$$

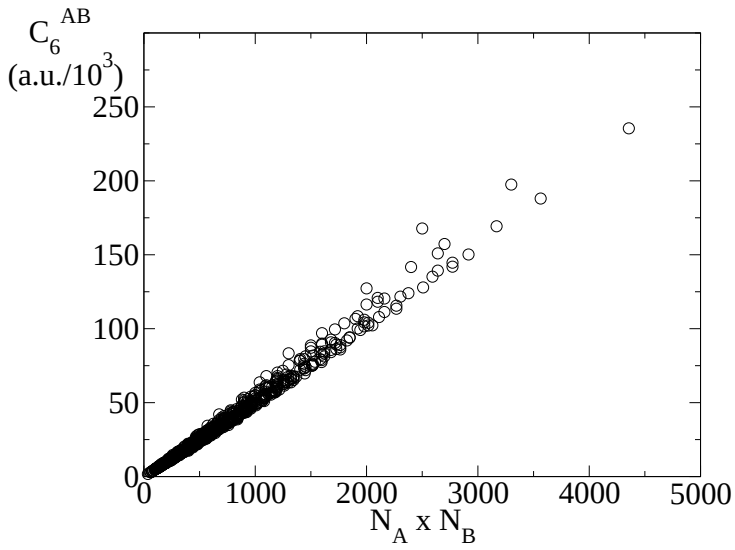

Figure 7.1: C_6^{AB} Hamaker constants for all the pairs of PAHs under study, as a function of the product of the number of Carbon atoms, $N_A \times N_B$.

leads to remarkable improvements for optical spectra of large gap systems with respect to calculations where the kernel is imposed to be static. Moreover, the dynamical approach has proved to be valid also for energies in the range of plasmons and for the determination of dielectric constants. Note that the parameters of both the static and the dynamical model can be related to physical quantities, like the experimental dielectric constant and the plasmon frequency.

In this work, we calculated the dielectric functions at imaginary frequency using the computer code DP[1], an ab initio linear response TDDFT code that works in reciprocal space and frequency domain, and is based on a plane waves basis set. Despite the enormous amount of studies concerning the accuracy of different approximations for the xc kernel for solids, it is not a priori clear which approximation is more suitable when one wants to work at imaginary frequency. To this purpose, we tested several approximations for the exchange-correlation kernel implemented in DP and in the following we discuss their effect on the quality of the van der Waals coefficient C_3.

7.3 Calculations

7.3.1 Polycyclic aromatic hydrocarbons

Polycyclic aromatic hydrocarbons (PAHs), a large class of conjugated π-electron systems, are of great importance in many areas, among which combustion and environmental chemistry, materials science, and astrochemistry. PAHs are found in carbonaceous meteorites, in interplanetary dust particles, and are thought to be the most abundant molecular species in space after H_2 and CO, playing a crucial role in the energy and ionization balance of interstellar matter in galaxies. Motivated by this astrochemical relevance, there have been extensive studies of these systems [289, 434, 435, 436]. This research is collected in a thorough compendium of molecular properties of PAHs [436]. The computation of van der Waals constants for pairs of PAHs, as a first approach to the analysis of their intermolecular

[1] `http://theory.polytechnique.fr/codes/dp`

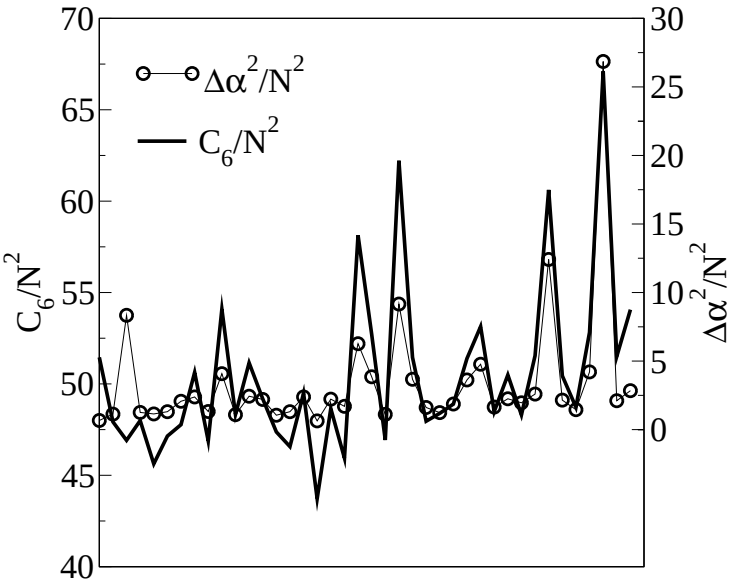

Figure 7.2: C_6 homo-molecular Hamaker constants divided by the square of the number of atoms (thick solid line, left axis), and dipole polarizability anisotropy, also divided by the square of the number of atoms (circles, right axis). Each data point corresponds with one PAH, ordered in the x-axis according to its number of atoms.

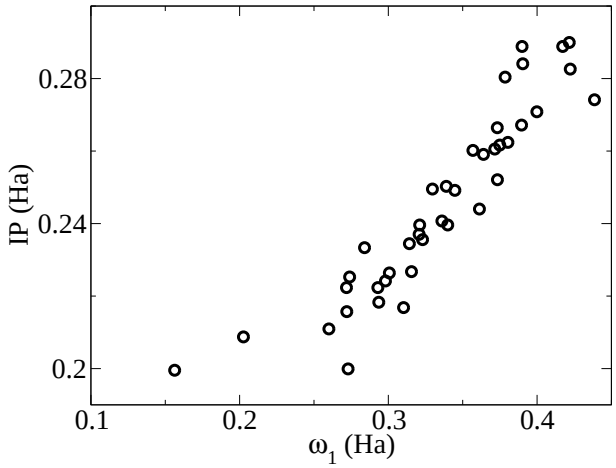

Figure 7.3: Ionization potentials (vertical axis) against dispersion frequencies (horizontal axis) for all the PAHs under study

properties, is therefore a natural extension of this work. In fact, van der Waals parameters are a crucial ingredient to model condensation and evaporation of PAH clusters, which are another important player in the physics/chemistry of the interstellar medium. In current works, people usually employ empirical van der Waals parameters for the relatively long-range part of the interaction in molecular dynamics simulations, together with some tight-binding approximation for the short-range part [437, 438].

One previous calculation of dispersion coefficients of PAHs, based on the complex linear polarization propagator method, was reported in Ref. [428], although limited to benzene, naphthalene, anthracene, and naphtacene. This fact adds a further motivation to our study, since it permits to compare the results of the two schemes.

We have computed the C_6^{AB} Hamaker constants for all possible pairs $\{A, B\}$ of a set of 41 PAHs using the time propagation technique. The homo-molecular Hamaker constants C_6^{AA} for all the PAHs studied are shown in Fig. 7.1 and 7.2; the full set can be consulted in the database described in Ref. [436]. In this database one can also find the average static dipole polarizability $\alpha(0)$, the effective London frequency ω_1 (see below) and the retarded van der Walls coefficient K.

It is very difficult to extract Hamaker constants experimentally; to our knowledge, there are no experimental results reported for any PAH to compare to. For benzene, however, Kumar and Meith [439] reported a value of 1723 a.u., by making use of the dipole oscillator strength distributions (DOSDs), which are constructed from experimental dipole oscillator strengths and molar refractivity data. This is in good agreement with our computed value of 1763 a.u.

There are also results, reported in Ref. [428], obtained by means of the complex linear polarization propagator scheme. This scheme was constructed on top of TDDFT, although making use of the B3LYP functional. These methodological differences, and further numerical details can explain the very small differences, in all cases below 2% for benzene, naphthalene, anthracene and tetracene (also known as naphthacene).

In the so-called London approximation, the polarizability at imaginary frequencies is modeled with the help of only two parameters: the static polarizability, and one effective frequency ω_1:

$$\alpha(\mathrm{i}u) = \frac{\alpha(0)}{1 + (u/\omega_1)^2}\,. \tag{7.13}$$

Upon substitution on the Casimir-Polder integral, this yields for a homo-molecular Hamaker constant:

$$C_6 = \frac{3\omega_1}{4}\alpha^2(0)\,. \tag{7.14}$$

With the knowledge of C_6 and $\alpha(0)$, one can obtain ω_1 from Eq. (7.14). They are roughly decreasing with the size of the PAH, from 0.482 Ha for benzene to the 0.156 Ha of pentarylene. The decrease is, however, strongly irregular. As it has been pointed out before [39], it can be related to the ionization potential of the molecules; this is demonstrated in Fig. 7.3, where we have plotted the ionization potentials of the PAHs (calculated at the DFT/B3LYP level of theory), versus the effective frequency ω_1. The data points approximately accumulate around a straight line, proving the correlation.

Equation (7.14) also gives us a hint on the dependency of C_6 with the size of the molecule: it is proportional to the square of the polarizability (the product of polarizabilities, if the molecules are different), which in turn typically grows with the volume, and therefore, with the number of atoms. Consequently, one should expect a linear dependency of C_6^{AB} with respect to the product of the number of atoms, $N_A \times N_B$. This is indeed confirmed in Fig. 7.1. Some cases, however, deviate from a straight line. These cases correspond to strongly anisotropic PAHs (with three very different axes). This is captured by

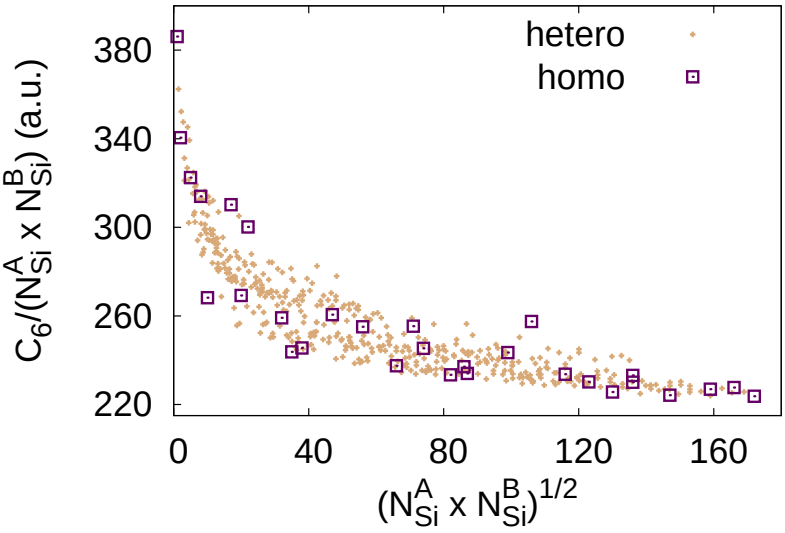

Figure 7.4: C_6^{AB} Hamaker constants as a function of the square root of the product of silicon atoms in cluster A and B. As C_6^{AB} scales basically as the product between the number of (silicon) atoms in A and B, we plot the Hamaker constants divided by this number. Values of C_6^{AB} when A and B are the same cluster are plotted as red squares, otherwise they are plotted as orange dots.

the dipole anisotropy:

$$\Delta\alpha^2 = \frac{1}{3}[(\alpha_{xx} - \alpha_{yy})^2 + (\alpha_{xx} - \alpha_{zz})^2 + (\alpha_{yy} - \alpha_{zz})^2]\,. \tag{7.15}$$

Figure 7.2 shows how the PAHs whose Hamaker constant deviates strongly from the general trend are those whose polarizability anisotropy is also stronger: we have overlaid the values of C_6 for all PAHs (divided by the square of the number of Carbon atoms N^2), with the values $\Delta\alpha^2$ (also divided by N^2). One can see how the two datasets are correlated – specially in the right side of the graph, which corresponds to the larger PAHs.

The crossover between the non-retarded and retarded regimes is given by the length scale $\lambda = 2\pi c/\bar{\omega}$, where $\bar{\omega}$ is a characteristic frequency of the electronic spectrum of the molecule. For $R/\lambda \gtrsim 10$ we enter the fully retarded regime, while for $R/\lambda \lesssim 0.1$ we can still use Eq. (7.1). Using for $\bar{\omega}$ the values of ω_1 obtained through the London approximation, we reach values in the range of $\lambda \sim 0.1\,\mu$m (for benzene) to $\lambda \sim 0.3\,\mu$m (for pentarylene).

It is interesting to notice that in the fully retarded regime we can write K^{AA} as a function solely of the Hamaker C_6^{AA} coefficient and the effective London frequency ω_1. Combining equations (7.4) and (7.14) we arrive at

$$K^{AA} = \frac{23c}{6\pi^2}\frac{C_6}{\omega_1}\,. \tag{7.16}$$

The values of homomolecular coefficients K^{AA} for the PAHs studied in this work can be found in the database described in Ref. [436].

7.3.2 Silicon clusters

These clusters were cut from bulk silicon, and then saturated with hydrogens along the tetrahedral direction of the surface atoms. The geometries were optimized with the com-

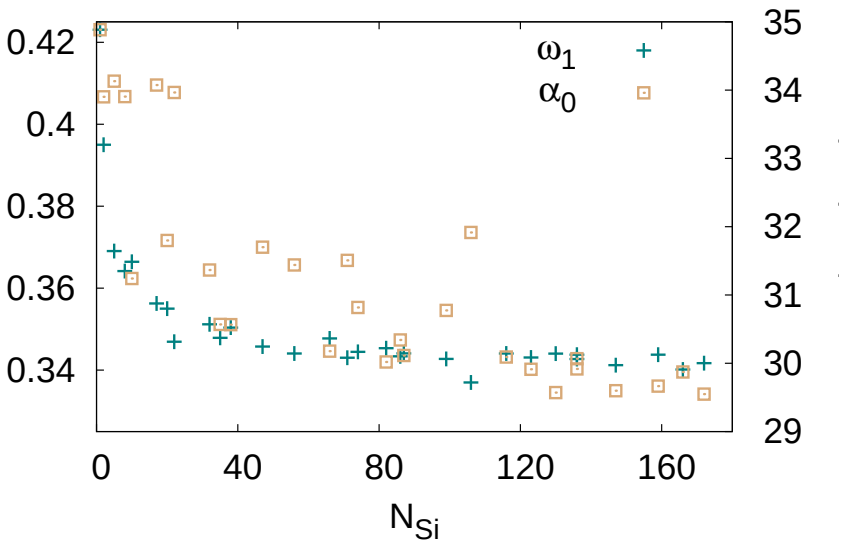

Figure 7.5: London effective frequency ω_1 for the silicon clusters under study as a function of the number of silicon atoms.

puter code siesta [237], employing a double ζ with polarization basis set, and the PBE parametrization [4] for the exchange-correlation potential.

From the optimized geometries, we then obtained the electric polarizability within TDDFT using the Sternheimer equation. Calculations were performed at zero temperature and fixed geometries. The electron-ion interaction is described through norm-conserving pseudopotentials [239] and the LDA [238] is employed in the adiabatic approximation for the exchange-correlation potential. We used a spacing of 0.275 Å and the simulation box was formed from the union of spheres centered around the atoms with radius 4.5 Å. The integrals in Eqs. (7.2) and (7.6) were performed with a Gauss-Legendre quadrature using 6 frequency values. With these parameters, we estimate the accuracy of our numerical calculations to better than 5%.

In Fig. 7.4 we show our results for the C_6 Hamaker constant between silicon clusters. As the value of C_6 scales as the product of the atoms in the cluster A ($N_{\rm Si}^A$) and in cluster B ($N_{\rm Si}^B$), we divided the Hamaker constant by $N_{\rm Si}^A N_{\rm Si}^B$ to eliminate this dependence. We show both constants between two identical clusters (homo-molecular – as red squares), and between different clusters (hetero-molecular – orange dots). We see that the largest C_6 per atom squared comes from the interaction between two SiH_4 clusters, and the its value decreases rapidly until slightly above 220 a.u, where it saturates. The few clusters that fall far from the line are the most asymmetric, for which a description in terms of the average of the dipole polarizability tensor is not necessarily as good.

As we have calculated both C_6 and $\alpha(0)$ within TDLDA, it is easy to extract ω_1 from Eq. (7.14). The resulting effective frequencies are plotted in Fig. 7.5, together with the calculated static polarizabilities per number of Si atoms. We can observe that ω_1 decreases with the number of Si atoms, but the dependence on the size of the cluster is rather weak, except for the singular case of the smallest aggregates. In the following, for our model calculations we will use a constant effective frequency of 0.343 Ha.

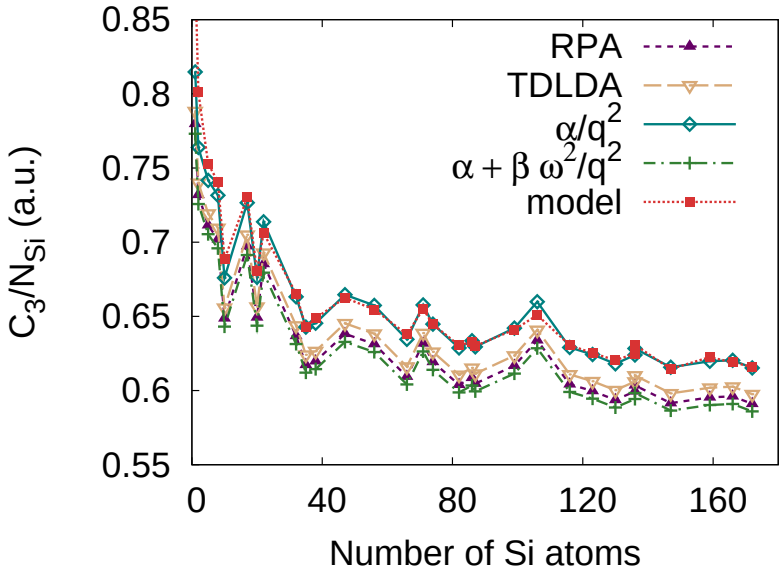

Figure 7.6: Van der Waals C_3 coefficients between silicon nanoclusters and a silicon surface. The C_3 coefficients were divided by the number of silicon atoms in the cluster. The different curves were calculated using different approximations for the dielectric constant of the bulk crystal at imaginary frequencies (see the text for details).

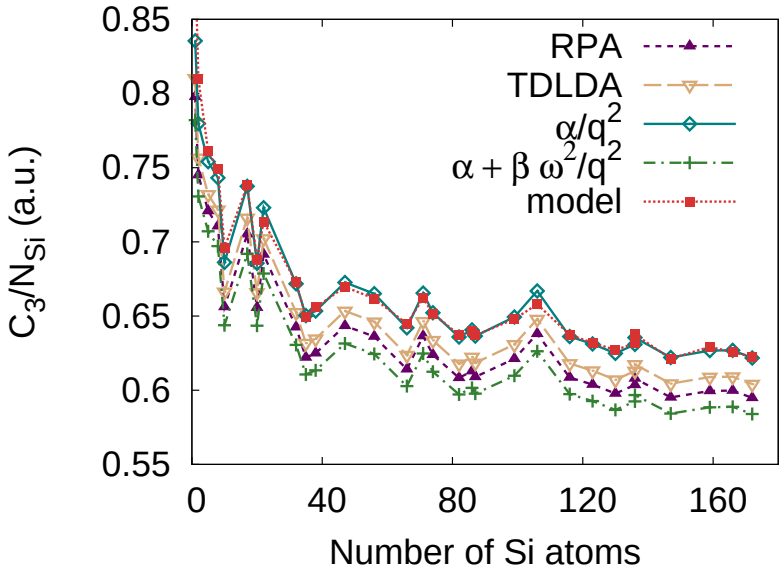

Figure 7.7: Van der Waals C_3 coefficient between silicon nanoclusters and a silicon carbide surface. The meaning of the curves is as in Fig. 7.6.

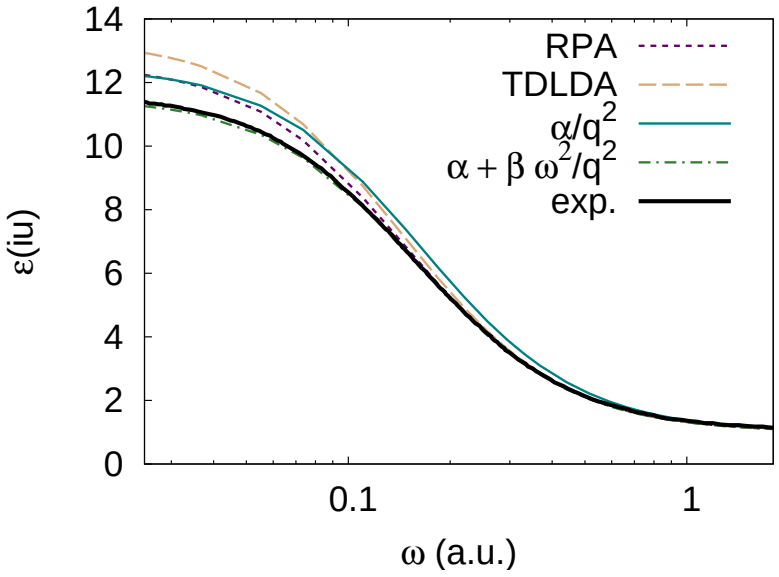

Figure 7.8: Dielectric function of Si along the imaginary axis as a function of the frequency in a logarithmic scale. Results obtained with different approximations for the xc kernel are compared to the curve extracted from experimental data by using (7.17).

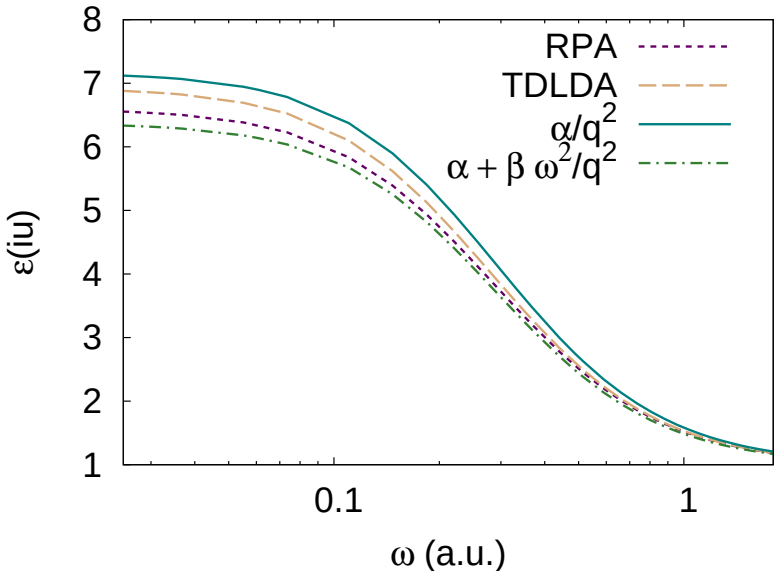

Figure 7.9: Dielectric function of SiC along the imaginary axis as a function of the frequency in a logarithmic scale. We compare results obtained within different approximations for the xc kernels.

7.3.3 Cluster-surface interactions

Now, we consider the case of a silicon cluster in proximity of a surface of Si or a SiC in the zincblende phase. In this case we want to calculate C_3 coefficients, that are determined both by the dynamical polarizability of the cluster and the dielectric function of the bulk crystal.

The ground state calculations for the bulk crystals were performed using the plane-wave code ABINIT with norm-conserving Hamman pseudopotentials for Si and C. We used a cutoff energy for the plane wave basis of 12.5 Ha for Si and 30 Ha for SiC. The unit cell was relaxed within the LDA approximation, yielding lattice parameters with an error smaller than 3%. The dielectric function at imaginary frequencies was calculated using the code DP. For more information about the convergence parameters we refer to Ref. [37].

From previous tests on the effect of different approximations for the xc potential, we know that the dynamical polarizability of the hydrogenated Si clusters is accurately described within TDLDA and the C_6 coefficients are not going to change by more than 5% by using different approximations. We decide thus to focus on the effect of different approximations for the xc-kernel in the calculation of the dielectric function at imaginary frequencies of Si and SiC.

In Figs. 7.6 and 7.6 we can compare C_3 coefficients for Si clusters on a Si surface and Si clusters on a SiC surface, respectively. We show here results obtained within the RPA (violet upright triangles), the TDLDA (beige inverted triangles), using the static LRC kernel (blue diamonds) and the dynamical LRC kernel (green crosses). Note that in the case of RPA and TDLDA calculations we used the Kohn-Sham band structure to build $\chi_{\rm s}$, while the quasiparticle states calculated in the GW approximation are used when the static or dynamical LRC kernels are employed (for details see [37, 104]). In Si and SiC the GW corrections to the band structures are essentially equivalent to a rigid shift of the conduction states, thus replacing Kohn-Sham energies with quasiparticle energies leads to a rigid shift of the absorption spectrum towards higher energies. We have also plotted in Figs. 7.6 and 7.6 the values of C_3 obtained using simple models (red squares) for both the dynamical polarizability of the cluster and the dielectric function of the crystal at imaginary frequencies (see Ref. [440]).

For the interaction of Si clusters on either a Si or a SiC surface, all the approximations used for the xc kernel give curves with very similar trends and a dispersion of the values which is smaller than 7–8%. This finding reflects the fact that the dielectric function at imaginary frequency is a well behaved curve, which gives the dielectric constant at $\mathrm{i}u = 0$ and then decreases monotonically to the asymptotic limit of one. In Figs. 7.8 and 7.9 we can observe the dielectric functions at imaginary frequencies (RPA: violet dashed curve, TDLDA: beige long-dashed curve, static LRC: blue continuous curve, dynamical LRC: green dot-dashed curve). An experimental curve can be obtained through a Kramers-Kronig transformation

$$\epsilon_{\rm M}(\mathrm{i}u) = 1 + \frac{2}{\pi}\int_0^\infty \mathrm{d}\omega\ \frac{\omega \Im\mathrm{m}\left[\epsilon_{\rm M}(\omega)\right]}{\omega^2 + u^2} \tag{7.17}$$

if the experimental absorption spectra has been measured on a spectral range large enough.

In Figs. 7.8 we include for comparison the experimental curve [441]. The curve calculated with the dynamical LRC approximation for the xc kernel is exactly superposed to the experimental curve. In fact, this is the only approximation which allows to get both a good dielectric constant, which fixes the interception with the y axis, and an overall good shape of the absorption spectrum over a large spectral range (see Ref. [104]). Both these elements are essential to get close to the data derived from the experiment, as it can be notice by

inspecting the form of (7.17). It is interesting to notice that the curve calculated using the static LRC kernel is even worse than the RPA curve, as the starting point at $\mathrm{i}u = 0$ is bad and the overall spectrum is then similar to the one obtained by the dynamical LRC approximation: there is thus no fortuitous compensation of errors as in the RPA curve, where the error due to the too high dielectric constant is balance by the shift of the spectral weight to lower energies. The TDLDA curve is the one that lays further from the dynamical LRC solution at lower frequencies due to the even higher dielectric constant, but it gets closer than the static LRC curve for $u \leq 0.1$, thanks to the same compensation of errors already observed for the RPA calculation. In the case of SiC (see Fig. 7.9) the static LRC results is the worst at any frequency as this approximation also overestimates the most the dielectric constant. Once again, the RPA curve is the closest to the dynamical LRC result, which is expected to be the most accurate.

After having analyzed the dielectric functions at imaginary frequencies, it is clear how to interpret the results for the C_3 coefficients. The experimental result is not shown in Fig. 7.6 as it coincides with the points calculated using the dynamical LRC kernel. Outside the limits of validity of the dynamical LRC model (large gap insulators, strongly bond excitons) only a calculation for the bulk crystal based on the solution of the BSE equation (or equivalently using the fully ab initio Bethe-Salpeter derived kernel) can guarantee the quality of the C_3 coefficients. This implies necessarily larger computational costs. The RPA and TDLDA results are quite good to evaluate C_3, despite the well known deficiencies of these approximations to calculate optical absorption spectra: they give errors smaller than 1%. This is not necessarily true for any kind of system, but it is probably true to some extent each time that the calculated dielectric function is larger than the experimental one. One should be very careful not to use the static LRC approximation for the kernel, despite the fact that it gives an absorption spectrum in overall agreement with the experimental spectrum. This is due to the fact that the van der Waals coefficients are very sensitive to the value of the dielectric constant.

Chapter 8

Conclusions

The response upon excitation of complex materials used in modern applications can nowadays be calculated from first-principles. This was made possible by recent theoretical developments together with the optimization of computer codes. When dealing with electronic excitations, the knowledge of the ground state density of the system is no more sufficient, which means that one has to find appropriate ways to go beyond density functional theory. Two paths have been intensively explored: one is based on the time-dependent density and the other one on Green's functions.

After the pioneering work of Zangwill and Soven [18], time dependent density functional theory (TDDFT) found a rigorous foundation in the work by Runge and Gross [19]. The time-dependent Kohn Sham equations are obtained as a generalization of the static case and, from these, the response functions describing the neutral excitations of the system. The main ingredient is the time dependent exchange-correlation potential $v_{\rm xc}[n](\mathbf{r},t)$, that depends on the density at all points in space, and at all past times.

Staying within linear response theory, one needs to know, in addition to the static exchange-correlation (xc) potential $v_{\rm xc}[n_{\rm GS}](\mathbf{r})$, the so called xc kernel $f_{\rm xc}[n](\mathbf{r},\mathbf{r}',t,t') = \delta v_{\rm xc}[n](\mathbf{r},t)/\delta n(\mathbf{r}',t')$. If these two quantities are known, TDDFT is an exact theory, yielding the exact linear response. The problem is, therefore, how to generate suitable approximations for the potential and the kernel. For finite systems, it is sometimes crucial to have a good $v_{\rm xc}$, whereas in extended systems in general the main problem is to find a good approximation for the kernel $f_{\rm xc}$.

Neutral excitations can also be calculated in the framework of Many-Body Perturbation Theory, via the solution of the Bethe-Salpeter equation. However, in that case one has to deal with two-particle Green's functions, that are four-point quantities, whereas TDDFT is based on two-point linear response functions. Therefore TDDFT promises to be computationally much more efficient, which motivates the search for good approximations.

The simplest approximation is the adiabatic LDA (TDLDA), which often yields good results for finite systems. Along those lines, we presented here applications of TDLDA to calculate response properties of different nanoparticles. The main shortcoming of the TDLDA kernel is to miss the long range part, proportional to $1/|\mathbf{r}-\mathbf{r}'|$, which may be important in extended systems. Nevertheless, the TDLDA describes well also some properties of extended systems, in particular the plasmon structures in the loss function or the dynamical structure factor. In these cases, indeed, the long range part of the kernel is not important, either because of cancellations or because of non-vanishing momentum transfer. However, TDLDA does not describe well the optical properties of extended systems, where the long range part is essential.

Therefore, one of the main challenges of recent years has been to find suitable approx-

imations to the long range part of $f_{\rm xc}$. Promising solutions came from a comparison of TDDFT and the many-body perturbation theory equations for the polarization. Different groups have suggested different approaches; all approaches have led to one and the same kernel, that is linear in the screened Coulomb interaction and based on quasi-particle ingredients. This kernel allows one to obtain a good description of the optical properties of extended systems, including bound excitons. It also describes well spectra for non-vanishing momentum transfer, and it has been demonstrated that it yields very good results for low-dimensional systems, including clusters, wires and surfaces. However, simple model approximations of the BSE-derived kernel, very useful to perform fast and reliable calculations for bulk systems, do not necessarily work well for nanostructured systems, as we have shown in the case of CdSe nanowires.

Fortunately, much work has been done in the optimization of algorithms and computer codes, which has led to considerable speedup. Indeed, it is now possible to calculate electronic excitations using a GW approach and eventually solving the Bethe-Salpeter equation (BSE) for complex materials of technological interest. We discussed some examples of applications to materials for data storage and photovoltaics in this manuscript.

At present, although the TDDFT linear response equation is relatively quick to solve because of its two-point nature, calculations involving the BSE-derived kernel are still computer-time intensive. In particular, for the calculation of the kernel itself current implementations use ingredients of the BSE approach, so that the performance of the two methods is comparable. In view of that, the solution of the BSE is still the state-of-the-art technique to obtain accurate spectra for extended system, whenever one needs to preserve a predictive power.

The way is open now for many possible applications of the techniques and algorithms that have been successfully developed for the past years. Indeed, the understanding of many materials of great complexity and technological interest is still lacking. Nevertheless, even if great physics insight can be obtained with the existing methods, the quest for improved exchange and correlation kernels for TDDFT, as well as the search for novel theoretical approaches, cannot be abandoned. Hopefully new developments will appear in the next years.

Bibliography

[1] W. Kohn, Rev. Mod. Phys. **71**, 1253 (1999).

[2] P. Hohenberg and W. Kohn, Phys. Rev. **136**, B864 (1964).

[3] W. Kohn and L. J. Sham, Phys. Rev. **140**, A1133 (1965).

[4] J. P. Perdew, K. Burke, and M. Ernzerhof, Phys. Rev. Lett. **77**, 3865 (1996), erratum: ibid. **78**, 1396(E) (1997).

[5] R. O. Jones and O. Gunnarsson, Rev. Mod. Phys. **61**, 689 (1989).

[6] S. Baroni and R. Resta, Phys. Rev. B **33**, 7017 (1986).

[7] G. Kotliar, S. Y. Savrasov, K. Haule, V. S. Oudovenko, O. Parcollet, and C. A. Marianetti, Rev. Mod. Phys. **78**, 865 (2006).

[8] F. Sim, A. St-Amand, I. Papai, and D. R. Salahub, J. Am. Chem. Soc. **114**, 4391 (1992).

[9] R. W. Godby, M. Schlüter, and L. J. Sham, Phys. Rev. B **36**, 6497 (1987).

[10] A. L. Fetter and J. D. Walecka, *Quantum Theory of Many-Particle Systems* (McGraw-Hill, New York, ADDRESS, 1971).

[11] L. Hedin, Phys. Rev. **139**, A796 (1965).

[12] S. V. Faleev, M. van Schilfgaarde, and T. Kotani, Phys. Rev. Lett. **93**, 126406 (2004).

[13] M. van Schilfgaarde, T. Kotani, and S. Faleev, Phys. Rev. Lett. **96**, 226402 (2006).

[14] F. Bruneval, N. Vast, and L. Reining, Phys. Rev. B **74**, 045102 (2006).

[15] L. J. Sham and T. M. Rice, Phys. Rev. **144**, 708 (1966).

[16] W. Hanke, Adv. Phys. **27**, 287 (1978).

[17] G. Onida, L. Reining, and A. Rubio, Rev. Mod. Phys. **74**, 601 (2002), and refereces therein.

[18] A. Zangwill and P. Soven, Phys. Rev. Lett. **45**, 204 (1980).

[19] E. Runge and E. K. U. Gross, Phys. Rev. Lett. **52**, 997 (1984).

[20] E. K. U. Gross and W. Kohn, Phys. Rev. Lett. **55**, 2850 (1985).

[21] E. K. U. Gross and W. Kohn, Phys. Rev. Lett. **57**, 923(E) (1986).

[22] R. van Leeuwen, Int. J. Mod. Phys. B **15**, 1969 (2001).

[23] M. Petersilka, U. J. Gossmann, and E. K. U. Gross, Phys. Rev. Lett. **76**, 1212 (1996).

[24] M. A. L. Marques and E. K. U. Gross, Annu. Rev. Phys. Chem. **55**, 427 (2004).

[25] M. Petersilka, E. K. U. Gross, and K. Burke, Int. J. Quantum Chem. **80**, 534 (2000).

[26] X. Gonze, Ph. Ghosez, , and R. W. Godby, Phys. Rev. Lett. **74**, 4035 (1995).

[27] S. J. A. van Gisbergen, F. Kootstra, P. R. T. Schipper, O. V. Gritsenko, J. G. Snijders, and E. J. Baerends, Phys. Rev. Lett. **83**, 694 (1999).

[28] N. E. Maddocks, R. W. Godby, and R. J. Needs, Europhys. Lett. **27**, 681 (1994).

[29] I. G. Gurtubay, W. Ku, J. M. Pitarke, A. G. Eguiluz, B. C. Larson, J. Tischler, and P. Zschack, Phys. Rev. B **72**, 125117 (2005).

[30] S. Waidmann, M. Knupfer, B. Arnold, J. Fink, A. Fleszar, and W. Hanke, Phys. Rev. B **61**, 10149 (2000).

[31] H.-Ch. Weissker, J. Serrano, S. Huotari, F. Bruneval, F. Sottile, G. Monaco, M. Krisch, V. Olevano, and L. Reining, Phys. Rev. Lett. **97**, 237602 (2006).

[32] L. Reining, V. Olevano, A. Rubio, and G. Onida, Phys. Rev. Lett. **88**, 066404 (2002).

[33] F. Sottile, V. Olevano, and L. Reining, Phys. Rev. Lett. **91**, 056402 (2003).

[34] G. Adragna, R. Del Sole, and A. Marini, Phys. Rev. B **68**, 165108 (2003).

[35] A. Marini, R. Del Sole, and A. Rubio, Phys. Rev. Lett. **91**, 256402 (2003).

[36] R. Stubner, I. V. Tokatly, and O. Pankratov, Phys. Rev. B **70**, 245119 (2004).

[37] S. Botti, F. Sottile, N. Vast, V. Olevano, H.-C. Weissker, L. Reining, G. Onida, A. Rubio, R. Del Sole, and R. W. Godby, Phys. Rev. B **69**, 155112 (2004).

[38] U. von Barth, N. E. Dahlen, R. van Leeuwen, and G. Stefanucci, Phys. Rev. B **72**, 235109 (2005).

[39] G. D. Mahan, *Many Particle Physics* (Plenum, New York, ADDRESS, 1990).

[40] L. Hedin and S. Lundqvist, in *Solid State Physics*, edited by F. Seitz, D. Turnbull, and H. Ehrenreich (Academic, New York, ADDRESS, 1969), Vol. 23, pp. 1–181.

[41] G. Strinati, Rivista del Nuovo Cimento **11**, 1 (1988).

[42] G. Strinati, H. J. Mattausch, and W. Hanke, Phys. Rev. B **25**, 2867 (1982).

[43] M. S. Hybertsen and S. G. Louie, Phys. Rev. Lett. **55**, 1418 (1985).

[44] M. S. Hybertsen and S. G. Louie, Phys. Rev. B **34**, 5390 (1986).

[45] R. W. Godby, M. Schlüter, and L. J. Sham, Phys. Rev. B **37**, 10159 (1988).

[46] R. Del Sole, L. Reining, and R. W. Godby, Phys. Rev. B **49**, 8024 (1994).

[47] W. G. Aulbur, L. Jönsson, and J. W. Wilkins, Solid State Physics **54**, 1 (1999).

[48] F. Bruneval, N. Vast, L. Reining, M. Izquierdo, F. Sirotti, and N. Barrett, Phys. Rev. Lett. **97**, 267601 (2006).

[49] M. Gatti, F. Bruneval, V. Olevano, and L. Reining, Phys. Rev. Lett. **99**, 266402 (2007).

[50] J. Vidal, S. Botti, P. Olsson, J.-F. Guillemoles, and L. Reining, Phys. Rev. Lett. **104**, 056401 (2010).

[51] J. Vidal, F. Trani, F. Bruneval, M. A. L. Marques, and S. Botti, (2010), submitted.

[52] J. L. Lii, G.M. Rignanese, E. K. Chang, X. Blase, and S. G. Louie, Phys. Rev. B 035102 (2002).

[53] P. Rinke, A. Qteish, J. Neugebauer, C. Freysoldt, and M. Scheffler, New J. Phys. **7**, 126 (2005).

[54] E. Kioupakis, P. Zhang, M. L. Cohen, and S. G. Louie, Phys. Rev. B **77**, 155114 (2008).

[55] H. Jiang, R. I. Gomez-Abal, P. Rinke, and M. Scheffler, Phys. Rev. Lett. **102**, 126403 (2009).

[56] F. Fuchs and F. Bechstedt, Phys. Rev. B **77**, 155107 (2008).

[57] R. W. Nunes and D. Vanderbilt, Phys. Rev. Lett. **73**, 712 (1994).

[58] N. T. Maitra and K. Burke, Phys. Rev. A **63**, 042501 (2001).

[59] N. T. Maitra and K. Burke, Phys. Rev. A **64**, 039901(E) (2001).

[60] R. van Leeuwen, Phys. Rev. Lett. **82**, 3863 (1999).

[61] M. Levy, Phys. Rev. A **26**, 1200 (1982).

[62] E. H. Lieb, Int. J. Quantum Chem. **24**, 243 (1983).

[63] R. van Leeuwen, Phys. Rev. Lett. **80**, 1280 (1998).

[64] E. K. U. Gross, C. A. Ullrich, and U. J. Grossman, in *Density Functional Theory*, Vol. 337 of *NATO ASI Ser. B*, edited by E. K. U. Gross and R. Dreizler (Plenum Press, New York, 1995), pp. 149–71.

[65] E. K. U. Gross, F. J. Dobson, and M. Petersilka, in *Topics in Current Chemistry*, nalewajski, r. f. ed. (Springer-Verlag, Heidelberg, 1996), Vol. 181, p. 81.

[66] L. V. Keldysh, Sov. Phys. JETP **20**, 1018 (1965).

[67] S. Mukamel, Phys. Rev. A **71**, 024503 (2005).

[68] C. A. Ullrich, U. Gossmann, and E. K. U. Gross, Phys. Rev. Lett. **74**, 872 (1995).

[69] A. Görling, Phys. Rev. A **55**, 2630 (1997).

[70] `http://etsf.polytechnique.fr/Software/DP`.

[71] `http://www.yambo-code.org/`.

[72] A. Marini, C. Hogan, M. Grüning, and Daniele Varsano, Comput. Phys. Comm. **180**, 1392 (2009).

[73] `http://exciting.sourceforge.net/`.

[74] G. F. Bertsch, J. I. Iwata, A. Rubio, and K. Yabana, Phys. Rev. B **62**, 7998 (2000).

[75] A. Castro, M. A. L. Marques, and A. Rubio, J. Chem. Phys. **121**, 3425 (2004).

[76] S. K. Ghosh and A. K. Dhara, Phys. Rev. A **38**, 1149 (1988).

[77] F. Kootstra, P. L. de Boeji, and J. G. Snijders, J. Chem. Phys. **112**, 6517 (2000).

[78] B. Walker, A. M. Saitta, R. Gebauer, and S. Baroni, Phys. Rev. Lett. **96**, 113001 (2006).

[79] D. Rocca, R. Gebauer, Y. Saad, and S. Baroni, J. Chem. Phys. **128**, 154105 (2008).

[80] O. Gunnarsson and B. I. Lundqvist, Phys. Rev. B **13**, 4274 (1976).

[81] O. Gunnarsson and B. I. Lundqvist, Phys. Rev. B **15**, 6006(E) (1977).

[82] J. P. Perdew and M. Levy, Phys. Rev. B **31**, 6264 (1985).

[83] H. Ehrenreich and M.H. Cohen, Phys. Rev. **115**, 786 (1959).

[84] S. L. Adler, Phys. Rev. **126**, 413 (1962).

[85] N. Wiser, Phys. Rev. **129**, 62 (1963).

[86] R. Del Sole and E. Fiorino, Phys. Rev. B **29**, 4631 (1984).

[87] F. Sottile, F. Bruneval, A. G. Marinopoulos, L. K. Dash, S. Botti, V. Olevano, N. Vast, A. Rubio, and L. Reining, Int. J. Quantum Chem. **102**, 684 (2005).

[88] M. A. L. Marques, A. Castro, and A. Rubio, J. Chem. Phys. **115**, 3006 (2001).

[89] J. P. Perdew and S. Kurth, in *A primer in Density Functional Theory* (Springer-Verlag, ADDRESS, 2003), pp. 1–51.

[90] J. Lindhard, K. Dan. Vidensk. Selsk. Mat. Fys. Medd. **28**, 57 (1954).

[91] J. P. Perdew and K. Burke, Int. J. Quantum Chem. **57**, 309 (1996).

[92] J. P. Perdew, S. Kurth, A. Zupan, and P. Blaha, Phys. Rev. Lett. **82**, 2544 (1999).

[93] J. P. Perdew, S. Kurth, A. Zupan, and P. Blaha, Phys. Rev. Lett. **82**, (E) 5179 (1999).

[94] A. Castro, M. A. L. Marques, J. A. Alonso, and A. Rubio, J. Comp. Theoret. Nanoscience **1**, 231 (2004).

[95] I. G. Gurtubay, J. M. Pitarke, W. Ku, A. G. Eguiluz, B. C. Larson, J. Tischler, P. Zschack, and K. D. Finkelstein, Phys. Rev. B **70**, 201201(R) (2004).

[96] T. Ando, Z. Phys. B **26**, 263 (1977).

[97] K. Yabana and G. F. Bertsch, Int. J. Quantum Chem. **75**, 55 (1999).

[98] G. Onida, W. G. Schmidt, O. Pulci, M. Palummo, A. Marini, C. Hogan, and R. Del Sole, Phys. Status Solidi (a) **188**, 1261 (2001).

[99] M. A. L. Marques, X. López, D. Varsano, A. Castro, and A. Rubio, Phys. Rev. Lett. **90**, 258101 (2003).

[100] M. A. L. Marques and S. Botti, J. Chem. Phys. **123**, 014310 (2005).

[101] D. Rappoport and F. Furchte, in *Time-Dependent Density Functional Theory*, Vol. 706 of *Lecture Notes in Physics*, edited by M. A. L. Marques, K. A. Ullrich, F. Nogueira, A. Rubio, K. Burke, and E. K. U. Gross (Springer, Berlin, Heidelberg, 2006), Chap. 23, pp. 337–54.

[102] B. Champagne, E. A. Perpète, S. J. A. van Gisbergen, E.-J. Baerends, J. G. Snijders, C. Soubra-Ghaoui, K. A. Robins, and B. Kirtman, J. Chem. Phys. **109**, 10489 (1998).

[103] O. V. Gritsenko and E. J. Baerends, Phys. Rev. A **64**, 042506 (2001).

[104] S. Botti, A. Fourreau, F. Nguyen, Y-O. Renault, F. Sottile, and L. Reining, Phys. Rev. B **72**, 125203 (2005).

[105] D. M. Roessler and W. C. Walker, J. Opt. Soc. Am. **57**, 835 (1967).

[106] S. Albrecht, L. Reining, R. Del Sole, and G. Onida, Phys. Rev. Lett. **80**, 4510 (1998).

[107] L. X. Benedict, E. L. Shirley, and R. B. Bohn, Phys. Rev. Lett. **80**, 4514 (1998).

[108] M. Rohlfing and S. G. Louie, Phys. Rev. Lett. **81**, 2312 (1998).

[109] M. Rohlfing and S. G. Louie, Phys. Rev. B **62**, 4927 (2000).

[110] P. Lautenschlager, M. Garriga, L. Viña, and M. Cardona, Phys. Rev. B **36**, 4821 (1987).

[111] J. Stiebling, Z. Phys. B **31**, 355 (1978).

[112] V. Olevano and L. Reining, Phys. Rev. Lett. **86**, 5962 (2001).

[113] A. Marinopoulos, L. Reining, V. Olevano, A. Rubio, T. Pichler, X. Liu, M. Knupfer, and J. Fink, Phys. Rev. Lett. **89**, 76402 (2002).

[114] N. Vast, L. Reining, V. Olevano, P. Schattschneider, and B. Jouffrey, Phys. Rev. Lett. **88**, 037601 (2002).

[115] L. K. Dash, N. Vast, Ph. Baranek, M.-C. Cheynet, and L. Reining, Phys. Rev. B **70**, 245116 (2004).

[116] R. van Leeuwen and E. J. Baerends, Phys. Rev. A **49**, 2421 (1994).

[117] J. F. Dobson, M. J. Bünner, and E. K. U. Gross, Phys. Rev. Lett. **79**, 1905 (1997).

[118] I. V. Tokatly, in *Time-Dependent Density Functional Theory*, Vol. 706 of *Lecures Notes in Physics*, edited by M. A. L. Marques, K. A. Ullrich, F. Nogueira, A. Rubio, K. Burke, and E. K. U. Gross (Springer, Berlin, Heidelberg, 2006), Chap. 8, pp. 123–36.

[119] N. T. Maitra, J. Chem. Phys. **122**, 234104 (2005).

[120] N. T. Maitra, F. Zhang, R. J. Cave, and K. Burke, J. Chem. Phys. **120**, 5932 (2004).

[121] R. J. Cave, F. Zhang, N. T. Maitra, and K. Burke, Chem. Phys. Lett. **389**, 39 (2004).

[122] M. E. Casida, J. Chem. Phys. **122**, 054111 (2005).

[123] D. J. Tozer and N. C. Handy, Phys. Chem. Chem. Phys. **2**, 2117 (2000).

[124] S. Hirata and M. Head-Gordon, Chem. Phys. Lett. **302**, 375 (1999).

[125] R. van Leeuwen, Phys. Rev. Lett. **76**, 3610 (1996).

[126] L. J. Sham and M. Schlüter, Phys. Rev. Lett. **51**, 1888 (1983).

[127] F. Bruneval, F. Sottile, V. Olevano, and L. Reining, J. Chem. Phys. **124**, 144113 (2006).

[128] Y.H. Kim and A. Görling, Phys. Rev. B **66**, 35114 (2002).

[129] Y.H. Kim and A. Görling, Phys. Rev. Lett. **89**, 96402 (2002).

[130] R. T. Sharp and G. K. Horton, Phys. Rev. **90**, 317 (1953).

[131] J. D. Talman and W. F. Shadwick, Phys. Rev. A **14**, 36 (1976).

[132] A. Görling, Phys. Rev. B **56**, 7024 (1996).

[133] A. Görling, Phys. Rev. B **59**, 10370(E) (1999).

[134] M. Städele, M. Moukara, J. A. Majewski, P. Vogl, and A. Görling, Phys. Rev. B **59**, 10031 (1999).

[135] T. Kotani, Phys. Rev. B **50**, 14816 (1994).

[136] T. Kotani, Phys. Rev. B **51**, 13903(E) (1995).

[137] T. Kotani, Phys. Rev. Lett. **74**, 2989 (1995).

[138] T. Kotani and H. Akai, Phys. Rev. B **54**, 16502 (1996).

[139] M. Städele, J. A. Majewski, P. Vogl, and A. Görling, Phys. Rev. Lett. **79**, 2089 (1997).

[140] R. J. Magyar, A. Fleszar, and E. K. U. Gross, Phys. Rev. B **69**, 045111 (2004).

[141] J. P. Perdew and M. Levy, Phys. Rev. Lett. **51**, 1884 (1983).

[142] I. V. Tokatly and O. Pankratov, Phys. Rev. Lett. **86**, 2078 (2001).

[143] C. F. Richardson and N. W. Ashcroft, Phys. Rev. B **50**, 8170 (1994).

[144] F. Brosens, J. T. Devrese, and L. F. Lemmens, Phys. Rev. B **21**, 1363 (1980).

[145] W. G. Aulbur, M. Städele, and A. Görling, Phys. Rev. B **62**, 7121 (2000).

[146] M. Grüning, A. Marini, and A. Rubio, J. Chem. Phys. **124**, 154108 (2006).

[147] F. Bruneval, F. Sottile, V. Olevano, R. Del Sole, and L. Reining, Phys. Rev. Lett. **94**, 186402 (2005).

[148] P. Streitenberger, Phys. Stat. Sol.(B) **125**, 681 (1884).

[149] P. Streitenberger, Phys. Lett. A **106**, 57 (1884).

[150] R. Del Sole, G. Adragna, V. Olevano, and L. Reining, Phys. Rev. B **67**, 045207 (2003).

[151] M. E. Casida, in *Recent Advances in Density Functional Methods* (World Scientific, Singapore, 1995), p. 155, ed. by D. P. Chong.

[152] *Time-Dependent Density Functional Theory*, *Lecture Notes in Physics*, edited by M. A. L. Marques, C. A. Ullrich, F. Nogueira, A. Rubio, K. Burke, and E. K. U. Gross (Springer, Heidelberg, 2006).

[153] I. V. Tokatly, R. Stubner, and O. Pankratov, Phys. Rev. B **65**, 113107 (2002).

[154] P. L. de Boeij, F. Kootstra, J. A. Berger, R. van Leeuwen, and G. Snijders, J. Chem. Phys. **115**, 1995 (2001).

[155] M. van Faassen, P. L. de Boeij, R. van Leeuwen, J. A. Berger, and J. G. Snijders, J. Chem. Phys. **118**, 1044 (2003).

[156] A. Marini, R. Del Sole, and A. Rubio, in *Time-Dependent Density Functional Theory*, Vol. 706 of *Lecture Notes in Physics*, edited by M. A. L. Marques, C. A. Ullrich, F. Nogueira, A. Rubio, K. Burke, and E. K. U. Gross (Springer, Berlin, Heidelberg, 2006), Chap. 20, pp. 301–16.

[157] D. Varsano, R. Di Felice, M. A. L. Marques, and A. Rubio, J. Phys. Chem. B **110**, 7129 (2006).

[158] Ph. Ghosez, X. Gonze, and R. W. Godby, Phys. Rev. B **56**, 12811 (1997).

[159] P. Lautenschlager, M. Garriga, S. Logothetidis, and M. Cardona, Phys. Rev. B **35**, 9174 (1987).

[160] F. Sottile, K. Karlsson, L. Reining, and F. Aryasetiawan, Phys. Rev. B **68**, 205112 (2003).

[161] R. W. Godby and L. J. Sham, Phys. Rev. B **49**, 1849 (1994).

[162] W. G. Aulbur, L. Jönsson, and J. W. Wilkins, Phys. Rev. B **54**, 8540 (1996).

[163] G. Vignale and W. Kohn, in *Electronic Density Functional Theory: Recent Progress and New Directions* (Plenum, New York, 1998), ed. by J. Dobson et al.

[164] L. X. Benedict, E. L. Shirley, and R. B. Bohn, Phys. Rev. B **57**, R9385 (1998).

[165] J.E. Rowe and D.E. Aspnes, Phys. Rev. Lett. **25**, 162 (1970).

[166] J.E. Rowe and D.E. Aspnes, Phys. Rev. Lett. **25**, 979 (E) (1970).

[167] R. M. Martin, J. A. van Vechten, J. E. Rowe, and D. E. Aspnes, Phys. Rev. B **6**, 2500 (1972).

[168] N. F. Schwabe and R. J. Elliott, Phys. Rev. B **53**, 5318 (1996).

[169] I. Egri, Physics Report **119**, 363 (1985), and references therein.

[170] M. Law, J. Goldberger, and P. Yang, Annu. Rev. Mater. Sci. **34**, 83 (2004).

[171] D. J. Sirbuly, M. Law, H. Yan, and P. Yang, The journal of Physical Chemistry B **109**, 15190 (2005).

[172] C. X. Shan, Z. Liu, and S. K. Hark, Phys. Rev. B **74**, 153402 (2006).

[173] Gregory D. Scholes and Garry Rumbles, Nat. Mater. **5**, 683 (2006).

[174] Yat Li, Fang Qian, Jie Xiang, and Charles M. Lieber, Mater. Today **9**, 18 (2006).

[175] J. Li and L.-W. Wang, Phys. Rev. B **72**, 125325 (2005).

[176] S. P. Huang, W. D. Cheng, D. S. Wu, J. M. Hu, J. Shen, Z. Xie, H. Zhang, and Y. J. Gong, Appl. Phys. Lett. **90**, 135301 (2007).

[177] Q. Zhao, P. A. Graf, W. B. Jones, A. Franceschetti, J. Li, L.-W. Wang, and K. Kim, Nano Lett. **7**, 3274 (2007).

[178] A. G. Marinopoulos, L. Reining, A. Rubio, and N. Vast, Phys. Rev. Lett. **91**, 046402 (2003).

[179] F. Bruneval, S. Botti, and L. Reining, Phys. Rev. Lett. **94**, 219701 (2005).

[180] X. Zhao, C. M. Wei, L. Yang, and M. Y. Chou, Phys. Rev. Lett. **92**, 236805 (2004).

[181] S. Botti, A. Schindlmayr, R. Del Sole, and L. Reining, Rep. Prog. Phys. **70**, 357 (2007).

[182] X. Gonze, J.M. Beuken, R. Caracas, F. Detraux, M. Fuchs, G.M. Rignanese, L. Sindic, M. Verstraete, G. Zerah, F. Jollet, M. Torrent, A. Roy, M. Mikami, P. Ghosez, J.Y. Raty, and D.C. Allan, Computational Materials Science **25**, 478 (2002).

[183] D. R. Hamann, Phys. Rev. B **40**, 2980 (1989).

[184] H. J. Monkhorst and J. D. Pack, Phys. Rev. B **13**, 5188 (1976).

[185] S. Li and G. W. Yang, Appl. Phys. Lett. **95**, 073106 (2009).

[186] O. Zakharov, A. Rubio, X. Blase, M. L. Cohen, and S. G. Louie, Phys. Rev. B **50**, 10780 (1994).

[187] F. Bruneval and X. Gonze, Phys. Rev. B **78**, 085125 (2008).

[188] S. Ismail-Beigi, Phys. Rev. B **73**, 233103 (2006).

[189] M. Bruno, M. Palummo, A. Marini, R. Del Sole, V. Olevano, A. N. Kholod, and S. Ossicini, Phys. Rev. B **72**, 153310 (2005).

[190] L.-Ch. Yang, M. L. Cohen, and S. G. Louie, Nano Lett. **7**, 3112 (2007).

[191] M. Bruno, M. Palummo, A. Marini, R. Del Sole, and S. Ossicini, Phys. Rev. Lett. **98**, 036807 (2007).

[192] C. D. Spataru, S. Ismail-Beigi, L. X. Benedict, and S. G. Louie, Phys. Rev. Lett. **92**, 077402 (2004).

[193] H. Yu, J. Li, R. A. Loomis, P. C. Gibbons, L.-W. Wang, and W. E. Buhro, J. Am. Chem. Soc. **125**, 16168 (2003).

[194] Q. Dai, Y. Song, D. Li, H. Chen, S. Kan, B. Zou, Y. Wang, Y. Deng, Y. Hou, S. Yu, L. Chen, B. Liu, and G. Zou, Chem. Phys. Lett. **439**, 65 (2007).

[195] M.G. Bawendi, M.L. Steigerwald, and L.E. Brus, Ann. Rev. Phys. Chem. **41**, 477 (1990).

[196] S. Coe, W.K. Woo, M. Bawendi, and V. Bulovic, Nature **420**, 800 (2002).

[197] M.J. Bowers, J.R. McBride, and S.J. Rosenthal, J. Am. Chem. Soc. **127**, 15378 (2005).

[198] N. Tessler, V. Medvedev, M. Kazes, S.H. Kan, and U. Banin, Science **295**, 1506 (2002).

[199] V.I. Klimov, Los Alamos Sci. **28**, 214 (2003).

[200] N.C. Greenham, X.G. Peng, and A.P. Alivisatos, Phys. Rev. B **54**, 17628 (1996).

[201] M.T. Harrison, S.V. Kershaw, M.G. Burt, A.L. Rogach, A. Kornowski, A. Eychmuller, and H. Weller, Pure and Applied Chemistry **72**, 295 (2000).

[202] M. Bruchez, M. Moronne, P. Gin, S. Weiss, and A.P. Alivisatos, Science **281**, 2013 (1998).

[203] X. Michalet, F.F. Pinaud, L.A. Bentolila, J.M. Tsay, S. Doose, J.J. Li, G. Sundaresan, A.M. Wu, S.S. Gambhir, and S. Weiss, Science **307**, 538 (2005).

[204] C.B. Murray, D.J. Norris, and M.G. Bawendi, J. Am. Chem. Soc. **115**, 8706 (1993).

[205] X.G. Peng, L. Manna, W.D. Yang, J. Wickham, E. Scher, A. Kadavanich, and A.P. Alivisatos, Nature **404**, 59 (2000).

[206] W.C.W. Chan and S.M. Nie, Science **281**, 2016 (1998).

[207] A. Kasuya, R. Sivamohan, Y.A. Barnakov, I.M. Dmitruk, T. Nirasawa, V.R. Romanyuk, V. Kumar, S.V. Mamykin, K. Tohji, B. Jeyadevan, K. Shinoda, T. Kudo, O. Terasaki, Z. Liu, R.V. Belosludov, V. Sundararajan, and Y. Kawazoe, Nature Materials **3**, 99 (2004).

[208] A. Kasuya, Y. Noda, I. Dmitruk, V. Romanyuk, Y. Barnakov, K. Tohji, V. Kumar, R. Belosludov, Y. Kawazoe, and N. Ohuchi, Eur. Phys. J. D **34**, 39 (2005).

[209] S. Botti and M. A. L. Marques, Phys. Rev. B **75**, 035311 (2007).

[210] J.E.B. Katari, V.L. Colvin, and A.P. Alivisatos, J. Phys. Chem. **98**, 4109 (1994).

[211] M.A. Hines and P. Guyot-Sionnest, J. Phys. Chem. **100**, 468 (1996).

[212] W. Chen, Z.G. Wang, Z.J. Lin, and L.Y. Lin, J. Appl. Phys. **82**, 3111 (1997).

[213] X.G. Peng, M.C. Schlamp, A.V. Kadavanich, and A.P. Alivisatos, J. Am. Chem. Soc. **119**, 7019 (1997).

[214] B.O. Dabbousi, J. RodriguezViejo, F.V. Mikulec, J.R. Heine, H. Mattoussi, R. Ober, K.F. Jensen, and M.G. Bawendi, J. Phys. Chem. B **101**, 9463 (1997).

[215] F.V. Mikulec and M.G. Bawendi, in *Nanophase and Nanocomposite Materials III*, Vol. 581 of *Materials Research Society Symposium Proceedings*, edited by S. Komarneni, J.C. Parker, and H. Hahn (PUBLISHER, ADDRESS, 2000), pp. 139–144.

[216] Z.A. Peng and X.G. Peng, J. Am. Chem. Soc. **123**, 183 (2001).

[217] D.V. Talapin, S. Haubold, A.L. Rogach, A. Kornowski, M. Haase, and H. Weller, J. Phys. Chem. B **105**, 2260 (2001).

[218] N Gaponik, DV Talapin, AL Rogach, A Eychmuller, and H Weller, Nano Letters **2**, 803 (2002).

[219] N. Gaponik, D.V. Talapin, A.L. Rogach, K. Hoppe, E.V. Shevchenko, A. Kornowski, A. Eychmuller, and H. Weller, J. Phys. Chem. B **106**, 7177 (2002).

[220] P. Reiss, J. Bleuse, and A. Pron, Nano Letters **2**, 781 (2002).

[221] W.W. Yu, Y.A. Wang, and X.G. Peng, Chemistry of Materials **15**, 4300 (2003).

[222] H. Zhang, Z.C. Cui, Y. Wang, K. Zhang, X.L. Ji, C.L. Lu, B. Yang, and M.Y. Gao, Advanced Materials **15**, 777 (2003).

[223] W.W. Yu, L.H. Qu, W.Z. Guo, and X.G. Peng, Chemistry of Materials **15**, 2854 (2003).

[224] X.H. Zhong, Z.H. Zhang, S.H. Liu, M.Y. Han, and W. Knoll, J. Phys. Chem. B **108**, 15552 (2004).

[225] Q. Dai, D. Li, H. Chen, S. Kan, H. Li, S. Gao, Y. Hou, B. Liu, and G. Zou, J. Phys. Chem. B **110**, 16508 (2006).

[226] N. Pradhan, H.F. Xu, and X.G. Peng, Nano Letters **6**, 720 (2006).

[227] V.N. Soloviev, A. Eichhofer, D. Fenske, and U. Banin, J. Am. Chem. Soc. **122**, 2673 (2000).

[228] C. Landes, M. Braun, C. Burda, and M.A. El-Sayed, Nano Letters **1**, 667 (2001).

[229] S. Kudera, M. Zanella, C. Giannini, A. Rizzo, Y. Li, G. Gigli, R. Cingolani, G. Ciccarella, W. Spahl, W. J. Parak, and L. Manna, Advanced Materials **19**, 548 (2007).

[230] Q. Dai, D. Li, J. Chang, Y. Song, S. Kan, H. Chen, B. Zou, W. Xu, S. Xu, B. Liu, and G. Zou, Nanotechnology **18**, 405603 (2007).

[231] J. Ouyang, Md. B. Zaman, F. J. Yan, D. Johnston, G. Li, X. Wu, D. Leek, C. I. Ratcliffe, J. A. Ripmeester, and K. Yu, **112**, 13805 (2008).

[232] E. Kucur, J. Ziegler, and T. Nann, Small **4**, 883 (2008).

[233] J.J. Shiang, A.V. Kadavanich, R.K. Grubbs, and A.P. Alivisatos, J. Phys. Chem. **99**, 17417 (1995).

[234] E. Rabani, J. Chem. Phys. **115**, 1493 (2001).

[235] P. Sarkar and M. Springborg, Phys. Rev. B **68**, 235409 (2003).

[236] A. Puzder, A.J. Williamson, F. Gygi, and G. Galli, Phys. Rev. Lett. **92**, 217401 (2004).

[237] J.M. Soler, E. Artacho, J.D. Gale, A. Garcia, J. Junquera, P. Ordejon, and D. Sanchez-Portal, J. Phys.: Condens. Matter **14**, 2745 (2002).

[238] J. P. Perdew and A. Zunger, Phys. Rev. B **23**, 5048 (1981).

[239] N. Troullier and J. L. Martins, Phys. Rev. B **43**, 1993 (1991).

[240] G. Kresse and J. Furthmüller, Phys. Rev. B **54**, 11169 (1996).

[241] D. Vanderbilt, Phys. Rev. B **41**, 7892 (1990).

[242] J.Y. Zhang, X.Y. Wang, M. Xiao, L. Qu, and X. Peng, Appl. Phys. Lett. **81**, 2076 (2002).

[243] M. A. L. Marques, A. Castro, G. F. Bertsch, and A. Rubio, Comp. Phys. Comm. **151**, 60 (2003).

[244] A. Castro, M. A. L. Marques, H. Appel, M. Oliveira, C. Rozzi, X. Andrade, F. Lorenzen, E. K. U. Gross, and A. Rubio, Phys. Stat. Sol. (b) **243**, 2465 (2006).

[245] A. Castro, M. A. L. Marques, J. A. Alonso, J. F. Bertsch, K. Yabana, and A. Rubio, J. Chem. Phys. **116**, 1930 (2002).

[246] D. E. H. Jones, New. Sci. **32**, 245 (1966).

[247] E. Osawa, Kagaku **25**, 854 (1970).

[248] D. A. Bochvar and E. G. Gal'pern, Proc. Adad. Sci. USSR **209**, 239 (1973).

[249] H. Kroto, J. Heath, S. O'Brien, R. Curl, and R. Smalley, Nature **318**, 162 (1985).

[250] N. Gonzalez Szwacki, A. Sardzadeh, and B. I. Yakobson, Phys. Rev. Lett. **98**, 166804 (2007), erratum: ibid. **100**, 159901 (2008).

[251] I. Boustani and A. Quandt, Europhys. Lett. **39**, 527 (1997).

[252] D. Ciuparu, R. F. Klie, Y. Zhu, and L. Pfefferle, J. Phys. Chem. B **108**, 3967 (2004).

[253] H. Tang and S. Ismail-Beigi, Phys. Rev. Lett. **99**, 115501 (2007).

[254] X. Yang, Y. Ding, and J. Ni, 77 **Phys. Rev. B**, 041402(R) (2008).

[255] G. Gopakumar, M. T. Nguyen, and Arnout Ceulemans, Chem. Phys. Lett. **450**, 175 (2008).

[256] A. Ceulemans, J. T. Muya, G. Gopakumar, and M. T. Nguyen, Chem. Phys. Lett. **461**, 226 (2008).

[257] T. Baruah, M. R. Pederson, and R. Zope, Phys. Rev. B **78**, 045408 (2008).

[258] A. Sadrzadeh, O. V. Pupysheva, A. K. Singh, and Boris I. Yakobson, J. Phys. Chem. A **112**, 13679 (2008).

[259] I. Boustani, Phys. Rev. B **55**, 16426 (1997).

[260] C. Amovilli and N. H. March, Chem. Phys. Lett. **347**, 459 (2001).

[261] L. Hanley, J. Witten, and S. L. Anderson, J. Phys. Chem. **92**, 5803 (1988).

[262] S. J. La Placa, P. A. Roland, and J. J. Wynne, j-CPL **190**, 163 (1992).

[263] H.-J. Zhai, L.-S. Wang, A. N. Alexandrova, and A. I. Boldyrev, J. Chem. Phys. **177**, 7917 (2002).

[264] H.-J. Zhai, A. N. Alexandrova, K. A. Birch, A. I. Boldyrev, and L.-S. Wang, Angew. Chem. Int. Ed. **42**, 6004 (2003).

[265] H.-J. Zhai, B. Kiran, J. Li, and L.-S. Wang, Nat. Mater **2**, 827 (2003).

[266] S. Kiran, S. Bulusu, H.-J. Zhai, S. Yoo, X. C. Zeng, and L.-S. Wang, Proc. Natl. Acad. Sci. U.S.A. **102**, 961 (2005).

[267] Q. B. Yan, X. L. Sheng, Q. R. Zheng, L. Z. Zhang, and G. Su, Phys. Rev. B **78**, 201401(R) (2008).

[268] X. M. Meng, J. Q. Hu, Y. Jiang, C. S. Lee, and S. T. Lee, Chem. Phys. Lett. **370**, 825 (2003).

[269] I. Boustani, A. Quandt, E. Hernández, and A. Rubio, J. Chem. Phys. **110**, 3176 (1999).

[270] A. Quandt and I. Boustani, Chem. Phys. Chem. **6**, 2001 (2005).

[271] R. N. Grimes, J. Chem. Education **81**, 657 (2004).

[272] H. Kato and E. Tanaka, J. Comput. Chem. **12**, 1097 (1992).

[273] H. Kato and K. Yamashita, Chem. Phys. Lett. **190**, 361 (1992).

[274] A. K. Ray, I. A. Howard, and K. M. Kanal, Phys. Rev. B **45**, 14247 (1992).

[275] A. C. Tang, Q. S. Li, C. W. Liu, and J. Li, Chem. Phys. Lett. **201**, 465 (1993).

[276] J. Niu, K. Rao, and P. Jena, J. Chem. Phys. **107**, 132 (1997).

[277] I. Boustani, A. Rubio, and J. A. Alonso, Chem. Phys. Lett. **311**, 21 (1999).

[278] S. Chacko, D. G. Kanhere, and I. Boustani, Phys. Rev. B **68**, 035414 (2003).

[279] V. Elser and R. C. Haddon, Nature **325**, 792 (1987).

[280] V. Elser and R. C. Haddon, Phys. Rev. A **36**, 4579 (1987).

[281] F. London, Phys. Rad. **8**, 397 (1937).

[282] R. C. Haddon et al., Nature **350**, 46 (1991).

[283] R. C. Haddon, Nature **378**, 249 (1995).

[284] L. Pauling, J. Chem. Phys. **4**, 673 (1936).

[285] M. Buhl and A. Hirsch, Chem. Rev. **101**, 1153 (2001).

[286] K. Y. Zubarev and A. I. Boldyrev, J. Comp. Chem. **28**, 251 (2006).

[287] M. P. Johansson, J. Phys. Chem. C **113**, 524 (2009).

[288] S. Baroni, S. De Gironcoli, A. Dal Corso, and P. Giannozzi, Rev. Mod. Phys. **73**, 515 (2001).

[289] G. Malloci, G. Mulas, and C. Joblin, A & A **426**, 105 (2004).

[290] X. López, M. A. L. Marques, A. Castro, and A. Rubio, J. Am. Chem. Soc. **127**, 12329 (2005).

[291] X. Andrade, S. Botti, M. A. L. Marques, and A.Rubio, J. Chem. Phys. **126**, 184106 (2007).

[292] C. J. Pickard and F. Mauri, Phys. Rev. Lett. **91**, 196401 (2003).

[293] D.L. Lichtenberger, M.E. Jatcko, K.W. Nebesny, C.D. Ray, D.R. Huffman, and L.D. Lamb, Chem. Phys. Lett. **176**, 203 (1991).

[294] O. Bisi, S. Ossicini, and L. Pavesi, Surf. Sci. Rep. **38**, 1 (2000).

[295] W. Lu and Ch. M Lieber, J. Physics D: Appl. Phys. **39**, R387 (2006).

[296] S. Takeoka, M. Fujii, S. Hayashi, and K. Yamamoto, Phys. Rev. B **58**, 7921 (1998).

[297] J. P. Wilcoxon, P. P. Provencio, and G. A. Samara, Phys. Rev. B **64**, 035417 (2001).

[298] Ch. Schubert, U. Kaiser, A. Hedler, W. Wesch, T. Gorelik, U. Glatzel, J. Kraeuß lich, B. Wunderlich, G. Heß, and K. Goetz, J. Appl. Phys. **91**, 1520 (2002).

[299] H.-Ch. Weissker, J. Furthmüller, and F. Bechstedt, Phys. Rev. B **65**, 155328 (2002).

[300] H.-Ch. Weissker, J. Furthmüller, and F. Bechstedt, Phys. Rev. B **67**, 245304 (2003).

[301] H.-Ch. Weissker, J Furthmüller, and F Bechstedt, Mat. Sci. Eng. B **101**, 39 (2003).

[302] A. N. Kholod, S. Ossicini, V. E. Borisenko, and F.A. d'Avitaya, Phys. Rev. B **65**, 115315 (2002).

[303] A. N. Kholod, V. L. Shaposhnikov, N. Sobolev, V. E. Borisenko, F. A. D'Avitaya, and S. Ossicini, Phys. Rev. B **70**, 035317 (2004).

[304] A. Tsolakidis and R. M. Martin, Phys. Rev. B **71**, 125319 (2005).

[305] D.V. Melnikov and J.R. Chelikowsky, Solid Stats Comm. **127**, 361 (2003).

[306] H.-Ch. Weissker, J. Furthmüller, and F. Bechstedt, Phys. Rev. B **69**, 115310 (2004).

[307] O. G. Schmidt, U. Denker, S. Christiansen, and F. Ernst, Appl. Phys. Lett. **81**, 2614 (2002).

[308] S. Takeoka, K. Toshikiyo, M. Fujii, S. Hayashi, and K. Yamamoto, Phys. Rev. B **61**, 15988 (2000).

[309] H.-Ch. Weissker, J. Furthmüller, and F. Bechstedt, Phys. Rev. Lett. **90**, 085501 (2003).

[310] J.-E. Yang, C.-B. Jin, C.-J. Kim, and M.-H. Jo, Nano Letters **6**, 2679 (2006).

[311] D. B. Migas and V. E. Borisenko, Phys. Rev. B **76**, 035440 (2007).

[312] C. Delerue, M. Lannoo, and G. Allan, Phys. Rev. Lett. **84**, 2457 (2000).

[313] H.-Ch. Weissker, J. Serrano, S. Huotari, F. Bruneval, F. Sottile, G. Monaco, M. Krisch, V. Olevano, and L. Reining, Phys. Rev. Lett. **97**, 237602 (2006).

[314] H.-Ch. Weissker, J. Furthmüller, and F. Bechstedt, Phys. Rev. B **67**, 165322 (2003).

[315] G. Kresse and J. Furthmüller, Comput. Mater. Sci. **6**, 15 (1996).

[316] P. E. Blöchl, Phys. Rev. B **50**, 17953 (1994).

[317] S. G. Louie, S. Froyen, , and M. L. Cohen, Phys. Rev. B **26**, 1738 (1982).

[318] M. E. Casida, in *Recent Developments and Applications of Modern Density Functional Theory*, edited by J.M. Seminario (Elsevier Science, Amsterdam, ADDRESS, 1996), p. 391.

[319] B. Adolph, J. Furthmüller, and F. Bechstedt, Phys. Rev. B **63**, 125108 (2001).

[320] H.-Ch. Weissker, J. Furthmüller, and F. Bechstedt, Phys. Rev. B **64**, 035105 (2001).

[321] P. Tognini, L. C. Andreani, M. Geddo, A. Stella, P. Cheyssac, R. Kofman, and A. Migliori, Phys. Rev. B **53**, 6992 (1996).

[322] E. Degoli, G. Cantele, E. Luppi, R. Magri, D. Ninno, O. Bisi, and S. Ossicini, Phys. Rev. B **69**, 155411 (2004).

[323] J.C. Maxwell-Garnett, Philos. Trans. R. Soc. **203**, 305 (1904).

[324] D. M. Wood and N. W. Ashcroft, Philos. Mag. **35**, 269 (1977).

[325] S. Botti, N. Vast, L. Reining, V. Olevano, and L.C. Andreani, Phys. Rev. Lett. **69**, 216803 (2002).

[326] S. Botti, N. Vast, L. Reining, V. Olevano, and L.C. Andreani, Phys. Rev. B **70**, 045301 (2004).

[327] J. Humlíček, M. Garriga, M. I. Alonso, and M. Cardona, J. Appl. Phys. **65**, 2827 (1989).

[328] H.-Ch. Weissker, Ralf Hambach, Valerio Olevano, and L. Reining, Phys. Rev. B **79**, 094102 (2009).

[329] DL Dexter, Solid State Physics – Advances in Research and Applications **6**, 353 (1958).

[330] C. Delerue, G. Allan, and M. Lannoo, Phys. Rev. B **48**, 11024 (1993).

[331] W. van Roosbroeck and W. Shockley, Phys. Rev. **94**, 1558 (1954).

[332] G. Cappellini, H.-Ch. Weissker, D. De Salvador, J., F. Bechstedt, G. Satta, F. Casula, and L. Colombo, JPCM **17**, 643 (2005).

[333] S. R. Ovshinsky, Phys. Rev. Lett. **21**, 1450 (1968).

[334] M. Libera and M. Chen, J. Appl. Phys. **73**, 2272 (1993).

[335] N. Yamada, MRS Bull. **21**, 48 (1996).

[336] M.H.R. Lankhorst, B.W. Ketelaars, and R.A.M. Wolters, Nature Materials **4**, 347 (2005).

[337] M. Wuttig, Nature Materials **4**, 265 (2005).

[338] J. Stuke and G. Zimmerer, Phys. Stat. Sol. B-Basic Research **49**, 513 (1972).

[339] A.V. Kolobov, P. Fons, A.I. Frenkel, A.L. Ankudinov, J. Tominaga, and T. Uruga, Nature Materials **3**, 703 (2004).

[340] A.V. Kolobov, P. Fons, J. Tominaga, A.L. Ankudinov, S.N. Yannopoulos, and K.S. Andrikopoulos, J. Phys.: Condens. Matter **16**, 5103 (2004).

[341] K. M. Rabe and J. D. Joannopoulos, Phys. Rev. B **36**, 6631 (1987).

[342] T. Matsunaga and N. Yamada, Phys. Rev. B **69**, 104111 (2004).

[343] W. Wełnic, A. Pamungkas, R. Detemple, C. Steimer, S. Blügel, and M. Wuttig, Nature Materials **5**, 56 (2006).

[344] V. Weidenhof, I. Friedrich, S. Ziegler, and M. Wuttig, J. Appl. Phys. **86**, 5879 (1999).

[345] W. E. Howard and R. Tsu, Phys. Rev. B **1**, 4709 (1970).

[346] V. Garbuio, M. Cascella, L. Reining, R. Del Sole, and O. Pulci, Phys. Rev. Lett. **97**, 137402 (2006).

[347] B.-S. Lee, J. R. Abelson, S. G. Bishop, D.-H. Kang, B.-K. Cheong, and K.-B. Kim, J. Appl. Phys. **97**, 093509 (2005).

[348] E. Garcia-Garcia, A. Mendoza-Galvan, Y. Vorobiev, E. Morales-Sanchez, J. Gonzalez-Hernandez, G. Martinez, and B.S. Chao, J. Vacuum Sciences & Technology A - Vacuum surfaces and thin films **17**, 1805 (1999).

[349] A. H. Edwards, A. C. Pineda, P. A. Schultz, M. G. Martin, A. P. Thompson, H. P. Hjalmarson, and C. J. Umrigar, Phys. Rev. B **73**, 045210 (2006).

[350] A. V. Kolobov, J. Tominaga, P. Fons, and T. Uruga, Appl. Phys. Lett. **82**, 382 (2003).

[351] M. Wuttig, D. Lüsebrink, D. Wamwangi, W. Wełnic, M. Gilleßen, and R. Dronskowski, Nature Materials **6**, 122 (2007).

[352] T. Kikukawa, T. Nakano, T. Shima, and J. Tominaga, Appl. Phys. Lett. **81**, 1 (2002).

[353] I. Repins, M. A. Contreras, B. Egaas, C. DeHart, J. Scharf, C. L. Perkins, B. To, and R. Noufi, Prog. Photovolt. **16**, 235 (2008).

[354] U. Rau and H.W. Schock, Appl. Phys. A **69**, 131 (1999).

[355] J. F. Guillemoles, L. Kronik, D. Cahen, U. Rau, A. Jasenek, and H. W. Schock, J. Phys. Chem. B **104**, 4849 (2000).

[356] J. E. Jaffe and A. Zunger, Phys. Rev. B **29**, 1882 (1984).

[357] J. M. Merino *et al.*, J. Appl. Phys. **80**, 5610 (1996).

[358] J. E. Jaffe and A. Zunger, Phys. Rev. B **27**, 5176 (1983).

[359] F. D. Jiang and J. Y. Feng, Semicond. Sci. Technol. **23**, 025001 (2008).

[360] M. I. Alonso *et al.*, Phys. Rev. B **63**, 075203 (2001).

[361] W. G. Aulbur, L. Jönsson, and JW Wilkins, Solid State Phys. **54**, 1 (2000).

[362] F. Aryasetiawan and O. Gunnarsson, Rep. Prog. Phys. **61**, 237 (1998).

[363] F. Fuchs, J. Furthmüller, F. Bechstedt, M. Shishkin, and G. Kresse, Phys. Rev. B **76**, 115109 (2007).

[364] X. Gonze *et al.*, Z. Kristallogr. **220**, 558 (2005).

[365] C. Domain, S. Laribia, S. Tauniera, and J. F. Guillemoles, J. Phys. Chem. Solids **64**, 1657 (2003).

[366] J. Łażewski, P. T. Jochym, and K. Parlinski, J. Chem. Phys. **117**, 2726 (2002).

[367] S.-H. Wei and Alex Zunger, Phys. Rev. B **37**, 8958 (1988).

[368] J. Heyd, G. E. Scuseria, and M. Ernzerhof, J. Chem. Phys. **118**, 8207 (2003).

[369] P.E. Blöchl, Phys. Rev. B **50**, 17953 (1994).

[370] G. Kresse and J. Joubert, Phys. Rev. B **59**, 1758 (1999).

[371] H. W. Spiess *et al.*, phys. stat. sol.(b) **62**, 183 (1974).

[372] S. C. Abrahams and J. L. Bernstein, J. Chem. Phys **59**, 5415 (1973).

[373] C. Persson and A. Zunger, Appl. Phys. Lett. **87**, 211904 (2005).

[374] S. B. Zhang *et al.*, Phys. Rev. B **57**, 9642 (1998).

[375] H. Z. Xiao, L.-Chung Yang, and A. Rockett, J. Appl. Phys. **76**, 1503 (1994).

[376] S. Lany and A. Zunger, Phys. Rev. B **78**, 235104 (2008).

[377] S. Nakamura, M. Senoh, and N. Iwasa, Jpn. J. Appl. Phys. **31**, L139 (1992).

[378] J. Neugebauer and Ch. G. Van de Walle, Phys. Rev. Lett. **75**, 4452 (1995).

[379] F.A. Benko and F.P. Koffyberg, J. Phys. Chem. Solids **45**, 57 (1984).

[380] H. Kawazoe, M. Yasukawa, H. Hyodo, M. Kurita, H. Yanagi, and H. Hosono, Nature **389**, 939 (1997).

[381] K. Ueda, T. Hase, H. Yanagi, H. Kawazoe, H. Hosono, H. Ohta, M. Orita, and M. Hirano, J. Appl. Phys. **89**, 1790 (2001).

[382] H. Yanagi, T. Hase, S. Ibuki, K. Ueda, and H. Hosono, Appl. Phys. Lett. **78**, 1583 (2001).

[383] H. Yanagi, S. Inoue, K. Ueda, H. Kawazoe, H. Hosono, and N. Hamada, J. Appl. Phys. **88**, 4159 (2000).

[384] A.N. Banerjee, S. Kundoo, and K.K. Chattopadhyay, Thin Solid Films **440**, 5 (2003).

[385] C.H. Ong and H. Gong, Thin Solid Films **445**, 299 (2003).

[386] T. Dittrich, L. Dloczik, T. Guminskaya, M.C. Lux-Steiner, N. Grigorieva, and I. Urban, Appl. Phys. Lett. **85**, 742 (2004).

[387] E.M. Alkoy and P.J. Kelly, Vacuum **79**, 221 (2005).

[388] A.N. Banerjee, R. Maity, and K.K. Chattopadhyay, Mat. Lett. **58**, 10 (2004).

[389] A.N. Banerjee and K.K. Chattopadhyay, J. Appl. Phys. **97**, 084308 (2005).

[390] A.N. Banerjee, C.K. Ghosh, S. Das, and K.K. Chattopadhyay, Physica B **370**, 264 (2005).

[391] R.-S. Yu, S.-C. Liang, C.-J. Lu, D.-C. Tasi, and F.-S. Shieu, Appl. Phys. Lett. **90**, 191117 (2007).

[392] S. Gilliland, J. Pellicer-Porres, A. Segura, A. Munoz, P. Rodriguez-Hernandez, D. Kim, M. S. Lee, and T. Y. Kim, Phys. Stat. Sol. (b) **244**, 309 (2007).

[393] J. Pellicer-Porres, A. Segura, A.S. Gilliland, A. Munoz, P. Rodriguez-Hernendez, D. Kim, M.S. Lee, and T.Y. Kim, Appl. Phys. Lett. **88**, 181904 (2006).

[394] Ch. W. Teplin, T. Kaydanova, D. L. Young, J. D. Perkins, D. S. Ginley, A. Ode, and D. W. Readey, Appl. Phys. Lett. **85**, 3789 (2004).

[395] M. Sasaki and M. Shimode, J. Phys. Chem. Solids **64**, 1675 (2003).

[396] E. N. Brothers, A. F. Izmaylov, J. O. Normand, V. Barone, and G. E. Scuseria, J. Chem. Phys. **129**, 011102 (2008).

[397] J. Paier, M. Marsman, and G. Kresse, Phys. Rev. B **78**, 121201 (2008).

[398] J. Hafner, J. Comput. Chem. **29**, 2044 (2008).

[399] R. Laskiwski, N. E. Christensen, P. Blaha, and B. Palanivel, Phys. Rev. B **79**, 165209 (2006).

[400] P.J. Stephens *et al.*, J. Phys. Chem. **98**, 11623 (1994).

[401] J. Heyd, G. E. Scuseria, and M. Ernzerhof, J. Chem. Phys. **124**, 219906 (2006).

[402] B. J. Ingram, T. O. Mason, R. Asahi, K. T. Park, and A. J. Freeman, Phys. Rev. B **64**, 155114 (2001).

[403] L.J. Shi, Z.J. Fang, and J. Li, J. Appl. Phys. **104**, 073527 (2008).

[404] X.L. Nie, S.H. Wei, and S.B. Zhang, Phys. Rev. Lett. **88**, 066405 (2002).

[405] J. Robertson, P.W. Peacock, M.D. Towler, and R. Needs, Thin Solid Films **411**, 96 (2002).

[406] Muhammad N. Huda, Yanfa Yan, Aron Walsh, Su-Huai Wei, and Mowafak M. Al-Jassim, Phys. Rev. B **80**, 035205 (2009).

[407] J Pellicer-Porres, A Segura, and D Kim, Semicond. Sci. Technol. **24**, 015002 (2009).

[408] F. Bechstedt, K. Seino, P. H. Hahn, and W. G. Schmidt, Phys. Rev. B **72**, 245114 (2005).

[409] I. Hamada and H. Katayama-Yoshida, Physica B **376–377**, 808 (2006).

[410] J. F. Dobson, K. McLennan, A. Rubio, J. Wang, T. Gould, H. M. Le, and B. P. Dinte, Aust. J. Chem. **54**, 513 (2001).

[411] P. W. Fowler, A. D. Buckingham, and J. M. Hunter, Chem. Rev. **88**, 963 (1988).

[412] J. S. Lee, Chem. Phys. Lett. **339**, 133 (2001).

[413] D. E. Woon, J. Chem. Phys. **100**, 2838 (1994).

[414] R. L. Rowley, C. M. Tracy, C. M. Pakkanen, and T. A Pakkanen, J. Chem. Phys. **125**, 154302 (2006).

[415] J. B. Anderson, C. A. Traynor, and B. M. Boghosian, J. Chem. Phys. **99**, 345 (1993).

[416] J. B. Anderson, J. Chem. Phys. **115**, 4546 (2001).

[417] J. F. Dobson, A. White, and A. Rubio, Phys. Rev. Lett. **96**, 073201 (2006).

[418] S. Grimme, J. Comput. Chem. **25**, 1463 (2004).

[419] B. Jeziorski, R. Moszynski, and K. Szalewicz, Chem. Rev. **94**, 1887 (1994).

[420] H. B. G. Casimir and D. Polder, Phys. Rev. **73**, 360 (1948).

[421] S. J. A. van Gisbergen, J. G. Snijders, and E. J. Baerends, J. Chem. Phys. **103**, 9347 (1995).

[422] H. C. Hamaker, Physica **4**, 1058 (1937).

[423] M. M. Calbi, S. M. Gatica, D. Velegol, and M. W. Cole, Phys. Rev. A **67**, 033201 (2003).

[424] H.-Y. Kim, J. O. Sofo, D. Velegol, and M. W. Cole, J. Chem. Phys. **125**, 174303 (2006).

[425] E. Zaremba and W. Kohn, Phys. Rev. B **13**, 2270 (1976).

[426] P. Norman, D. M. Bishop, H. J. A. Jensen, and J. Oddershede, J. Chem. Phys. **115**, 10323 (2001).

[427] P. Norman, A. Jiemchooroj, and B. E. Semelius, J. Chem. Phys. **118**, 9167 (2003).

[428] A. Jiemchooroj, P. Norman, and B. E. Semelius, J. Chem. Phys. **123**, 124312 (2005).

[429] A. Jiemchooroj, P. Norman, and B. E. Semelius, J. Chem. Phys. **125**, 124306 (2006).

[430] A. Banerjee and M. K. Harbola, J. Chem. Phys. **117**, 7845 (2002).

[431] A. Banerjee and M. K. Harbola, PRAMANA J. Phys. **66**, 423 (2006).

[432] L. Hedin, Phys. Scripta **21**, 477 (1980).

[433] R. Del Sole and R. Girlanda, Phys. Rev. B **48**, 11789 (1993).

[434] G. Malloci, G. Mulas, G. Cappellini, V. Fiorentini, and I. Porceddu, Astron. Astrophys. **432**, 585 (2005).

[435] G. Malloci, C. Joblin, and G. Mulas, Astron. Astrophys. **462**, 627 (2007).

[436] C. Joblin, G. Malloci, and G. Mulas, Chem. Phys. **332**, 353 (2007).

[437] M. Rapacioli, F. Calvo, F. Spiegelman, C. Joblin, and D. J. Wales, J. Phys. Chem. A. **109**, 2487 (2005).

[438] M. Rapacioli, F. Calvo, C. Joblin, P. Parneix, D. Toublanc, and F. Spiegelman, Astron. Astrophys. **460**, 519 (2006).

[439] A. Kumar and W. J. Meath, Mol. Phys. **75**, 311 (1992).

[440] S. Botti, A. Castro, X. Andrade, A. Rubio, and M. A. L. Marques, Phys. Rev. B **78**, 035333 (2008).

[441] A. O. Caride, G. L. Klimchitskaya, V. M. Mostepanenko, and S. I. Zanette, Phys. Rev. A **71**, 042901 (2005).

Acknowledgements

It is a pleasure to take the opportunity and thank those who made this mémoire of HDR possible with their help and support.

I want to express my deepest gratitude to the colleagues and collaborators at the Laboratorire des Solides Irradiés of the École Polytechnique, directed by Martine Soyer. In particular, I am grateful to the friends of the Theoretical Spectroscopy Group and ETSF for the many interesting discussions and for the good time we shared. I am heartily thankful to Lucia Reining for her enthusiastic encouragement and valuable guidance: working with her is always great. I miss the years spent at the LSI.
The colleagues at the Laboratoire de Physique de la Matière Condensée et Nanostructures of the Université "Claude Bernard" Lyon 1, directed by Jean-Louis Barrat, supported me in a number of ways: thank you for the warm welcome and the good working environment provided since my arrival. I am specially grateful to Miguel Marques for his enriching and generous participation in many common projects.
It is an honor for me to thank the "Rapporteurs", Claudia Amborsch-Draxl, Friedhelm Bechstedt and Claudine Noguera, who accepted the work of examining and reporting. My gratitude and appreciation go to the "Examinateurs", Lucia Reining, Alfonso San Miguel, Susanne Siebentritt and Ludger Wirtz.
Lastly, I wish to show my gratitude to all the collaborators and friends, without whom this work would not have been the same, in particular (in alphabetical order): Irene Aguilera, Xavier Andrade, Gaëlle Bruant, Fabien Bruneval, Alberto Castro, Andrea Cucca, Matteo Gatti, Christine Giorgetti, Jean-François Guillemoles, Marc Hayoun, Nektarios Lathiotakis, Xochitl Lopez-Lozano, Margherita Marsili, Fernando Nogueira, Valerio Olevano, Micael Oliveira, Pär Olsson, France Pochard, Angel Rubio, Francesco Sottile, Fabio Trani, Valérie Véniard, Julien Vidal, Guilherme Vilhena, Hansi Weissker, Wojtek Welnic, Ludger Wirtz.

I cannot finish without thanking Miguel, Samuel and Sara for being always there and making every day so special. I remain indebted to my parents who taught me to do my best in all matters of life.

Curriculum Vitæ

Personal data

- Born in Bergamo (Italy) on May 15, 1974.
- Nationality: Italian.
- Two children.
- Position (since 2004):
  Permanent Researcher of CNRS, the *French National Center for Scientific Research*.
- Permanent Address:
  Laboratoire des Solides Irradiés (LSI)
  and European Theoretical Spectroscopy Facility (ETSF)
  Ecole Polytechnique
  91128 Palaiseau
  France
- Present Address (since December 2007):
  Laboratoire de Physique de la Matière Condensée et Nanostructures (LPMCN)
  University of Lyon I
  Bâtiment Brillouin, Domaine scientifique de la DOUA,
  69622 Villeurbanne
- E-mail: silvana.botti@polytechnique.edu
- Web-page: `http://etsf.polytechnique.fr/People/`

Academic qualifications

- **July 17, 1998**: *Laurea* degree in Physics at the Università degli Studi di Pavia (Italy) with full marks (110/110) and *cum laude*.

  Title of the undergraduate thesis: "Computational methods for the electronic states and the optical properties of bulk semiconductors and superlattices".

  Supervisor: Prof. L.C. Andreani.

- **F**rom October 1998 to November 2001: *PhD studies* at the Università degli Studi di Pavia (Italy) and at the LSI-Ecole Polytechnique (France) under the supervision of Prof. L.C. Andreani and Dr. Lucia Reining.

- **February 1, 2002**: Ph.D. in Physics at the Università degli Studi di Pavia (Italy) with the highest mark ("Ottimo").

  Title of the thesis: "Semi-empirical and ab initio calculations of optical properties in semiconductor superlattices".

- "Qualification Maître de Conférence" awarded in 2003.

Professional experience

- **From November 2001 to November 2002**: Post-doc fellowship at the LSI-Ecole Polytechnique to work on developments of time-dependent density functional theory.
  Supervisor: Dr. Lucia Reining.
- **From December 2002 to November 2004**: Individual Marie Curie EU post-doc fellowship at the LSI-Ecole Polytechnique on the project "Electronic excitations in quantum wires: confinement, local fields and excitons".
  Supervisor: Dr. Lucia Reining.
- **Since September 2003**: Professor ("Enseignant vacataire") of the course PHY576 "Theoretical approaches to quantum properties of materials" at the Ecole Polytechnique.
- **Since December 2004**: Permanent researcher at the French National Center for Scientific Research (CNRS).
- **From April to September 2006**: Invited Professor at the Department of Physics, Universidade de Coimbra (Portugal).
- **From February to August 2007**: Visiting Researcher at the Department of Physics, Universidade de Coimbra (Portugal).
- **Since December 2007**: Visiting Researcher at the Laboratoire de Physique de la Matière Condensée et Nanostructures (LPMCN) of the University of Lyon I (France).
- **Since December 2008**: "Chargé de Recherche de prémière classe" at CNRS.
- **From April to August 2009**: Visiting Researcher within the program HPC Europa2 in the group of Prof. Angel Rubio at the Nano-bio Spectroscopy Group and European Theoretical Spectroscopy Facility, San Sebastian (Spain).

Teaching and training

Undergraduate courses:

- **From 1996 to 1998**: Tutor for the courses "General Physics II" and "Physics Laboratory II" at the Università degli Studi di Pavia (Italy).
- **From October 2002 to March 2003**: Supervisor for the Scientific Project of the 2nd year of 5 students of the Ecole Polytechnique (Physics major).
- **Since September 2003**: Professor of the course PHY576 (Programme d'approfondissement, 1st semester, 3rd year of the Physics major, Ecole Polytechnique):
  "Theoretical approaches to quantum properties of materials".
  Number of hours: 36
  Crédits ECTS : 5

  This course includes an introduction to density functional theory and a personal work using sophisticated software to compute the electronic properties of advanced materials and nanostructures. It is composed of three parts : The first part consists of theoretical classes where the students get familiar with the many-body problem in condensed matter and are introduced to density functional theory ; In the second part of the course the students learn how to use scientific programs based on density functional theory to study the electronic properties of materials. Finally, they perform an individual research project. These projects are truly original, and have already led to a publication in an international journal, coauthored by some of the students (Publication [16] of the publication list). The topics of the individual projects presented by the students have so far ranged from nanotechnologies (nanoclusters, nanotubes, nanowires..), biophysics, cold atoms to a bibliographical study of the mathematical foundations of density functional theory.

  `http://catalogue.polytechnique.fr/cours.php?id=3082&langue=FR`

Graduate courses:

- **November 24-28, 2003**: Teacher of theoretical and practical classes on TDDFT for solids at the "First Spectroscopy Lectures" held at the Ecole Polytechnique, Palaiseau (France).
- **August 28 - September 7, 2004**: Teacher of practical classes on TDDFT for solids at the International School: "Time dependent density-functional theory: prospects and applications" held in Benasque, Spain (8 hours of classes).
- **November 23-26, 2004**:Teacher of theoretical and practical classes on TDDFT for solids at the "Second Spectroscopy Lectures" held at the Ecole Polytechnique, Palaiseau (France).
- **August 27 - September 7, 2006**: Teacher of practical classes on TDDFT for solids at the 2nd International School "Time-Dependent Density Functional Theory: prospects and applications" held in Benasque (Spain).
- **December 11-15, 2006**: Teacher of practical classes on TDDFT for solids at the CECAM Workshop: "Electronic excitations and spectroscopies : theory and codes", held at CECAM in Lyon (France).
- **June 26-28, 2007**: Organizer and Teacher (in collaboration with Dr. Lucia Reining and Dr. Francesco Sottile, LSI Ecole Polytechnique) of the intensive training unit "Electronic excitations in materials and in nano-structures: theoretical methods, algorithms and computer tools" held at the Queen's University of Belfast (UK).
- **December 10-14, 2007**: Teacher of practical classes on TDDFT for solids at the CECAM Workshop: "Theoretical Spectroscopy Lectures: theory and codes", held at CECAM in Lyon (France).
- **April 14-16, 2008**: Teacher of the theoretical and practical classes "Key concepts in density functional theory" at the school "Curso de (TD)DFT: abinit e octopus" held at the University of Coimbra (Portugal).
- **August 31 - September 9, 2008**: Teacher of the theoretical classes "Theoretical Spectroscopy" and "Linear Response" at the 3nd International School "Time-Dependent Density Functional Theory: prospects and applications" held in Benasque (Spain).
- **January 2 - 10, 2010**: Teacher of the theoretical classes "Theoretical Spectroscopy" and "Linear Response" at the 4th International School "Time-Dependent Density Functional Theory: prospects and applications" held in Benasque (Spain).

Supervision of Students and Post-docs

See the publication list for the bibliographic references.

- **From October 2003 to September 2004**: Scientific supervisor of Wojtek Welnic (Ph.D. student of the Technical University of Aachen, Germany) for a 1-year stage within the Marie Curie Training Site action of the European Commission on the optical properties of phase change materials.
  Publications: [8],[11]
- **Since 2005**: Co-supervisor (together with Prof. A. Rubio, University of the Basque Country of San Sebastian, Spain) of the Ph.D. thesis of Xavier Andrade Valencia (Ph.D. student of the University of the Basque Country of San Sebastian, Spain) on the spectroscopic properties of finite systems within TDDFT.
  Publications: [7],[9],[12]
- **From Novembre 2006 to July 2009**: Supervisor of the post-doc researcher Dr. Xochitl Lopez-Lozano (funded by the ANR project CPONN n. JC05_46741 of the French National Research Agency (ANR)), who worked on the optical properties of nanotubes and nanowires.
  Publications: submitted.

- **Since 2007:** Co-supervisor (with Dr. Lucia Reining at LSI and Dr. Jean Francois Guillemoles at IRDEP, Chatou, France) of the Ph.D. thesis of Julien Vidal (LSI Ecole Polytechnique-EDF) on the photoexcitation properties of new chacopyrite materials for solar cells. This thesis if funded by EDF (French energy company).
  Publications: [3],[5]
- **From December 2007 to February 2008 and from July 2008 to September 2008**: Supervisor of two 3 month-stages of Irene Aguilera (Ph.D. student of the Universidad Politécnica de Madrid, Spain) on the optical properties of intermediate band materials for photovoltaic applications.
  Publications: in preparation.
- From December 2008 to November 2009: Co-supervisor (with Dr. Miguel Marques at LPMCN) of the post-doc researcher Dr. Fabio Trani (post-doc CNRS), who worked on the optical properties of transparent conductive oxides of the delafossite family.
  Publications: [3]
- From FEbruary 2009: Co-supervisor (with Dr. Miguel Marques at LPMCN) of the post-doc researcher Dr. Micael Oliveira (funded by the Portuguese Fundação para a Ciência e a Tecnologia (FCT).
  Publications: in preparation.

Administration

- **From May 2004 to December 2008**: Member of the NANOQUANTA network of excellence of the European Commission (FP6), and active member of the Integration Team of the network in charge of creating the *European Theoretical Spectroscopy Facility* (ETSF), a permanent "knowledge center" which will gather expertise, theory and related software, to study the properties of electronic excited states in nanoscale systems and advanced materials.
- **Since January 2008**: Member of the European Theoretical Spectroscopic Facility (ETSF) and "team leader" in the ETSF-I3 project funded by the FP7 Infrastructures Program of the European Commission. I am also participating in the activities of the "Work Package" WP6 "Delivering external training", in charge of the organization of training activities for the ETSF users.

  http://www.etsf.eu

Main research interests

- Theoretical study of electronic excitations in complex materials of technological interest: nanoparticles, quantum wires, superlattices, p or n type materials, systems with defect, etc., by ab initio calculations (density functional theory (DFT), time-dependent density functional theory (TDDFT), GW and Bethe-Salpeter equation techniques) and semi-empirical pseudopotential methods.
- Development of new approximations within TDDFT.
- Experience in classical and quantum Monte Carlo techniques (in particular for the study of spin systems) .
- Study of the optical response of photonic crystals.

Projects and Grants

- ANR Young Researchers project CPONN n. JC05_46741. Period: January 2006 - December 2008. Funded by the French National Research Agency (ANR). Project partners: Ludger Wirtz and Silvana Botti. Topic: Optical properties of nanotubes and nanowires within density functional theory and tight-binding.

Languages

- Italian (mother language), English and French (high level), Portuguese (good level), German (school level).

Recent Communications

Invited

- **January 11, 2010**: "Electronic properties of materials for thin-film solar cells: Which ab initio approaches can we trust?" at the 4th International Workshop "Time dependent Density-Functional Theory: Prospects and Applications" held in Benasque (Spain).
- **November 16, 2009**: "Electronic properties of materials for thin-film solar cells: Which ab initio approaches can we trust?" at the French-American Young Engineering Scientists Symposium 2009" held at the Synchrotron in Soleil, France.
- **September 14, 2009**: "Electronic properties of CIGS materials for photovoltaic conversion: self-consistent GW calculations" at the Computational Nanoscience for Renewable Energy Solutions Psi-k summer school held in Helsinki, Finland.
- **June 19, 2009**: "Electronic properties of materials for solar cells: which ab initio approaches can we trust?" at the Donostia International Physics Center, San Sebastian, Spain.
- **September 12, 2008**: "GW calculations of electronic properties of chalcopyrites for photovoltaic conversion" at the 3rd International Workshop "Time dependent Density-Functional Theory: Prospects and Applications" held in Benasque (Spain).
- **June 3, 2008**: "Ab initio modeling of optoelectronic properties of chalcopyrites for photovoltaic conversion" at the CECAM Workshop "Critical materials issues in photovoltaics: searching for solutions via theory and simulations" held at CECAM-EPFL, Lausanne (Switzerland).
- **May 23, 2008**:"Cluster-surface and cluster-cluster interactions: ab initio calculations and modelling of van der Waals forces" at the LPMCN, Lyon (France).
- **March 14, 2008**: "Density-functional based study of nanomaterials", at the IEMN, Département ISEN, Lille (France).
- **June 26-29, 2007**: Organization and teaching of the intensive training unit "Electronic excitations in materials and in nano-structures: theoretical methods, algorithms and computer tools" (with Francesco Sottile and Lucia Reining) at the Queen's University of Belfast (UK).

  Scientific seminar given during this event: "How do rewritable DVDs work? Optical properties of phase-change materials".
- **September 7-11, 2006**: "How do rewritable DVDs work: optical properties of phase-change materials" at the 2nd International Workshop "Time dependent Density-Functional Theory: Prospects and Applications" held in Benasque (Spain).
- **November 22, 2005**: "Effets de la taille sur les propriétés des nano-particules" at the "Atelier synthèse et traitement de nano-particules par plasmas basse pression" held in Gif sur Yvette (France).
- **May 6, 2005**: "TDDFT from clusters to solids" at the "Mini-workshop TDDFT" held at the University of Coimbra (Portugal).

Oral

- **September 21, 2005**: "The physics of CdSe nanocrystals" at the conference "Ψ_k 2005" held in Schwäbisch Gmünd (Germany).
- **May 2, 2005**: "TDDFT from clusters to solids" at the "2nd NANOQUANTA Young Researchers' meeting" held at the Fritz Haber Institute of Berlin (Germany).

Organization of scientific conferences

- Co-organizer of the “1st NANOPHASE/NANOQUANTA Young Researchers’ Meeting” held at the Ecole Polytechnique (Palaiseau) from May 6 to May 8, 2004 .

Publication List

For my researcher ID see http://www.researcherid.com/rid/A-6241-2010.
My current h-index is 9.

Books

Chapters of Books

1 S. Botti, "Fullerene-like CdSe nanoparticles", to be published in *Handbook of Nanophysics*, ed. by Klaus D. Sattler, Taylor&Francis Publisher, CRC Press, (2010).

2 C. Andreani, M. Agio, and S. Botti, "Symmetry properties of two-dimensional photonic crystals" in *Electrons and Photons in Solids*, Quaderni della Scuola Normale Superiore di Pisa, Pisa, Italy, 71 (2001).

Papers

International Journals

3 J. Vidal, F. Trani, F. Bruneval, M. A. L. Marques, and S. Botti, "Effects of electronic and lattice polarization on the band structure of delafossite transparent conductive oxides", submitted to Phys. Rev. Lett. (2010).

4 J. G. Vilhena, S. Botti and M. A. L. Marques "Excitonic effects in the optical properties of CdSe nanowires", accepted for publication in Appl. Phys. Lett. (2010).

5 J. Vidal, S. Botti, P. Olsson, J-F. Guillemoles, and L. Reining, "Strong interplay between structure and electronic properties in $CuIn(S,Se)_2$: a first-principle study", Phys. Rev. Lett. **104**, 056401 (2010).

6 S. Botti, H-Ch. Weissker, and M. A. L. Marques, "Alloying effects on the optical properties of Ge_{1-x} Si_x nanocrystals from time-dependent density functional theory and comparison with effective-medium theory", Phys. Rev. B **79**, 155440 (2009).

7 S. Botti, A. Castro, N. N. Lathiotakis, X. Andrade and M. A. L. Marques, "Optical and magnetic properties of boron fullerenes", Phys. Chem. Chem. Phys. **11**, 4523 (2009).

8 W. Welnic, M. Wuttig, S. Botti, and L. Reining, "Local atomic order and optical properties in amorphous and laser-crystallized GeTe", C.R. Physique **10**, 514 (2009).

9 S. Botti, A. Castro, X. Andrade, A. Rubio and M. A. L. Marques, "Cluster-surface and cluster-cluster interactions: ab initio calculations and modeling of asymptotic van der Waals forces", Phys. Rev. B **78**, 035333 (2008).

10 M. A. L. Marques, A. Castro, G. Malloci, G. Mulas, and S. Botti, "Efficient calculations of van der Waals coefficients with time-dependent density functional theory in real time: application to polycyclic aromatic hydrocarbons" , J. Chem. Phys. **127**, 014107 (2007).

11 W. Welnic, S. Botti, L. Reining, and M. Wuttig, "Origin of the optical contrast in phase change materials", Phys. Rev. Lett. **98**, 236403 (2007).

12 X. Andrade, S. Botti, M. A. L. Marques, and A. Rubio, "Time-dependent density-functional theory for efficient calculations of dynamic (hyper)polarizabilities", J. Chem. Phys. **126**, 184106 (2007).

13 S. Botti, A. Schindlmayr, R. Del Sole, and L. Reining, "Time-dependent density-functional theory for extended systems", Rep. Prog. Phys. **70**, 357-407 (2007).

14 S. Botti and M. A. L. Marques, "Identification of fullerene-like CdSe nanoparticles from optical spectroscopy calculations", Phys. Rev. B **75**, 035311 (2007).

15 H. Vach, Q. Brulin, N. Chaabane, T. Novikova, P. Roca i Cabarrocas, B. Kalache, K. Hassouni, S. Botti, and L. Reining, "Growth dynamics of hydrogenated silicon nanoparticles under realistic conditions of a plasma reactor", Comp. Mater. Sci. **35**, 216 (2006).

16 S. Botti, A. Fourreau, F. Nguyen, Y-O. Renault, F. Sottile, and L. Reining, "Energy dependence of the exchange-correlation kernel of time-dependent density functional theory", Phys. Rev. B **72**, 125203 (2005).

17 M.A.L. Marques and S. Botti, "The planar-to-tubular structural transition in boron clusters from optical absorption", J. Chem. Phys. **123**, 014310 (2005).

18 F. Bruneval, S. Botti, and L. Reining, "Comment on quantum confinement and electronic properties of silicon nanowires", Phys. Rev. Lett. **94**, 219701 (2005).

19 F. Sottile, F. Bruneval, A. G. Marinopoulos, L. K. Dash, S. Botti, V. Olevano, N. Vast, A. Rubio, and L. Reining, "TDDFT from molecules to solids: the role of long-range interactions", Int. J. Quantum Chem. **102**, 684 (2005).

20 S. Botti, N. Vast, L. Reining, V. Olevano, and L.C. Andreani, "Ab initio and semi-empirical dielectric response of superlattices", Phys. Rev. B **70**, 045301 (2004).

21 S. Botti, F. Sottile, N. Vast, V. Olevano, L. Reining, H-Ch. Weissker, A. Rubio, G. Onida, R. Del Sole, and R.W. Godby, "Long range contribution to the exchange-correlation kernel of time-dependent density functional theory", Phys. Rev. B **69**, 155112 (2004).

22 S. Botti, "Applications of time dependent density functional theory", Physica Scripta **T109**, 54 (2004).

23 S. Botti, N. Vast, L. Reining, V. Olevano, and L.C. Andreani, "Ab initio calculations of the anisotropic dielectric tensor of GaAs/AlAs superlattices", Phys. Rev. Lett. **89**, 216803 (2002).

24 Botti and L.C. Andreani, "Electronic states and optical properties of GaAs/AlAs and GaAs/vacuum superlattices by the linear combination of bulk bands method", Phys. Rev. B **63**, 2353133 (2001).

25 S. Botti, A. Rosso, R. Santachiara, and F. Tedoldi, "On-site magnetization in open antiferromagnetic chains: a classical analysis versus NMR experiments in a spin-1 compound", Phys. Rev. B **63**, 012409 (2001).

Popular Science

26 "O que é a Teoria dos Funcionais da Densidade?", M. A. L. Marques and S. Botti, Gazeta de Física **29-4**, 10-15 (2006).

27 L. Reining, A. Marinopoulos, M. Hayoun, O. Hardouin Duparc, V. Olevano, S. Botti, F. Sottile, and N. Vast,"Calculs des spectres électroniques : quelle réponse?", La lettre de l'IDRIS **16**, N. 4 (2002).

Ph.D. Thesis

28 S. Botti, "Semi-empirical and ab initio calculations of the optical properties of semiconductor superlattices" (University of Pavia, Italy, 2002).

29 S. Botti, "Electronic excitations in complex systems: beyond density functional theory for real materials", mémoire de Habilitation à Diriger des Recherches (HDR) (Université "Claude Bernard" Lyon 1, France, 2010).